UNIVERSIDAD COMPLUTENSE DE MADRID

FACULTAD DE CIENCIAS QUÍMICAS

Departamento de Química Física I

MICROPARTICLES PRECIPITATION USING SUPERCRITICAL CO_2 AS AN ANTISOLVENT: ROLE OF THERMAL EFFECTS AND PHASE EQUILIBRIA

MEMORIA PARA OPTAR AL GRADO DE DOCTOR
PRESENTADA POR

Fouad Ramadan Fouad Zahranra

Bajo la dirección de los doctores

Concepción Pando-García Pumarino
Albertina Cabañas Poveda

Madrid, 2012

Universidad Complutense de Madrid

Facultad de Ciencias Químicas

Departamento de Química Física I

Microparticles Precipitation using Supercritical CO_2 as an Antisolvent. Role of Thermal Effects and Phase Equilibria

Doctoral Thesis

Fouad Ramadan Fouad Zahran

Supervisors

Concepción Pando García- Pumarino
Albertina Cabañas Poveda

Madrid, 2012

Universidad Complutense de Madrid

Facultad de Ciencias Químicas

Departamento de Química Física I

Precipitación de Micropartículas Utilizando CO_2 Supercrítico como Agente Antidisolvente. Efectos Energéticos y del Equilibrio de Fases

Memoria que presenta

Fouad Ramadan Fouad Zahran

para optar al grado de doctor

Directores

Concepción Pando García- Pumarino
Albertina Cabañas Poveda

Madrid, 2012

Concepción Pando García- Pumarino, Catedrática y **Albertina Cabañas Poveda,** Profesora Titular del Departamento de Química Física I de la Facultad de Ciencias Químicas de la Universidad de Complutense

CERTIFICAN: que el trabajo presentado como Tesis Doctoral en esta memoria titulada: "Precipitación de Micropartículas Utilizando CO_2 Supercrítico como Agente Antidisolvente. Efectos Energéticos y del Equilibrio de Fases" por Fouad Ramadan Fouad Zahran, para optar al grado de doctor dentro del programa de doctorado en Química Avanzada ("Advanced Chemistry") ha sido realizado en el Departamento de Química Física I, bajo la dirección de dichas personas, autorizando la presentación de la misma para su defensa y calificación por el tribunal correspondiente.

Y para que así conste, expiden el presente certificado en Madrid a 20 de febrero de 2012.

Fdo: Concepción Pando Gª-Pumarino **Fdo: Albertina Cabañas Poveda**

To my parents, my wife and to the memory of the Egyptians dead during 25th January 2011 revolution.

Acknowledgment

After three years of hard working of all of us, I have my thesis done. All thanks to ALLAH “Gracias a Dios”.

I am extremely grateful to Prof. Concepción Pando, for suggesting the thesis theme, the plan of work, and for her continuous supervision, valuable discussions and keen interest.

Great thanks to Prof. Albertina Cabañas for her kind help and valuable discussions through this study. In addition to being a supervisor, she is a partner and a friend. Without the sincere help of Prof. Concepción Pando and Prof. Albertina Cabañas, the realization of this work would not have been possible.

Appreciation is extended to Prof. Juan Antonio Rodríguez Renuncio for his sincere help and careful guidance through the work.

I would like to devote some lines to my wife Shaimaa and my sons Abdulrahman and Eyad who are now 4 years and 4 months old, respectively, for their kind patient for my absent and their support during the study.

Also I would like to thank Prof. José Antonio Rodríguez Cheda, Prof. Eduardo Enciso, Prof. Emilia Sánchez de la Blanca, Prof. María Isabel Redondo and Mr. Miguel Ramos Riesco for their kind help and attention during the characterization of the micronized particles.

Next, I would like to express a general recognition to all researchers and professors in the Department of Physical Chemistry I for their warm welcome and for giving me a helping hand when needed, in especial, my friends and partners in work María José Tenorio and Jacobo Morère.

All thanks to Ehap Yousef, Mohamed Moaid, Walid Fouad, Hitham Elhosiny, Hitham Alashry, Mahmoud Rabei, Mohamed Salah and all my friends who make me fill like I am in my own home.

Finally, I would like to thanks the European Union for its financial support through an Erasmus Mundus University II pre-doctoral grant. All thanks to every person who helped me during the work.

Table of Contents

Chapter 5. Supercritical Antisolvent Micronization of Pharmaceuticals

List of abbreviations

Aerosol solvent extraction	ASES
Back Pressure Regulator	BPR
Cefuroxime axetil	CFA
Dichloromethane	DCM
Dynamic interfacial tension	DIT
N,*N*-dimethylformamide	DMF
Dimethylsulfoxide	DMSO
Design of Experiments	DOE
Differential scanning calorimetry	DSC
Thymidine monophosphate	dTMP
Thymidylate synthase methylates deoxyuridine monophosphate	dUMP
Digital Voltmeter	DVM
Ethyl acetate	EA
Equations of state	EOS
Fourier transform infrared Spectrometer	FTIR
Gas antisolvent	GAS
Infrared spectroscopy	IR
Lower critical end point	LCEP
Liquid-liquid	LL
Liquid-liquid-vapor	LLV
Mixture critical point	MCP
N-methyl-2-pyrrolidone	NMP
Non-steroidal anti-inflammatory drug	NSAID
Precipitation by compressed antisolvent	PCA
Polyethylene glycol	PEG
Particles from Gas-Saturated Solutions (or Suspensions)	PGSS
Poly-DL-lactide acid	PLA
Poly lactide-co-glycolide	PLGA
Particle size	PS
Particle size distribution	PSD
Polyvinylpyrrolidone	PVP
Rapid Expansion of Supercritical Solutions	RESS

Supercritical Antisolvent	SAS
Supercritical carbon dioxide	SC-CO_2
Supercritical fluid	SCF
Standard deviation	SD
Simultaneous DSC and TGA device	SDT
Solution enhanced dispersion by supercritical fluid	SEDS
Scanning electron microscope	SEM
Supercritical fluid chromatography	SFC
Supercritical Fluid Extraction	SFE
Thermal gravimetric analysis	TGA
Upper critical end point	UCEP
Vapor-liquid equilibrium	VLE
X-ray diffraction	XRD
5-Fluorouracil	5-FU

Chapter 1. Introduction

Introduction

1.1. Supercritical Fluids

Supercritical fluids (SCFs) are pure substances or mixtures at a temperature and pressure higher than their critical coordinates. The main distinctive characteristic of a supercritical fluid is its density that is very sensitive to small changes in temperature and pressure; the fluid behavior may be tuned from that of a liquid at a high pressure to that of a gas at low pressure.

Carbon dioxide is the most commonly used supercritical fluid because it is nontoxic, nonflammable, and has a moderate critical temperature and pressure. Fig. 1.1 shows the pressure-temperature phase diagram of carbon dioxide.

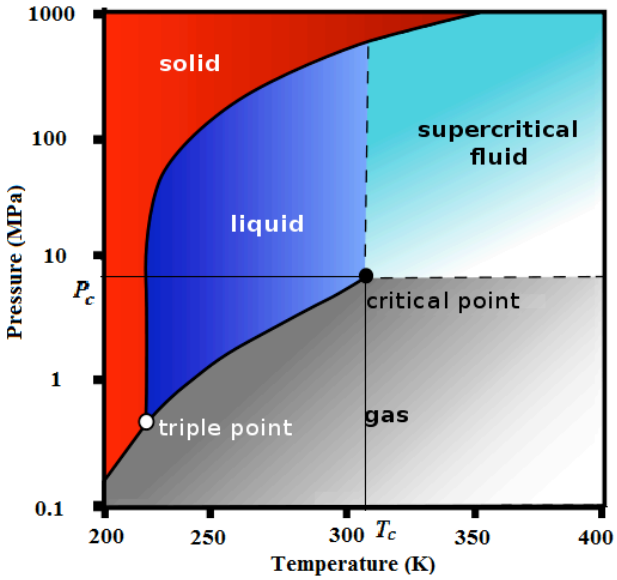

Fig.1.1 Pressure- temperature phase diagram of carbon dioxide [1].

Fig. 1.1 presents conditions where the two phases coexist along with the areas where the single phases exist, and also the point where the three phases coexist at the triple point. The diagram shows the critical pressure (P_c) and the critical temperature (T_c). The supercritical fluid region extends above both P_c and T_c. In this area, lowering the pressure or the temperature will bring the substance into the vapor or the liquid region, respectively, without any phase change occurring. Carbon dioxide has a critical temperature of 304.12 K and a critical pressure of 7.37 MPa [2].

Table 1.1 lists values for the molar masses and the critical temperature, pressure and density of some compounds commonly used as supercritical fluids.

Table 1.1 The critical properties of selected compounds [2].

Component	**Molecular Weight (g/mol)**	T_c **(K)**	P_c **(MPa)**	ρ_c **(g/mL)**
Carbon dioxide	44.01	304.1	7.37	0.469
Water	18.02	647.3	22.12	0.348
Methane	16.04	190.4	4.60	0.162
Ethane	30.07	305.3	4.87	0.203
Propane	44.09	369.8	4.25	0.217
Ethylene	28.05	282.4	5.04	0.215
Propylene	42.08	364.9	4.60	0.323
Methanol	32.04	512.6	8.09	0.272
Ethanol	46.07	513.9	6.14	0.276
Acetone	58.08	508.1	4.70	0.278

As shown, light molecules tend to have lower critical temperatures and higher critical densities than those of larger molecular weight. The critical pressures of most substances range from 3 to 6 MPa. The presence of hydrogen bonds or the polarity of the molecules tend to increase the critical temperature or pressure of the compound. Although a variety of components can be utilized in supercritical fluid processing, common substances such as light hydrocarbons, water and carbon dioxide have received the greatest attention.

1.1.1. Properties of Supercritical Fluids

The distinctive properties of a supercritical fluid in comparison with those typical of gases and liquids are shown in table 1.2. The thermophysical properties of SCF include liquid-like densities, gas-like viscosities and diffusivities much higher than those of liquids.

Table 1.2 Comparison of gases, supercritical fluids and liquids [3].

Property	**Gas**	**SCF**	**Liquid**
Density (kg/m^3)	1	100-800	1000
Viscosity (cP)	0.01	0.05-0.1	0.5-1.0
Diffusivity (mm^2/s)	1-10	0.01-0.1	0.001
Thermal conductivity ($10^{-3}W/mK$)	1	1-100	100

Density is a very important factor in determining the solubility of different compounds. A high-density SCF exhibits a high solvent power similar to that of liquid solvents. On the contrary, in comparison to liquid solvents SCFs have relatively low viscosity and diffusivity values which provide appreciable penetrating power into a solid matrix. These properties give rise to higher rates of mass transfer of solutes into a SCF than into a liquid. On the other hand, heat transfer is favored in a SCF because SCFs have high values of the thermal conductivity in comparison to gases although still lower than those of liquids. Additionally, the low surface tension of SCF allows the fluid to penetrate inside porous materials.

As a result of this combination of properties, SCFs are very interesting substances for different technological applications such as supercritical fluid extraction, material treatment and fabrication, material micronization and reaction media. Supercritical fluid science and technology is a growing field with a wide variety of applications ranging from the extraction of pharmaceutical active ingredients to the synthesis of advantage materials.

One of the most important properties is the solubility of the different materials in the fluid. The solubility in the supercritical fluid tends to increase with an increase of the fluid density at a constant temperature. Fig. 1.2 shows the density of carbon dioxide as a function of pressure and temperature.

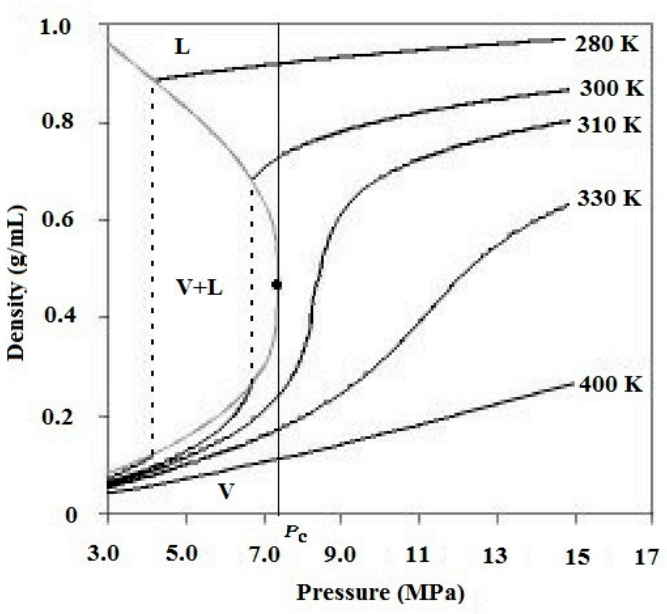

Fig.1.2 Density- pressure phase diagram of carbon dioxide [1].

At a temperature below the critical temperature ($T < T_c$), e.g. at 280 K, as the pressure increases, the density of gaseous carbon dioxide increases. Further increase in pressure results in phase splitting, vapor-liquid equilibrium that is represented as a discontinuous line. By increasing temperature to 300 K, the CO_2 compresses and condenses into a less dense liquid; however, the vapor-liquid equilibrium still exists. At the critical point the two phases become one supercritical fluid phase. At temperatures below T_c, it is required a great increase of pressure in order to slightly increase the density. However, in the supercritical region close to the critical point, small changes in pressure result in large changes in density allowing many properties to be tuned. For carbon dioxide at 310 K ($T > T_c$) a small increase in pressure causes a large increase in the density of the supercritical phase. At higher temperatures, the fluid starts to behave like a gas.

Many pressurized gases are actually supercritical fluids. For example, nitrogen has a critical point of 126.2 K and 3.4 MPa. Therefore, nitrogen (or compressed air) in a gas cylinder above this pressure is actually a supercritical fluid. At room temperature, it behaves as a gas, similar to CO_2 at 400 K and above.

1.1.2. Phase Diagrams of Mixtures Involving Supercritical Fluids

We have defined a supercritical fluid as a substance under a temperature and pressure above their critical coordinates. The same definition may be used for a pure compound and a

mixture. Binary mixtures are usually studied in the first place, then ternary and high order mixtures. This strategy allows us to use our knowledge of mixtures with two or three components in the analysis of multi-component mixtures.

At conditions of temperature or pressure away from the critical point, the P-x and T-x diagrams for a binary mixture are easily understood. However, when we approach the critical point of one of the components, the phase diagram is similar to that shown in Fig. 1.3 for the CO_2 + pentane system at 344 K [4].

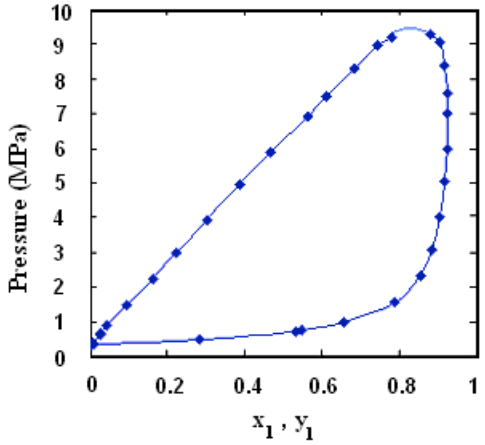

Fig.1.3 Phase diagram of carbon dioxide + pentane at 344 K [4].

For a value of pressure of 5 MPa, the intersection of a parallel to the composition axis with the upper curve provides the CO_2 mole fraction value in the pentane-rich liquid phase (x_1) while the intersection of this line with the lower curve provides the CO_2 mole fraction value in the CO_2-rich vapor phase (y_1). These are the compositions of the liquid and vapor mixtures in equilibrium at 344 K and 5 MPa. Each pair of composition values thus obtained for a given pressure describes possible liquid-vapor equilibrium states for this system. As the pressure goes up, the values of x_1 and y_1 become more similar. At a pressure of 9.5 MPa, the two curves come together, the coincident value of x_1 and y_1 is the composition of the mixture with critical coordinates 344 K and 9.5 MPa. To obtain other critical *P*, *T*, *x* coordinates for this system it is necessary to plot diagrams similar to that of Fig. 1.3 at other temperatures. The set of critical *P*, *T*, *x* coordinates thus obtained defines the so-called critical locus for this particular system. Therefore, a three-dimensional P-T-x plot is necessary in order to analyze the critical behavior of a binary system. Fig. 1.4 shows this plot for a system such as CO_2 + pentane. This is the simplest critical behavior. C_1 and C_2 represent the CO_2 and pentane critical points, respectively.

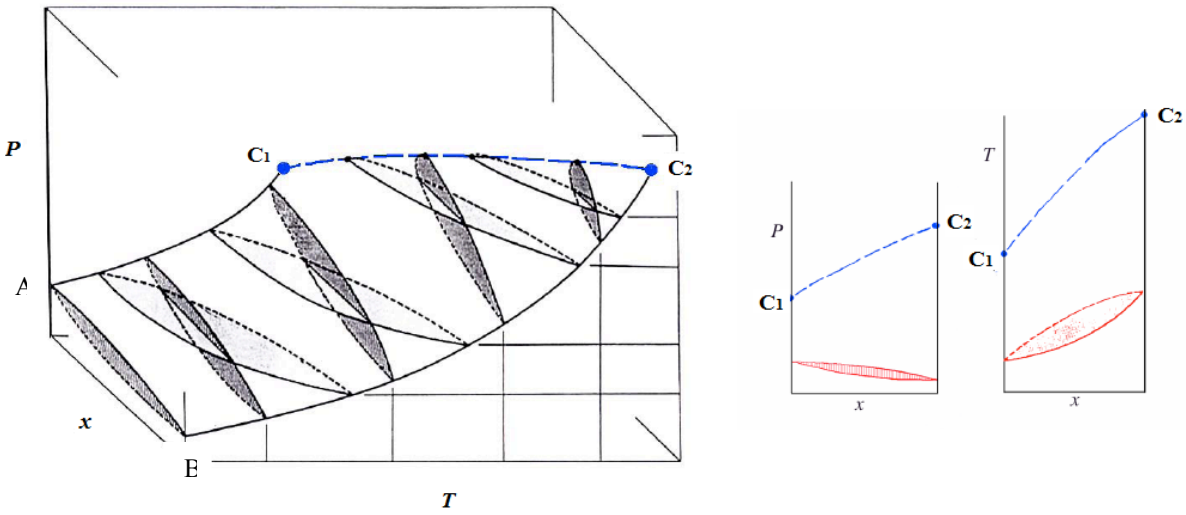

1.4 Left: Tl ree-dimensional P-T-x diagram for the CO_2 + pentane system. Right: P-x and T-x projections.

The full line A-C_1 and B-C_2 represent the vapor pressure curves of both pure components. The h line connecting C_1 and C_2 is the critical locus for the CO_2 + pentane system. The two faces describing the liquid and vapor phase are confined within the curves A-C_1, B-C_2 and C_1-C_2. Fig. 1.4 also shows some isotherm and isobar sections comprised between the liquid and vapor phase surfaces. These sections give rise to the bidimensional P-x and T-x plots shown separately in Fig. 1.4. The P-T diagrams at constant composition for the ethane + heptane system (isoplets, left) together with the projection of the three-dimensional phase diagram on the *PT* plane (right) are shown in Fig. 1.5.

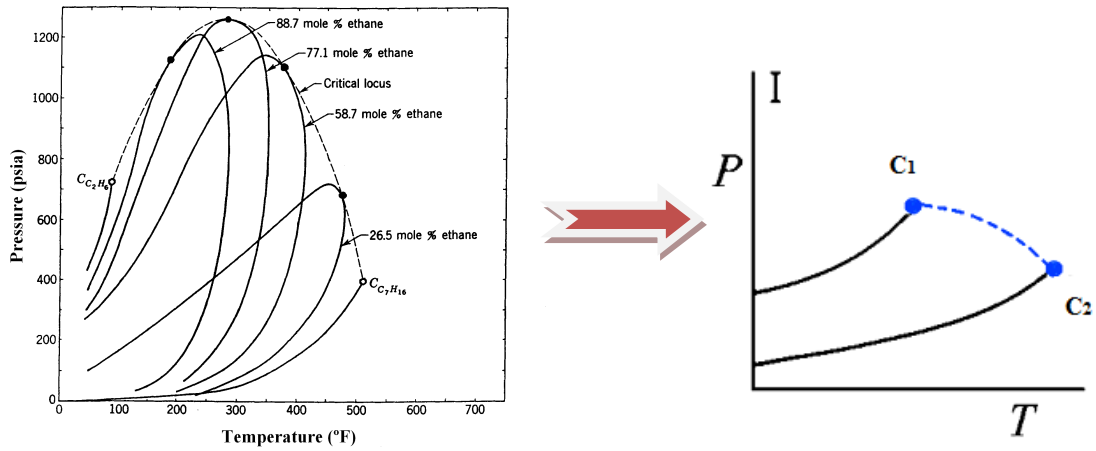

Fig.1.5 Left: Isoplets and critical locus for the ethane + heptane system. Right: P-T projection.

Usually, only the information given in the P-T projection is given. This projection also represents the behavior of the CO_2 + pentane system. In this case, the points of the critical locus close to C_1 would correspond to critical coordinates of CO_2-rich mixtures while those close to C_2 would correspond to pentane-rich mixtures. This simplified representation is the basis of the Scott and van Konynenburg classification [5] of the binary system phase diagrams shown in Fig. 1.6.

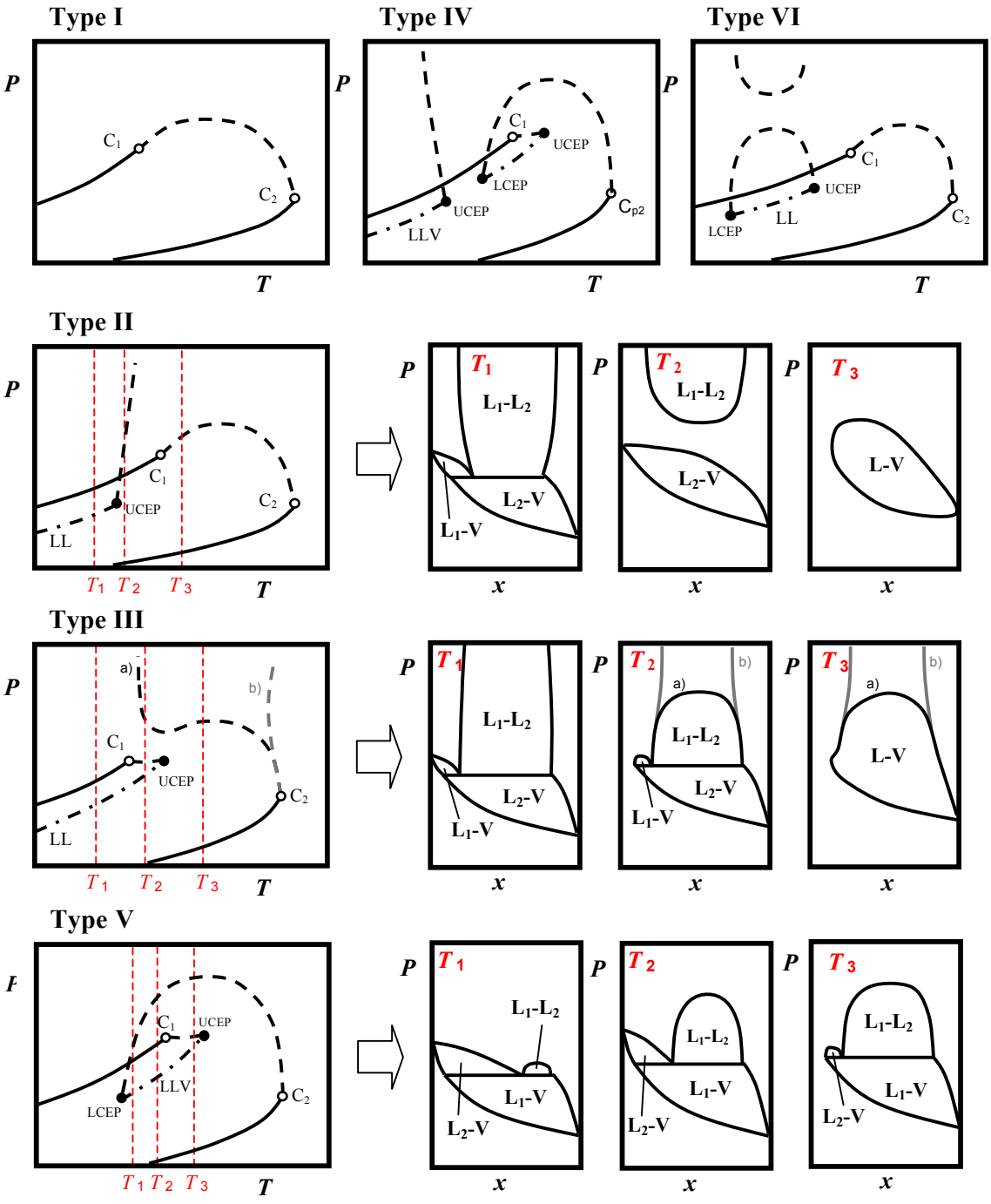

Figure 1.6 Six types of phase behavior in binary fluid systems, points C_1 and C_2 are the critical points of pure components; L = liquid; V = vapor; UCEP = upper critical end point; LCEP = lower critical end point.

Scott and van Konynenburg showed that almost all known types of binary fluid-phase equilibria (vapor-liquid, liquid-liquid and gas-gas equilibria) could be qualitatively predicted using the van der Waals equation of state and the quadratic mixing rules. Using this equation, they were able to generate five types. A type VI phase diagram was added to complete this description by Street [6] but it is much less common. Phase behavior is classified in these six types according to the shape of the critical line and the absence or presence of three-phase equilibrium lines. The appearance and explanation of the various P-T-x diagrams for the all six types are given in details by Mc Hugh and Krukonis [7]. The CO_2 + pentane phase diagram belongs to the type I diagram is characterized for a continuous critical line connecting the critical points of the pure components C_1 and C_2 and the complete miscibility in the liquid phase.

In the type II diagram the two components are not completely miscible and a three-phase equilibrium is possible at temperatures below the critical points of both components. This is the situation along the liquid-liquid-gas line (LLV). The point UCEP indicates the upper consolute temperature for the liquid-liquid equilibrium (L-L) more commonly known as the upper critical end point. At pressures above this point the vapor phase condenses and a dashed line represents the L-L equilibrium.

When the immiscibility extends to temperatures close to the critical temperature of one of the components, the phase diagram may be a type III. In this case the critical line has two sections. The section starting in the critical point of the less volatile component (C_2) reaches high pressures and may exhibit a maximum or a minimum in temperature and/or pressure. When the temperatures in this critical line are higher than that of the component 2, the line is described as a gas-gas critical line (b). The other section of the critical locus is found at lower temperatures and connects the critical point of the more volatile component (C_1) and the upper critical end point (UCEP) that intersects the three-phase equilibrium line (LLV).

In the type IV and V phase diagrams the gas-liquid critical line starts in C_2 and ends in the lower critical end point usually denoted by the acronym LCEP. This point intersects with the three-phase equilibrium line LLV. This line ends in the upper critical end point (UCEP) and is connected to the critical point of the other component through the critical line VL. In the type IV diagram at low temperatures appears a liquid-liquid equilibrium (LL) similar to that exhibited in the type II diagram.

Usually when the two components of the binary system have a similar chemical nature the phase behavior is a type I. When the two components differ, the phase behavior becomes more complicate and type II, III, etc. are observed [8]. For instance, in the CO_2 + alkane series, the phase behavior evolves as the hydrocarbon chain becomes larger. Type I is observed for the systems CO_2 + methane to CO_2 + pentane, type II for CO_2 + octane to CO_2 + undecane, type III for CO_2+ hexadecane and type IV for CO_2 + tridecane [9].

Finally, for some binary systems where one or the two components are self-associated through hydrogen bonding the phase behavior is a type VI. In this case two critical lines are present: a continuous critical line similar to that of types I and II and a LLV equilibrium line at lower temperatures limited by an upper critical end point (UCEP) and a lower critical end point (LCEP). This LCEP distinguishes type VI from type II systems.

The description of high-pressure phase equilibria is not limited to fluid phases. In many SCF applications a solid phase is involved. In this thesis, binary and ternary diagrams without solid interference are involved. For the sake of brevity, the diagrams with solid interference are not described in this introduction.

The critical locus in a ternary system is a surface stretching from the locus of the three related binary systems involved. In the case of type I binary systems the surface will be continuous. In other cases, the critical locus surface presents discontinuities and may become extremely complicate. The analysis of the locus may be simplified if the ternary system is considered as a set of pseudobinary systems. The critical locus for the ternary system CO_2 + hexane + methanol based on this simplification is shown in Fig. 1.7 [10].

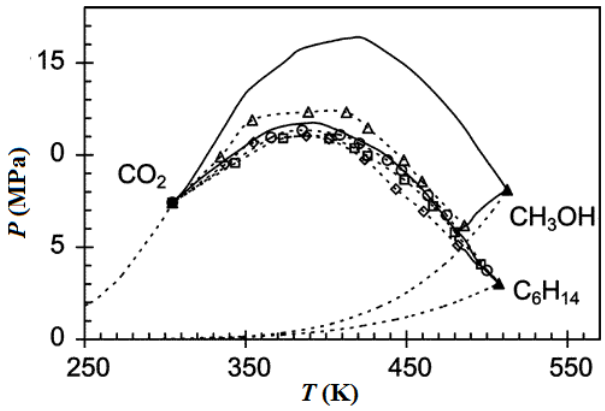

Fig. 1.7 Critical locus of CO_2 (x_1) + hexane (x_2) + methanol (x_3) ternary system. (△): $x_2/x_3 = 1/3$; (◇): $x_2/x_3 = 1$; (□): $x_2/x_3 = 3$; (○): $x_2/x_3 = 5$.

The critical full lines correspond to the three binary systems involved. The symbols connected by dashed lines are critical data obtained for mixtures of CO_2 and a methanol + hexane mixture of fixed composition. In this diagram the pseudobinary component is the hexane + methanol mixture. Each pseudobinary locus (dash lines) will start in the common component CO_2 and will end in a point of the hexane + methanol locus. CO_2 + hexane and CO_2 + methanol are type I systems; methanol + hexane is a type II system.

In the SCF processes involved in this thesis two kinds of ternary systems appear. In the first kind CO_2 is one component and two organic solvents are the second and third components; these are systems that can be treated in a similar way to that above described for the CO_2 + hexane + methanol. In the second kind of systems, the first component is CO_2, the second component is an organic solvent and the third component is a solid that has been previously dissolved in the organic solvent. The nature of this solid is diverse: it may be a drug such as cefonicid or a polymer such as dextran or polyvinylpyrrolidone.

Reverchon et al. [11] have studied the effect of cefonicid on the binary phase diagram of carbon dioxide + dimethylsulfoxide (DMSO). In Fig. 1.8, the P-x diagram for carbon dioxide + DMSO binary system at 60 ºC is represented along with the experimental data obtained in presence of cefonicid.

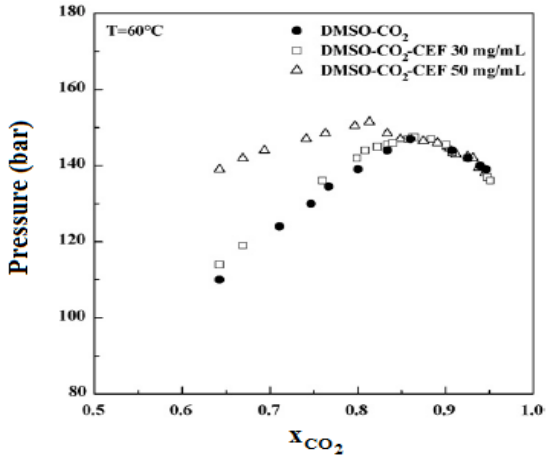

Fig.1.8 The P-x diagram and experimental data for the binary system for CO_2 + DMSO system and the ternary system CO_2 + DMSO + cefonicid [8].

In that study, a view cell was used to analyze the effect that the presence of cefonicid has on the binary CO_2 + DMSO system. They found that at low concentration of cefonicid (30 mg/mL) the experimental vapor-liquid equilibrium (VLE) data for the ternary CO_2 + DMSO

+ cefonicid system is close to the VLE data for the binary CO_2 + DMSO system. On the other hand, at a higher concentration of cefonicid (50 mg/mL) the experimental VLE data for the ternary CO_2 + DMSO + cefonicid system differs from the binary system data at the CO_2-poor region while at the CO_2-rich region the VLE data for the ternary system become almost coincident with the binary data. Differences between the VLE of the binary and ternary systems decrease as the concentration of the solute diminishes and the CO_2 mole fraction increases. Generally, the mixture critical point (MCP) of the ternary system is not coincident with that of the binary system [11]. The binary system MCP is coincident with that of the ternary system when the amount of the third component (cefonicid) is small.

Diego et al. [12] have used a view cell to study the phase behavior of the CO_2 + DMSO + dextran system at pressures up to 8-12 MPa and temperatures ranging from 283.69 to 363.66 K. Phase transition measurements were performed keeping the concentration of CO_2 constant at 20 wt. %. They found that at very low concentrations of dextran polymer (0.1 wt. %) no liquid–liquid phase splitting was observed. When the concentration of dextran is increased to 0.85 wt. %, vapor-liquid, liquid-liquid and the vapor-liquid-liquid splitting were observed. Further increase in concentration of dextran to 8 wt. % made the liquid-liquid splitting occurs at a lower temperature. In the case of dextran that interacts with carbon dioxide the pseudo binary phase diagram, the ternary phase diagram at low concentration of the solute, differs to a great extent from the binary phase diagram [12]. On the contrary, for solutes such as cefonicid that interact weakly with carbon dioxide the ternary phase diagram for the low solute concentration is coincident with the binary one at least in the CO_2-rich region [11].

The knowledge of the phase diagram is a key factor to analyze the phase behavior of systems involved in SCFs applications. For instance, the solubility of a solid or a liquid in a supercritical fluid as a function of pressure at a given temperature is obtained from P-x diagrams such as that shown in Fig. 1.3. The phase diagrams such as that shown in Fig. 1.5 will help us to find the critical temperature and pressure for a given binary mixture. From this information the state of the mixture (liquid, supercritical, vapor-liquid equilibrium) will be established. In the following chapters we will see that phase diagrams are necessary both to understand the fundamentals and to optimize the operating condition in SCF processes. Unfortunately, although data for many binary systems involving a supercritical fluid are available in the literature, data for ternary and higher-order systems are scarce.

1.2. Supercritical Fluid Technology

The environmentally friendly nature of supercritical fluids such as supercritical carbon dioxide (SC-CO_2) has led to the exploration of their use in a range of applications in various fields such as food industry, chemical processing, pharmaceutical industry, textile industry and cleaning of precious components [13-16].

- **Supercritical Fluid Extraction**

Supercritical Fluid Extraction (SFE) is extremely used in industries such as petroleum, chemical and textile industries and to produce high quality extracts from natural raw materials in the food industry. In the pharmaceutical industry this is more challenging because the standards for recovery and reproducibility are more rigorous than for other applications [13]. SFE can be used as a sample preparation step for analytical purposes, or on a larger scale to either strip unwanted component from a product (e.g. decaffeination) [17] or to collect a desired product (e.g. essential oils) [18].

- **Supercritical Fluid Chromatography**

Supercritical fluid chromatography (SFC) is an analytical technique used for the separation of complex chemical mixtures into individual components using a supercritical fluid as a carrier. In SFC the sample is carried through a separating column by a supercritical fluid (typically carbon dioxide) where the mixture is divided into unique bands based on the different interaction between the individual analytes and the stationary phase in the column. As these bands leave the column their identities and quantities are determined by a detector [19]. Preparative SFC can be used for separation of high pressure extracts or for cleaning of product mixtures from reactions. It is also possible to concentrate an extract by removing impurities or unwanted by-products. Preparative SFC is a technically feasible process for purifying a polypeptide from other peptides and from other constituents obtained from fermentation. For example, cyclosporine A can be separated from mycelial extracts by SFC and purified by subsequent crystallization [20].

- **Supercritical Fluid Fractionation**

Fractional separation of the extracts is another well-known concept that can be useful to improve the SFE process selectivity. In several cases, it is not possible to avoid the co-extraction of some compound families (with different solubilities, but also with different mass transfer resistances in the raw matter). In these cases, it is possible to perform an

extraction in successive steps at increasing pressures to obtain the fractional extraction of the soluble compounds contained in the organic matrix, selected by decreasing solubilities in the supercritical solvent. Fractional separation allows the fractionation of the SCF extracts, operating the plant with some separators in series at different pressures and temperatures. The scope of this operation is to induce the selective precipitation of different compound families as a function of their different saturation conditions in the supercritical fluid. Industrial supercritical fluid fractionation generally operates in continuous mode with carbon dioxide as solvent, possibly added with a co-solvent (ethanol most often) to increase its polarity. The equipment mainly consists in a fractionation column through which the supercritical solvent and the raw material flow counter-currently, and separations sections. In contrast to SFE, this process is easy to operate with full automation, leading to very limited manpower expenses and resulting in low operating costs [21].

- **Chemical Reactions**

The use of supercritical fluids as a reaction media offers the chemical and pharmaceutical industries the opportunity to replace conventional hazardous organic solvents and simultaneously optimize and control more precisely the effect of the solvent on reactions. This is related to the unique properties of SCFs in comparison to those of liquids and gases. The reactants and the SCF frequently form a single supercritical fluid phase. SCFs share many of the advantages of gas phase reactions including miscibility with other gases, low viscosity, and high diffusivities providing enhanced mass and heat transfer and the potential for fast reactions. Several chemical reactions, such as oxygenation, hydrogenation and alkylation have been studied in supercritical fluids [22-23].

- **Polymer Processing**

In some applications it is difficult to produce polymers with narrow molecular weight distributions by traditional methods. The solubility parameter of supercritical fluids can be varied carefully and systematically by pressure and temperature to fractionate materials according to molecular weight, because the solubility varies according to the molecular weight or chain length. Therefore, selective extraction and fractionation are possible from a multi-component mixture [13]. Also polymeric foams and the polymer impregnation can be achieved with good control of both processes using SCFs.

- **Particle Coating and Encapsulation**

Drug release profile is an important aspect in pharmaceutical applications. Most of the active pharmaceutical ingredients have a low solubility in aqueous media. Therefore, in the last years the attention of many researches was focused on biodegradable polymeric systems for drug delivery to enhance the therapeutic properties of drugs and patient compliance [24]. Conventional pharmaceuticals methods for the production of protein-loaded microparticles include emulsion or double-emulsion and solvent extraction, spray drying and freeze-drying. Often these techniques use organic solvent, which may cause the drug inactivation, lead to high residual contents of them in the final product and low drugs encapsulation efficiencies [25]. Supercritical fluids can be used to coat tablets and particles of active substance, which have the desired size, with a coating agent [26].

- **Material Micronization**

Fine particles with defined grain size distribution are of interest for many fields of applications. For example, particle size is a critical parameter that determines the rate of dissolution of a drug in biological fluids and thus has significant effect on bioavailability. Particle design is presently a major development of supercritical fluids applications, mainly in the pharmaceutical, nutraceutical, cosmetic and specialty chemistry industries [26, 27]. Next section discusses in more detail particle production using SCFs and in particular the supercritical antisolvent technique.

1.3. Production of Microparticles using Supercritical Fluids

The morphology, size and size distribution of particles are key properties that must meet requirements connected to the subsequent use of these materials. Micro and nanoparticles are increasingly important in the manufacture of advanced ceramic materials, dyes, explosives, catalysts, coating materials, microsensors, polymers, food ingredients and pharmaceuticals. Several conventional micronization techniques are currently used: milling, crystallization, spray drying, spray freezing and recrystallization using solvent evaporation or liquid anti-solvent. This latter technique is based on the use of two liquid solvents that are completely miscible. The solute to be micronized is soluble in the first solvent, but not soluble in the second. Consequently, the addition of the second solvent (antisolvent) induces the formation of a solution formed by the two liquids and the supersaturation and precipitation of the solute. However, liquid antisolvent and solvent evaporation recrystallizations require complex post-

processing treatments for the complete elimination of solvent residues. The other techniques present their own specific disadvantages. For example, spray-drying usually requires high operation temperatures that may lead to thermal degradation of sensitive materials such as pharmaceuticals. Furthermore, all the conventional techniques share the disadvantage of poor control of size and size distribution; usually a wide range of particle sizes is obtained [28].

In the last years, many researchers have successfully tried to overcome the limitations of conventional techniques by exploring the unique properties of supercritical fluids. Processing with supercritical fluids in general and with carbon dioxide in particular has several advantages: non-toxicity and easy removal of the solvent, operation at moderate temperatures in an inert atmosphere thus avoiding the product degradation and the possibility of tuning the fluid properties with changes in temperature and pressure that enables us to control the particle size and/or morphology. Jung and Perrut [26] reviewed in 2001 the different techniques available for particle design using supercritical fluids. Two years before Reverchon [29] reviewed those based on the use of supercritical carbon dioxide as antisolvent agent. In 2003 Shariati and Peters [30] updated these reviews. Later on, other authors reviewed the developments concerning several types of materials: explosives (Pourmortazavi and Hajimirsadeghi, 2005) [31]; polymers (Yeo and Kiran, 2005 [32] and Reverchon et al., 2009 [33]); inorganic materials (Aymonier et al., 2006 [34]); biomedical materials (Byrappa et al., 2008 [35] and Okamoto and Danjo, 2008 [36]); food ingredients (Weidner, 2009 [37]). The techniques can be classified into two groups; the non reactive techniques only involve physical transformations while other techniques use a supercritical fluid as medium (or both solvent and reactant) to carry out a reaction leading to particle formation. Both pure material microparticles and composite microparticles can be obtained using these techniques. Composite microparticles are very important in areas such as pharmaceuticals, agrochemicals, cosmetics or food ingredients and will be introduced in the next section. Next, the non reactive techniques most frequently used will be briefly described.

1.3.1. Composite Microparticles

Many formulations of pharmaceuticals, agrochemicals or cosmetics consist in an active substance encapsulated or embedded in a coating or carrier material that confers additional properties to them. Although composite microparticles have a variety of structures, they are usually classified into microspheres and microcapsules. Microspheres are particles with irregular geometry, composed of an active substance in form of aggregates or molecularly

dispersed solids embedded into a matrix. Microcapsules have spherical geometry; they are composed of a core of active substance surrounded by a solid polymeric or proteic shell. According to their size, microparticles may be classified into nano-spheres/capsules if they are smaller than 1 μm, macro-spheres/capsules if they are larger than 1000 μm and micro-spheres/capsules if they present an intermediate size.

Microspheres Microcapsules

A wide range of materials including pharmaceuticals, flavors, enzymes, and agrochemicals has been embedded/encapsulated. The carrier/shell materials are usually natural or synthetic polymers but fats, sugar and waxes may be also used.

Composite microparticles present several advantages, in the first place, they are easier to handle and dose than the pure particles of an active substance. The material chosen as shell/carrier depends on the intended use of the composite microparticles and improves its properties. A biodegradable carrier is used to achieve a controlled delivery of the active ingredient into the targeted media (the organism of a patient, the soil in agriculture, etc.). If the active substance is susceptible of degradation, the carrier acts a protection against aggressive agents. If the active substance is poorly soluble in the targeted media, the carrier facilitates solubilization. This is the case of a number of poorly water soluble drugs. For drugs with low solubility in the crystalline state, the possibility of improving their solubility, dissolution rate and bioavailability due to the formation of an amorphous form in the composite material presents additional advantages.

As was already mentioned, several conventional techniques to obtain composite materials are available. Cocero et al. [38] have recently reviewed these methods and those resulting from the application of supercritical technologies. The latter have been the subject of numerous investigations during the last years; essentially they are modifications of techniques used to obtain pure particles. The advantages already mentioned for pure material processing using supercritical fluids are also applicable in the case of composites. Furthermore, the supercritical fluid may be used to modify the properties of the carrier (plasticizing, swelling,

or reducing the melting temperature, in the case of a polymer) or the interactions between the carrier and the active substance. These interactions are not fully understood and composite production is still a matter of empirical knowledge.

1.3.2. Rapid Expansion of Supercritical Solutions (RESS)

Val Kukronis [39] was the first scientist who ever tried to apply supercritical fluids for recrystallizing solid materials with the intention of producing fine particles with narrow size distributions. The technique proposed by him was named Rapid Expansion of Supercritical Solutions (RESS) and is based on the supercritical fluid acting as the solvent. The solid material to be micronized is first solubilized in the fluid using an extractor (Fig. 1.9). This is followed by a rapid depressurization of the solution through a nozzle into an expansion vessel where the nucleation of the product leads to a highly dispersed material. Fine particles with a narrow size distribution can be produced at relatively low temperatures using RESS.

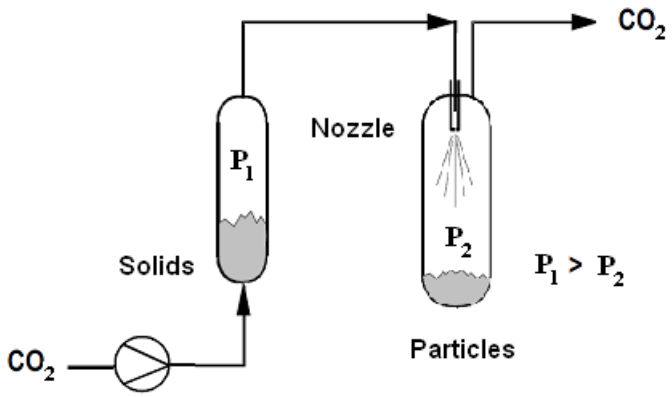

Fig.1.9 Schematic illustration of the Rapid Expansion of Supercritical Solutions (RESS) technique.

Turk [40] has recently reviewed this technique. RESS has the advantage of the absence of organic solvents but its application is restricted to solids that present a good solubility in pure carbon dioxide which is the fluid most frequently used. The low solubility of big and polar molecules such as pharmaceuticals in CO_2 limits RESS application. Otherwise, RESS would be the first choice for particle design. Co-precipitation is also possible but both the carrier and the active substance have to be soluble in CO_2. Since RESS is a very fast process, it is also difficult to control the morphology and loading of the composites. An alternative is the precipitation of the carrier over previously formed microparticles of the active substance.

1.3.3. Particles from Gas-Saturated Solutions (or Suspensions) (PGSS) and Related Processes

Another supercritical fluid process for particle design is the Particles from Gas-saturated Solutions (or Suspensions) (PGSS). In this process the supercritical fluid is dissolved into a liquid substrate, or a solution of the substrate(s) in a solvent, or a suspension of the substrate(s) in a solvent (Fig. 1.10). Next, the liquid mixture is rapidly depressurized through a nozzle causing the formation of solid particles or liquid droplets depending on the mixture and the conditions. This process is based on the high solubilities of compressed gases in liquids and solids such as polymers in comparison with the low solubilities of such liquids and solids in the compressed phase and allows the formation of particles from a variety of substances that do not need to be soluble in the supercritical fluid. PGSS can also be used with suspensions of active substrate(s) in a polymer or other carrier substance leading to composite microspheres.

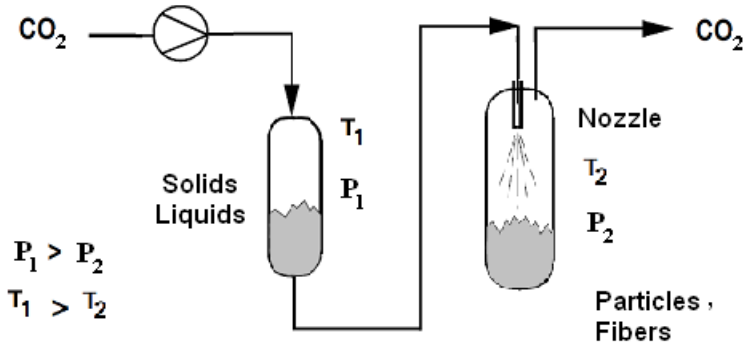

Fig.1.10 Schematic illustration of the Particles from Gas Saturated Solutions (PGSS) technique.

Also, PGSS has been used to apply paintings or other type of coatings such as adhesives. The main drawback of this process is the difficulty to produce submicronic particle and to control particle size distributions. Co-precipitation is possible; the plasticizing and swelling effect caused by CO_2 dissolution in polymers can enhance the incorporation of the active substance. However, if the carrier material has to be used in molten form, high temperatures may be required to melt substances like the semicrystalline polymers that are used for some applications.

Related to the PGSS process is the Depressurization of an Expanded Liquid Organic Solution (DELOS) process proposed by Ventosa et al. [41]. In this process, a compressed gas in an autoclave expands the liquid solution consisting of the solute to be micronized and a

conventional solvent. At this point, the compressed gas acts as a cosolvent, not as an antisolvent. The expanded solution of the ternary mixture of solute-solvent-compressed gas is depressurized by rapid reduction of the system pressure to atmospheric pressure in an expansion chamber. As a consequence, the solution evaporates and its temperature sharply decreases, supersaturation takes place over all the solution and the solute precipitates as fine particles with a narrow size distribution.

1.3.4. Supercritical Antisolvent (SAS) Precipitation

Krukonis et al. [42] were the first to propose the use of supercritical carbon dioxide as an antisolvent to induce controlled precipitation of various solutes from organic solvent solutions. This approach is based on the relatively low solvent power of CO_2 for solutes such as polymers or pharmaceutical products and its good miscibility with many organic solvents. This is the so-called supercritical antisolvent (SAS) precipitation. Different process arrangements, apparatuses and acronyms have been used: GAS (gas antisolvent), PCA (precipitation by compressed antisolvent), ASES (aerosol solvent extraction), SEDS (solution enhanced dispersion by supercritical fluid) and SAS (supercritical antisolvent). The acronym GAS is usually employed for the batch process while SAS provides a good description of the continuous processes. Batch or continuous operation antisolvent techniques are based on the same concept illustrated in Fig. 1.11.

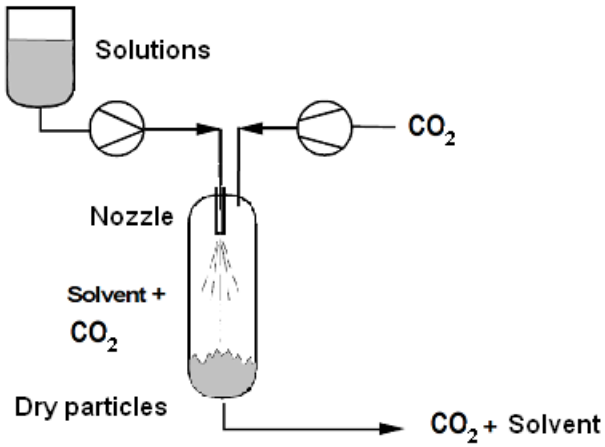

Fig.1.11 Schematic illustration of a supercritical antisolvent micronization.

The compound to precipitate is dissolved in an organic solvent and the solution is mixed in the precipitation chamber with CO_2. When the supercritical CO_2 dissolves in the organic solvent, the liquid experiences a volumetric expansion and becomes a bad solvent for the solute that precipitates from the solution in micro and nanoparticles. The particle size may be

tuned by varying the process parameters such as pressure, temperature, solute concentration, etc. CO_2 accessible critical parameters allow operation at moderate temperatures. Furthermore, these are solvent-free particles exhibiting a narrow size distribution. From the point of view of Sustainable Chemistry, the only disadvantage of SAS is the use of organic solvents but the pressure of operation is much lower than in the RESS technique. In some cases agglomeration retardants or crystal habit modifiers have been used in SAS. As in the RESS process, it is possible to produce composites by simultaneously co-precipitating the active substance and the carrier or by encapsulation of previously formed particles. In the latter case, particles are suspended in a solution of the carrier in the organic solvent and the carrier is precipitated by SAS. In the case of co-precipitation of a drug and a polymer excipient, drug-polymer ratios can be easily modified by varying their relative amounts in the organic solvent solution.

1.3.5. Reactions in Supercritical Media Leading to Particle Formation

Reactions in supercritical media leading to particle formation have also received considerable attention as a mean to synthesize ceramics or oxide materials powders. Contrary to the RESS, SAS, and PGSS processes, the supercritical fluid is used to carry out a chemical reaction. For instance, precursors are dissolved in the fluid and thermally decomposed. Upon depressurization in CO_2, the solvent turns to the gas phase and separates from the particles that are obtained in a highly divided state. Also, a sol-gel reaction may be carried out at high pressure and high temperature. In the hydrothermal synthesis, a supercritical fluid is used both as solvent and reactant. For oxide powders formation, precursors (inorganic salts) are first dissolved in water and the solution is introduced into a reactor operated at supercritical conditions. The crystal growth, morphology, particle size and distribution can be controlled by modifying the thermodynamic and transport properties through changes in pressure and temperature. This technique avoids the crushing and calcination steps used in conventional processes but filtration, washing and drying are still necessary. Unfortunately, corrosion problems associated to the use of supercritical water have to be addressed.

1.4. Fundamentals of Supercritical Antisolvent (SAS) Precipitation

The general applicability of SAS has contributed to its increasing use. In the last years, a variety of compounds including explosives, polymers, pharmaceutical compounds, colorants, catalysts and inorganic compounds has been successfully micronized. As to the particle morphology, different amorphous particle morphologies have been obtained: nanoparticles

with mean diameters in the 30-200 nm range, microparticles in the 0,25-20 μm range and expanded (hollow) microparticles with diameters between 10 and 200 μm. Crystals with various habits and dimensions have been also obtained. Based on these characteristics, SAS has been chosen as the technique to be used in this study.

SAS precipitation consists of several steps:

- Supercritical carbon dioxide is introduced in the precipitation chamber using a high-pressure pump at constant flow rate. Then the solvent or directly the solution is fed also at a constant flow rate reaching steady state operating conditions and an adequate supercritical fluid/solvent ratio. The chamber is heated and both temperature and pressure are controlled.

- The fluid dissolves in the solution formed by the solid and a polar organic solvent such as dimethylsulfoxide (DMSO) or *N*-methyl-2-pyrrolidone (NMP). The liquid expands, the mixture becomes supersaturated and precipitation starts. The solute is collected at the precipitation chamber.

- At the end of the precipitation process, the chamber is washed with the antisolvent to eliminate the liquid solvent. The mixture CO_2 + organic solvent passes to a separation chamber where the solvent is recovered.

The volumetric expansion of the liquid solvent is the result of the massive dissolution of the supercritical antisolvent into the liquid phase. The percentage volume expansion ΔV % is defined as

$$\Delta V\,\% = \frac{V(P,T) - V_0}{V_0} * 100 \qquad (1.1)$$

where V (P, T) is the volume of the liquid phase loaded with the antisolvent and V_0 is the volume of the pure liquid phase at atmospheric conditions.

Many authors have studied the volumetric expansion isotherms for various CO_2 + solvent systems [29, 43]. However, the effect of the solute on the volume expansion at different solution concentrations should be also taken into account. This type of studies is rare. Reverchon et al. [44] have studied this effect in the case of the CO_2 + DMSO + dextran ternary system at 30 °C. Fig. 1.12 shows the expansion curves obtained for the CO_2 + DMSO and CO_2 + DMSO + dextran.

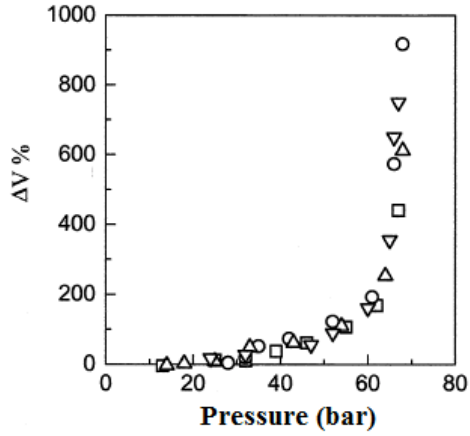

Fig.1.12 Expansion curves for the system CO_2 + DMSO + dextran at 30°C and at increasing dextran contents, ▽, 0%, □, 0.05%, ○, 0.5% and △, 5% [44].

Dextran percentages vary from 0.05 to 5 %. The presence of dextran does not modify the expansion behavior. Values of ΔV % for the ternary mixtures follow the same isotherm of the binary CO_2 + solvent system. Although these data correspond to a temperature lower than those usually employed in SAS, they point out that for the low solute concentration used in this technique volume expansion may be described using the binary data.

The feasibility of SAS and the particle morphology, size and size distribution depend on a large number of process parameters: temperature, pressure, solute concentration, choice of the solvent, injection mode of the antisolvent, etc. These parameters simultaneously influence high-pressure phase equilibria, hydrodynamics, mass transfer and particle formation and growth. All these influences must be taken into account and their interrelation has to be elucidated for a better understanding of SAS. Experimental studies usually explore different combinations of the process parameters and the optimum values are selected after considerable work. Sometimes, a design of experiment strategy is followed to minimize the number of micronization experiments. Nevertheless, it is difficult to extract general conclusions from this type of studies or to obtain information about the scale-up necessary for commercial applications. This has prompted many authors to carry out experimental and theoretical studies aimed to a more detailed understanding of the fundamentals and mechanisms of SAS. Interactions between high-pressure vapor-liquid equilibria, surface tension variations, jet fluid dynamics, mass transfer, nucleation and growth have to be taken into account to establish the mechanisms of particle precipitation. A detailed review of all these contributions is beyond the scope of this introduction.

Prof. E. Reverchon and Prof. M. J. Cocero, and their groups at the University of Salerno (Italy) and Universidad de Valladolid (Spain), respectively, have contributed to a large extent both to SAS experimental studies and to the analysis of the precipitation mechanisms. Martín and Cocero [45] reviewed in 2008 the contributions to SAS fundamentals and mechanisms. Attention was paid to the fluid mechanics, the transport and thermodynamic properties, mass transfer and particle formation and growth. As shown by Reverchon, Brauer and coworkers using light and laser scattering techniques [46, 47], SAS mechanisms result from an interplay of these phenomena. In two recently published papers, De Marco and Reverchon [48, 49] summarized these contributions and the most important conclusions.

Some authors attempted an explanation of SAS mechanisms, starting from the analysis of the fluid dynamic behavior of the solution injected into the pressurized antisolvent. Lengsfeld et al. [50] indicated that gas-like jet mixing is the characteristic mechanism when completely miscible conditions for the system solvent–antisolvent are set in the precipitator, and is due to the disappearance of the dynamic surface tension, related to the formation of a supercritical solution. Successively, Dukhin et al. [51], Sarkari et al. [52], Badens et al. [53], Gokhale et al. [54] and Obrzut et al. [55] studied the jet atomization in pressurized gases. Two process characteristic times were observed: a relaxation time τ and a jet break-up time t. If $t < \tau$, a real interface exists between the liquid and the fluid phase, and jet break-up prevails transforming the liquid jet in droplets. If $\tau < t$, near the nozzle orifice a short jet is present, then, gas-like jet mixing is obtained in the absence of any interface. Dukhin et al. [51] also discussed the existence of a different dynamic interfacial tension (DIT) mechanism driven by enthalpy gradients. A new nonisothermic DIT mode was introduced and shown to contribute to the jet stability in the case of exothermic mixing. Debenedetti and Werling [56, 57] introduced mathematical models of the mass transfer. Baldyga et al. [58] and Martín and Cocero [59] proposed models for the precipitation process above and below the critical point for the CO_2 + solvent mixture, MCP.

In agreement with this description of the different fluid mechanic mechanisms, Reverchon et al. [60] found that when operating at pressures above the mixture critical point, the parameters which affect the mixing between the two streams, as the design of the nozzle and the precipitator, or the Reynolds number in the nozzle, have a negligible effect on the precipitation. This indicates that, in these conditions, the mixing between solution and CO_2 occurs faster than the precipitation, and thus the mixing parameters cannot influence the

precipitation. However, at pressures below the mixture critical point, there was a significant effect of these parameters. Moreover, a change in particle morphology was frequently observed when pressure was reduced below this point, and sometimes, the particles were agglomerated forming empty spheres, which could indicate that the atomization and precipitation occurs through the formation of droplets. A correlation between SAS particles dimension and the position of the SAS operating point in the vapor–liquid equilibrium (VLE) diagram has been established. At pressures far above the MCP nanoparticles can be precipitated [11, 61, 62]; near above the MCP, microparticles can be obtained [63]. In some cases nanoparticles and microparticles can coexist. The uniformity of the resulting products becomes worse when the precipitation conditions approach the critical locus. Irregular micro-scale aggregated particles are formed in the vapor region and both dense cake and spherical clusters are produced in the vapor-liquid region. This is illustrated by the relationship between particle morphology and the phase equilibria for the CO_2 + DMSO in the micronization of α-chymotrypsin studied by Chang et al. [61]. Their findings are summarized in Fig. 1.13.

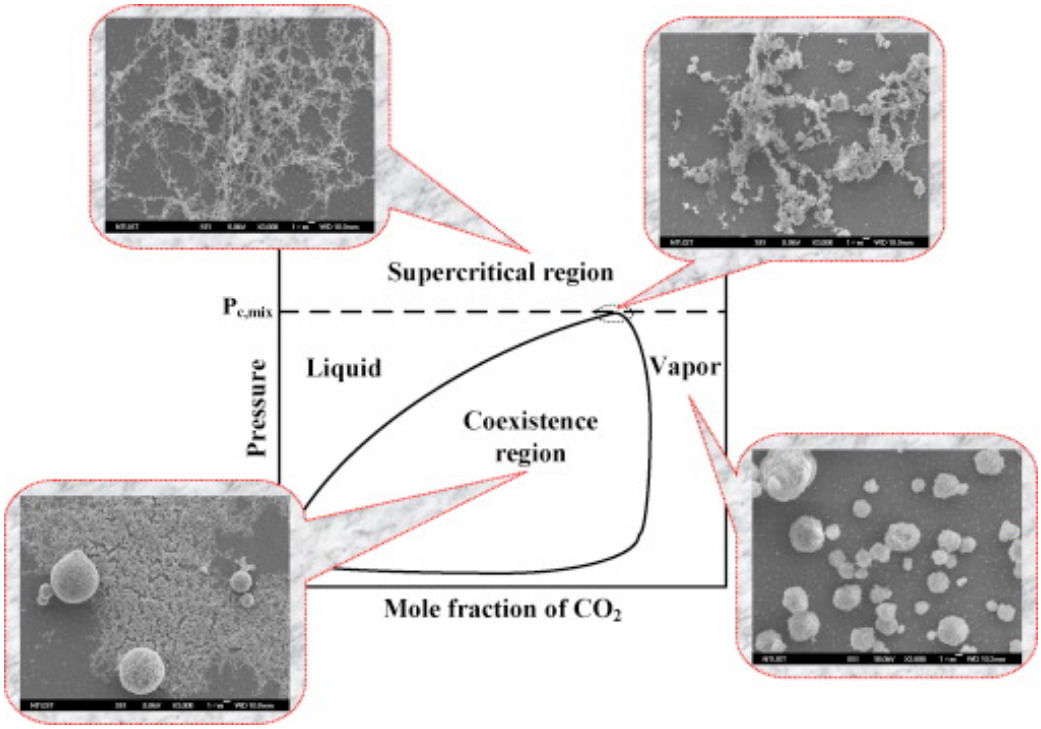

Fig. 1.13 Scanning electron microscopy images of micronized α-chymotrypsin prepared from different CO_2 + DMSO phase regions [61].

An interpretation of the results obtained operating at different pressures has been proposed [46, 48, 63] showing that the switch between nanoparticles and microparticles production is related to the competition between the jet break-up of the liquid injected in the precipitator and gas mixing. When jet break-up prevails, liquid droplets are formed that can produce micrometric particles by liquid solvent extraction; when gas mixing develops in the precipitator without jet break-up, nanoparticles are produced by precipitation from the fluid phase. The competition between these two processes can be explained taking into account their characteristic times: when the time for jet break-up is shorter than the time occurring for the vanishing of the dynamic surface tension, droplets are formed; in the opposite case, gas mixing prevails [46, 63, 64]. Nanoparticles differ from microparticles not only for their diameter but also for the fact that are irregularly spherical as a consequence of the gas-to-solid precipitation in absence of surface tension. De Marco and Reverchon [48] also showed that these precipitation mechanisms can be modulated either by varying the pressure, temperature or solute concentration, thus selecting the range of particle sizes required for a given application.

Mechanisms differ when the compound precipitates as crystals [49]. In this case two possible mechanisms are involved. Crystals with a spherical predominant shape are formed when the droplets drying is followed by a fast crystallization kinetics. When precipitation takes place in an expanded liquid phase, crystals of various habits and dimensions are obtained depending on the interactions with the liquid solvent used.

Since the phase behavior is one of the crucial factors governing the morphology and the mean size of particles obtained in the SAS process, the high-pressure phase equilibria of binary mixtures formed by CO_2 and the organic solvents usually employed in SAS have received considerable attention in the last years. The presence of solutes such polymers can induce modifications in the phase diagram. Unfortunately, data for the ternary systems including the solute are scarce. However, when the solute has little interaction with carbon dioxide the ternary phase diagram for the low solute concentrations usually employed in SAS is coincident with the binary one in the CO_2-rich region which is the region for mixtures involved in SAS. As previously mentioned in section 1.1.2., this is the case for the CO_2 + DMSO + cefonicid systems. Therefore, in many cases the mixtures formed in the precipitation chamber may be treated as binary CO_2 + organic solvent systems. Volumetric properties, densities and critical parameters for this type of binary systems have been the

subject of numerous studies. However, with the exception of Dukhin et al. [51], no attention has been paid to the heat evolved when supercritical CO_2 dissolves into the organic solvent. The heat of mixing (excess enthalpy) at these conditions can be quite high. Thus, thermal effects during this process may have an effect on the phase separation path and must be considered in order to fully understand SAS micronization. The contribution to this magnitude due to solute interactions may be neglected: thermal effects can be analyzed by measuring the excess enthalpies for the CO_2 + organic solvent mixtures formed in SAS precipitation chamber.

By measuring the heat of mixing supercritical CO_2 and *N*-methyl-2-pyrrolidone at the conditions of temperature and pressure used in SAS experiments, our group has shown in a previous study [65] that thermal effects have an important role on SAS and seem to be related to marked coalescence phenomena reported for antibiotic particles obtained using NMP. The conditions of temperature and pressure leading to this undesirable coalescence are coincident with those for extremely exothermic heats of mixing. A systematic study of excess enthalpies for these CO_2 + organic solvent mixtures and parallel CO_2 micronizations should be carried out in order to elucidate the effect of temperature, pressure and the interactions between phase equilibria and the heat evolved when the supercritical fluid and the solution are mixed. The heat of mixing supercritical CO_2 and methanol and ethanol has been previously studied [66-68]. However, this magnitude is not known for other solvents widely used in SAS such as DMSO and acetone.

1.5. Application of Supercritical Antisolvent Precipitation in the Field of Pharmaceuticals

In addition to the interest in SAS fundamentals, the application of SAS in the field of pharmaceuticals is a very active field of research [33, 35, 36]. In the case of pure substances, SAS allows a good control of size and morphology. Crystals, nanoparticles and microparticles for improved drug delivery of many pharmaceuticals have been produced. All the studies mentioned in the previous section can be applied in this case.

The formation of composite microparticles is less understood [33, 38]. In the precipitation over a suspension of particles, the particles behave as nuclei for the precipitation of the polymer and a polymer matrix of encapsulated particles is produced by agglomeration. This procedure is especially suitable for organic insoluble materials such as proteins. Co-

precipitation is preferred for organic soluble drugs. Nanoparticles precipitation does not give co-precipitation due to the gas-to-particle mechanism that governs this process. Polymer-drug composite microparticles seem to be formed by the solvent elimination from liquid droplets. The process is more complicate than that for pure drugs. New parameters such as the polymer mass or the polymer to drug ratio have to be considered.

In contrast to pure material micronization, co-precipitation is still a matter of empirical knowledge. As Reverchon et al. pointed out [33], although a polymer such as poly(L-lactide) (PLLA) has been used in many studies, no systematic investigation on how composite properties are influenced by the SAS process parameters has been undertaken. Polymer-drug interactions need to be studied in order to obtain information about what one can expect for the same polymer in combination with a different drug.

The selection of the carrier or coating material is crucial. Several requisites must be fulfilled: biocompatibility, lack of toxicity, preservation of the properties and activity of the drug, and affinity between both substances. Thanks to this affinity, the drug is included in the carrier in the amorphous state. The coating or carrier material should be also easy to process with the SAS technique. The incorporation of the drug in its amorphous state leads to composite particles much smaller than the size of pure material precipitated under the same conditions. This is an additional advantage to be added to the improved solubility, dissolution rate and bioavailability of the amorphous pharmaceutical.

Several polymers have been used in SAS co-precipitation: PLLA, polyethylene glycol (PEG), polyvinylpyrrolidone (PVP), lactide glycolide copolymer (PLGA), poly-DL-lactide acid (PLA), eudragit. In this study, PVP has been chosen because this polymeric lactam is one of the major additives in pharmaceutical preparations. Its inclusion in dry form pharmaceuticals improves the dissolution rates and bioavailability of drugs with low solubility.

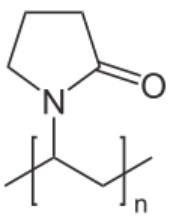

Poly[1-(2-oxo-1-pyrrolidinyl)ethylene], IUPAC name of PVP.

Enhancement of dissolution rates is caused by the inhibition of crystallization of drugs. This is mostly due to the plasticizing effect of PVP and its surface adsorption and efficient steric hindrance for nucleation and crystal growth [69-70]. Furthermore, PVP is a synthetic water-soluble linear polymer that is also able to dissolve in a variety of organic solvent. The properties of PVP and the analytical techniques used to characterize drug-PVP systems in solid and liquid states have been reviewed by Chadha et al. [71]. Depending on the conditions of polymerization, PVP can be prepared in a variety of molecular weights expressed by the so called *K*-values.

$$K\text{-value} = [\{300\ C\log Z + (C + 1.5\ C\log Z)^2\}^{0.5} + 1.5\ C(\log Z) - C]/\{0.15\ C + 0.003\ C^2\} \quad (1.2)$$

where Z is the viscosity of PVP at concentration C relative to water.

From the following equations the number average ($\overline{M}_n$), the weight average ($\overline{M}_w$) and the viscosity average molecular weight ($\overline{M}_v$) may be determined:

$$\overline{M}_n = 24^* K^2,\ \overline{M}_w = 15^* K^{2.3},\ \overline{M}_v = 22.22\ (K + 0.0075\ K^2)^{1.65} \quad (1.3)$$

The glass transition temperature (T_g) of linear PVP increases with increasing molecular weight and is calculated according to the following equation:

$$T_g\ [^\circ C] = 175 - (9685/K^2) \quad (1.4)$$

Recently, PVP has been used in combination with SAS micronization as a carrier or excipient for several pharmaceuticals. Lim et al. [72] obtained amorphous indomethacin composite microparticles by co-precipitation with PVP *K*-90. Indomethacin is a crystalline non-steroidal anti-inflammatory drug. Uzun et al. [73] also obtained composite microparticles formed by the antibiotic cefuroxime axetil and PVP *K* -30. Badens and coworkers [74, 75] prepared solid dispersions of oxeglitazar in PVP *K*-17. Oxeglitar is a new drug used in the treatment of type II diabetes. Composite microparticles formed by piroxicam and PVP *K*-25 were obtained by Wu et al. [76] by PCA. Processes related to SAS have been also used. Hydrocortisone-PVP composite microparticles were successfully prepared by Corrigan and Crean [77] using GAS. Good morphologies and improved dissolution rates were obtained in most cases.

PVP interacts with the drug molecule by electrostatic bonds (ion to ion, ion to dipole, dipole to dipole), van der Waals forces and H-bonds. A number of physicochemical techniques provide information about the interactions drug-PVP: X-ray diffraction (XRD), differential scanning calorimetry (DSC) and infrared spectroscopy (IR) are the most used ones. XRD also provides information about changes in the crystallinity and polymorphic form of the drug as a consequence of SAS micronization. DSC may be used to establish the glass transition temperatures. IR is used to detect hydrogen bonding between the drug and PVP through the nitrogen or the carbonyl group in the pyrole ring. Scanning electron microscopy provides information about the morphology of the pure drug, PVP and the composites. The solubility and dissolution rate of the drug-PVP combination or composite is another key aspect. Dissolution tests are carried out in simulated intestinal fluid (pH = 7.4) and results are compared to those obtained for the pure drug.

References

[1] S. Angus, B. Armstrong and K. De Reuck. International Thermodynamic Tables of the Fluid State, Vol. 3., Carbon Dioxide, IUPAC, Pergamon Press, Oxford (1976).

[2] B. E. Poling, J. M. Prausnitz and J. P. O'Connell. Properties of Gases and Liquids, 5th Ed., McGraw-Hill Inc. New York (2001).

[3] C. Erkey. Supercritical Fluids and Organometallic Compounds, From Recovery of Trace Metals to Synthesis of Nanostructured Materials, 1st Ed., Elsevier Science & Technology Books, Butterworth-Heinemann Amsterdam (2011).

[4] G. J. Besserer and D. B. Robinson. Equilibrium phase properties of n-pentane-carbon dioxide system, *J. Chem. Eng. Data* 18 (1973) 416–419.

[5] R. L. Scott, P. H. van Konynenburg. Van der Waals and related models for hydrocarbon mixtures, *Discuss. Faraday Soc.* 49 (1970) 87–97.

[6] W. Street. Phase Equilibria in Fluid and Solid Mixtures at High Pressure, In Chemical Engineering at Supercritical Fluid Conditions, M. E. Paulaitis, J. M. Penninger, R. D. Gray Jr. and P. Davidson (Eds.) Ann Arbor Science Collingwood, Chap.1 (1983) 3–30.

[7] M. McHuch and V. Krukonis. Supercritical Fluid Extraction: Principles and Practice, 2nd Ed., Butterworth-Heinemann Boston (1994).

[8] G. M. Schneider. The continuity and family concepts: useful tools in fluid phase science, *Phys. Chem. Chem. Phys.* 6 (2004) 2285–2290.

[9] M. Prausnitz, R. N. Lichtenthaler and E. G. Azevedo. Molecular Thermodynamics of Fluid-Phase Equilibria, 3rd Ed., Prentice Hall PTR New Jersey (1999).

[10] J. Liu, Z. Qin, G. Wang, X. Hou and J. Wang. Critical Properties of Binary and Ternary Mixtures of Hexane + Methanol, Hexane + Carbon Dioxide, Methanol + Carbon Dioxide, and Hexane + Carbon Dioxide + Methanol, *J. Chem. Eng. Data* 48 (2003) 1610–1613.

[11] E. Reverchon, I. De Marco, E. Torino. Nanoparticles production by supercritical antisolvent precipitation: A general interpretation, *J. Supercrit. Fluids* 43 (2007) 126–138.

[12] Y. P. de Diego, F.E. Wubbolts, G. J. Witkamp, Th. W. de Loos and P. J. Jansens. Measurements of the phase behaviour of the system dextran/DMSO/CO2 at high pressures, *J. Supercrit. Fluids* 35 (2005) 1–9.

[13] K. Vasukumar and A. Bansal. Supercritical Fluid Technology in Pharmaceutical Research, *Crips*, 4 (2003) 8–12.

[14] E. Stahl, K. W. Quirin and D. Gerard. Dense Gases for Extraction and Refining. Springer-Verlag Berlin (1988).

[15] M. B. King and T. R. Bott. Extraction of natural products using near-critical solvents, 1st Ed., Springer US (1993).

[16] S. S. H. Rizvi. Supercritical fluid processing of Food and Biomaterials, 1st Ed., Springer US (1998).

[17] M. D. A Saldaña, C. Zetzl, R. S. Mohamed and G. Brunner. Decaffeination of guaraná seeds in a micro extraction column using water-saturated CO_2, *J. Supercrit. Fluids* 22 (2002) 119–127.

[18] H. Sovová. Steps of supercritical fluid extraction of natural products and their characteristic times, *J. Supercrit. Fluids* doi:10.1016/j.supflu.2011.11.004.

[19] L. T. Taylor. Supercritical fluid chromatography for the 21st century, *J. Supercrit. Fluids* 47 (2009) 566–573.

[20] O. Aaltonen, M. Alkio, J. Lundell, S. Ruohonen, S. Parvinen, and V. Suoninen. Polypeptide Purification with Industrial-Scale Supercritical Fluid Chromatography, *Pharma Tech. Europe.* 10 (1998) A 42–54.

[21] E. Reverchon and I. De Marco. Supercritical fluid extraction and fractionation of natural matter, *J. Supercrit. Fluids* 38 (2006) 146–166.

[22] C. Jessop and W. Leitner. Chemical Synthesis Using Supercritical Fluids, 1st Ed., Wiley-VCH, Weinheim Germany (1999).

[23] M. Rantakylä and O. Aaltonen. Enantioselective Esterification of Ibuprofen in Supercritical Carbon Dioxide by Immobilized Lipase, *Biotechnol. Lett.* 16 (1994) 825–830.

[24] M. Vajdy and D. T. O'Hagan. Microparticles for intranasal immunization, *Adv. Drug Delivery Rev.* 51(2000) 127–141.

[25] N. Elvassore, K. Vezzù, A. Bertucco, A. Cecchi and P. Caliceti. Protein Loading in Biodegradable Polymeric Micro-Particles Produced by Compressed Gas Antisolvent Techniques, *Proceedings of the 4th International Symposium on High Pressure Technology and Chemical Engineering*. Venice, Italy (2002).

[26] J. Jung and M. Perrut. Particle Design Using Supercritical Fluids: Literature and Patent Survey, *J. Supercrit. Fluids* 20 (2001) 179–219.

[27] Ž. Knez and E. Weidner. Particles formation and particle design using supercritical fluids, *Curr. Opin. Solid State Mater. Sci.* 7 (2003) 353–361.

[28] N. Rasenack, H. Hartenhauer and B. W. Müller. Microcrystals for dissolution rate enhancement of poorly water-soluble drugs*, Int. J. Pharm.* 254 (2003) 137–145.

[29] E. Reverchon. Supercritical antisolvent precipitation of micro- and nano-particles, *J. Supercrit. Fluids* 15 (1999) 1–21.

[30] A. Shariati and C. J. Peters. Recent developments in particle design using supercritical fluids, *Curr. Opin. Solid State Mater. Sci.* 7 (2003) 371–383.

[31] S. M. Pourmortazavi and S. S. Hajimirsadeghi. Application of Supercritical Carbon Dioxide in Energetic Materials Processes: A Review, *Ind. Eng. Chem. Res.* 44 (2005) 6523–6533.

[32] S.-D. Yeo and E. Kiran. Formation of polymer particles with supercritical fluids: A review, *J. Supercrit. Fluids* 34 (2005) 287–308.

[33] E. Reverchon, R. Adami, S. Cardea and G. D. Porta. Supercritical fluid processing of polymers for pharmaceutical and medical applications, *J. Supercrit. Fluids* 47 (2009) 484–492.

[34] C. Aymonier, A. Loppinet-Serani, H. Reverón, Y. Garrabos and F. Cansell. Review of supercritical fluids in inorganic materials science, *J. Supercrit. Fluids* 38 (2006) 242–251.

[35] K. Byrappa, S. Ohara and T. Adschiri. Nanoparticles synthesis using supercritical fluid technology - towards biomedical applications, *Adv. Drug Deliv. Rev.* 60 (2008) 299–327.

[36] H. Okamoto and K. Danjo. Application of supercritical fluid to preparation of powders of high-molecular weight drugs for inhalation, *Adv. Drug Deliv. Rev.* 60 (2008) 433–446.

[37] E. Weidner. High pressure micronization for food applications, *J. Supercrit. Fluids* 47 (2009) 556–565.

[38] M. J. Cocero, Á. Martín, F. Mattea and S. Varona. Encapsulation and co-precipitation processes with supercritical fluids: Fundamentals and applications, *J. Supercrit. Fluids* 47 (2009) 546–555.

[39] V. Kukronis. Supercritical nucleation of difficult-to-comminute solids, Annual AIChE Meeting, San Franciso (1984).

[40] M. Turk. Manufacture of submicron drug particles with enhanced dissolution behaviour by rapid expansion processes, *J. Supercrit. Fluids* 47 (2009) 537–545.

[41] N. Ventosa, S. Sala and J. Veciana. DELOS process: a crystallization technique using compressed fluids. 1. Comparison to the GAS crystallization method, *J. Supercrit. Fluids* 26 (2003) 33–45.

[42] P.M. Gallagher, M.P. Coffey, V.J. Krukonis and N. Klasutis. Gas anti-solvent recrystallization: new process to recrystallize compounds insoluble in supercritical fluids, in: Supercritical Science and Technology, *ACS Symp. Ser.* 406 (1989) 334–354.

[43] J. C. F. Badilla, C. J. Peters and J. S. Arons. Volume expansion in relation to the gas–antisolvent process, *J. Supercrit. Fluids* 17 (2000) 13–23.

[44] E. Reverchon, G. D. Porta, I. De Rosa, P. Subra, D. Letourneur, Supercritical antisolvent micronization of some biopolymers. *J. Supercrit. Fluids* 18 (2000) 239-245.

[45] A. Martín and M. J. Cocero. Micronization processes with supercritical fluids: fundamentals and mechanisms. *Adv. Drug Delivery Rev.* 60 (2008) 339–350.

[46] E. Reverchon, E. Torino, S. Dowy, A. Brauer and A. Leipertz. Interactions of phase equilibria, jet fluid dynamics and mass transfer during supercritical antisolvent micronization, *Chem. Eng. J.* 156 (2010) 446–458.

[47] A. Brauer, S. Dowy, E. Torino, M. Rossmann, S.K. Luther, E. Schluecker A. Leipertz and E. Reverchon. Analysis of the supercritical antisolvent mechanisms governing particles precipitation and morphology by in situ laser scattering techniques, *Chem. Eng. J.* 173 (2011) 258–266.

[48] I. De Marco and E. Reverchon. Influence of pressure, temperature and concentration on the mechanisms of particle precipitation in supercritical antisolvent micronization, *J. Supercrit. Fluids* 58 (2011) 295-302.

[49] E. Reverchon and I. De Marco. Mechanisms controlling supercritical antisolvent precipitate morphology, *Chem. Eng. J.* 169 (2011) 358-370.

[50] C. S. Lengsfeld, J. P. Delplanque, V. H. Barocas and T. W. Randolph. Mechanism governing microparticle morphology during precipitation by a compressed antisolvent: atomization vs. nucleation and growth. *J. Phys. Chem. B* 104 (2000) 2725–2735.

[51] S. S. Dukhin, C. Zhu, R. Dave, R. Pfeffer, J. J. Luo, F. Chávez and Y. Shen. Dynamical interfacial tension near critical point of a solvent-antisolvent mixture and laminar jet stabilization, *Colloids Surf., A* 229 (2003) 181–189.

[52] M. Sarkari, I. Darrat and B. L. Knutson. Generation of microparticles using CO_2 and CO_2-philic antisolvents, *AIChE J.* 46 (2000) 1850–1859.

[53] E. Badens, O. Boutin and G. Charbit. Laminar jet dispersion and jet atomization in pressurized carbon dioxide, *J. Supercrit. Fluids* 36 (2005) 81–90.

[54] A. Gokhale, B. Khusid, R.N. Dave and R. Pfeffer. Effect of solvent strength and operating pressure on the formation of submicrometer polymer particles in supercritical microjets, *J. Supercrit. Fluids* 43 (2007) 341–356.

[55] D. L. Obrzut, P. W. Bell, C. B. Roberts and S. R. Duke. Effect of process conditions on the spray characteristics of a PLA plus methylene chloride solution in the supercritical antisolvent precipitation process, *J. Supercrit. Fluids* 42 (2007) 299–309.

[56] J. O. Werling and P.G. Debenedetti. Numerical modeling of mass transfer in the supercritical antisolvent process, *J. Supercrit. Fluids* 16 (2) (1999) 167–181.

[57] J. O. Werling and P. G. Debenedetti. Numerical modeling of mass transfer in the supercritical antisolvent process: miscible conditions, *J. Supercrit. Fluids* 18 (2000) 11–24.

[58] J. Bałdyga, D. Kubicki, B. Y. Shekunov and K. B. Smith. Mixing effects on particle formation in supercritical fluids, *Chem. Eng. Res. Des.* 88 (2010) 1131–1141.

[59] A. Martín and M. J. Cocero. Numerical modeling of jet hydrodynamics, mass transfer and crystallization kinetics in the Supercritical Anti Solvent Process, *J. Supercrit. Fluids* 32 (2004) 203–219.

[60] E. Reverchon, G. Caputo and I. De Marco. Role of Phase Behavior and Atomization in the Supercritical Antisolvent Precipitation, *Ind. Eng. Chem. Res.* 42 (2003) 6406–6414.

[61] S. C. Chang, M. J. Lee and H. M. Lin. The influence of phase behaviour on the morphology of protein α-chymotrypsin prepared via a supercritical anti-solvent process, *J. Supercrit. Fluids* 44 (2008) 219–229.

[62] S. C. Chang, M. J. Lee and H. M. Lin. Role of phase behavior in micronization of lysozyme via a supercritical anti-solvent process, *Chem. Eng. J.* 139 (2008) 416–425.

[63] E. Reverchon, R. Adami, G. Caputo and I. De Marco. Spherical microparticles production by supercritical antisolvent precipitation: interpretation of results, *J. Supercrit. Fluids* 44 (2008) 70–84.

[64] S. S. Dukhin, Y. Shen, R. Dave and R. Pfeffer. Droplet mass transfer, intradroplet nucleation and submicron particle production in two-phase flow of solvent-supercritical antisolvent emulsion, *Colloids Surf., A.* 261 (2005) 163–176.

[65] M. J. Dávila, A. Cabañas and C. Pando. Excess molar enthalpies for binary mixtures related to supercritical antisolvent precipitation: carbon dioxide + *N*-metil-2-pirrolidone, *J. Supercrit. Fluids* 42 (2007) 172–179.

[66] D. R. Cordray, R. M. Izatt, J. J. Christensen and J. L. Oscarson. The excess enthalpies of (carbon dioxide + ethanol) at 308.15, 325.15, 373.15, 413.15, and 473.15 K from 5.00 to 14.91 MPa, *J. Chem. Thermodyn.* 20 (1988) 655–663.

[67] R. A. Hauser, J. P. Zhao, P. R. Tremaine and A. E. Mather. Excess molar enthalpies of six (carbon dioxide + a polar solvent) mixture at the temperatures 298.15 and 308.15 K and pressures from 7.5 to 12.6 MPa, *J. Chem. Thermodyn.* 28 (1996) 1303–1317.

[68] J. J. Christensen, D. R. Cordray, J. L. Oscarson and R. M. Izatt. The excess enthalpies of four (carbon dioxide + an alkanol) mixtures from 308.15 to 573.15 K at 7.50 to 12.50 MPa, *J. Chem. Thermodyn.* 20 (1988) 867–875.

[69] M. Yoshioka, B. C. Hancock and G. Zografi. Inhibition of indomethacin crystallization in poly(vinylpyrrolidone) coprecipitates, *J. Pharm. Sci.* 84(1995) 983–986.

[70] M. Savva, V. P. Torchilin and L. Huang. Effect of polyvinyl pyrrolidone on the thermal phase transition of 1, 2 dipalmitoyl-sn-glycero-3-phosphocholine bilayer, *J. Colloid Interface Sci.* 217 (1999) 160–165.

[71] R. Chadha, V. K. Kapoor and A. Kumar. Analytical techniques used to characterize drug-polyvinylpyrrolidone systems in solid and liquid states- An overview, *J. Sci. Ind. Res.* 65 (2006) 459–469.

[72] R. T. Y. Lim, W. K. Ng and R. B. H. Tan. Amorphization of pharmaceutical compound by co-precipitation using supercritical anti-solvent (SAS) process (Part I), *J. Supercrit. Fluids* 53 (2010) 179–184.

[73] I. N. Uzun, O. Sipahigil and S. Dincer. Coprecipitation of Cefuroxime Axetil–PVP composite microparticles by batch supercritical antisolvent process, *J. Supercrit. Fluids* 55 (2011) 1059–1069.

[74] V. Majerik, G. Charbit, E. Badens, G. Horváth, L. Szokonya, N. Bosc and E. Teillaud. Bioavailability enhancement of an active substance by supercritical antisolvent precipitation, *J. Supercrit. Fluids* 40 (2007) 101–110.

[75] E. Badens, V. Majerik, G. Horváth, L. Szokonya, N. Bosc, E. Teillaud and G. Charbit. Comparison of solid dispersions produced by supercritical antisolvent and spray-freezing technologies, *Int. J. Pharm.* 377 (2009) 25–34

[76] K. Wu, J. Li, W. Wang, D. A. Winstead. Formation and characterization of solid dispersions of piroxicam and polyvinylpyrrolidone using spray drying and precipitation with compressed antisolvent, *J. Pharm. Sci.* 98 (2009) 2422–2431.

[77] O. I. Corrigan and A. M. Crean. Comparative physicochemical properties of hydrocortisone-PVP composites prepared using supercritical carbon dioxide by the GAS anti-solvent recrystallization process, by coprecipitation and by spray drying, *Int. J. Pharm.* 245 (2002) 75–82.

Chapter 2. Objectives

Objectives

This thesis deals with the micronization of compounds using supercritical fluids. Among the different techniques the SAS method was chosen because of the unique properties of materials micronized using supercritical carbon dioxide as an antisolvent.

The reasons for this study are twofold: the need for further study of SAS processes in order to correctly design and scale-up them and the need for further development of pharmaceuticals micronizations.

Our preliminary study about the role of thermal effects in the SAS precipitation of antibiotics using NMP as solvent has been extended obtaining heat of mixing (excess enthalpy) data for CO_2 + organic solvent systems typically used in these micronizations. The interaction between the excess enthalpies and phase equilibria in the SAS precipitation chamber has been elucidated. Pharmaceuticals micronizations using these solvents and CO_2 as antisolvent have been carried out and the role of SAS parameters has been analyzed paying special attention to the temperature and pressure conditions, phase equilibria and the heat evolved when the supercritical fluid and the solution are mixed. Two pharmaceuticals have been micronized as pure substances forming micro and nanoparticles and as composite microparticles.

The specific objectives of this study were:

1. Measurement of Excess Enthalpy Data for Supercritical CO_2 + Organic Solvent Systems

Excess enthalpies were measured using a high-pressure isothermal flow calorimeter available at our laboratory under the conditions of temperature and pressure usually employed in SAS micronizations. Since these data are already available for the solvents *N*-methyl-2-pyrrolidone, ethanol and methanol, the solvents dimethylsulfoxide (DMSO), acetone, *N*,*N*-dimethylformamide (DMF) and ethyl acetate (EA) were studied. The excess enthalpy data obtained were correlated using cubic equations of state.

2. Study of High-Pressure Phase Behavior and Critical Data for Supercritical CO_2 + Organic Solvent Systems. Interaction between Phase Equilibria and Excess Enthalpies during SAS Experiments

The isothermal vapor-liquid equilibrium (VLE) and critical data for the CO_2 + organic solvent mixtures involved in this study are available in the literature. Nevertheless, critical data are scarce. For each system a literature review was carried out. If necessary, critical locus and VLE data were predicted or calculated using cubic equations of state. Data gathered in objectives 1 and 2 were used to discuss the thermodynamic behavior of the mixtures formed in SAS precipitation chamber and the influence of thermal effects on phase equilibria and the particles morphology.

3. Assembly of a SAS Apparatus

A SAS apparatus was built at our laboratory. Validation was carried out by micronizing yttrium acetate using DMSO as a solvent. This is a micronization well described in the literature.

4. Micronization of Pharmaceuticals

Precipitation experiments were performed in order to determine the optimum condition for these processes taking into account the requirements on particle size and morphology of the precipitates. A design of experiment strategy was followed in order to minimize the number of experiments. The relation between temperature and pressure conditions, phase equilibria and excess enthalpy was discussed. The optimal conditions of precipitation were established. Drugs to be micronized were selected after a literature survey. 5-fluorouracil, a drug widely used in the treatment of different types of cancer is one of the candidates. The second candidate is diflunisal, a salicylic acid derivative with analgesic and anti-inflammatory activity. Both drugs have a low solubility in supercritical CO_2. 5-fluorouracil has been previously micronized using methanol or mixtures formed by methanol and a second solvent. Diflunisal has not been micronized using any supercritical technique. SAS processed particles were studied using scanning electron microscope (SEM) and particle size and particle size distribution were established. X-ray diffraction (XRD) was used as a tool to detect changes in the crystallinity and polymorphic form of the drug as a consequence of SAS micronization.

5. Co-precipitation of pharmaceuticals and PVP

Diflunisal was co-precipitated using PVP *K*-15 and *K*-30 as a carrier or coating material. The solvent or solvent combination was chosen taking into account the pure pharmaceutical experiments and PVP solubility. The optimal conditions of precipitation were established. Different drug to polymer ratios have been used. Microparticles were studied using SEM, XRD, infrared spectroscopy (IR), differential scanning calorimetry (DSC), and thermal gravimetric analysis (TGA). The solubility and dissolution rate of the drug-PVP composite were measured. Polymer-drug interactions were studied. A systematic comparison with previous drug-PVP composites obtained by SAS was carried out.

Chapter 3. Methodology

Methodology

The experimental and theoretical methods used in this study are described in this chapter. In the first place, the excess molar enthalpy, and the isothermal high-pressure flow calorimeter used to perform the H_m^E measurements are introduced. Next, the equations of state and procedures used to analyze the H_m^E data, and the related phase equilibrium and critical data are given. Finally, the SAS apparatus and the method used to design the precipitation experiments and to characterize the particles are described.

3.1. Residual and Excess Molar Enthalpies

Energy is interchanged in any chemical or physical process. This interchange involves different types of energy such as electrical energy in galvanic cells, work in engines and heat in reactions and mixing processes. Enthalpy is a thermodynamic property very often used to evaluate the heat involved in a process because the enthalpy variation equals the heat evolved or absorbed at constant pressure:

$$\Delta H = Q_p \tag{3.1}$$

In particular, for a mixing process at constant pressure the heat absorbed or released upon mixing corresponds to the excess enthalpy, H^E. An excess property is defined as the difference between the value of a magnitude for the mixture and that for an ideal mixture at the same conditions of temperature, pressure and composition. For 1 mole of mixture the excess molar enthalpy is given by:

$$H_m^E = H_m^E \text{ (real mixture)} - H_m^E \text{ (ideal mixture)} \tag{3.2}$$

This magnitude is coincident with the molar enthalpy of mixing H_m^M which is given by

$$H_m^M = H_m^E \text{ (real mixture)} - \sum_i x_i H_{m,i} \tag{3.3}$$

where x_i is the mole fraction for each component and $H_{m,i}$ is the molar enthalpy for each pure component at a given *P* and *T*. H_m^E may be evaluated in terms of the residual molar enthalpy, H_m^R, which is defined as

$$H_m^R = H_m \text{ (real system)} - H_m \text{ (ideal gas)} \qquad (3.4)$$

Residual molar enthalpies will be used to calculate H_m^E by means of equations of state. The experimental device used for H_{m}^E measurements is the isothermal flow calorimeter described next.

3.1.1. Isothermal Flow Calorimeter

An isothermal high-pressure flow calorimeter (Hart Scientific model 7501) [1] was used to perform the excess molar enthalpies measurements. With this device we can measure excess enthalpies, heats of solution and enthalpies of reaction. The isothermal flow calorimeter operates at pressures between 2 and 30 MPa and temperatures between 273 and 473 K. This device allows to measure the energy required to keep constant the temperature of the system located in the cell during the mixing, reaction or dilution process.

The reactants are pumped into the calorimetric cell by two thermostated pumps (ISCO, model LC-2600) at constant flow rates. Volume flow rates are selected to cover the entire concentration range. Temperature of the pumps is controlled within ± 0.02 K. The calorimetric cell is located into a silicon bath in which temperature is controlled within ± 0.001 K. A Peltier cooling device and a pulsed heater keep the cell under isothermal conditions. The pulse energy is determined by a heater calibration. The pressure is measured using a calibrated pressure transducer (Lucas Schaevitz, model P721-0001). A back-pressure regulator located outside the calorimeter keeps the pressure within ± 0.01 MPa.

A schematic diagram of the isothermal flow calorimeter, details of the flow cell and the control units are shown in Fig. 3.1.

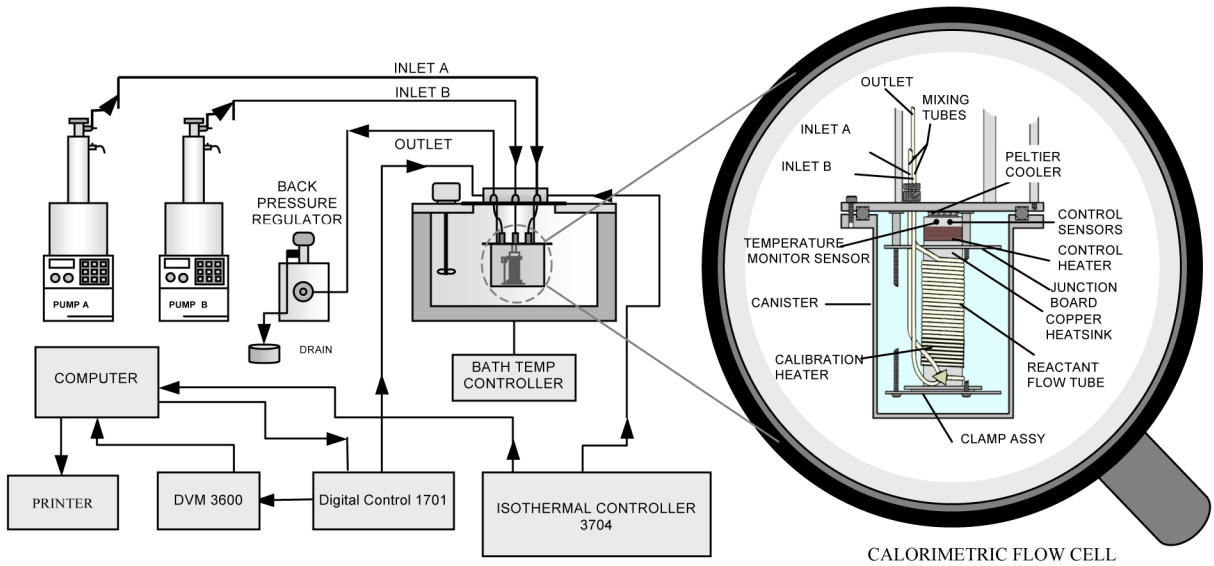

Fig. 3.1 Schematic diagram of the isothermal flow calorimeter and details of the calorimetric flow cell.

3.1.2. Pumps

The pumps used to drive the reactants to the calorimetric cell are two piston pumps (ISCO, model LC-2600) of 260 mL. They consist of a cylindrical chamber containing the fluid and a piston that runs inside and drives the components to the outside.

Fig. 3.2 (ISCO, model LC-2600) Pump.

The pumps can operate at constant flow from 0.1 to 200 mL/h and pressures up to 25.5 MPa. H_{m}^{E} measurements were carried out at total volume flow rates of 0.0014 and 0.0028 mL s^{-1}. These values were chosen to cover the entire mole fraction range by combining adequate values for the flow rates of the two pumps. The control device of the pump is shown in Fig. 3.2.

To control the temperature, each pump is fitted with a cooling jacket connected to a cryostat Julabo F25- MP for regulating the temperature with an accuracy of ± 0.05 K. According to the manufacturer, the accuracy of the pumps is 1% of the selected flow ± 0.09 mL/ h. For each pump, the uncertainty in the volume flow rate was obtained by a previous calibration. The flow rate stability was ± 1 % over the total volume of the cylinder.

Two commercial three-way Swagelok valves have been installed to select the filling or the output of the reactants to the calorimetric cell. The valves are attached to each of the pumps and to the calorimeter by 1/8" and 1/16" stainless steel tubes, respectively.

3.1.3. Calorimetric Flow Cell

The calorimetric flow cell (see Figs. 3.1 and 3.3) is the core of the calorimeter, and it is responsible for perceiving heat changes that occur as a result of the mixing of the reactants. The calorimetric cell is immersed in a silicone bath whose temperature is kept constant (± 0.001 K) with a temperature controller (Hart Scientific model 2100). The controller operates correctly between 273 and 473 K. The cell is coupled to the junction box that houses the electronic connections and insulates the top of the silicon bath.

For a proper control of the temperature, the silicone bath is refrigerated using another water bath outside that has a thermostatic head (SELECTA, TECTRON BIO MEDIC 60) and is kept between 5 and 10 degrees below the temperature fixed in the calorimeter.

The calorimetric cell is cylindrical, 5/8" in diameter and 3½" long. The cell assembly comprises eleven main parts that are shown in detail in Fig. 3.3.

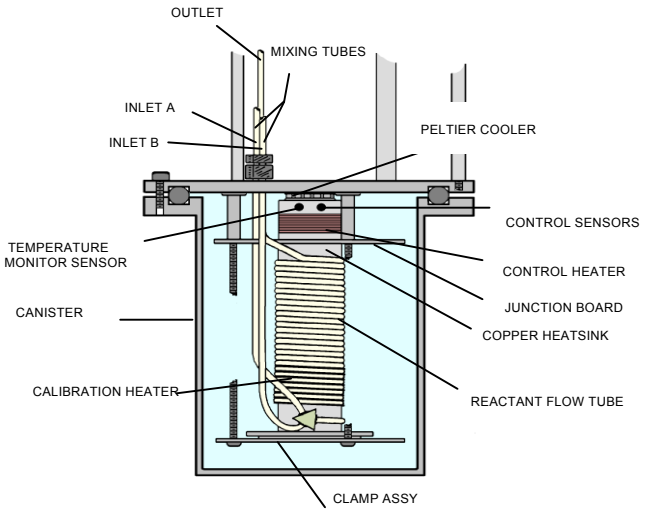

Fig. 3.3 Details of the calorimetric flow cell.

The reactants enter the cell through two 1/16" tubes and are mixed in a T-shaped piece. The fluids exit through a tube of the same size that is wound around a copper cylinder that serves as conductor of heat, plus support of the output tube. Welded to this block are calibrating and heating resistors. The heating resistance is 100 ± 10 Ω and is used together

with the refrigeration unit to regulate the heat absorbed or released by the mixture by means of heat pulses.

The cooling unit is a Peltier device, a thermoelectric heat pump that operates by pumping heat from a cold to a hot reservoir. It is used to extract heat from the calorimetric cell to the silicon bath. It consists of two parallel thin ceramic plates bonded together by two columns of a semiconductor material. The refrigeration unit is located at the top of the copper block. When heat is released or absorbed upon a reaction or mixing process, the number of pulses is decreased or increased, respectively, to compensate this heat difference. The magnitude of the pulse is established in a previous heater calibration.

Control sensors and a temperature sensor are used to monitor and measure the temperature. Control sensors are two 10 and 100 kW thermistors that are used in temperature ranges between 273 and 373 K and between 373 and 473 K, respectively. The choice of the thermistor is important for the proper functioning of the equipment, and is selected with a knob on the junction box. The thermistors are located between the cooling device and the heating element. The temperature sensor measures the magnitude at that point, an area very close to the outlet pipe of the mixture. The temperature measured by the sensor is recorded on the front panel of the 1701 unit.

3.1.4. Control Units and Data Collection

- **Digital Control 1701 Unit**

This device controls the circuits of the calibration resistor and monitors the temperature of the calorimetric cell. It comprises four subsystems: a preamplifier, a temperature monitor, the circuits of calibration resistors and a digital multimeter. Calibration resistor circuits control the heating power. Calibration resistance at a given temperature is constant, but varying the amount of current passing through it, with a selector provided on the front panel, the power dissipated can be regulated. Since the calibration resistance located in the calorimetric cell varies with temperature, its exact value is determined with a standard resistor of 1000 Ω connected in series with the calibration resistor. Knowing the potential difference that exists on both sides of the calibration resistor and the standard resistor value, the heating power by Joule effect may be established.

The unit includes a DVM selector (Digital Voltmeter) for selecting the temperature or the difference of the input signal that displays the temperature or potential differences. This voltmeter provides an initial reading for temperature. For a more precise measurement, the voltmeter is connected in parallel to a 6 ½-digit multimeter DATA PRECISION 3600.

- **Isothermal Controller 3704 Unit**

The 3704 module is a precise temperature controller that maintains constant this property at the checkpoint of the cell to compensate for the heat absorbed or evolved by the reaction or mixing process. The isothermal controller has three subsystems: an alternating-current bridge, the drivers of the pulsed heater intensity and the refrigeration unit intensity.

The pulsed heater controller consists of a unit that transforms potential differences in frequency of heat pulses fixed between 0 and 20 μJ. Another unit controls the amount of energy through the number of pulses at stake during the mixing process to compensate for the sum of the power of cooling and that generated or absorbed by the mixture. The cooling device is a Peltier unit that removes heat at a constant power. The current can be adjusted between 0 and 2 A.

The alternating-current bridge is a temperature controller. The bridge output is amplified, rectified and passed continuously through an integrator that integrates the difference between the final state and the reference state to provide an adequate response to the heating element.

Fig. 3.4 Control units and digital voltmeter.

The Wheatstone bridge is part of this control system and can be calibrated for each temperature to get a good performance. The signal amplification (gain) allows rapid responses of the instrument with minor oscillations. The gain is set according to the heating conditions. Control Units and Data Collection are shown in Fig. 3.4.

- **Data Logging**

The units 3704, 1701 and the digital multimeter are connected to an IBM AT computer so their data can be acquired through a LAB TENDER card with an AM9515 time controller to transform analogical signals to digital. Several computer programs are used to gather and process the data and to carry out the calibration experiments

3.1.5. Back Pressure Regulator (BPR)

H_{m}^{E} measurements were carried out at pressures ranged from 9 to 18 MPa. The pressure is regulated by a diaphragm regulator. This device consists of a stainless steel cylinder divided into two chambers separated by a Teflon membrane. The upper section is connected to a nitrogen cylinder and a pressure transducer. The working pressure is selected at this side while the other side of the membrane is connected to the calorimeter and goes directly into the drain (Fig. 3.5).

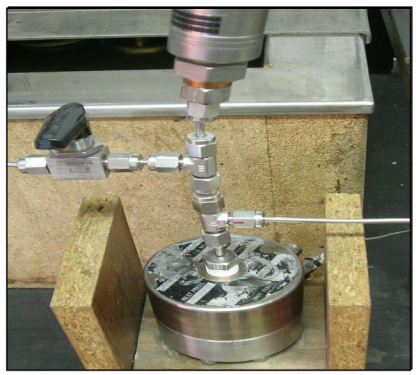

Fig 3.5. Back pressure regulator.

The Teflon membrane acts as a regulating valve for pressure: when the pressure of nitrogen is higher than that of the other chamber, the way to the drain is blocked. For finer adjustment of pressure, a piston is installed between the pressure transducer and the diaphragm regulator at the upper section. The pressure is fixed by introducing a certain amount of nitrogen into the upper chamber of the stainless steel cylinder.The nitrogen pressure can be regulated and measured and therefore also the pressure of the circuit.

For pressure measurement a differential pressure transducer (LUCAS Schaevitz, model P721-0001) is used. This is a torque transducer with an aperture of known geometry that when subjected to pressure at one end, is deflected in proportion to the applied pressure, so it returns a voltage V proportional to the difference between the actual pressure and atmospheric (P - P_0) according to the following equation:

$$(P - P_0) = -0{,}4123 + 0{,}99423 \cdot V + 3{,}05 \cdot V^2 \qquad (3.5)$$

where the pressure is given in MPa and the voltage in mV. The maximum error made in measurement is estimated to be 0.01 MPa.

3.1.6. Experimental Procedure

- **Establishment of Working Conditions**

The pressure is fixed by introducing nitrogen into the upper section of the pressure regulator. A fine adjustment is achieved using the manual piston connected in line with the regulator. Since the regulator is located at the end of the calorimeter circuit, the pressure is maintained throughout the system.

The measurement temperature is set by selecting the controller of the silicone bath that contains the calorimetric cell. For proper control of temperature, the temperature in the external bath that cools the silicon bath is set to a value between 5 and 10 degrees below the calorimeter temperature measurement. Two to three days are necessary to get a steady temperature. Once the temperature is stabilized, the calorimeter is set to zero by balancing the Wheatstone bridge in the isothermal controller 3704.

To balance the bridge, heating and cooling selectors are set to zero, and the gain is set at the desired value for the measurements. Under these conditions the device is manipulated to balance the Wheatstone bridge in order to get in the frequency counter a constant value around 44.5 ± 0.5.This value corresponds to a balanced bridge.

In addition, pumps should also be kept at a constant temperature in order to transform subsequently volumetric flow into mass flow. The temperature of the pumps is set at a value at which the density of the pumped fluid is known and that temperature can be different to the temperature of the measurements as reactants are thermostated in the silicon bath prior to mixing.

Once the pressure and temperature are fixed, the heating power and the intensity of cooling in the 3704 unit are set through the dials and selectors on the front panel of this device. Both values are set depending on the amount of heat to be measured, so that before and after mixing the number of pulses is within the range of the equipment (0 to 100000 pulses/s). If the magnitude of the heating resistance is too low, it would take too many pulses to compensate for the heat absorbed by the mixture. Conversely, if it is too high, a few pulses will suffice and consequently the accuracy will be low.

The choice of flow must be conditioned mainly by the diffusivity of the mixture components. For compounds that are diffused in each other easily, flow rates between 5 and 10 mL/h are enough. However, if the diffusivity is not high, higher flow rates are required. Values between 40 and 70 mL/h are required to promote turbulent flow. In this study we have used flow rates between 5 and 10 mL/h, temperature conditions of 313.15, 323.15 and 333.15 K and pressures of 9.00, 12.00, 15.00 and 18.00 MPa.

- **Calibration and Implementation of Measurements**

The first step before carrying out the measurements in the calorimeter is to clean the lines and fill the pumps. A small amount of cleaning fluid, acetone, in 3 portions is used to clean the pumps and the lines by introducing the liquid at the empty pump and discarding it by the line repeatedly. The same operation is repeated with the liquid or fluid to be used in each pump. Then pumps are filled. Liquids are degasified by pressurizing and depressurizing at the atmospheric pressure several times. To fill a pump with pressurized fluids such as CO_2, the pump is first cooled at a temperature between 278 and 288 K, thus the fluid from the cylinder that contains the gas condenses within the pump and this serves to increase the amount of fluid in it.

The pumps are thermostated at a temperature for which the density of the components they contain is known. In our case, we selected a temperature of 303 K. To drive components inside the calorimeter, we raise the pump pressure slightly above the working pressure then the valve is open.

The next step to take is the calibration, to know the exact value of the energy equivalent to a pulse. This calibration simulates an exothermic mixing through a calibration resistor. The calibration consists of the following stages:

1) Measure the frequency of the baseline for 20 minutes.
2) Connect the calibration resistor to simulate the exothermic reaction. The heating frequency decreases to maintain constant temperature. At this stage the potential differences for the calibration and the standard resistors are measured. This will help us to determine the calibration power.
3) Calculate the frequency difference observed between these first two steps of calibration (Δf_c).
4) Switch off the calibration power and recover the frequency of the baseline.

The heating power of the heating resistor is produced by Joule effect. Through a dial on the front panel of the 1701 unit , the intensity of current passing through it can be controlled and therefore, different heats to calibrate the different values of the pulse can be generated.

The power of the calibration resistor is determined using a calibrated standard resistor of 1000 Ω connected in series with it. By measuring the potential difference with the standard resistor, V_1, we can know the current, using Ohm's law. Once the intensity and potential difference of the calibration resistance V_2 are known, we can determine the calibration power W_{cal} using the following expression:

$$W_{cal} = \frac{V_1 \cdot V_2}{1000} = k \cdot \Delta f_c \tag{3.6}$$

where k is the heat dissipated by pulse whose value may be obtained from the above equation.

Once the device is calibrated, we can start with the implementation of the measurements. The baseline measurement takes place by pushing one of the reactants, the high viscous one, at the total flow to be used during the measurements. Under these conditions, the pulsed heater frequency compensates for the removal of heat through the Peltier device and the temperature of the calorimetric cell is kept constant. The frequency of the baseline should be high if the mixing is exothermic because the pulsed heater frequency decreases to maintain constant temperature. Otherwise, the baseline should be low to maintain isothermal conditions by increasing the frequency of the pulses. During the recording of the baseline, the heating power counteracts the Peltier cooling power to maintain constant temperature. Then the reagents are pumped in the right proportion to the calorimetric cell. The heat absorbed or released upon mixing causes an increase or decrease in frequency with respect to that of the baseline. Therefore, temperature is kept constant. The frequency variations are collected in the computer through a program and displayed on the screen. The average frequency is taken when this magnitude stabilizes, which usually occurs between 45 and 60 minutes, depending on the studied mixture.

The power generated by the mixture, W_r, and the power of the heating resistance, W_{cal}, compensate the Peltier cooling power, W_p, and the temperature is kept constant.

$$W_{cal} = W_r + W_p \tag{3.7}$$

By measuring the variation of the heating power, which is associated with the frequency difference between the baseline and mixing, Δf, we can determine the amount of power generated by mixing in a precise manner. Knowing the total molar flow, $J_{m,total}$, we can obtain the excess molar enthalpy, by the following expression:

$$H_m^E = \frac{k \cdot \Delta f}{J_{m,total}} \tag{3.8}$$

where k is the constant for the heat dissipated per pulse (in μJ/pulse). This value has been estimated in the calibration process.

3.1.7. Uncertainties

The molar flow rate $J_{\mathrm{m},i}$ is calculated using the volume flow rate $J_{\mathrm{v},i}$, the density ρ_i of the mixture component at the temperature and pressure of the pumps and the molar mass M_i :

$$J_{\mathrm{m},i} = \frac{J_{\mathrm{v},i} \cdot \rho_i}{M_i} \tag{3.9}$$

The mole fraction of each component is given by:

$$x_i = \frac{J_{\mathrm{m},i}}{J_{m,total}} \tag{3.10}$$

For each pump the uncertainty in $J_{\mathrm{v},i}$ was obtained by a previous calibration. Since densities are affected by temperature and pressure changes, the uncertainty in molar flow rates was derived taking into account contributions from variations in volume flow rates, pressure, and pumps temperature. The mole fraction uncertainty is based on the molar flow rates uncertainty and was estimated to be better than ± 0.001. The uncertainty in H_m^{E} was obtained taking into account contributions from molar flow rates, pulse energy and frequency and was estimated to be ± 1 % or at least ± 1 J mol^{-1}.The uncertainties in T and P, ± 0.001 K and 0.01 MPa, respectively, were already given. More details about the error treatment are given in reference [2].

3.2. Equations of State Calculations

The data obtained in this study for the mixtures formed by carbon dioxide and organic polar solvents in supercritical antisolvent micronizations together with related phase equilibria and critical data taken from the literature have been modeled using equations of state (EOS).

3.2.1 Equations of State and their Application to Mixtures

An analytical equation of state describes the relationship between temperature, pressure and volume for a given substance, $f(P,V,T) = 0$. In the case of a mixture of substances the composition variable has to be included through the mixing rules that allow the calculation of the mixture parameters from those of the pure components. From this equation of state all the thermodynamic properties of the system such as phase equilibria or excess enthalpies may be obtained. Many analytical EOS of varying complexity are available in the literature; unfortunately, none of them may be applied for any type of system in the whole range of experimental conditions. For mixtures involving supercritical fluids and short chain molecules, equations derived from the van der Waals EOS are the most widely used.

The van der Waals equation was the first EOS that provided a qualitative description of the liquid and vapor phases and critical phenomena. Van der Waals proposed this pressure-explicit equation in 1873.

$$P = \frac{RT}{(V_m - b)} - \frac{a}{V_m^{\,2}} \tag{3.11}$$

The first term in this equation accounts for the short range repulsive forces and depends on a parameter b describing a correction for the volume occupied by the molecules themselves. V_m is the molar volume. The second term accounts for the attractive forces and depends on the parameter a that reflects the strength of attraction between two molecules. This equation is cubic in V. At temperatures below the critical, there are three real roots but only two values correspond to stable states. The van der Waals equation roughly approximates fluid behavior in the two-phase region. At the critical temperature where liquid and vapor become indistinguishable the following conditions have to be met:

$$\left(\frac{\partial^2 A}{\partial V^2}\right)_T = \left(\frac{\partial P}{\partial V}\right)_T = 0 \tag{3.12}$$

$$\left(\frac{\partial^3 A}{\partial V^3}\right)_T = \left(\frac{\partial^2 P}{\partial V^2}\right)_T = 0 \tag{3.13}$$

where A is the Helmholtz energy. Evaluating these derivatives and equation (3.11) at the critical point results in three equations involving a, b and the critical parameters T_c, P_c and V_c. Because V_c is not always available, it can be eliminated and the remaining equations solved for a and b in terms of T_c and P_c. For the van der Waals equation this results in

$$a = \frac{27R^2T_c^{\,2}}{64P_c} \quad ; \quad b = \frac{RT_c}{8P_c} \tag{3.14}$$

Thus, a and b are independent of temperature for this EOS and can be easily calculated from the critical parameters P_c and T_c.

The van der Waals equation is the starting point for other cubic EOS able to represent *PVT* data in the two-phase region. Many modifications have been proposed; in this study the Peng-Robinson and the Soave-Redlich-Kwong equations have been used [3, 4]. These EOS retain the repulsive term and introduce temperature dependence in the attractive term of the van der Waals equation.

- **Peng-Robinson Equation of State**

  The Peng-Robinson EOS is given by

$$P = \frac{RT}{(V_m - b)} - \frac{a(T)}{V_m \cdot (V_m + b) + b \cdot (V_m - b)} \tag{3.15}$$

The volume dependence of the attractive term provides a better description of liquid volumes. The parameters a and b are calculated according to the procedure used for the van der Waals EOS. The temperature dependence of a and b leads to a better description of vapor pressures.

$$a(T) = \frac{\Omega_a \cdot R^2 T_c^{\,2}}{P_c} \cdot \alpha(T) \tag{3.16}$$

$$b = \frac{\Omega_b \cdot RT_c}{P_c} \tag{3.17}$$

where

$$\Omega_a = 0.457235 \;;\; \Omega_b = 0.077796 \tag{3.18}$$

$$\alpha(T) = \left[1 + m \cdot \left(1 - T_r^{0.5}\right)\right]^2 \tag{3.19}$$

$$m = \left(0.37464 + 1.54226\omega - 0.26992\omega^2\right) \tag{3.20}$$

where T_r is the reduced temperature ($T_r = T/T_c$) and ω is the acentric factor introduced by Pitzer [5] in order to describe deviations in pressure with respect to values observed for fluids formed by spherical molecules. Pitzer defined the acentric factor as

$$\omega = -\log\left(P^{sat} / P_c\right)_{T_r=0.7} - 1 \tag{3.21}$$

where P^{sat} is the saturation pressure. The coefficients in equation (3.20) are obtained from a correlation of vapor pressure taken at temperatures ranging from the boiling to the critical temperature.

- **Soave-Redlich-Kwong Equation of State**

  Redlich and Kwong [6] proposed in 1949 the following EOS:

$$P = \frac{RT}{(V_m - b)} - \frac{a(T)}{V_m \cdot (V_m + b)} \tag{3.22}$$

the parameters $a(T)$ and b are calculated in terms of the critical parameters using equations (3.16) and (3.17) where $\alpha(T) = 1/T_r^{0.5}$, Ω_a = 0.42784 and Ω_b = 0.08664. Values for Ω_a and Ω_b are obtained by applying equation (3.12) and (3.13) to the Redlich-Kwong EOS.

In order to improve the description of vapor pressures and liquid densities Soave modified the expression of $\alpha(T)$ in the Redlich-Kwong EOS:

$$\alpha(T) = \left[1 + (0.480 + 1.574\omega - 0.176\omega^2)(1 - T_r^{0.5})\right]^2 \tag{3.23}$$

The coefficients in equation (3.23) are obtained by applying the condition of equal fugacities at the reduced saturation pressure. When this modification is used, the EOS is known as the Soave-Redlich-Kwong equation.

- **Application to Mixtures and Mixing Rules**

The EOS described in equations (3.11) to (3.23) are defined for pure substances. In order to extend them to mixtures, it is necessary to introduce a mixing rule. A mixing rule is an expression that relates the a and b parameters of the mixture to those of the pure components and the composition. A large variety of mixing rules are found in the literature. The simplest one is the classical mixing rule that has been used in this study:

$$a = \sum_i \sum_j x_i x_j a_{ij} \tag{3.24}$$

$$b = \sum_i \sum_j x_i x_j b_{ij} \tag{3.25}$$

Parameters a_{ij} and b_{ij} are calculated from the pure component parameters using the combination rules given by

$$a_{ij} = (a_{ii} a_{jj})^{1/2} (1 - k_{ij}) \tag{3.26}$$

$$b_{ij} = \frac{(b_{ii} + b_{jj})}{2} (1 - \delta_{ij}) \tag{3.27}$$

where $k_{ij} = k_{ji}$ and $\delta_{ij} = \delta_{ji}$ are binary interaction parameters obtained by correlation of vapor-liquid equilibrium or excess enthalpy data. The absolute values adopted by k_{ij} and δ_{ij} are usually much smaller than one. k_{ij} is related to molecular interactions between two unlike molecules. δ_{ij} is related to the free volume and the fluid compressibility.

3.2.2. Phase Equilibria Calculations

Phase equilibrium is characterized by temperature, pressure and the composition of each phase. For two phases α and β in equilibrium the fugacity of each component f_i must satisfy the condition:

$$f_i^{\alpha} = f_i^{\beta} \tag{3.28}$$

In order to solve this equation, fugacities are evaluated from an EOS using the following expression for the fugacity coefficient φ_i of each component [7]

$$RT\ln\varphi_i = RT\ln\frac{f_i}{y_i P} = \int_V^\infty \left[\left(\frac{\partial P}{\partial n_i}\right)_{T,V,n_j} - \frac{RT}{V}\right]dV - RT\ln z \tag{3.29}$$

where y_i is the mole fraction and $z = PV_m / RT$ is the compressibility factor of the mixture. For the Peng-Robinson EOS the fugacity coefficient is given by

$$\ln\varphi_i = \frac{2\sum_k x_k b_{ik} - b}{b}(z-1) - \ln(z-B) - \\ -\frac{A}{2\sqrt{2}\cdot B}\left(\frac{2\sum_j x_j a_{ij}}{a} - \frac{2\sum_k x_k b_{ik} - b}{b}\right)\ln\left(\frac{z+\left(1+\sqrt{2}\right)B}{z+\left(1-\sqrt{2}\right)B}\right) \tag{3.30}$$

where

$$A = \frac{aP}{R^2T^2}\ ; \qquad B = \frac{bP}{RT} \tag{3.31}$$

a, b, a_{ij} and b_{ij} are calculated using equations (3.24)-(3.27). A similar equation is obtained for the Soave-Redlich-Kwong EOS.

Different algorithms may be used to solve equation (3.28) depending on the type of phase equilibrium. In this study, calculations involve a liquid and a vapor phase for a binary system at constant temperature. This is the so-called bubble point calculation: T and x (composition of the liquid phase) are known and P and y (composition of the vapor phase) are calculated. Equations (3.28) and (3.30) must be applied to each component. The liquid and vapor molar volumes required in equation (3.30) are calculated using the EOS twice. The PE 2000 program developed by G. Brunner and coworkers was used in this calculation [8]. The binary interaction parameters k_{12} and δ_{12} may be set equal to zero in equations (3.26) and (3.27). In this case, binary phase equilibria data are predicted using only pure component data: critical parameters, acentric factors and vapor pressures at a given temperature. Usually, values of k_{12} and δ_{12} are determined by correlation of VLE data at a given temperature. Then binary interaction parameters can be used for calculations in multicomponent behavior assuming that the binary interactions add up to the multicomponent behavior. Assuming that k_{12} and δ_{12} obtained from VLE data taken at a given temperature ought to be temperature-independent,

values for k_{12} and δ_{12} obtained from VLE data taken at a given temperature may be used to predict VLE at a different temperature, the critical locus or binary excess enthalpy data for the same binary system.

3.2.3 Excess Enthalpy Calculations

The excess molar enthalpy, H_m^E, for a binary mixture may be calculated in terms of the residual enthalpies

$$H_m^E = H_m(\text{mixture}) - \sum_i x_i \cdot H_{m,i} = H_m^R(\text{mixture}) - \sum_i x_i \cdot H_{m,i}^R \tag{3.32}$$

where H_m^R is the residual molar enthalpy of the mixture and $H_{m,i}^R$ is that for pure components.

The residual molar enthalpy is given by

$$\frac{H_m^R}{RT} = z - 1 + \frac{1}{RT}\int_\infty^v \left[T\left(\frac{\partial P}{\partial T}\right)_V - P \right] dV \tag{3.33}$$

For a pressure-explicit EOS, the integral appearing in equation (3.33) can be solved analytically. Thus, for the Soave-Redlich-Kwong EOS the following expression is obtained

$$\frac{H_m^R}{RT} = z - 1 + \frac{T\frac{\partial a}{\partial T} - a(T)}{b(T)RT}\ln\left(\frac{V + b(T)}{V}\right) - \frac{T\frac{\partial b}{\partial T}}{V - b(T)} \tag{3.34}$$
$$- \frac{a(T)\frac{\partial b}{\partial T}}{b(T)^2 R}\ln\left(\frac{V + b(T)}{V}\right) + \frac{a(T)\frac{\partial b}{\partial T}}{b(T)(V + b(T))R}$$

If the Peng-Robinson EOS is used in equation (3.33), the residual molar enthalpy of the mixture is given by

$$\frac{H_m^R}{RT} = z - 1 + \frac{T\dfrac{\partial a}{\partial T} - a(T)}{2\sqrt{2}b(T)RT}\ln\left[\frac{V + (1+\sqrt{2})b(T)}{V + (1-\sqrt{2})b(T)}\right] - \frac{T\dfrac{\partial b}{\partial T}}{V - b(T)} \tag{3.35}$$

$$- \frac{a(T)\dfrac{\partial b}{\partial T}}{2\sqrt{2}b(T)^2 R}\ln\left[\frac{V + (1+\sqrt{2})b(T)}{V + (1-\sqrt{2})b(T)}\right] + \frac{a(T)\dfrac{\partial b}{\partial T}V}{(V^2 + 2b(T)V - b(T)^2)b(T)R}$$

In equations (3.34) and (3.35) the expressions of a and b for mixtures have to be obtained using the mixing rules described by equation (3.24)-(3.27). Usually, values for the binary interaction parameters k_{12} and δ_{12} are determined by a correlation of H_m^E data taken at different pressures and a given temperature.

3.2.4. Critical Locus Calculations

There are several methods to estimate the mixture critical locus using an equation of state. They differ in the formulation of the stability criteria and critical point conditions. For pressure-explicit EOS it is convenient to use a formulation based on the Helmholtz function A. Heidemann and Khalil have developed a procedure based on A that has been used in this study [9]. The independent variables are the compositions expressed as amount of substance n_i. The critical point first condition is expressed in matricial form

$$W = Det\left[\overline{B}\right] = 0 \tag{3.36}$$

where the elements of $\overline{B}$ are given by

$$b_{ij} = (\partial^2 A / \partial n_i \partial n_j)_{T,V} \tag{3.37}$$

The condition expressed by equation (3.36) is met if the vector $\Delta n = (\Delta n_1, \Delta n_2, ..., \Delta n_N)$ satisfies the equation

$$\left[\overline{B}\right]\Delta n = 0 \tag{3.38}$$

This leads to the second critical condition

$$C = \sum_i \sum_j \sum_k (\partial^3 A / \partial n_i \partial n_j \partial n_k)_{T,V} \cdot \Delta n_i \cdot \Delta n_j \cdot \Delta n_k = 0 \tag{3.39}$$

The second and third derivatives of A are obtained using the EOS and thermodynamic relationships:

$$(\partial^2 A / \partial n_i \partial n_j)_{T,V} = RT \cdot (\partial \ln \varphi_i / \partial n_j) \tag{3.40}$$

$$(\partial^3 A / \partial n_i \partial n_j \partial n_k)_{T,V} = RT \cdot (\partial^2 \ln \varphi_i / \partial n_j \partial n_k) \tag{3.41}$$

Fugacity coefficients are evaluated using equation (3.29). When this procedure is applied to a gas-liquid critical line, the root providing the largest volume is selected. However, in the case of a liquid-liquid critical line the root providing the smallest volume is selected.

The Heidemann and Khalil procedure has been used to calculate the critical locus of the CO_2 + organic solvent systems involved in this study which exhibit type I critical behavior according to the Scott and van Konynenburg classification [10]. The critical locus may be predicted from pure component data if the binary interaction parameters k_{12} and δ_{12} involved in the calculations of fugacity coefficients are set equal to zero. Otherwise, the critical locus may be determined from a correlation of the critical data available for the binary system. In this case, values for k_{12} and δ_{12} are required to draw the gas-liquid critical line.

3.3. Supercritical Antisolvent Micronizations

Liquid antisolvent processes are largely used in micronizations. They are based on the use of two liquid solvents that are completely miscible. The solute to be micronized is soluble in the first solvent, but not soluble in the second. Consequently, the addition of the second solvent (antisolvent) induces the formation of a solution formed by the two liquids and the supersaturation and precipitation of the solute.

Supercritical fluid antisolvent micronizations have been used in the last years as alternatives to liquid antisolvent processes [11-13]. Thanks to the relatively low solvent power of supercritical CO_2 for solutes such as polymers or pharmaceutical products and its good miscibility with many polar organic solvents, the controlled micronization of the solid from an organic solvent solution may be achieved at moderate temperatures. As previously

described in the introduction, different process arrangements, apparatuses and acronyms have been used: GAS (gas antisolvent), PCA (precipitation by compressed antisolvent), ASES (aerosol solvent extraction), SEDS (solution enhanced dispersion by supercritical fluid) and SAS (supercritical antisolvent), among others.

The higher diffusivities of supercritical fluids with respect to those of liquids lead to its very fast diffusion into the liquid solvent and the supersaturation and precipitation in particles much smaller than those obtained using liquid antisolvents. Carbon dioxide is the most frequently used supercritical fluid used as an antisolvent. Its accessible critical parameters (T_c = 304.1 K, P_c = 7.38 MPa) allow operation at moderate temperatures. The particle size may be tuned by varying the process parameters such as pressure, temperature, solute concentration, etc. Furthermore, these are solvent-free particles exhibiting a narrow size distribution.

- **Batch Operation**

The precipitation vessel is loaded with a given quantity of the liquid solution and then the supercritical antisolvent is added until the final pressure is reached. Typically, moderate pressures are used (5-8 MPa). In this mode of operation, the rate of the supercritical antisolvent addition can be an important parameter in controlling the morphology and the size of the solid particles. The antisolvent can be added from the bottom or from the top of the chamber. It is also possible to charge the precipitation chamber with the antisolvent and then to perform a discontinuous injection of the liquid solution. The difference between these two operational modes is that in the first case the precipitation occurs in a liquid rich phase, whereas, in the second case it occurs in a supercritical fluid rich phase. The results can be very different. In both cases the operation performed is not at the steady state; therefore, it is difficult to analyze the effect of the process parameters on the final characteristics of the powders. Moreover, batch operation is usually not suitable for industrial production. When relatively large volumes of solution are processed, a stirrer may be necessary to improve the mixing between the solution and the CO_2.

At the end of the precipitation process, the vessel is washed with the antisolvent to eliminate the liquid. This operation is very important. If the washing is not performed or the washing time is not sufficient, the liquid solvent may be released from the supercritical

solution during the depressurization of the apparatus and may resolubilize the solute. The acronym commonly used for batch processes is GAS.

- **Continuous Operation**

In the SAS, ASES, PCA and SED processes the liquid solution and the supercritical antisolvent are continuously delivered to the precipitation vessel in co-current or counter-current mode. As their titles indicate, there are differences between these processes. For example, in the SED process an aqueous solution containing biomaterials is dispersed using CO_2 and a polar organic solvent in a coaxial nozzle. Supercritical CO_2 is used to extract the aqueous phase from the product. The organic solvent acts both as precipitating agent and as modifier, enabling the non-polar CO_2 to remove the water. The following discussion is mainly centered in ASES, SAS and PCA, and the acronym most frequently used, SAS, will be our choice to refer to them. In the continuous mode of operation the flow rates and their ratio are important for the precipitation process. The pressure, at which the operation is performed, and the liquid solution injection device are also relevant process parameters. This is the mode of operation chosen in this study. A schematic representation of the continuous supercritical antisolvent apparatus used in this thesis is shown in Fig. 3.6.

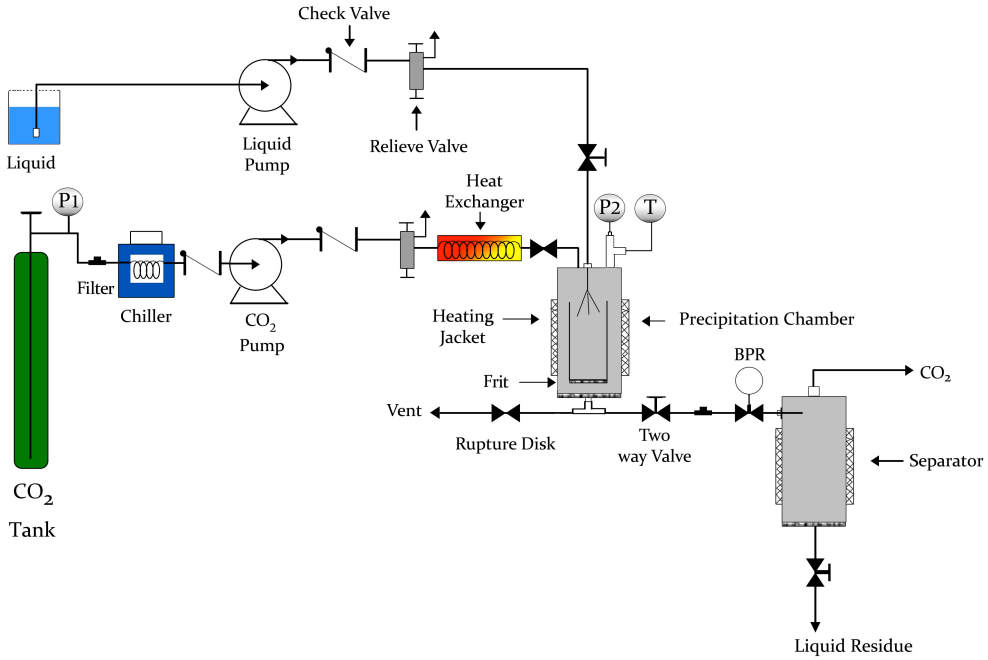

Fig. 3.6 Schematic diagram of the laboratory scale SAS apparatus.

The injector is designed to produce liquid-jet break-up and the formation of small micronic droplets that expand in the precipitator. The solid solute is released when its local

concentration exceeds the saturation limit. Particles are collected on a filter (frit) at the bottom of the basket installed inside the precipitation chamber. The solution formed by the supercritical fluid and the organic solvent passes through this filter and after depressurizing at the BPR it is introduced in a separator where the organic solvent is recovered. Various injection devices have been proposed in the literature. A nozzle is a very common choice; capillary tubes or vibrating orifices are also used. Coaxial devices use two capillary tubes to deliver continuously the liquid solution and the supercritical antisolvent. In the SAS apparatus built up in this study, the liquid solution is introduced separately from the supercritical antisolvent using a nozzle. In order to obtain a good mixing between the two streams without the aid of a mechanical device, this process operates at higher pressures than the GAS process, typically in the range 9-15 MPa. The washing step with pure supercritical antisolvent at the end of the precipitation process is also very important in continuous operation to avoid the condensation of the liquid phase and the solute resolubilization. Although smaller than in batch processes, the length of washing has to be carefully estimated.

The SAS production capacity is much larger than that of GAS. Therefore, SAS processes are preferred; a large number of solutes have been micronized using this procedure in the last years [14-15]. Co-precipitation of natural substances or pharmaceuticals with a biocompatible or biodegradable carrier material is also possible [16]. On the other hand, fundamental studies aimed at understanding the role of phase equilibria, hydrodynamics and mass transfer in SAS have been carried out [17-23].

3.3.1. Description of SAS Apparatus

The schematic diagram and image for our laboratory scale SAS apparatus are shown in Figs. 3.6 and 3.7, respectively. In this apparatus, an HPLC pump (Series III Pump, 10 mL head) is used for solution delivery; it can produce flow rates from 0.01 to 10.00 mL/min, these flow rates can be set in 0.01 mL increments. A high pressure pump (Thar-SCF CO_2 Pump P-50) is used to deliver carbon dioxide; it can produce flow rates from 1 to 50 g/min, these flow rates can be set in 1 g increments. Prior to mixing, CO_2 is heated in the heat exchanger at the precipitation temperature. The desired mole fraction required for SAS precipitation is obtained by combining adequate values for the flow rate of both pumps. Both the solution and CO_2 are pumped separately into the precipitation chamber where they contact with each other producing the microparticles.

Fig. 3.7 SAS apparatus used for micronization.

A stainless steel cylinder vessel of 500 mL (THAR-SCF) is used as a precipitation chamber. Sealing is made using a spring-energized O-ring made out of polyimide. The solution is sprayed in the precipitation chamber through a thin stainless steel nozzle of diameter 100 μm. Supercritical CO_2 is pumped through another inlet port located on the top of the chamber.

A stainless steel basket with a removable filter (frit, 2 μm) is installed inside the precipitation chamber to collect the microparticles, allowing the CO_2 + organic solvent mixture to pass through. A cylinder piece of aluminum of dimension 4.5 cm x 2.5 cm x 0.2 cm was used to keep a suitable distance between the basket and the bottom of the cylinder vessel. A schematic diagram for the precipitation chamber is shown in Fig. 3.8.

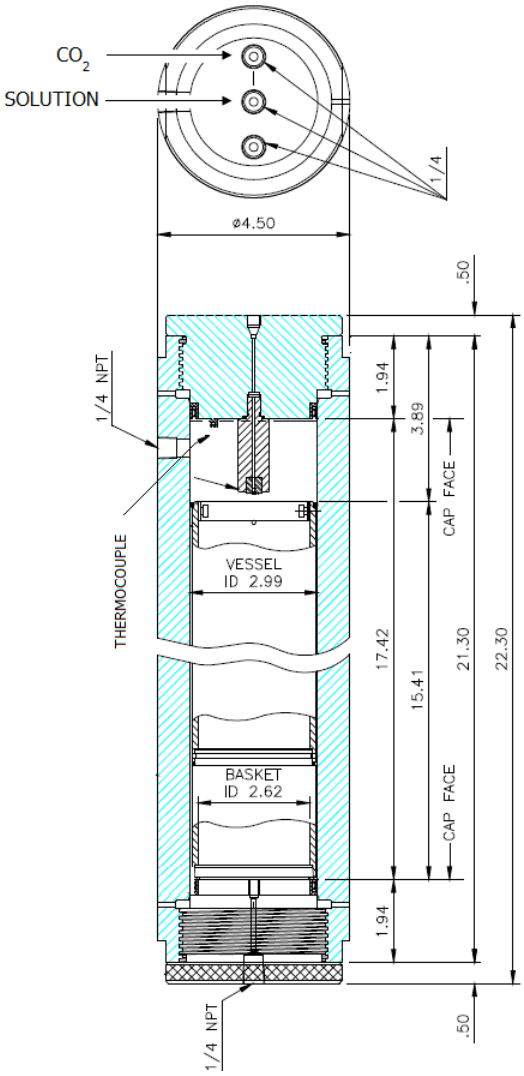

Fig. 3.8 Schematic diagram of the precipitation chamber, dimensions in inches.

Several types of nozzles can be used in the SAS system, specifically a single nozzle, a coaxial nozzle, capillary tubing, a laser-drilled orifice and a valve nozzle. A nozzle of internal diameter of 100 μm was used in this study. Fig 3.9 shows the schematic diagram of the nebulizer. The nozzle is drilled in the sapphire plate.

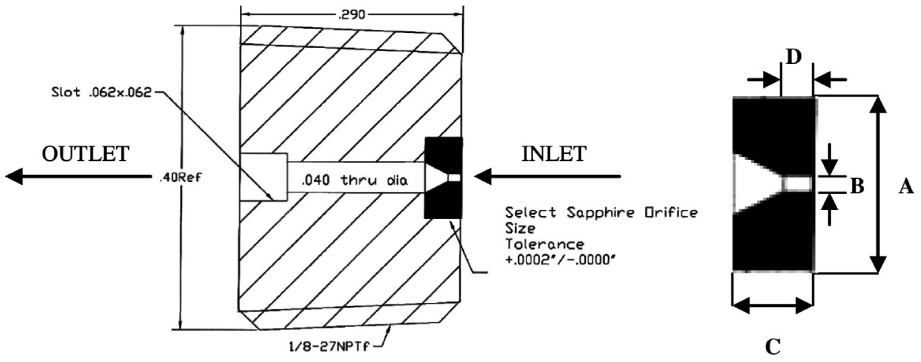

Fig. 3.9 Schematic diagram of the nebulizer utilized with a sapphire plate; outside diameter (A) = 2210 μm; inside diameter (B) =100 μm; thickness (C) = 1194 μm; length of the hole (D) = 254 μm.

Then a back pressure regulator (TESCOM, Pressure Reducer Series 26-1700) located after the precipitation chamber allows keeping constant pressure in the system, Fig 3.10.

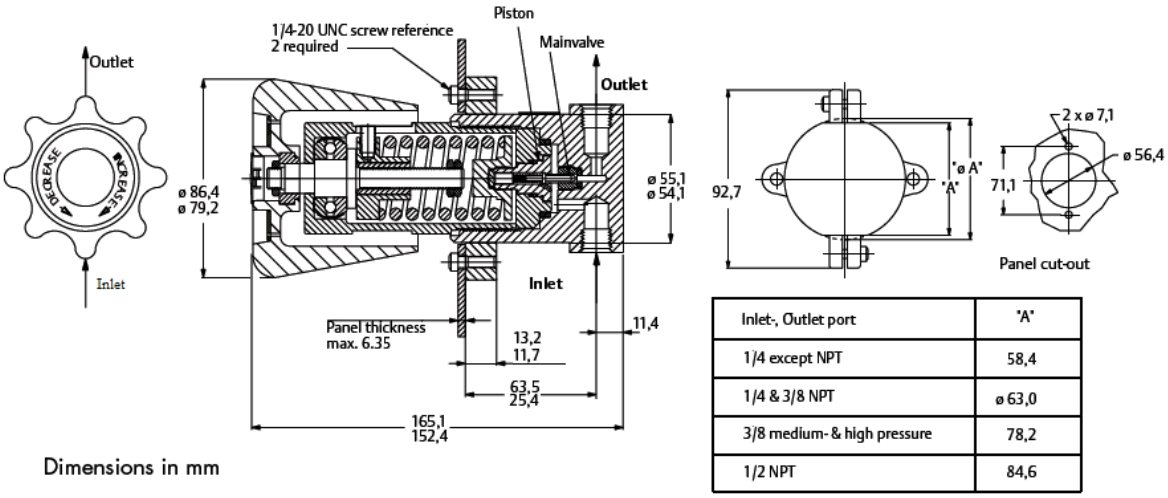

Inlet-, Outlet port	"A"
1/4 except NPT	58,4
1/4 & 3/8 NPT	ø 63,0
3/8 medium- & high pressure	78,2
1/2 NPT	84,6

Fig. 3.10 TESCOM BPR.

Another stainless steel cylinder vessel of 500 mL (THAR-SCF) (Fig. 3.11) with the same sealing mechanism as the precipitation chamber is used as the cyclone separator where the mixture is introduced tangentially at a high velocity. Centrifugal forces act on the liquid droplets forcing them to the bottom of the separator and allowing the light gases to exit through a port at the top.

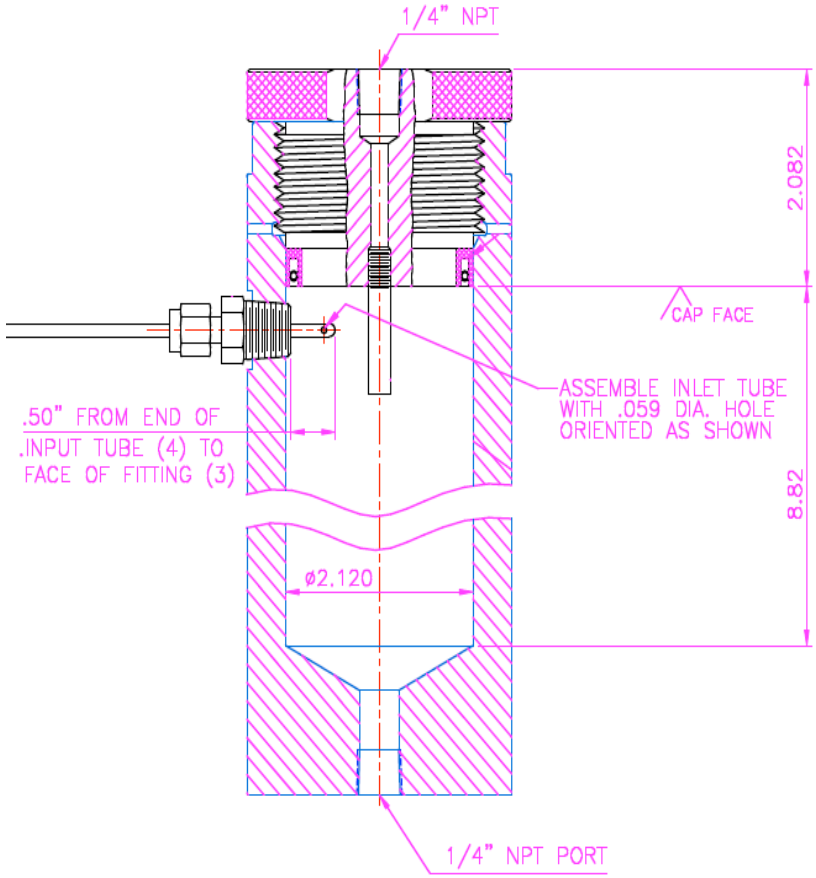

Fig. 3.11 Schematic diagram of the cyclone separator chamber.

The temperature of the precipitation chamber and the separator is controlled using temperature controllers (CAL 9400) and two electrical heating jackets. For further accurate temperature reading an additional digital thermocouple is installed to read the temperature inside the precipitation chamber (see Fig. 3.8 for localization of the thermocouple in the precipitation chamber). Usually in SAS experiments temperatures are expressed in celsius. For this reason, this unit will be used in this section and in chapter five.

The CO_2 line passes through two heat exchangers as a helix coil of length 3 m and 5 m, respectively. The first one is a chiller operated at 3°C located just before the high pressure pump to liquefy the CO_2. This allows filling the pump with liquid CO_2 thus increasing pump efficiency and preventing pump cavitation. The other heat exchanger is a water bath operated at temperatures ranging from 40-60°C that is located just before the precipitation chamber to achieve the supercritical temperature condition for CO_2. Loss of pressure upstream of the point where the supercritical mixture is depressurized is compensated by using the back pressure regulator. Joule-Thompson cooling as a result of the large volumetric expansion

across the BPR leads to a drop in temperature of the supercritical mixture and precipitation of the solution and/or CO_2 dry ice. This leads to inconsistent flow rates and plugging on the lines. So an independent electrical heating coil is installed to maintain the BPR at a temperature higher than that of the precipitation chamber.

The equipment contains auxiliary components: safety elements such as two relieve valves (Swagelok, model SS-4R3A), three check valves (Parker, model 25-BN-SS) and four two-way valves (Swagelok, model SS-OVS2) to protect the system from backward flow and pressure increases. In addition, two manometers P1 and P2 are used to measure the pressure at different points; P1 is a pressure gauge used to measure the pressure inside the CO_2 tank to be sure that the cylinder is full during the experiment while P2 is a pressure transducer (Gems Sensors & Controls, 2800 CVD series, model, 2800BGC4001D3003A001) used to measure the pressure inside the precipitation chamber. Furthermore, two stainless steel filters of 5 micron (Parker, model 2A-FT4-5-BN-SS) and 15 micron (Swagelok, model SS-4TF-15) are installed before the CO_2 pump and BPR, respectively, to trap any impurities that may lead to malfunction of the pump or the BPR. The different components are connected to each other by 1/8" chemically cleaned and passivated stainless steel tubing (Autoclave Engineers, model MS 15-200 316 SS) of 0.05 " wall thickness and 0.052 " inside diameter.

The main units (solvent pump, high pressure CO_2 pump, precipitation chamber and separation chamber) have been purchased from THAR-SCF. Tubing and valves were supplied from Swagelok and Parker companies. Pressure control units and temperature controllers were supplied from TESCOM and RS Co. High purity (99.98 mol % pure) CO_2 tank was supplied from Air Liquide Co. All those units have been integrated together to build up our laboratory scale SAS apparatus.

The SAS apparatus can be divided into hot regions and cold regions. The hot regions include the precipitation chamber and the BPR unit. The rest of the components belong to the cold region, not heated units. Table 3.1 shows the limiting pressure and temperature for the essential SAS components.

Table 3.1 Rating of the essential SAS components.

Component	Max. Pressure (MPa)	Max.Temperature (°C)
Precipitation Chamber	69	90
Separator Chamber	40	150
BPR	69	70
Tubing	103	93
Pressure Sensor	30	125
CO_2 Pump	65	5 - cold region
Solvent Pump	41	30 - cold region
Relief Valve	27	300 - cold region
Pressure Gauge	25	120 - cold region
Swagelok Valves	34	35 - cold region

According to the data shown in table 3.1 the precipitator in our SAS apparatus is rated up to 69 MPa and 90 °C but because of the pressure and temperature limits of the pressure gauge, valves and the BPR used, our SAS apparatus is rated up to 25 MPa and 70 °C, which is enough for micronization of pharmaceutical active ingredients. Further improvement of the SAS equipment would include the replacement of the current BPR for one rated at a higher temperature as well as using pressure gauges and valves working at a higher pressure.

3.3.2. Experimental Procedure

All the experiments were performed following the same procedure: first of all, the nozzle and the frit are ultrasonicated for 30 min in acetone to dissolve any residuals or impurities that may accumulate at the orifice or the frit, then left to be dried at air. Once the precipitator is closed and put in place, the heat exchangers are switched on: when the desired temperatures are achieved, the CO_2 is pumped into the precipitation vessel at low flow rate (10 g/min). In parallel, the BPR is used to adjust the pressure inside the precipitation chamber. The time required to fill the precipitation chamber ranges from 30-45 min depending on the working pressure and temperature. Once the supercritical conditions (temperature and pressure) are obtained, at the precipitation chamber an excess of CO_2 is flushed for 20-30 min through the system at the selected flow rate (15-20 g/min) to clean the lines and obtain steady conditions. Meanwhile, the solution pump is primed and filled with the liquid solution. In the next step, the solution is pumped to the chamber at 1-3 mL/min depending on the working conditions and sprayed inside the vessel itself by means of the nozzle. To minimize the amount of solvent during the process, pure solvent is not pumped into the chamber prior to the liquid solution. The small drops of solvent are dissolved by supercritical CO_2 causing

supersaturation of the liquid solution and the consequent precipitation of the solute in the form of a powder that accumulates on the frit located at the bottom of the vessel, as well as being deposited on the internal wall of the vessel. The precipitation process finishes when the desired amount of liquid solution has been fed into the system, then the liquid pump is turned off and the supercritical CO_2 continues flowing through the precipitator vessel. The precipitate is washed by excess CO_2 to remove the residual content of the liquid solvent solubilized into the supercritical CO_2 antisolvent. The washing time is assumed to be 3 times the time required to fill the precipitation chamber with CO_2 and it is estimated using the following expressions:

$$t_{washing} = 3 * t_{f\,ill} \tag{3.42}$$

$$t_{f\,ill} = \frac{V_R * \rho}{F} \tag{3.43}$$

where $t_{washing}$ is the washing time, $t_{f\,ill}$ is the time required to fill the precipitation chamber, V_R is the volume of the precipitation chamber, F is the CO_2 mass flow rate and ρ is the density of CO_2 at the working pressure and temperature.

The washing stage lasts approximately 60-120 min. After that the supercritical CO_2 flow is stopped and the system is depressurized down to atmospheric pressure. Finally, all the precipitate is recovered from both the wall and the frit of the precipitator vessel; the analyses required, such as scanning electron microscope (SEM) and X-ray diffraction (XRD), are then carried out.

Most SAS experiments were carried out at flow rates of 1mL/min and 15-20 g/min for solution and CO_2, respectively. These values were chosen to obtain mole fractions ≥ 0.96 by combining adequate values for the flow rates of the two pumps.

3.3.3. Design of Experiments (DOE)

The "one-factor-at-a-time" has been a common route for investigating the effects of parameters on a process. By this method the effect of one variable or factor is examined by running all the factors at one condition and then repeating and changing the condition of one

factor. Continuing to hold that factor at that condition, the experiment is repeated with another factor at its second condition, etc. This process is repeated until all factors become at their optimum conditions. Nevertheless, this method is slow, expensive and requires many tests for a few factors.

Design of Experiments (DOE) is a statistics-based approach and powerful technique used for exploring new processes, gaining increased knowledge of the existing ones and optimizing theses processes for achieving high performance. DOE is aimed to reduce the number of factors to be studied by identifying the key ones that affect product quality or process performance and allowing us to focus our efforts on the few really important factors, or the 'vital few' [24-25]. In particular, applying the factorial design at two levels for each factor allows us to focus on the important factors, with only a few trials. In general, for K factors, the one-factor-at-a-time method would require K times more trials to be performed than the factorial design approach (2^K). However, the number of trials required in a factorial design at two levels (2^K) increases with the number of factors K. As a consequence, the costs of resources needed to conduct experiments of a full factorial design can quickly become prohibitive. Fortunately, in most cases, when K is too high, the desired information can be obtained using only a fraction of the full factorial design. A fractional factorial design is normally used for the early stages of an investigation where the study of the approximate influence of a large number of factors is more advisable than an accurate study of a few factors that could prove to be relatively unimportant.

In general, a fractional factorial design is created from the full factorial design at two levels. Some of the high-order interaction terms of the full factorial design are associated with additional experimental factors. Each pair of associated factors is called an alias, so the fractional factorial design is denoted as 2^{k-p}, where p is the number of aliases (pairs of allied factors).

The factors that could have effects on the performance of the SAS process are: the initial concentration of the solution (C), the temperature (T), the pressure (P), the liquid flow rate (Q_L), the supercritical CO_2 flow rate (Q_{CO2}), the drying time (t), and the nozzle diameter ($\varnothing_n$). In our study, the drying time and the nozzle diameter are kept constant at 3 times the time required to fill the precipitation chamber and 100 μm, respectively. Consequently, we have five factors to be studied.

The coding scheme used to describe the factor levels is based on the + and - signs, where + and - denote the high and low levels, respectively, of a factor. The full matrix 2^5 design and the magnitude assigned to each factor are shown in table 3.2.

Table 3.2 The full matrix 2^5 design.

Run	*C* (1)	*T* (2)	*P*(3)	Q_L(4)	Q_{CO2} (5)
1	-	-	-	-	-
2	+	-	-	-	-
3	-	+	-	-	-
4	+	+	-	-	-
5	-	-	+	-	-
6	+	-	+	-	-
7	-	+	+	-	-
8	+	+	+	-	-
9	-	-	-	+	-
10	+	-	-	+	-
11	-	+	-	+	-
12	+	+	-	+	-
13	-	-	+	+	-
14	+	-	+	+	-
15	-	+	+	+	-
16	+	+	+	+	-
17	-	-	-	-	+
18	+	-	-	-	+
19	-	+	-	-	+
20	+	+	-	-	+
21	-	-	+	-	+
22	+	-	+	-	+
23	-	+	+	-	+
24	+	+	+	-	+
25	-	-	-	+	+
26	+	-	-	+	+
27	-	+	-	+	+
28	+	+	-	+	+
29	-	-	+	+	+
30	+	-	+	+	+
31	-	+	+	+	+
32	+	+	+	+	+

To further reduce in the large number of experiments (32), factors Q_L(4) and Q_{CO2} (5) were thought to have the less influence on the process performance, and therefore they are considered as allied factors.

Among all possible fractional factorial designs for five factors at two levels, the design 2^{5-2} was selected. The fractional factorial 2^{5-2} design was obtained as follows:

1. The full factorial design at two levels for concentration (1), temperature (2), and pressure (3) was built following Yates standard order [24].
2. Two pairs of allied factors (p = 2), liquid flow rate (4) and supercritical CO_2 flow rate (5) were associated with concentration/temperature interaction (12) and concentration /pressure interaction (13), respectively. This association was obtained using MINITAB 15 SOFTWARE [26].
3. The signs of the new columns of allied factors (Q_L(4) and Q_{CO2} (5)) were obtained by multiplying the signs of the interaction variables. For example, the signs of the liquid flow rate (4 = 12) column were obtained by multiplying the signs of the concentration (1) column by the signs of the temperature (2) column.

As a result, we generated eight different combinations of signs for the five factors as shown in table 3.3. The generated combinations are eight different trails (25, 2, 19, 12, 13, 22, 7 and 32) out of the full factorial design at two levels 2^5. Thus, the design is a fraction of ¼ of the full 2^5 design.

Table 3.3 The fractional factorial 2^{5-2} design.

Run	Run No. in the Full 2^5 Matrix	*C* (1)	*T* (2)	*P*(3)	Q_L (4=12)	Q_{CO2} (5=13)	Response
1	25	-	-	-	+	+	
2	2	+	-	-	-	-	
3	19	-	+	-	-	+	
4	12	+	+	-	+	-	
5	13	-	-	+	+	-	
6	22	+	-	+	-	+	
7	7	-	+	+	-	-	
8	32	+	+	+	+	+	
Contrast							

To determine the complete meaning of each column, a simple procedure involving the response, contrast calculations and alias generators was performed.

- **Response and Contrast Calculation**

The dimensional properties of the final product are the most important characteristics because they define the processing behavior. In the case of pharmaceuticals, particle morphology and size are key parameters that determine the drug rate of dissolution in the

biological fluid and the bioavailability of poorly water-soluble drugs. Therefore, the mean particle size (PS) and the particle morphology were used as a response to evaluate the process performance.

Which main factors or interactions might affect the response? What is the optimum process condition? To answer these questions we need to calculate the mean effect (contrast) of each factor. The mean effect (contrast) can be calculated using the following equation:

$$l_i = \frac{1}{N_+}\sum y_+ - \frac{1}{N_-}\sum y_- \tag{3.44}$$

where N_+, N_- are the number of runs with high and low levels for each factor, respectively. And y_+, y_- are the response of each run at the high and low levels, respectively.

The order of importance of the factors for particle size and morphology can be summarized in view of their mean effect.

- **Alias Structure**

A fractional factorial design is generated from a full factorial design by choosing an alias structure. The alias structure determines which effects are confounded with each other. MINITAB 15 SOFTWARE [26] was used also to generate the alias structure and simplified alias structure that are shown in tables 3.4 and 3.5, respectively.

Table 3.4 The alias structure.

Concentration	Effect l_1 = 1 + 24 + 35 + 12345
Temperature	Effect l_2 = 2 + 14 + 345 + 1235
Pressure	Effect l_3 = 3 + 15 + 245 + 1234
Liquid flow rate	Effect l_4 = 4 + 12 + 235 + 1345
Supercritical CO_2 flow rate	Effect l_5 = 5 + 13 + 234 + 1245

L_I is calculated by adding the l_i values obtained using Eq. (3.44) for the products of factors specified in table 3.4.

The simplified structure obtained by neglecting three order and higher interactions [24] is given in the following table.

Table 3.5 The simplified alias structure.

Concentration	Effect l_1 = 1 + 24 + 35
Temperature	Effect l_2 = 2 + 14
Pressure	Effect l_3 = 3 + 15
Liquid flow rate	Effect l_4 = 4 + 12
Supercritical CO_2 flow rate	Effect l_5 = 5 + 13

In table 3.3 the effect (contrast) in each column is due to both the main variables (C, T, P, Q_L and Q_{CO2}) and the effects of the interactions are shown in table 3.5. For screening purposes, the interactions between two factors were also considered negligible [25], so the effect value l_i is caused only by the main factor, by other words, concentration for column 1, temperature for column 2, and so on.

- **Level Identification**

As mentioned before the code used to describe the factor levels is based on the + and - signs, the high and low levels, respectively. The two levels were chosen mainly on the basis of phase diagrams and previous studies on SAS precipitation.

The low level of concentration was set to obtain a sufficient amount of precipitate for subsequent analysis; the high level was limited by the saturation of the solution at room temperature.

The lower temperature and pressure limits were determined by the phase diagram of the CO_2 + binary solvent system aiming to stay within the one phase supercritical region; the superior limits were based on reducing energy costs and previous studies.

Flow rate limits were chosen to obtain CO_2 mole fractions ≥ 0.96, in the carbon dioxide-rich region taking into account the equipment limitations.

3.3.4. Characterization of the Particles

The solid state properties and characteristics of the precipitated particles have been evaluated using scanning electron microscopy (SEM), powder X-ray diffraction, Infrared spectroscopy (IR) and differential scanning calorimetry (DSC).

- **Scanning Electron Microscopy**

Scanning electron microscopy (SEM) is a type of electron microscopy that images a sample by scanning it with a high-energy beam of electrons in a raster scan pattern. The electrons interact with the atoms that make up the sample producing signals that contain information about the sample's surface topography, composition, and other properties such as electrical conductivity. A JEOL-6400 electron microscope working at 10 kV was used to characterize the microparticles obtained in SAS experiments. Prior to analysis, samples were gold coated. This study was carried out in the National Center of Electron Microscopy located at the Universidad Complutense de Madrid.

- **Particle Size and Particle Size Distribution Analysis**

The size and size distribution of the precipitated particles are important characteristics because they define processing behavior, particle solubility and bioavailability. The particle size may vary over a wide range. This range is called the particle size distribution (PSD), and it can be represented in the form of a table or a histogram (see Fig. 3.12).

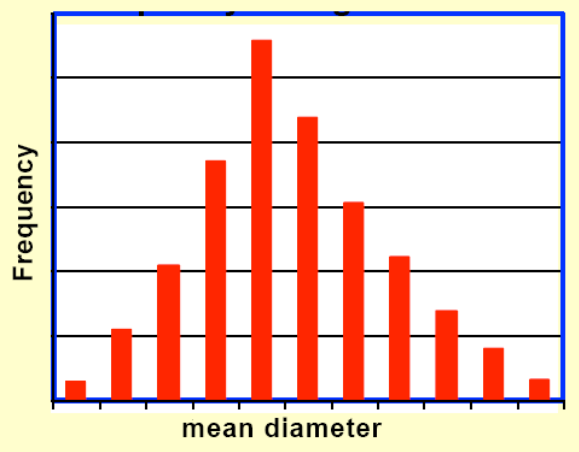

Fig. 3.12 Typical PSD in the form of a histogram.

A PSD such as that shown in Fig. 3.12 is obtained by counting the particles of different sizes in an electron microscope image using SEMAFORCE program [27] and the frequency using STATEXT program [28].

Another feature to describe the variation in particle size is the normal distribution curve; the Normal curve is a symmetrical curve with a single central peak at the mean (average) μ of the data. The shape of the curve is described as a bell-shaped with the graph falling off

evenly on either side of the mean. Fifty percent of the distribution lies to the left of the mean and fifty percent lies to the right of the mean. The spread of a normal distribution is controlled by the standard deviation σ of the data; the smaller the standard deviation the more concentrated in the data (see Fig. 3.13).

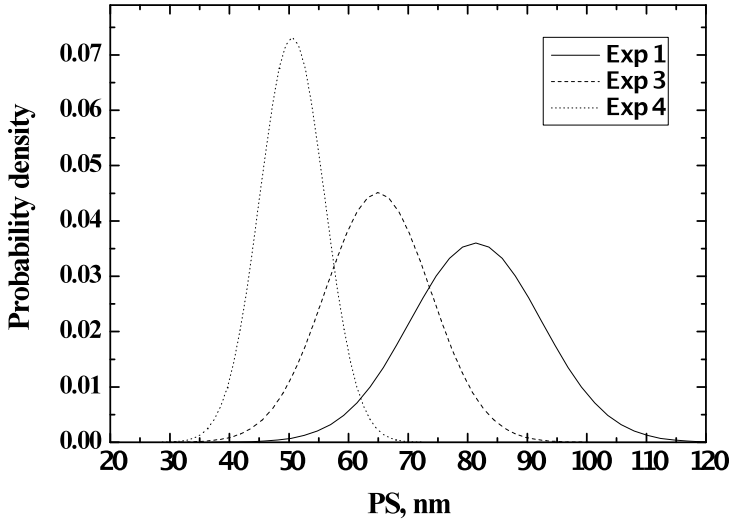

Fig. 3.13 Probability density as a function of particle size.

A normal distribution curve such as that shown in Fig. 3.13 is obtained also by counting the particles of different sizes and calculating the normal distribution using the following equation:

$$Y(x) = \frac{1}{\sigma\sqrt{2\pi}} e^{\frac{-(x-\mu)^2}{2\sigma^2}} \tag{3.45}$$

where x is a normal random variable (size), μ is the mean and σ is the standard deviation

- **Powder X-ray Diffraction**

Powder X-ray diffraction (XRD) is a scientific technique using X-ray diffraction on powder or microcrystalline samples for structural characterization of materials. XRD patterns of the solids prior and after micronization were obtained using (Philips X'pert, model MPD) powder diffraction system. The X-ray source was nickel-filtered Kα emission of copper (1.541837Å). Samples were scanned over the range of 5-50 2θ degrees using the Bragg-Brentano geometry.

- **Infrared Spectroscopy (IR)**

Infrared spectroscopy (IR spectroscopy) deals with the infrared region of the electromagnetic spectrum. Molecules absorb specific frequencies that are characteristic of their structure. These absorptions are resonant frequencies, i.e. the frequency of the absorbed radiation matches the frequency of the bond or group that vibrates. The energies are determined by the shape of the molecular potential energy surfaces, the masses of the atoms, and the associated vibronic coupling. Nowadays most common laboratory instruments are Fourier transform infrared (FTIR) spectrometers. FTIR is used to obtain an infrared spectrum of absorption, emission, photoconductivity or Raman scattering of a solid, liquid or gas. An FTIR spectrometer simultaneously collects spectral data in a wide spectral range.

Solid samples were prepared by crushing the sample with purified potassium bromide to remove scattering effects from large crystals. This powder mixture was then pressed in a mechanical press to form a translucent pellet through which the beam of the spectrometer can pass. IR spectra of the solids prior and after micronization were obtained in the 4000–400 cm^{-1} frequency range. Spectra were collected using a Perkin-Elmer model Spectrum 100 FTIR spectrophotometer.

- **Differential Scanning Calorimetry (DSC)**

A differential scanning calorimeter or DSC is a thermoanalytical apparatus in which the difference in the amount of heat required to increase the temperature of a sample and the reference is measured as a function of temperature. Both the sample and reference are maintained at nearly the same temperature throughout the experiment. DSC curves of the solids prior and after micronization were obtained using a TA Instruments DSC model Q10, connected to a RCS cooling unit. Tightly sealed aluminum volatile pans were used, in dry nitrogen, flowing at 50.0 mL min^{-1}. A MT5 Mettler microbalance was used to weigh the samples, ranging between 3 and 10 mg (with an error of ± 0.001 mg). The calorimeter was calibrated in temperature using standard samples of In and Sn, supplied by TA Instruments (purity > 99.999% and > 99.9%, respectively), and of benzoic acid (purity > 99.97%), supplied by the former NBS (lot 39i), and in enthalpy with the In and Sn standards already described.

- **Thermogravimetric Analysis (TGA)**

Thermogravimetric Analysis measures the amount and rate of change in the weight of a material as a function of temperature or time in a controlled atmosphere. Measurements are used primarily to determine the composition of materials and to predict their thermal stability at temperatures up to 1000°C. The technique can characterize materials that exhibit weight loss or gain due to decomposition, oxidation, or dehydration. TGA can tell us about: the composition of multicomponent systems, thermal stability of materials, oxidative stability of materials, estimated lifetime of a product, decomposition kinetics of materials, the effect of reactive or corrosive atmospheres on materials, moisture and volatiles content of materials. DSC and TGA studies of SAS co-precipitated diflunisal + PVP *K*-30 from acetone/DCM (80:20, v/v %) as well as the pure materials were performed using a Delta Series TA-SDT (Simultaneous DSC and TGA) Model Q-600 in nitrogen atmosphere using open aluminum crucibles.

- **Dissolution Test**

Dissolution tests were carried out in pH 7.4 phosphate buffer medium (0.01 M phosphate buffer) using phosphate buffer saline supplied from Sigma-Aldrich. A hydraulic press at 5000 kg/cm^2 was used to prepare compressed disks in similar fashion to those used for IR spectroscopy by the conventional procedure; 100 mg of the diflunisal powder were used in each case. Bath temperature and paddle speed were set at 100 rpm and 37 °C. Aliquots of 5 mL were taken at 5, 10, 20, 30, 45, 60, 90, up to 480 min time intervals and analyzed using a Perkin-Elmer spectrophotometer model Lambda 35 at λ_{max} = 275 nm. The volume of the solution kept constant by adding 5 mL of the phosphate buffer to solution each time.

References

[1] J. J. Christensen, L.D. Hansen, R. M. Izatt, D. J. Eatough and R. M. Hart. Isothermal high pressure flow calorimeter, *Rev. Sci. Instrum.* 47 (1976) 730–734.

[2] A. Cabañas. Doctoral Thesis, Complutense University of Madrid (1998).

[3] D. Peng and D. B. Robinson. New two constant equation of state, *Ind. Eng. Chem. Fundam.* 15 (1976) 59–64.

[4] G. Soave. Equilibrium constants from a modified Redlich-Kwong equation of state, *Chem. Eng. Sci.* 27(1972) 1197–1203.

[5] K. S. Pitzer, D. Z. Lippmann, R. F. Curl Jr., C. M. Huggins and D. E. Petersen. The Volumetric and Thermodynamic Properties of Fluids. II. Compressibility Factor, Vapor Pressure and Entropy of Vaporization, *J. Am. Chem. Soc.* 77 (1955) 3433–3440.

[6] O. Redlich and J. N. S. Kwong. On the thermodynamics of solutions V. An equation of state - fugacities of gaseous solutions, *Chem. Rev.* 44 (1949) 233–244.

[7] M. Prausnitz, R. N. Lichtenthaler and E. G. Azevedo. Molecular Thermodynamics of Fluid-Phase Equilibria, 3rd Ed., Prentice Hall PTR New Jersey (1999).

[8] O. Pfohl, S. Petkov and G. Brunner. PE 2000, Available from: www.tu-harburg.de/v8/gruppe-prof-smirnova/veroeffentlichungen/pe-000/download.html.

[9] R. A. Heidemann and A. M. Khalil. The calculation of critical points. *AlChE J.* 26 (1980) 769–779.

[10] R. L. Scott and P. H. van Konynenburg. Van der Waals and related models for hydrocarbon mixtures, *Discuss. Faraday Soc.* 49 (1970) 87–97.

[11] E. Reverchon. Supercritical antisolvent precipitation of micro- and nano-particles, *J. Supercrit. Fluids* 15 (1999) 1–21.

[12] J. Jung and M. Perrut. Particle design using supercritical fluids: Literature and patent survey, *J. Supercrit. Fluids* 20 (2001) 179–219.

[13] A. Shariati and C.J. Peters. Recent developments in particle design using supercritical fluids, *Curr. Opin. Solid State Mater. Sci.* 7 (2003) 371–383.

[14] S.-D. Yeo and E. Kiran. Formation of polymer particles with supercritical fluids: A review, *J. Supercrit. Fluids* 34 (2005) 287–308.

[15] E. Reverchon, R. Adami, G. Caputo and I. De Marco, Spherical microparticle production by the Supercritical Antisolvent Precipitation, *J. Supercrit. Fluids* 47 (2008) 70–84.

[16] M. J. Cocero, A. Martín, F. Mattea and S. Varoma. Encapsulation and co-precipitation processes with supercritical fluids: fundamentals and applications, *J. Supercrit. Fluids* 47 (2008) 546–555.

[17] E. Reverchon, G. Caputo and I. De Marco. Role of Phase Behavior and Atomization in the Supercritical Antisolvent Precipitation, *Ind. Eng. Chem. Res.* 42 (2003) 6406–6414.

[18] S. S. Dukhin, C. Zhu, R. Dave, R. Pfeffer, J. J. Luo, F. Chávez and Y. Shen, Dynamical interfacial tension near critical point of a solvent-antisolvent mixture and laminar jet stabilization, *Colloids Surf. A,* 229 (2003) 181–189.

[19] S. S. Dukhin, Y. Shen, R. Dave and R. Pfeffer, Droplet mass transfer, intradroplet nucleation and submicron particle production in two-phase flow of solvent-supercritical antisolvent emulsion. *Colloids Surf. A,* 261 (2005) 163–176.

[20] A. Martín and M. J. Cocero. Micronization processes with supercritical fluids: fundamentals and mechanisms, *Adv. Drug Delivery Rev.* 60 (2008) 339–350.

[21] T. Petit-Gas, O. Boutin, I. Raspo and E. Badens. Role of hydrodynamics in supercritical antisolvent processes, *J. Supercrit. Fluids* 51 (2009) 248–255.

[22] A. Tenorio, P. Jaeger, M. D. Gordillo, C. M. Pereyra and E. J. Martínez de la Ossa. On the selection of limiting hydrodynamic conditions for the supercritical antisolvent (SAS) process, *Ind. Eng. Chem. Res.* 48 (2009) 9224–9232.

[23] E. Reverchon, E. Torino, S. Dowy, A. Brauer and A. Leipertz. Interactions of phase equilibria, jet fluid dynamics and mass transfer during supercritical antisolvent micronization, *Chem. Eng. J.* 156 (2010) 446–458.

[24] G. E. P. Box, W. G. Hunter and J. S. Hunter. Statistics for Experimenters. An Introduction to Design, Data Analysis and Model Building; 2nd Ed., J. Wiley and Sons: New York (1993).

[25] J. Antony. Design of Experiments for Engineers and Scientists, Elsevier Science & Technology Books, Butterworth-Heinemann Amsterdam (2003).

[26] MINITAB 15 SOFTWARE. Available from: http://www.minitab.com/en-US/products/minitab/free-trial.aspx?langType=1033

[27] SEMAFORCE. Available from: http://www.jeol.se/?page=sema4down

[28] STATEXT. Available from: http://www.statext.com/index.htm

Chapter 4. Thermal Effects in Supercritical Antisolvent Micronizations

4.1. Discussion of results already published for the solvents acetone, *N,N*-dimethylformamide, dimethylsulfoxide and ethyl acetate

References

4.2. Excess Molar Enthalpies of CO_2 + Acetone at Pressures from (9.00 to 18.00) MPa and Temperatures from (313.15 to 333.15) K
The Journal of Chemical and Engineering Data, volume 55 (2010) 3649–3654

4.3. Measurements and modeling of high-pressure excess molar enthalpies and
isothermal vapor–liquid equilibria of the carbon dioxide + *N,N*-dimethyl formamide system
The Journal of Supercritical Fluids, volume 55 (2010) 566–572

4.4. Role of excess molar enthalpies in supercritical antisolvent micronizations using dimethylsulfoxide as the polar solvent
The Journal of Supercritical Fluids, volume 60 (2011) 45– 50

4.5. Excess molar enthalpies for mixtures of supercritical CO_2 and ethyl acetate and their role in supercritical fluid applications
The Journal of Chemical Thermodynamics, accepted paper

Thermal Effects in Supercritical Antisolvent Micronizations

4.1 Discussion of Results Already Published for the Solvents Acetone, *N*,*N*-Dimethylformamide, Dimethylsulfoxide and Ethyl Acetate

As indicated in chapter two of this thesis, the role of thermal effects in SAS micronizations has been studied. Since CO_2 is fed into the precipitation chamber at a flow rate much higher than that of the solution and the solute concentration is very low, the contribution to the excess enthalpy due to solute interactions may be neglected and the thermal effects in SAS experiments can be considered mainly due to the formation of [CO_2 (x) + organic solvent (1-x)] mixtures very rich in carbon dioxide ($x \geq 0.95$). In the first step, we determined the excess enthalpy data for the CO_2 + organic solvent systems typically used in these micronizations. In a second step, the interaction between the excess enthalpies and phase equilibria in the SAS precipitation chamber has been elucidated. Therefore, the specific objectives of this thesis covered in this chapter are:

1. Measurement of Excess Enthalpy Data for Supercritical CO_2 + Organic Solvent Systems

Heats of mixing were measured using a high-pressure isothermal flow calorimeter available at our laboratory under the conditions of temperature and pressure usually employed in SAS micronizations. Since these data are already available for the solvents *N*-methyl-2-pyrrolidone (NMP), ethanol and methanol, the solvents acetone (Ac), *N*,*N*-dimethylformamide (DMF), dimethylsulfoxide (DMSO) and ethyl acetate (EA) were studied. The excess enthalpy data obtained were correlated using cubic equations of state.

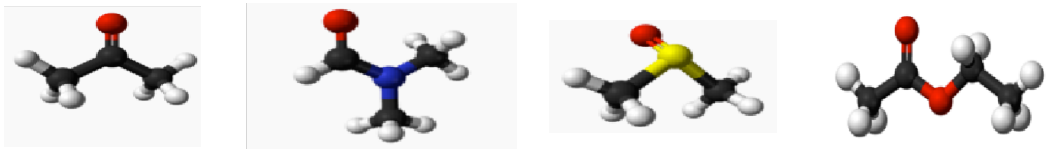

Ac	DMF	DMSO	EA
C_3H_6O 58.08 g/mol	C_3H_7NO 73.09 g/mol	C_2H_6OS 78.13 g/mol	$C_4H_8O_2$ 88.105 g/mol

Fig. 4.1 Solvents included in this study

2. Study of High-Pressure Phase Behavior and Critical Data for Supercritical CO_2 + Organic Solvent Systems. Interaction between Phase Equilibria and Excess Enthalpies during SAS Experiments

The isothermal vapor-liquid equilibrium (VLE) and critical data for the CO_2 + organic solvent mixtures involved in this study are available in the literature. Nevertheless, critical data are scarce. For each system a bibliographic review was carried out. If necessary, critical locus and VLE were predicted or calculated using cubic equations of state. Data gathered in objectives 1 and 2 were used to discuss the thermodynamic behavior of the mixtures formed in the SAS precipitation chamber and the influence of thermal effects on phase equilibria and the particles morphology.

This part of the thesis has been already published in references [1-4]. The publications are included after this comprehensive discussion.

The high-pressure isothermal flow calorimeter used for these measurements was described in detail in chapter three. The conditions for temperature and pressure were 313.15 and 323.15 K and 9.00, 12.00, 15.00 and 18.00 MPa as well as 333.15 K and 9.00 and 15.00 MPa. By combining adequate values for the flow rates of the two pumps the entire mole fraction range was covered. Details about the experimental procedure, the source of the densities required to convert volume flow rates into molar flow rates and values for the excess molar enthalpy (H_m^E) can be found in references [1-4]. It is necessary to know the CO_2 and organic liquid densities at the temperature of the pumps and the pressure of each experiment. Plots of H_m^E vs CO_2 mole fraction (x) are also included in references [1-4]. For the sake of comparison, all the results have been combined in Figs. 4.2 - 4.6 together with those obtained for CO_2 + NMP at the same conditions of temperature and pressure [5]. At each temperature and pressure H_m^E data have been correlated using the Padé functions described in reference [1]. Results from these correlations are also shown in Figs. 4.2 - 4.6.

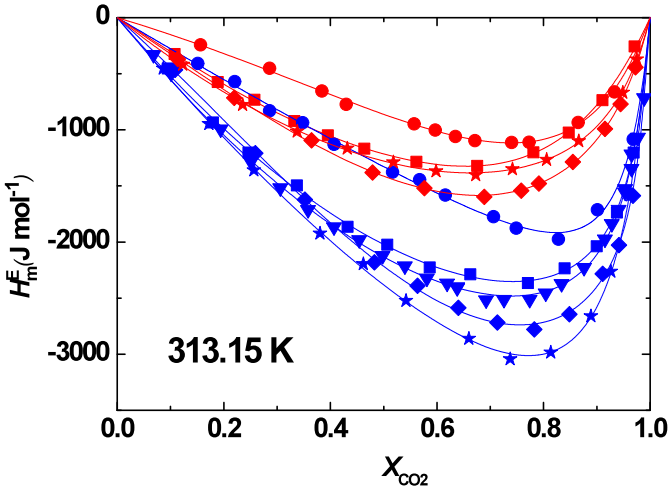

Fig. 4.2 Excess molar enthalpies at 313.15 K for the binary systems [CO_2(x) + organic solvent (1 − x)] at 9.00 MPa (blue) and 12.00 MPa (red) for NMP (▼), Ac (■), DMF (♦), DMSO (●) and EA (★).

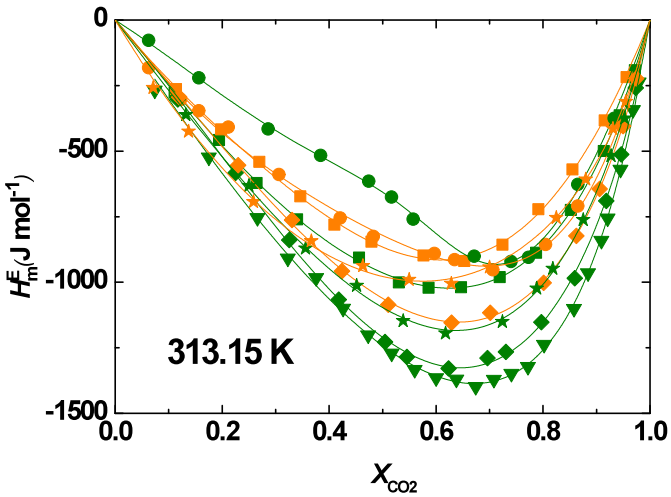

Fig. 4.3 Excess molar enthalpies at 313.15 K for the binary systems [CO_2(x) + organic solvent (1 − x)] at 15.00 MPa (green) and 18.00 MPa (orange) for NMP (▼), Ac (■), DMF (♦), DMSO (●) and EA (★).

Similar trends for the variation of H^E_m with mole fraction, temperature and pressure were observed for all the CO_2 + organic solvent systems studied. In most cases, mixtures showed very exothermic mixing. H^E_m minimum values may be as low as –4500 J mol^{-1}. For most conditions of temperature and pressure, excess molar enthalpies exhibit this minimum in the CO_2 rich region. For CO_2 + DMSO at 333.15 K and 9.00 MPa the minimum appears for $x \approx$ 0.5 due to the beginning of a two-phase region in which H^E_m varies linearly with x because a gaseous and a liquid mixture of fixed composition are at equilibrium. These linear sections appear for several conditions of temperature and pressure, and are explained in detail in

reference [1]. The liquid and vapor-phase compositions are shown to correspond to the x coordinates of the beginning and end of the linear sections. Usually, the CO_2 vapor-phase composition is very close to one and cannot be established from the calorimetric measurements. The liquid phase composition is determined as the intersection of the two Padé functions describing the two-phase and the one-phase sections of the isotherm-isobar. The values thus obtained are in agreement with vapor-liquid equilibrium data described in the literature. Two phase regions have been observed for every system at different T and P conditions.

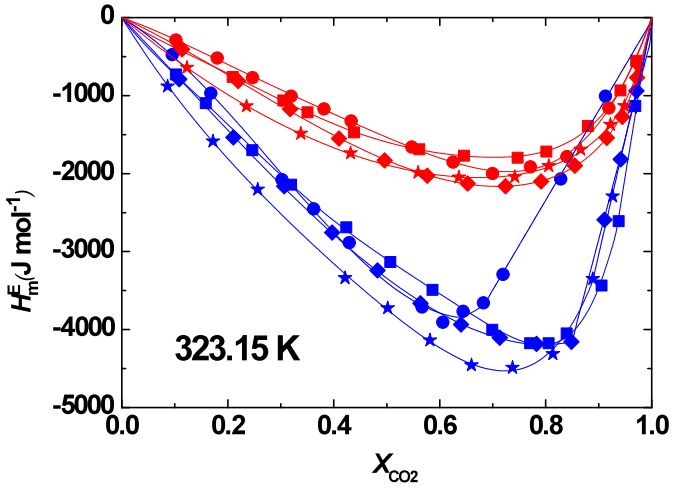

Fig. 4.4 Excess molar enthalpies at 323.15 K for the binary systems [CO_2(x) + organic solvent ($1 - x$)] at 9.00 MPa (blue) and 12.00 MPa (red) for Ac (■), DMF (♦), DMSO (●) and EA (★).

The effects of temperature and pressure on H^{E}_{m} are large. For a given system and mole fraction, in general, mixtures become less exothermic as pressure increases or temperature decreases. The effect of the nature of the organic solvent depends on the conditions of temperature and pressure. For instance CO_2 + EA mixtures are the most exothermic ones at the three temperatures studied and 9.00 MPa. However, at the other pressures studied they exhibit values intermediate between those observed for the other systems studied.

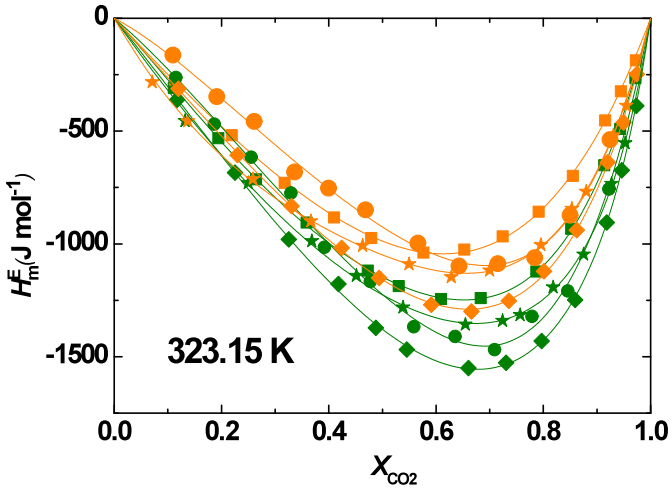

Fig. 4.5 Excess molar enthalpies at 323.15 K for the binary systems [CO_2(x) + organic solvent (1 − x)] at 15.00 MPa (green) and 18.00 MPa (orange) for Ac (■), DMF (♦), DMSO (●) and EA (★).

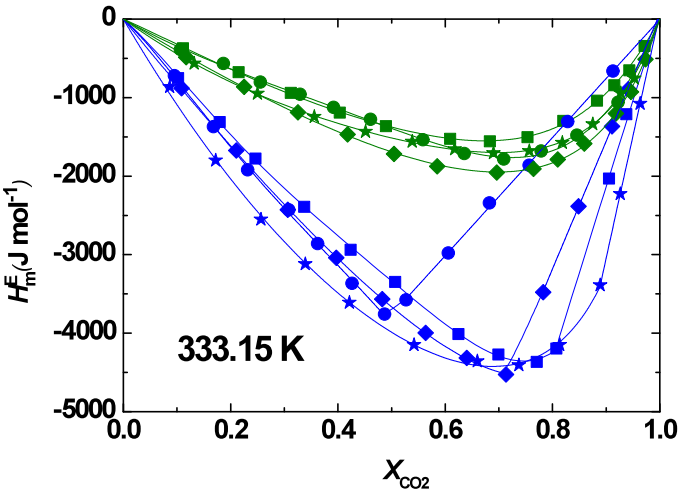

Fig. 4.6 Excess molar enthalpies at 333.15 K for the binary systems [CO_2(x) + organic solvent (1 − x)] at 9.00 MPa (blue) and 15.00 MPa (green) for Ac (■), DMF (♦), DMSO (●) and EA (★).

Excess molar enthalpies for CO_2 + acetone, DMF, EA or NMP were accurately correlated using the Peng-Robinson [6] and Soave-Redlich-Kwong [7] equations of state (EOS), and the classical mixing rule with two adjustable binary parameters for each temperature. The equations of state and the excess enthalpy calculations are described in detail in sections 3.2.1 and 3.2.3 of this thesis. As was already discussed in section 3.1.7, the uncertainties in temperature, pressure and composition are smaller than those of the excess molar enthalpies and a least square-procedure was used to minimize relative deviations between experimental and calculated $H^{\mathrm{E}}_{\mathrm{m}}$. The source of the critical constants and acentric factors required in this

calculation, the values adopted by the binary interaction parameters k_{12} and δ_{12}, and values for the standard deviation between experimental and calculated binary excess enthalpies, σ, for each condition of temperature and pressure can be found in references [1, 2, 4 and 5]. These parameter values may be used to predict enthalpies in the temperature and pressure intervals considered in this study. For the sake of simplicity, results from these calculations are not shown in Figs. 4.2 - 4.6; plots including calculated enthalpies can be examined in references [1, 2, 4 and 5]. Excess molar enthalpies could not be correlated for the CO_2 + DMSO system; this could be related to the complex critical behavior exhibited by this system that is discussed next in this chapter.

In the case of the CO_2 + DMF system, the Peng-Robinson and the Soave-Redlich-Kwong EOS were used in conjunction with the classical mixing rules to correlate VLE data for CO_2 + DMF at 293.95, 313.05 and 338.05 K available in the literature. Phase equilibria calculations are described in section 3.2.2. Best results were obtained for the Peng-Robinson EOS. Using the 313.05 K set of parameters, this equation was shown to provide a simultaneous and accurate description of VLE and critical data for the CO_2 + DMF system. On the other hand, predictions of excess molar enthalpies using the Peng-Robinson EOS and the 313.05 K set of parameters were considerably more accurate than those obtained using the Soave-Redlich-Kwong EOS.

The trends of the excess enthalpies with temperature and pressure may be analyzed in terms of molecular interactions, phase equilibria, density and critical parameters previously reported for these systems. A literature search has been carried out and all the available information for CO_2 + acetone, DMF, DMSO or EA is gathered in references [1-4]. These systems have been the subject of numerous investigations due to their relation to supercritical fluid applications. The excess molar enthalpy is shown to be the sum of two contributions: one contribution is associated to changes in molecular interactions due to the disruption of the organic solvent liquid structure by carbon dioxide and the formation of complexes among CO_2 and the organic solvent molecules. The second contribution to H_m^E is due to the carbon dioxide change of state from that of a gas-like or liquid-like fluid to that of a liquid mixture component. We will refer to these two contributions as the molecular interactions contribution and the change of state contribution, respectively.

Table 4.1 shows values for the dipole moment of the organic solvents involved in this study at ambient temperature. These organic solvents are unassociated but all of them present high dipolar moments and solvent structures dominated by dipole-dipole interactions. However, carbon dioxide does not have a dipole moment although it does have a relatively large quadrupole moment. Table 4.1 also summarizes studies carried out either on the pure liquid structure or about the interactions between CO_2 and the organic solvent molecules. The high dipolar moments lead to highly structured liquids with relatively high densities. In the case of NMP, the ring enables an efficient packing and as shown in table 3 of reference [5] NMP densities reach a value of 1.02 g mL^{-1} at 313.15 K and pressures in the 9.00-20.00 MPa range. The solvent structure is disrupted upon mixing with carbon dioxide leading to an endothermic contribution to H_m^E. Moderately exothermic enthalpies are the result of a balance between the endothermic contribution and an exothermic one due to strong organic solvent- CO_2 interactions. This is the molecular interaction contribution to H_m^E that may be expected to change only slightly with temperature and pressure. The organic solvent- CO_2 interactions have been so far studied for acetone, DMSO and EA but similar results may be expected for DMF and NMP.

Table 4.1 Dipole moment of the solvents involved in this study and interactions between CO_2 and the organic solvent molecules.

Solvent	**Dipole moment[a] /D**	**Type of study**	**Main conclusion**	**Reference**
acetone	2.9[b]	IR spectroscopy and ab initio calculations Molecular dynamics calculation	Acetone carbonyl atom attracts very strongly CO_2 molecules	Sala et al. [12] Aida et al. [13]
DMF	3.9[c]	-	-	
DMSO	4.1[d]	Ab initio calculations	S=O bond is involved in the CO_2-DMSO complex	Raveendran and Wallen [14]
EA	1.9[b]	Molecular dynamics calculation	EA carbonyl atom attracts very strongly CO_2 molecules	Aida et al. [15]
NMP	4.1[e] (303.15 K)	Pure solvent PVT measurements	NMP presents high density because the NMP ring enables efficient packing	García et al. [16]

[a] Dipole moment at 298.15 K, unless otherwise indicated.
[b] Poling et al. [8].
[c] Marcus [9].
[d] McClellan [10].
[e] Lee and Kumler [11].

In order to analyze the change of state contribution to H_m^E we need to consider the state and densities of the pure components and those of the mixtures formed in the calorimeter. The organic solvents are liquid at the conditions of temperature and pressure of the experiments. Their densities have been measured in the intervals of *T* and *P* considered in this study. For a given solvent, density values vary slightly with temperature and pressure and can be found in references [1-4]. However the state and density of carbon dioxide differ to a great extent from one (*P*,*T*) coordinate to another. Carbon dioxide is a supercritical fluid that may be either a high-density (liquid-like) fluid or a low-density (gas-like) fluid. Carbon dioxide densities at the *P*, *T* conditions of H_m^E measurements are listed in table 4.2. For instance, at 323.15 K carbon dioxide is a gas-like fluid at 9.00 MPa (ρ = 0.2850 g mL^{-1}) and a liquid-like fluid at 18.00 MPa (ρ = 0.7571 g mL^{-1}).

Table 4.2 Densities of carbon dioxide at the *P* and *T* conditions of H_m^E measurements [17].

***T* (K)**	***P* (MPa)**	**ρ (g mL^{-1})**
313.15	9	0.4855
	12	0.7178
	15	0.7802
	18	0.8195
323.15	9	0.2850
	12	0.5847
	15	0.6998
	18	0.7571
333.15	9	0.2354
	15	0.6041

The state of the mixtures formed in the calorimeter (liquid, fluid, two-phase) may be established by examining the situation of the (*P*, *T*) coordinate with respect to the system critical locus and taking into account the critical composition and the vapor-liquid equilibrium data. The CO_2 + NMP, CO_2 + acetone, CO_2 + DMF and CO_2 + EA systems exhibit type I critical behavior in the classification of Scott and van Konynenburg [18]. Several authors have reported critical data for CO_2 + acetone in the 304 to 350 K interval and Ziegler et al. [19] also reported data covering the entire composition range. There is a good agreement between the different sets of data. In Fig. 4 (a) of ref. [1] the complete P-T projection of the critical locus is shown for this system; in Fig. 4 (b) the locus obtained by a linear regression of

data available in the 304 to 350 K interval is shown together with the temperature and pressure coordinates where experimental H_m^E data were taken.

For the systems CO_2 + NMP, CO_2 + DMF and CO_2 + EA there is only one set of critical data. In these cases, the P-T projections of the critical locus were calculated using these data and the Peng-Robinson equation of state. The critical locus calculation is described in section 3.2.3. P-T projections are shown in Fig. 4 of reference [2] and [3] and Fig. 5 of reference [5]. In all these plots the (*P*, *T*) coordinates for H_m^E measurements are indicated so that the state of the mixtures formed in the calorimeter may be established. As discussed in detail in reference [3], the critical behavior of the CO_2 + DMSO system is more complicate; it belongs either to type III or IV in the Scott and van Konynenburg classification; more data in the lower temperature range are required to reach a definitive conclusion. Equation-of-state calculations for this system do not lead to a good agreement with experimental data. However, the gas-liquid critical data taken by González et al. [20] and Chiu et al. [21] shown in Fig. 2 of reference [3] may be used to establish the state of the mixtures formed in the calorimeter.

It turns out that most mixtures formed in the calorimeter are either liquid or a gaseous and a liquid mixture in equilibrium. Only mixtures very rich in CO_2 are fluid; this type of mixtures are confined to such a narrow mole fraction range that very few experimental H_m^E data could have been taken in this region. In most cases, the fluid carbon dioxide mixes with the liquid solvent forming a liquid mixture or the gaseous and liquid mixtures in equilibrium. As a consequence of the CO_2 change of state, this contribution to the excess enthalpy is exothermic and becomes increasingly exothermic when low-density CO_2 is mixed. This effect is sometimes called the fluid condensation effect. When carbon dioxide enters the calorimeter as a liquid-like fluid, the change-of-state contribution to H_m^E is small and excess molar enthalpy values may be considered mainly the result of the molecular interactions contribution to H_m^E. When carbon dioxide enters the calorimeter as a gas-like fluid, the fluid condensation effect is very pronounced and the change-of-state contribution to H_m^E is extremely exothermic. As a result, the excess molar enthalpy may reach values of – 4500 J mol^{-1}. A detailed discussion for each binary system studied may be found in references [1-4].

For a given temperature, pressure and mole fraction the variations due to the organic solvent nature observed may be attributed to the type of critical diagram and differences in

intermolecular interactions in the pure liquid and the mixtures. These differences lead to varying values for the molecular interactions contribution to H_m^E. However, the magnitude of the change-of-state contribution may be expected to be rather similar for the different solvents at a given temperature, pressure and mole fraction when no phase equilibria are involved.

Mixtures formed by supercritical CO_2 and an organic polar solvent are involved in several supercritical applications. Their role in supercritical antisolvent precipitation (SAS) was already explained in the introduction chapter. They are also involved in other supercritical or near critical crystallization processes such as the Gas antisolvent (GAS) and the Depressurization of an Expanded Liquid Organic Solution (DELOS) techniques described in chapter one. Organic polar solvents such as NMP or DMF are used in polymer solutions when membranes are formed using supercritical carbon dioxide to induce the phase separation. On the other hand, CO_2-expanded using these solvents is also used as reaction media. Examples of these applications are found in references [1-4]. The excess enthalpy data reported in this thesis may be used to model or optimize these processes. However, the aim of this study is to understand the interaction between phase equilibria and excess enthalpies during SAS experiments. The extremely exothermic values obtained at many of the *P*, *T* conditions studied are likely to influence other magnitudes of the system.

As was already pointed out in chapter one, the phase behavior of the CO_2 + organic solvent is one of the crucial factors governing the morphology and the mean size of particles obtained in the SAS process. The presence of the solute can induce modifications in the phase diagram. This is the case of polymers; however, when the solute has little interaction with carbon dioxide the ternary phase diagram for the low solute concentrations usually employed in SAS is coincident with the binary one in the CO_2-rich region which is the region for mixtures involved in SAS. Therefore, the mixtures formed in the precipitation chamber may be treated as binary CO_2 + organic solvent systems. The heat evolved when the supercritical CO_2 dissolves into the organic solution has an important role in the phase behavior. The temperature control in the precipitation chamber is not very precise and the local temperature increase may lead to *T* and *P* conditions where phase splitting takes place.

Since CO_2 is fed into the chamber at a flow rate much higher than that of the solution and the solute concentration is very low, the contribution to H_m^E due to solute interactions may be neglected and the thermal effects in SAS experiments can be considered mainly due to the

formation of CO_2 + organic solvent mixtures very rich in carbon dioxide ($x \geq 0.95$). Consequently, the temperature increase ΔT may be estimated using the H_m^E data reported in this thesis. Since carbon dioxide is the predominant component in these mixtures, its isobaric heat capacity [22] was used to calculate the local temperature increase assuming an adiabatic process and using H_m^E correlation equations to evaluate the heat evolved when a mol of mixture is formed. Values for ΔT thus obtained are shown in table 3 of reference [1] for x = 0.95, in table 3 of reference [3] for the x interval 0.95-0.98 and in table 3 of reference [4] for x = 0.95. An examination of these values together with literature vapor-liquid equilibrium data indicates how the heat evolved upon mixing affects the phase behavior. For instance, at x = 0.95, P = 9.00 MPa and T = 313.15 or 323.15 K carbon dioxide and EA are completely miscible (see Fig. 4.7) and the values estimated for the temperature increase are 7.1 and 8.3 K, respectively. A 8.3 K local temperature increase at 323.15 K and 9.00 MPa would induce immiscibility because the new isotherm is close to that shown in Fig. 4.7 at T = 333.15 K. The 7.1 K local temperature increase at 313.15 K and 9.00 MPa would approach precipitation conditions to the critical locus or even induce immiscibility for the CO_2-rich mixtures formed in the SAS experiments. In both cases the particle morphology would not correspond to that expected in a supercritical phase. This effect is a consequence of the enlargement of the immiscibility window as the temperature increases.

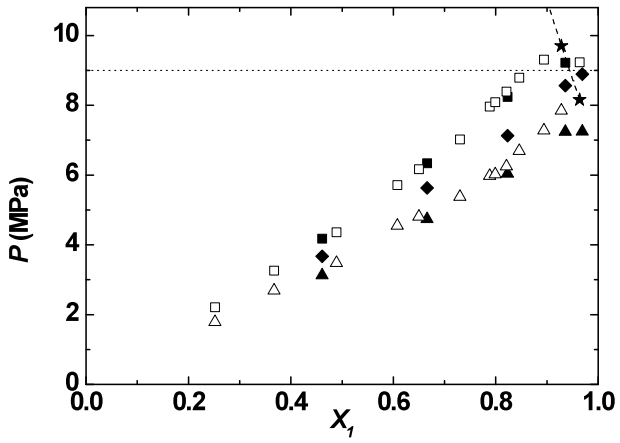

Fig. 4.7 Isothermal vapor-liquid equilibrium for the binary system [CO_2 (x) + EA (1-x)] reported by Byun et al. [23] (Δ, 313.15 K; □, 333.15 K) and Borges et al. [24] (▲, 313.15 K; ◆, 323.15 K; ■, 333.15 K), pressure condition of H_m^E measurements (· · · ·), and critical line (- - -) based on critical data reported by Byun et al. [23] (★).

The enthalpy effect on the phase equilibria has been clearly shown in SAS micronizations using DMSO as the polar solvent. Reverchon et al. [25] precipitated YAc from its DMSO solutions using CO_2 as the antisolvent agent at 313.15, 323.15 and 333.15 K, x = 0.98 and pressures up to 16.0 MPa. A windowed vessel was used to observe the phase behavior of the [CO_2 (x) + DMSO (1-x)] mixtures formed in the precipitation chamber. Immiscibility was observed for initial temperature and pressure conditions where one supercritical phase was expected according to the phase equilibria data available for this system. By measuring the excess molar enthalpies for CO_2 + DMSO mixtures at these T and P conditions and carrying out ΔT calculations similar to those above described, we have shown that Reverchon et al. phase equilibria observations may be a consequence of temperature increases due to the enthalpy effect. Fig. 4.8 shows VLE and critical data for the CO_2 + DMSO system in the temperature interval 309.41 - 348.15 K.

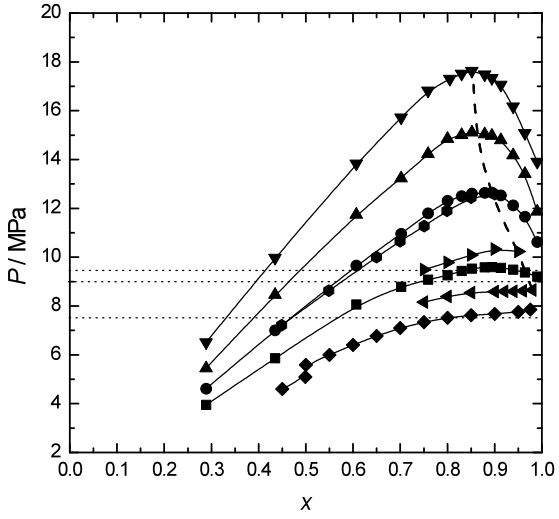

Fig. 4.8 (Fig. 2 in ref. [3]). Isothermal vapor-liquid equilibrium and critical data for the binary system [CO_2(x) + dimethylsulfoxide (1–x)] reported by González et al. [20]: (◆), 309.41 K; (◀) 314.49 K; (▶), 321.28 K; (⬢) 328.94 K, and Chiu et al. [21]: (■) 318.15 K; (●) 328.95 K; (▲) 338.15 K; (▼) 348.15 K, critical line (– – –), and pressure conditions of SAS experiments carried out by Reverchon et al. [25] at 313.15 K using DMSO (· · ·).

According to González et al. [20] the critical temperature and pressure for x = 0.98 are 314.9 K and 8.65 MPa. At 313.15 K and 1.36 wt% of YAc in DMSO, Reverchon et al. reported two phases and agglomerated nanoparticles at 7.5 MPa, two phases and a mixture of nanoparticles and microparticles at 9.0 MPa, one phase and balloon-like particles at 9.5 MPa and one phase and uniform nanoparticles from 10 to 15 MPa. An inspection of Fig. 4.7 indicates that one phase should have been observed already at 9.00 MPa. However, the

temperature increase of 2.9 K calculated for these x, P and T conditions explains the immiscibility observed for mixtures formed in the SAS experiments and a particle morphology that does not correspond to the uniform nanoparticles expected in a supercritical phase. As the pressure rises for this condition of temperature, the heat evolved upon mixing and the local temperature increase are of smaller magnitude and the phase behavior is not affected. Similar effects are observed for experiments carried out by Reverchon et al. at 323.15 and 333.15 K.

Chang et al. used DMSO as a solvent in the SAS precipitation of α-chymotrypsin [26] and lysozyme [27] at 308.15, 318.15, 328.15 and 338.15 K and pressures up to 20 MPa (see Fig. 1.13). In both cases agglomerated or irregular particles are obtained at pressures below 10 MPa when the considerable heat evolved may lead to a local temperature increase in the precipitator. The very exothermic $H_{\mathrm{m}}^{\mathrm{E}}$ values correlate with T and P conditions where micronization is less successful. The solubility of both proteins in CO_2 and its concentration in the solution are very low and the binary phase diagram shown in Fig. 4.8 may be used to discuss results. For instance, in the case of lysozyme at 308.15 K for identical values of lysozyme concentration, capillary size, and CO_2 and solution flow rates, irregular nanoparticles are obtained at 8.5, 10, and 12 MPa and uniform nanoparticles are obtained at 15 and 20 MPa. At this temperature one phase is already expected at 8.5 MPa and at 10 and 12 MPa particle morphologies should correspond to the uniform nanoparticles expected for the supercritical region well above the critical boundary. As mentioned in chapter one, there are other factors that may simultaneously influence the particle morphology but the heat evolved upon mixing CO_2 and the polar solvent is shown to play an important role. By modifying the phase equilibria, excess molar enthalpies will affect the particle precipitation mechanism.

References

[1] F. Zahran, C. Pando, J. A. R. Renuncio, and A. Cabañas. Excess Molar Enthalpies of CO_2 + Acetone at Pressures from (9.00 to 18.00) MPa and Temperatures from (313.15 to 333.15) K, *J. Chem. Eng. Data* 55 (2010)3649–3654.

[2] F. Zahran, C. Pando, J. A. R. Renuncio, and A. Cabañas. Measurements and modeling of high-pressure excess molar enthalpies and isothermal vapor–liquid equilibria of the carbon dioxide + *N*,*N*-dimethylformamide system, *J. Supercrit. Fluids* 55 (2010) 566–572.

[3] F. Zahran, J. Morère, A. Cabañas, J. A.R. Renuncio and C. Pando. Role of excess molar enthalpies in supercritical antisolvent micronizations using dimethylsulfoxide as the polar solvent, *J. Supercrit. Fluids* 60 (2011) 45– 50.

[4] F. Zahran, C. Pando, J. A. R. Renuncio, and A. Cabañas. Excess molar enthalpies for mixtures of supercritical CO_2 and ethyl acetate and their role in supercritical fluid applications. *J. Chem. Thermodyn.* (accepted paper, 2012).

[5] M. J. Dávila, A. Cabañas and C. Pando. Excess molar enthalpies for binary mixtures related to supercritical antisolvent precipitation: carbon dioxide + *N*-metil-2-pirrolidone, *J. Supercrit. Fluids* 42 (2007) 172–179.

[25] E. Reverchon, G. Caputo and I. De Marco. Role of Phase Behavior and Atomization in the Supercritical Antisolvent Precipitation, *Ind. Eng. Chem. Res.* 42 (2003) 6406–6414.

[6] D.Y. Peng and D.B. Robinson. A new two-constant equation of state, *Ind. Eng. Chem. Fundam.* 15 (1976) 59–64.

[7] G. Soave. Equilibrium constants from a modified Redlich–Kwong equation of state, *Chem. Eng. Sci.* 27 (1972) 1197–1203.

[8] B. E. Poling, J. M. Prausnitz and J. P. O'Connell. Properties of Gases and Liquids, 5th Ed., McGraw-Hill Inc. New York (2001).

[9] Y. Marcus. Introduction to Liquid-state Chemistry, Wiley Interscience, London (1977).

[10] A. L. McClellan, Tables of Experimental Dipole Moments, Rahara Entrerprises, El Cerrito (1974).

[11] C.M. Lee and W.D. Kumler. The dipole moment and structure of the imide group. I. Five- and six-membered cyclic imides, *J. Am. Chem. Soc.* 83 (1961) 4586–4590.

[12] S. Sala, Y. Danten, N. Ventosa, T. Tassaing, M. Besnard and J. Veciana. Solute-solvent interactions governing preferential salvation phenomena of acetaminophen in CO_2 expanded solutions. A spectroscopic and theoretical study. *J. Supercrit. Fluids* 38 (2006) 295–305.

[13] T. Aida, T. Aizawa, M. Kanakubo and H. Nanjo. Molecular motility and affinity of expanded carbon dioxide+ketone systems analyzed by molecular dynamics simulations, *Fluid Phase Equilib.* 297 (2010) 172–177.

[14] P. Raveendran and S. L. Wallen. Cooperative C–H· · ·O hydrogen bonding in CO_2 – Lewis base complexes: implications for solvation in supercritical CO_2, *J. Am. Chem. Soc.* 124 (2001) 12590–12599.

[15] T. Aida, T. Aizawa, M. Kanakubo and H. Nanjo. Analysis of volume expansion mechanism of CO_2-acetate systems at 40 degrees C, *J. Supercrit. Fluids* 55 (2010) 56– 61.

[16] B. García, S. Aparicio, R. Alcalde, M. J. Dávila and J. M. Leal. Modeling the PVT*x* behavior of the *N*-methylpyrrolidinone/water mixed solvent, *Ind. Eng. Chem. Res.* 43 (2004) 3205–3215.

[17] NIST Standard Reference Database Number 69, which can be accessed electronically through the NIST Chemistry Web Book. Available from: http://webbook.nist.gov/chemistry/.

[18] R. L. Scott and P. H. van Konynenburg. Van der Waals and related models for hydrocarbon mixtures, *Discuss. Faraday Soc.* 49 (1970) 87–97.

[19] J. W. Ziegler, J. G. Dorsey, T. L. Chester and D. P. Innis. Estimation of liquid-vapor critical loci for CO2-solvent mixtures using a peak shape method, *Anal. Chem.* 67 (1995) 456–461.

[20] A.V. González, R. Tufeu and P. Subra. High-pressure vapor–liquid equilibrium for the binary systems carbon dioxide + dimethyl sulfoxide and carbon dioxide + dichloromethane, *J. Chem. Eng. Data* 47 (2002) 492–495.

[21] H.-Y. Chiu, R.-F. Jung, M.-J. Lee and H.-M. Lin. Vapor–liquid phase equilibrium behaviour of mixtures containing supercritical carbon dioxide near critical region, *J. Supercrit. Fluids* 44 (2008) 273–278.

[22] R. Span and W. Wagner. A new equation of state for carbon dioxide covering the fluid region from the triple-point temperature to 1100 K and pressures up to 800 MPa, *J. Phys. Chem. Ref. Data* 25 (1996) 1509–1596.

[23] H. S. Byun, M. Y. Choi and J. S. Lim. High-pressure phase behavior and modeling of binary mixtures for alkyl acetate in supercritical carbon dioxide, *J. Supercrit. Fluids* 37 (2006) 323–332.

[24] G. R. Borges, A. Junges, E. Franceschi, F. C. Corazza, M. L. Corazza, J. V. Oliveira and C. Dariva. High-Pressure Vapor−Liquid Equilibrium Data for Systems Involving Carbon Dioxide + Organic Solvent + *β*-Carotene, *J. Chem. Eng. Data.* 52 (2007) 1437–1441.

[25] T. Petit-Gas, O. Boutin, I. Raspo and E. Badens. Role of hydrodynamics in supercritical antisolvent processes, *J. Supercrit. Fluids* 51 (2009) 248–255.

[26] S. C. Chang, M. J. Lee and H. M. Lin. The influence of phase behaviour on the morphology of protein α-chymotrypsin prepared via a supercritical anti-solvent process, *J. Supercrit. Fluids* 44 (2008) 219–229.

[27] S. C. Chang, M. J. Lee and H. M. Lin. Role of phase behavior in micronization of lysozyme via a supercritical anti-solvent process. *Chem. Eng. J.* 139 (2008) 416–425.

Copy of the Published/Accepted Papers

Excess Molar Enthalpies of CO_2 + Acetone at Pressures from (9.00 to 18.00) MPa and Temperatures from (313.15 to 333.15) K

Fouad Zahran, Concepción Pando,* Juan A. R. Renuncio, and Albertina Cabañas

Departamento de Química Física I, Universidad Complutense, E-28040 Madrid, Spain

Mixtures of supercritical CO_2 and acetone are very often involved in supercritical fluid applications, and their thermodynamic properties are required to understand and design these processes. Excess molar enthalpies (H_m^E) for CO_2 + acetone mixtures were measured using an isothermal high-pressure flow calorimeter under conditions of temperature and pressure typically used in supercritical processes: pressures from (9.00 to 18.00) MPa and temperatures from (313.15 to 333.15) K. Mixtures showed exothermic mixing; excess molar enthalpies exhibited a minimum in the CO_2-rich region. The effects of pressure and temperature on the excess molar enthalpy of CO_2 + acetone are large. The most exothermic H_m^E values were observed for a coincident CO_2 mole fraction value of 0.771 at (323.15 and 333.15) K and 9.00 MPa: (−4176 and −4366) J·mol^{-1}, respectively. Two-phase vapor−liquid CO_2-rich regions are observed at (323.15 and 333.15) K and 9.00 MPa where H_m^E linearly varies with CO_2 mole fraction. For a given mole fraction and temperature, mixtures become more exothermic as pressure decreases. These trends were analyzed in terms of molecular interactions, phase equilibria, density, and critical parameters previously reported for CO_2 + acetone. Excess molar enthalpies here reported were correlated using the Peng−Robinson equation of state and the classical mixing rule with two binary interaction parameters. The influence of the thermal effects on the phase behavior of CO_2 + acetone mixtures formed in supercritical antisolvent precipitation experiments was discussed.

Introduction

The mixtures formed by supercritical carbon dioxide and organic solvents such as acetone have received considerable attention in the recent past due to the advantages of CO_2 over conventional organic solvents and its numerous applications in sustainable chemistry.[1] Supercritical carbon dioxide is often promoted as a green solvent since it is nontoxic, has low cost, is nonflammable, and allows operation at low temperatures and moderate pressures (T_c = 304.1 K, P_c = 7.38 MPa).[2] Carbon dioxide physical properties such as density, viscosity, and diffusion coefficient may be varied continuously from liquid-like to gas-like values by simply changing pressure and temperature conditions. Furthermore, a small amount of an organic polar solvent such as acetone may be added to the pure supercritical fluid to increase the solute solubility and/or selectivity in extraction applications.

Mixtures formed by supercritical CO_2 and acetone are also used in the micronization of solutes such as polymers, pharmaceutical compounds, explosives, and colorants. The so-called supercritical antisolvent precipitation (SAS) is based on using supercritical carbon dioxide as an antisolvent to induce controlled precipitation of solutes from their organic solvent solutions thanks to the relatively low solvent power of CO_2 for these solutes and its good miscibility with many organic solvents. SAS precipitation has been extensively used during the last years, and several reviews are available.[3−6] When the supercritical antisolvent dissolves in the organic solvent, the liquid experiences a volumetric expansion and becomes a bad solvent for the solute that precipitates from the solution in micro- and nanoparticles. Other typical polar organic solvents used are dimethylsulfoxide, *N*,*N*-dimethylformamide, dichloromethane, and *N*-methyl-2-pyrrolidone. On the other hand, CO_2-expanded solvents may also be used as reaction media.[7]

The numerous applications of mixtures formed by supercritical carbon dioxide and acetone have prompted researchers like Sala et al.[8] to undertake their study from a fundamental point of view. On the other hand, the physical and thermodynamic properties of the CO_2 + organic polar solvent mixtures are also required to understand and design supercritical fluid applications. Consequently, the high-pressure density and phase behavior and the volumetric expansion of CO_2 + acetone mixtures have received considerable attention in the last years.[9−23] However, not much attention has been paid to the heat evolved when supercritical CO_2 dissolves into the organic solvent. The excess molar enthalpies (H_m^E) at these conditions can be quite high. Thus, thermal effects during this process have an effect on the phase separation path and must be considered to optimize precipitation and reaction conditions. In a previous study,[24] H_m^E values for CO_2 + *N*-methyl-2-pyrrolidone mixtures were reported at (313.15 and 338.15) K and (9.48, 15.00, and 20.00) MPa. Furthermore, the relationship between thermal effects and phase behavior and coalescence phenomena observed in SAS micronization of several antibiotics was discussed. In this paper, we report excess molar enthalpies for the binary system CO_2 + acetone under conditions of temperature and pressure typically used in supercritical CO_2 applications: (313.15 and 323.15) K and (9.00, 12.00, 15.00, and 18.00) MPa and 333.15 K and (9.00 and 15.00) MPa. The excess enthalpy data for mixtures of CO_2 and acetone will be analyzed in terms of molecular interactions, phase equilibria, and density data and critical parameters. The influence of these thermal effects on the phase behavior of mixtures formed in the precipitation chamber in SAS experiments will be examined.

* Corresponding author. Phone: +34 91394 4304. Fax: +34 91394 4135. E-mail: pando@ quim.ucm.es.

10.1021/je100220c
Published on Web 07/13/2010

Experimental Section

The materials employed were CO_2 (Air Liquide, 99.98 % in mole) and acetone (Sigma-Aldrich, 99.9 % in mole). Commercial materials were used without further purification.

An isothermal high-pressure flow calorimeter (Hart Scientific model 7501) was used to perform H_m^E measurements. The calorimeter was first described by Christensen et al.,[25] and the experimental procedure is described elsewhere.[24] The reactants were pumped into the calorimetric cell by two thermostatted syringe pumps (model: LC-2600, ISCO) at constant flow rates. The temperature of the pumps was controlled within ± 0.02 K. Volume flow rates were selected to cover the entire concentration range. For each pump, the uncertainty in the volume flow rate was obtained by a previous calibration. The flow rate stability was ± 1 % over the total volume of the cylinder. The calorimetric cell was located in a silicon bath in which temperature was controlled within ± 0.001 K. A Peltier cooling device and a pulsed heater kept the cell under isothermal conditions. The pulse energy was determined by a previous heater calibration based on the Joule effect. The pressure was measured using a calibrated pressure transducer (Lucas Schaevitz, model P721-0001). A back-pressure regulator located outside the calorimeter kept the pressure within ± 0.01 MPa.

All runs were made in the steady-state fixed composition mode. Measurements at all the P and T conditions studied were carried out at total volume flow rates of (0.0014 and 0.0028) $cm^3 \cdot s^{-1}$. The CO_2 mole fraction range is covered by combining adequate values for the flow rates of the two pumps at these total volume flow rates. Also, the coincidence within the experimental error of results obtained using different total flow rates is an indication of equilibrium conditions in the calorimeter. The volume flow rates were converted to molar flow rates using the densities and molar masses. CO_2 densities at the temperature and pressure of the pumps were obtained from NIST webbook.[26] Acetone densities were obtained from the Tait equation provided by Adams and Laidler.[27] Since densities are affected by temperature and pressure changes, the error in molar flow rates was derived taking into account contributions from variations in volume flow rates, pressure, and pumps temperature. The mole fraction precision is based on the error in molar flow rates and was estimated to be better than ± 0.001. The error in H_m^E was obtained taking into account contributions from molar flow rates, pulse energy, and frequency and was estimated to be ± 1 % or at least ± 1 $J \cdot mol^{-1}$. Periodically, H_m^E values obtained using this calorimeter for the ethanol + H_2O system at 323.15 K and 15.00 MPa were compared to those previously reported by Ott et al.[28] This set of data has been proposed as a reference for isothermal dilution and flow calorimeters.[29]

Results and Discussion

H_m^E data for the binary system [$CO_2(x)$ + acetone$(1 - x)$] were determined at (313.15 and 323.15) K and (9.00, 12.00, 15.00, and 18.00) MPa as well as at 333.15 K and (9.00 and 15.00) MPa over the entire composition range and are given in Table 1. Figures 1 to 3 show plots of H_m^E vs CO_2 mole fraction at (313.15, 323.15, and 333.15) K, respectively. For comparison purposes, the same scale has been used for H_m^E in Figures 1 to 3.

Similar trends are observed for the variation of H_m^E with mole fraction and pressure. For a given mole fraction and temperature, mixtures become increasingly exothermic as the pressure decreases. At each condition of temperature and pressure, excess molar enthalpies exhibit a minimum in the CO_2-rich region. As the temperature increases for a given mole fraction and pressure, mixtures show more exothermic mixing. The most exothermic H_m^E values were observed at 9.00 MPa and (323.15 and 333.15) K. Minimum values of

Table 1. Excess Molar Enthalpy, H_m^E, for the Binary System [$CO_2(x)$ + Acetone$(1 - x)$]

x	H_m^E / $J \cdot mol^{-1}$	x	H_m^E / $J \cdot mol^{-1}$	x	H_m^E / $J \cdot mol^{-1}$
			T/K = 313.15; P/MPa = 9.00		
0.095	−454	0.507	−2023	0.900	−2038
0.180	−935	0.586	−2226	0.938	−1736
0.246	−1202	0.662	−2288	0.969	−1202
0.337	−1494	0.771	−2366		
0.432	−1864	0.840	−2234		
			T/K = 313.15, P/MPa = 12.00		
0.108	−323	0.395	−1049	0.781	−1201
0.189	−574	0.464	−1167	0.847	−1025
0.258	−732	0.562	−1284	0.911	−736
0.332	−922	0.675	−1321	0.971	−256
			T/K = 313.15, P/MPa = 15.00		
0.111	−277	0.530	−1000	0.852	−724
0.194	−457	0.586	−1021	0.913	−499
0.264	−621	0.647	−1019	0.943	−364
0.340	−760	0.719	−980	0.972	−191
0.456	−906	0.787	−887		
			T/K = 313.15, P/MPa = 18.00		
0.114	−264	0.479	−846	0.855	−569
0.198	−417	0.577	−898	0.915	−383
0.269	−541	0.652	−919	0.956	−218
0.346	−672	0.724	−857		
0.410	−781	0.791	−722		
			T/K = 323.15, P/MPa = 9.00		
0.102	−728	0.507	−3132	0.840	−4050
0.158	−1096	0.586	−3491	0.906	−3434
0.246	−1699	0.699	−4003	0.938	−2609
0.319	−2142	0.771	−4176	0.969	−1132
0.424	−2689	0.805	−4174		
			T/K = 323.15, P/MPa = 12.00		
0.108	−403	0.438	−1471	0.801	−1719
0.209	−761	0.562	−1687	0.879	−1389
0.305	−1062	0.646	−1771	0.941	−933
0.351	−1213	0.747	−1796	0.971	−553
			T/K = 323.15, P/MPa = 15.00		
0.111	−308	0.530	−1186	0.913	−651
0.194	−531	0.609	−1244	0.943	−490
0.264	−714	0.683	−1240	0.972	−265
0.359	−905	0.787	−1122		
0.473	−1118	0.852	−932		
			T/K = 323.15, P/MPa = 18.00		
0.114	−271	0.577	−1039	0.915	−453
0.219	−518	0.652	−1025	0.944	−324
0.318	−729	0.724	−967	0.973	−186
0.410	−883	0.791	−857		
0.479	−974	0.855	−698		
			T/K = 333.15, P/MPa = 9.00		
0.102	−753	0.424	−2938	0.771	−4366
0.180	−1309	0.507	−3347	0.807	−4196
0.246	−1776	0.625	−4010	0.906	−2031
0.337	−2389	0.699	−4272	0.938	−1210
			T/K = 333.15, P/MPa = 15.00		
0.111	−371	0.609	−1524	0.915	−844
0.215	−677	0.683	−1558	0.943	−653
0.312	−941	0.753	−1505	0.972	−342
0.404	−1191	0.820	−1296		
0.489	−1363	0.883	−1039		

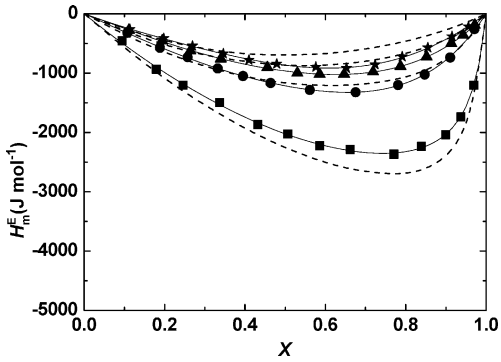

Figure 1. Excess molar enthalpies, H_m^E, for the binary system [$CO_2(x)$ + acetone$(1 - x)$] at 313.15 K and: ■, 9.00 MPa; ●, 12.00 MPa; ▲, 15.00 MPa; ★, 18.00 MPa; —, calculated using eq 3 and coefficients given in Table 2; - - -, calculated using the Peng−Robinson equation of state.[30]

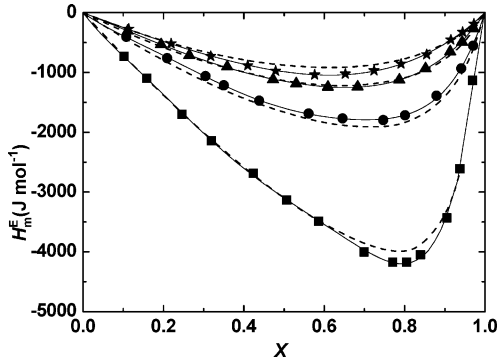

Figure 2. Excess molar enthalpies, H_m^E, for the binary system [$CO_2(x)$ + acetone$(1 - x)$] at 323.15 K and: ■, 9.00 MPa; ●, 12.00 MPa; ▲, 15.00 MPa; ★, 18.00 MPa; —, calculated using eq 3 and coefficients given in Table 2; - - -, calculated using the Peng−Robinson equation of state.[30]

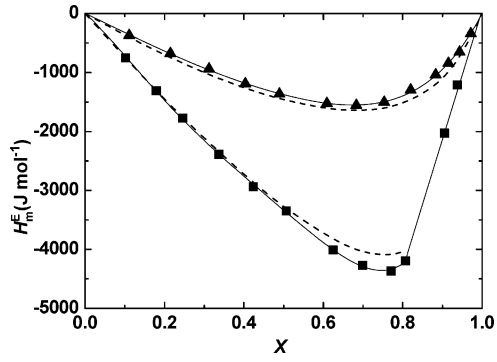

Figure 3. Excess molar enthalpies, H_m^E, for the binary system [$CO_2(x)$ + acetone$(1 - x)$] at 333.15 K and: ■, 9.00 MPa; ▲ 15.00 MPa; —, calculated using eq 3 and coefficients given in Table 2; - - -, calculated using the Peng−Robinson equation of state.[30]

(−4176 and −4366) J·mol^{-1} are reached, respectively, at these two temperatures for mixtures with a coincident CO_2 mole fraction value of 0.771. On the other hand, a linear section is observed in the H_m^E vs CO_2 mole fraction plot at these conditions of temperature and pressure. At 9.00 MPa and 323.15 K, this linear section is confined in the CO_2-rich region ($x > 0.931$). However, at 9.00 MPa and 333.15 K the linear section includes mixtures with $x > 0.788$. H_m^E varies linearly with CO_2 mole fraction due to the appearance of a two-phase region where a gaseous and a liquid mixture of fixed compositions, for a given condition of temperature and pressure, are in equilibrium. For a mixture of global composition x, the enthalpy effect in the two-phase region is the sum of two contributions due to the n_l moles of liquid mixture of composition x_l and n_v moles of vapor mixture of composition x_v

$$H_m^E = H_{m,l}^E n_l + H_{m,v}^E n_v \quad (1)$$

where $H_{m,l}^E$ is the excess molar enthalpy of the liquid mixture and $H_{m,v}^E$ is the excess molar enthalpy of the vapor mixture. Equation 1 may rewritten as[24]

$$H_m^E = H_{m,v}^E + \frac{x - x_v}{x_l - x_v}(H_{m,l}^E - H_{m,v}^E) \quad (2)$$

Since $H_{m,l}^E$, $H_{m,v}^E$, x_l, and x_v have constant values for each isotherm, the second member of eq 2 is a first-degree polynomial in x. When $x = x_l$, $H_m^E = H_{m,l}^E$, and when $x = x_v$, $H_m^E = H_{m,v}^E$. Therefore, the liquid- and vapor-phase compositions are shown to correspond to the x coordinates of the beginning and the end of the linear sections shown in Figures 2 and 3. A considerable amount of acetone may be present in the liquid mixture, but only a very small amount is dissolved in the vapor phase; in both linear sections, the CO_2 vapor-phase composition is very close to one and cannot be established from the calorimetric measurements. Two-phase regions do not appear for the other conditions of temperature and pressure studied in this paper. This is in agreement with high-pressure phase equilibria data previously reported for CO_2 + acetone at the same or similar temperatures.[9,13,16−19,21,23] The only exception is the data reported by Han et al. at 333.15 K.[20]

H_m^E data for [CO_2 (x) + acetone $(1 - x)$] were fitted to an (n, m) Padé function given by

$$H_m^E = x(1 - x)\frac{\sum_{i=0}^{n} A_i(2x - 1)^i}{1 + \sum_{j=1}^{m} B_j(2x - 1)^j} \quad (3)$$

where A_i and B_j are adjustable coefficients. A least-squares procedure was used to minimize deviations between experimental and calculated excess molar enthalpies. For those conditions of temperature and pressure where phase-splitting occurs, two different sets of coefficients are used to represent data in the two-phase and one-phase region, respectively. In the linear section, a (1, 2) Padé function with fixed values for the denominator coefficients, $B_1 = 0$ and $B_2 = -1$, may be used to keep the weight factor $x(1 - x)$. This results in a first-degree polynomial in the composition variable: the slope is $A_1/2$, and the zero intercept is $(A_0 - A_1)/4$. The H_m^E representation using eq 3 is shown in Figures 1 to 3. Table 2 lists values for the coefficients A_i and B_j and the standard deviation between experimental and calculated H_m^E values. The beginning of the linear section shown in Table 2 at (323.15 and 333.15) K and 9.00 MPa provides the value for the liquid-phase composition in the two-phase region.

The excess molar enthalpies of CO_2 + acetone were also calculated using the Peng−Robinson (PR) equation of state.[30]

Table 2. Coefficients A_i and B_j and Standard Deviation, σ, for Least-Squares Representation of H_m^E (J·mol^{-1}) for [CO_2 (x) + Acetone ($1 - x$)] at (313.15, 323.15, and 333.15) K using Equation 3

T	P									
K	MPa	interval	A_0	A_1	A_2	A_3	A_4	B_1	B_2	σ
313.15	9.00	$0 \le x \le 1$	−8088.28	2551.90	98.842	0	−26.213	−0.92178	0	7.3
	12.00	$0 \le x \le 1$	−4857.29	−2573.23	−1795.62	−1155.02	0	0	0	3.0
	15.00	$0 \le x \le 1$	−3858.17	−1754.55	−929.53	−659.27	0	0	0	1.8
	18.00	$0 \le x \le 1$	−3464.80	−1695.88	−296.08	441.31	0	0	0	2.7
323.15	9.00	$0 \le x \le 0.938$	−12389.48	−9127.38	−9809.38	−15590.29	−11435.57	0	0	9.7
		$0.938 \le x \le 1$	−83430.12	83644.97	0	0	0	0	−1	6.6
	12.00	$0 \le x \le 1$	−6385.06	−3743.81	−1717.40	−4039.31	−4543.33	0	0	5.5
	15.00	$0 \le x \le 1$	−4587.26	−2440.15	−1537.87	−1157.72	0	0	0	2.5
	18.00	$0 \le x \le 1$	−3951.52	−1883.26	−493.40	0	0	0	0	2.6
333.15	9.00	$0 \le x \le 0.807$	−13340.27	−11369.69	−12569.90	−8530.71	0	0	0	8.1
		$0.807 \le x \le 1$	−43631.78	43866.78	0	0	0	0	−1	4.6
	15.00	$0 \le x \le 1$	−5504.58	−3473.48	−2375.90	−1348.43	0	0	0	5.3

The excess molar enthalpy for a binary mixture is given by

$$H_m^E = H_m^R(\text{mixture}) - \sum_i x_i H_{m,i}^R \quad (4)$$

where H_m^R is the residual molar enthalpy of the mixture and $H_{m,i}^R$ is that of pure components. The residual molar enthalpy is given by

$$H_m^R = RT(z - 1) + \int_\infty^V \left[T\left(\frac{\partial P}{\partial T}\right)_V - P\right] dV \quad (5)$$

where z is the compressibility factor. The equation-of-state parameters a and b were evaluated for the mixtures using the classical mixing rule given by the equations

$$a = \sum_i \sum_j x_i x_j a_{ij}; \quad a_{ij} = (a_{ii}a_{jj})^{1/2}(1 - k_{ij})$$
$$b = \sum_i \sum_j x_i x_j b_{ij}; \quad b_{ij} = \frac{(b_{ii} + b_{jj})}{2}(1 - \delta_{ij}) \quad (6)$$

where $k_{ij} = k_{ji}$ and $\delta_{ij} = \delta_{ij}$ are binary interaction parameters. Values for the pure component parameters a and b were calculated using the acentric factor and the critical constants values given by Poling et al.[2] H_m^E data taken in the one-phase region at each of the three temperatures considered were simultaneously correlated using eqs 4 to 6. As was already discussed in the Experimental Section, the uncertainties in temperature, pressure, and composition are smaller than those of the excess molar enthalpies, and a least-squares-procedure was used to minimize relative deviations between experimental and calculated H_m^E. Table 3 lists values adopted by the binary interaction parameters k_{12} and δ_{12} and values for the standard deviation between experimental and calculated binary excess enthalpies, σ, for each condition of temperature and pressure. Results from the PR correlations are shown in Figures 1 to 3. A comparison of values for σ and the maximum absolute value of H_m^E for each condition of temperature and pressure indicates that relative deviations are larger for the 313.15 K correlation. The correlations are accurate at the higher temperatures of (323.15 and 333.15) K, thus allowing the prediction of excess molar enthalpies at temperatures and pressures in the T = (323.15 to 333.15) K and P = (9.00 to 18.00) MPa intervals.

Table 3. Densities of Carbon Dioxide,[26] Estimated Temperature Increments at Mixing, and Correlation of H_m^E Data for Carbon Dioxide + Acetone Binary Mixtures at (313.15, 323.15, and 333.15) K Using the PR Equation of State: Binary Parameters k_{12} and δ_{12} and Standard Deviation Between Experimental and Calculated Excess Enthalpies, σ

T	P	ρ_{CO2}	ΔT	PR		
K	MPa	g·cm^{-3}	K	k_{12}	δ_{12}	σ/J·mol^{-1}
313.15	9.00	0.4855	6.1	0.1127	0.0862	260
	12.00	0.7178	2.4			55
	15.00	0.7802	2.7			110
	18.00	0.8195	2.2			160
323.15	9.00	0.2850	11	0.0644	0.0478	78
	12.00	0.5847	5.1			110
	15.00	0.6998	3.1			36
	18.00	0.7571	2.5			62
333.15	9.00	0.2354	9.4	0.0405	0.0312	140
	15.00	0.6041	3.6			88

The large effects of pressure and temperature on the excess molar enthalpy values are related to changes in the state and densities of the pure components and their mixtures. The CO_2 + acetone system presents a liquid−gas type I diagram in the classification of Scott and van Konynenburg.[31] Figure 4 shows the P, T projection of CO_2 + acetone critical locus and the conditions of temperature and pressure for the experimental H_m^E data reported in this paper. The curve shown in Figure 4a covering the entire composition range was reported by Ziegler et al.[10] Several other authors reported critical data for CO_2-rich mixtures. In the T = (304 to 350) K interval, P_c varies linearly with T_c, and there is good agreement between literature critical data. The line shown in Figure 4b was obtained by a linear regression of data reported by Ziegler et al.,[10] Adrian and Maurer,[13] Reaves et al.,[15] Chen et al.,[18] and Chiu et al.[23] in this temperature interval. The state of the mixtures formed in the calorimeter (liquid, fluid, two-phase) may be established using Figure 4b and taking into account the critical composition and vapor−liquid equilibrium data.[9,13,16,9,21,23] At the conditions of H_m^E measurements, acetone is a liquid (T_c = 508.1 K, P_c = 4.70 MPa),[2] and its density does not change to a great extent with temperature and pressure.[27] However, carbon dioxide may be either a high-density (liquid-like) fluid or a low-density (gas-like) fluid. Densities of carbon dioxide are listed in Table 3. When carbon dioxide and acetone are mixed at 313.15 K and pressures greater than 9.00 MPa, carbon dioxide is a liquid-like fluid, and the resulting mixtures are mostly liquid. Critical data indicate that fluid mixtures are confined to a very narrow mole fraction range where $x > 0.975$. H_m^E values are moderately exothermic. The change-of-state contribution to H_m^E is small, and excess molar enthalpy values may be considered mainly the result of the molecular interaction contribution to H_m^E. Acetone presents a solvent structure dominated by dipole−dipole

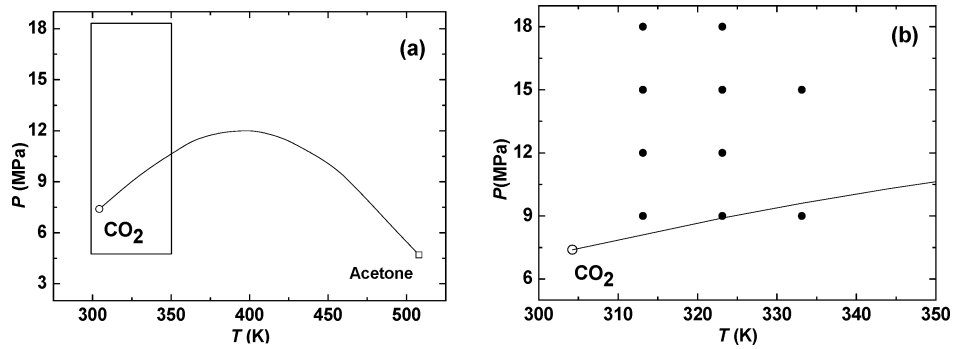

Figure 4. *P*, *T* projection of the CO_2 + acetone critical curve showing ○, the critical point of carbon dioxide and (a) locus reported by Ziegler et al.[10] and □, the critical point of acetone. (b) Locus in the CO_2-rich region based on data reported by Ziegler et al.,[10] Adrian and Maurer,[13] Reaves et al.,[15] Chen et al.,[18] and Chiu et al.[23]and the (*P*, *T*) coordinates where experimental data were taken, ●.

interactions that is disrupted upon mixing with carbon dioxide leading to an endothermic contribution to H_m^E. Moderately exothermic enthalpies are the result of a balance between the endothermic contribution and an exothermic one due to strong DMF−CO_2 interactions. This molecular interaction contribution may be expected to change only slightly with temperature and pressure in the intervals considered in this study. Mixing at 313.15 K and 9.00 MPa becomes considerably more exothermic as a result of combining a gas-like carbon dioxide with a liquid acetone to obtain liquid mixtures. The contribution to H_m^E due to intermolecular interactions is combined with another exothermic contribution due to the CO_2 change of state from that of a gas-like fluid to that of a liquid mixture component. This fluid condensation effect is even more pronounced at (323.15 or 333.15) K and 9.00 MPa when acetone is mixed with a fluid of very low density, and the resulting mixtures are a liquid or a gaseous and a liquid mixture in equilibrium. Fluid mixtures are also confined to a narrow mole fraction range at these conditions of temperature and pressure. Minimum values of (−4176 and −4366) $J \cdot mol^{-1}$ are reached for $x \approx 0.8$ at 9.00 MPa and (323.15 and 333.15) K, respectively. As the pressure is increased from (9.00 to 18.00) MPa at (323.15 or 333.15) K, carbon dioxide density increases, reaching values typical of a liquid at (15.00 or 18.00) MPa, and mixing becomes much less exothermic than that observed at the same temperature and 9.00 MPa.

Several authors[32−37] have pointed out that the phase behavior of CO_2 + organic solvent is one of the crucial factors governing the morphology and the mean size of particles obtained in the SAS process. The presence of the solute can induce modifications in the phase diagram. This is the case of polymers; however, when the solute has little interaction with carbon dioxide, the ternary phase diagram for the low solute concentrations usually employed in SAS is coincident with the binary one in the CO_2-rich region which is the region for mixtures involved in SAS.[33] Therefore, the mixtures formed in the precipitation chamber may be treated as binary CO_2 + organic solvent systems. In general, nanoparticles are obtained when the precipitation is carried out in the supercritical region. The uniformity of the resulting products becomes worse when the precipitation conditions approach the critical locus. Irregular microscale aggregated particles are formed in the vapor region, and both dense cake and spherical clusters are produced in the vapor−liquid region. The heat evolved when the supercritical CO_2 dissolves into the organic solution has an important role in the phase behavior. The temperature control in the precipitation chamber is not very precise, and the local temperature increase may lead to *T* and *P* conditions where phase splitting takes place. Since CO_2 is fed into the chamber at a flow rate much higher than that of the solution and the solute concentration is very low, the contribution to H_m^E due to solute interactions may be neglected, and the thermal effect in SAS experiments can be considered mainly due to the formation of CO_2 + acetone mixtures very rich in carbon dioxide ($x \geq 0.95$). Consequently, the temperature increase ΔT may be estimated using the H_m^E data reported in this paper. Since carbon dioxide is the predominant component in these mixtures, its isobaric heat capacity[38] was used to calculate the local temperature increase assuming an adiabatic process and using eq 3 to evaluate the heat evolved when a mole of mixture of composition $x = 0.95$ is formed. Values for ΔT thus obtained are shown in Table 3. An examination of these values together with literature vapor−liquid equilibrium data indicates how the heat evolved upon mixing affects the phase behavior. For instance, at 313.15 K and 9.00 MPa or at 323.15 K and 12.00 MPa carbon dioxide and acetone are completely miscible. However, a (6.1 or 5.1) K local temperature increase would approach precipitation conditions to the critical locus or even induce immiscibility for CO_2-rich mixtures formed in the SAS experiments, and the particle morphology would not correspond to that expected in a supercritical phase.

Conclusions

Excess molar enthalpies for mixtures of supercritical CO_2 and acetone were measured at (313.15 and 323.15) K and (9.00, 12.00, 15.00, and 18.00) MPa and 333.15 K and (9.00 and 15.00) MPa. The CO_2 + acetone system presents immiscibility at (323.15 and 333.15) K and 9.00 MPa; in this range, H_m^E varies linearly with mole fraction due to vapor−liquid equilibria.

The effects of pressure and temperature on the excess molar enthalpy are large. H_m^E values are exothermic at all the conditions of temperature and pressure studied and become extremely exothermic when low-density supercritical carbon dioxide is mixed with the liquid acetone and the resulting mixture is a liquid or a gaseous and a liquid mixture in equilibrium.

Excess molar enthalpies for CO_2 + acetone can be correlated using the PR equation of state and the classical mixing rule with two adjustable binary parameters for each temperature (T = (313.15, 323.15, and 333.15) K) in the P = (9.00 to 18.00) MPa interval.

Thermal effects in SAS experiments are shown to modify the phase behavior of CO_2 + acetone mixtures formed in the precipitation chamber thus affecting the morphology of the particles.

Literature Cited

(1) Beckmann, E. J. Supercritical and near-critical CO_2 in green chemical synthesis and processing. *J. Supercrit. Fluids* **2004**, *28*, 121–191.

(2) Poling, B. E.; Prausnitz, J. M.; O'Connell, J. P. *The properties of gases and liquids*; McGraw-Hill International ed.s: Singapore, 2001.
(3) Reverchon, E. Supercritical antisolvent precipitation of micro- and nano-particles. *J. Supercrit. Fluids* **1999**, *15*, 1–21.
(4) Jung, J.; Perrut, M. Particle design using supercritical fluids: Literature and patent survey. *J. Supercrit. Fluids* **2001**, *20*, 179–219.
(5) Pourmortazavi, S. M.; Hajimirsadeghi, S. S. Application of Supercritical Carbon Dioxide in Energetic Materials Processes: A Review. *Ind. Eng. Chem. Res.* **2005**, *44*, 6523–6533.
(6) Yeo, S. D.; Kiran, E. Formation of polymer particles with supercritical fluids: A review. *J. Supercrit. Fluids* **2005**, *34*, 287–308.
(7) Wei, M.; Musie, G. T.; Busch, D. H.; Subramaniam, B. CO_2-Expanded solvents: unique and versatile media for performing homogeneous catalytic oxidations. *J. Am. Chem. Soc.* **2002**, *124*, 2513–2517.
(8) Sala, S.; Danten, Y.; Ventosa, N.; Tassaing, T.; Besnard, M.; Veciana, J. Solute-solvent interactions governing preferential salvation phenomena of acetaminophen in CO_2 expanded solutions. A spectroscopic and theoretical study. *J. Supercrit. Fluids* **2006**, *38*, 295–305.
(9) Katayama, T.; Ohgaki, K.; Maekawa, G. G.; Nagano, T. Isothermal vapour-liquid equilibria of acetone-carbon dioxide and methanol-carbon dioxide at high pressures. *J. Chem. Eng. Jpn.* **1975**, *8*, 89–92.
(10) Ziegler, J. W.; Dorsey, J. G.; Chester, T. L.; Innis, D. P. Estimation of liquid-vapor critical loci for CO_2-solvent mixtures using a peak shape method. *Anal. Chem.* **1995**, *67*, 456–461.
(11) Day, C. Y.; Chang, C. J.; Chen, C. Y. Phase equilibrium of ethanol + CO_2 and acetone + CO_2 at elevated pressures. *J. Chem. Eng. Data* **1996**, *41*, 839–843.
(12) Pöhler, H.; Kiran, E. Volumetric properties of carbon dioxide + acetone at high pressures. *J. Chem. Eng. Data* **1997**, *42*, 379–383.
(13) Adrian, T.; Maurer, G. Solubility of carbon dioxide in acetone and propionic acid at temperatures between 298 and 333 K. *J. Chem. Eng. Data* **1997**, *42*, 668–672.
(14) Chang, C. J.; Day, C. Y.; Ko, C. M.; Chiu, K. L. Densities and *P-x-y* diagrams for carbon dioxide dissolution in methanol, ethanol, and acetone mixtures. *Fluid Phase Equilib.* **1997**, *131*, 243–258.
(15) Reaves, J. T.; Griffith, A. T.; Roberts, C. B. Critical properties of dilute carbon dioxide + entrainer and ethane + entrainer mixtures. *J. Chem. Eng. Data* **1998**, *43*, 683–686.
(16) Day, C. Y.; Chang, C. J.; Chen, C. Y. Phase equilibrium of ethanol + CO_2 and acetone + CO_2 at elevated pressures. *J. Chem. Eng. Data* **1999**, *44*, 365.
(17) Bamberger, A.; Maurer, G. High-pressure (vapour-liquid) equilibria in carbon dioxide + acetone or 2-propanol) at temperatures from 293 to 333 K. *J. Chem. Thermodyn.* **2000**, *32*, 685–700.
(18) Chen, J.; Wu, W.; Han, B.; Gao, L.; Mu, T.; Liu, Z.; Du, J. Phase behavior, densities, and isothermal compressibilities of CO_2 + pentane and CO_2 + acetone systems in various phase regions. *J. Chem. Eng. Data* **2003**, *48*, 1544–1548.
(19) Stievano, M.; Elvassore, N. High-pressure density and vapor-liquid equilibrium for the binary systems carbon dioxide-ethanol, carbon dioxide-acetone and carbon dioxide-dichloromethane. *J. Supercrit. Fluids* **2005**, *33*, 7–14.
(20) Han, F.; Xue, Y.; Tian, Y.; Zhao, X.; Chen, L. Vapor-liquid equilibria of the carbon dioxide + acetone system at pressures from (2.36 to 11.7) MPa and temperatures from (333.15 to 393.15) K. *J. Chem. Eng. Data* **2005**, *50*, 36–39.
(21) Lazzaroni, M. J.; Bush, D.; Brown, J. S.; Eckert, C. A. High-Pressure Vapor-Liquid Equilibria of Some Carbon Dioxide + Organic Binary Systems. *J. Chem. Eng. Data* **2005**, *50*, 60–65.
(22) Wu, W.; Ke, J.; Poliakoff, M. Phase boundaries of CO_2 + toluene, CO_2 + acetone, and CO_2 + ethanol at high temperatures and high pressures. *J. Chem. Eng. Data* **2006**, *51*, 1398–1403.
(23) Chiu, H. Y.; Lee, M. J.; Lin, H. Vapor-liquid phase boundaries of binary mixtures of carbon dioxide with ethanol and acetone. *J. Chem. Eng. Data* **2008**, *53*, 2393–2402.
(24) Dávila, M. J.; Cabañas, A.; Pando, C. Excess molar enthalpies for binary mixtures related to supercritical antisolvent precipitation: carbon dioxide + *N*-methyl-2-pyrrolidone. *J. Supercrit. Fluids* **2007**, *42*, 172–179.
(25) Christensen, J. J.; Hansen, L. D.; Izatt, R. M.; Eatough, D. J.; Hart, R. M. Isothermal flow calorimeter. *Rev. Sci. Instrum.* **1976**, *47*, 730–734.
(26) NIST Standard Reference Database Number 69, which can be accessed electronically through the NIST Chemistry Web Book (http://webbook.nist.gov/chemistry/).
(27) Adams, W. A.; Laidler, K. J. Effect of pressure and temperature on the structure of liquid acetone. *Can. J. Chem.* **1967**, *45*, 123–130.
(28) Ott, J. B.; Cornett, G. V.; Stouffer, C. E.; Woodfield, B. F.; Guanquan, C.; Christensen, J. J. Excess-enthalpies of (ethanol + water) at 323.15, 333.15, 348.15, and 373.15 K and from 0.4 to 15 MPa. *J. Chem. Thermodyn.* **1986**, *18*, 867–875.
(29) Sabbah, R.; Xu, A.; Chickos, J. S.; Planas-Leitão, M. L.; Roux, M. V.; Torres, L. A. Reference materials for calorimetry and differential thermal analysis. *Thermochim. Acta* **1999**, *331*, 93–204.
(30) Peng, D. Y.; Robinson, D. B. A new two-constant equation of state. *Ind. Eng. Chem. Fundam.* **1976**, *15*, 59–64.
(31) Scott, R. L.; van Konynenburg, P. H. Van der Waals and related models for hydrocarbon mixtures. *Discuss. Faraday Soc.* **1970**, *49*, 87–97.
(32) Reverchon, E.; Caputo, G.; De Marco, I. Role of Phase Behavior and Atomization in the Supercritical Antisolvent Precipitation. *Ind. Eng. Chem. Res.* **2003**, *42*, 6406–6414.
(33) Reverchon, E.; De Marco, I.; Torino, E. Nanoparticles production by supercritical antisolvent precipitation: A general interpretation. *J. Supercrit. Fluids* **2007**, *43*, 126–138.
(34) Chang, S. C.; Lee, M. J.; Lin, H. M. The influence of phase behaviour on the morphology of protein α-chymotrypsin prepared via a supercritical anti-solvent process. *J. Supercrit. Fluids* **2008**, *44*, 219–229.
(35) Chang, S. C.; Lee, M. J.; Lin, H. M. Role of phase behavior in micronization of lysozyme via a supercritical anti-solvent process. *Chem. Eng. J.* **2008**, *139*, 416–425.
(36) Martín, A.; Cocero, M. J. Micronization processes with supercritical fluids: fundamentals and mechanisms. *Adv. Drug Delivery Rev.* **2008**, *60*, 339–350.
(37) Reverchon, E.; Torino, E.; Dowy, S.; Brauer, A.; Leipertz, A. Interactions of phase equilibria, jet fluid dynamics and mass transfer during supercritical antisolvent micronization. *Chem. Eng. J.* **2010**, *156*, 446–458.
(38) Span, R.; Wagner, W. A new equation of state for carbon dioxide covering the fluid region from the triple-point temperature to 1100 K and pressures up to 800 MPa. *J. Phys. Chem. Ref. Data* **1996**, *25*, 1509–1596.

Received for review March 10, 2010. Accepted June 29, 2010. We gratefully acknowledge the financial support of the Santander-Universidad Complutense de Madrid, research project PR34/07-15789, and the Spanish Ministry of Education and Science (MEC), research project CTQ2009-09707. F.Z. thanks the E. U. for its support through an Erasmus Mundus University II predoctoral grant.

JE100220C

J. of Supercritical Fluids 55 (2010) 566–572

Contents lists available at ScienceDirect

The Journal of Supercritical Fluids

journal homepage: www.elsevier.com/locate/supflu

Measurements and modeling of high-pressure excess molar enthalpies and isothermal vapor–liquid equilibria of the carbon dioxide + *N*,*N*-dimethylformamide system

Fouad Zahran, Concepción Pando*, Albertina Cabañas, Juan A.R. Renuncio

Dpto. de Química Física I, Universidad Complutense, E-28040 Madrid, Spain

ARTICLE INFO

Article history:
Received 15 June 2010
Received in revised form
10 September 2010
Accepted 15 September 2010

Keywords:
Supercritical carbon dioxide
N,*N*-dimethylformamide
Excess molar enthalpies
Vapor–liquid equilibria
Equation of state

ABSTRACT

Mixtures of supercritical CO_2 and *N*,*N*-dimethylformamide (DMF) are very often involved in supercritical fluid applications and their thermodynamic properties are required to understand and design these processes. Excess molar enthalpies (H_m^E) for CO_2 + DMF mixtures were measured using an isothermal high-pressure flow calorimeter under conditions of temperature and pressure typically used in supercritical processes: 313.15 and 323.15 K at 9.00, 12.00, 15.00 and 18.00 MPa and 333.15 K at 9.00 and 15.00 MPa. The Peng–Robinson and the Soave–Redlich–Kwong equations of state were used in conjunction with the classical mixing rules to model the literature vapor–liquid equilibrium and critical data and the excess enthalpy data. In most cases, CO_2 + DMF mixtures showed very exothermic mixing and excess molar enthalpies exhibited a minimum in the CO_2-rich region. The lowest H_m^E value ($-4526\ J\ mol^{-1}$) was observed for a CO_2 mole fraction value of 0.713 at 9.00 MPa and 333.15 K. On the other hand, H_m^E at 9.00 MPa and 323.15 and 333.15 K varies linearly with CO_2 mole fraction in the two-phase region where a gaseous and a liquid mixture of fixed composition are in equilibrium. The effects of pressure and temperature on the excess molar enthalpy are large. For a given mole fraction, mixtures become less exothermic as pressure increases or temperature decreases. These excess enthalpy data were analyzed in terms of molecular interactions, phase equilibria, density and critical parameters previously reported for CO_2 + DMF. All throughout this paper, the key concepts and modeling tools originate from the work of van der Waals: the paper is intended as a small piece of recognition of van der Waals overwhelming contributions to thermodynamics.

1. Introduction

The mixtures formed by supercritical carbon dioxide and organic solvents have received considerable attention in the recent past due to the advantages of CO_2 over conventional organic solvents and its numerous technological applications [1]. Supercritical carbon dioxide is a non toxic, low cost, non flammable solvent that allows operation at low temperatures and moderate pressures (T_c = 304.1 K, P_c = 7.38 MPa [2]). Carbon dioxide physical properties such as density, viscosity, and diffusion coefficient may be varied continuously from liquid-like to gas-like values by simply changing pressure and temperature conditions. Furthermore, a small amount of an organic polar solvent may be added to the pure supercritical fluid to increase the solute solubility and/or selectivity. These compounds are referred to as cosolvents, modifiers or entrainers and their mixtures with CO_2 are of interest in applications such as extraction or chromatography.

N,*N*-dimethylformamide (DMF) is a dipolar aprotic and unassociated solvent. Thanks to its high dipolar moment and moderately high dielectric constant (μ = 3.8 D, ε = 36.76 at 298.15 K [3]), DMF is a powerful organic solvent that may be used in combination with carbon dioxide in a variety of processes. CO_2 + DMF mixtures are involved in the micronization of solutes such as polymers, pharmaceutical compounds, explosives and colorants. The so-called gas antisolvent (GAS) or supercritical antisolvent (SAS) precipitation is based on the relatively low solvent power of CO_2 for these solutes and its good miscibility with many organic solvents such as DMF [4,5]. When the supercritical antisolvent dissolves in the organic solvent, the liquid experiences a volumetric expansion and becomes a bad solvent for the solute that precipitates from the solution in micro and nanoparticles. There are many examples of DMF use in GAS or SAS micronization and in other material processing [4–8]. Charoenchaitrakool et al. recently proposed to extract an

* Corresponding author at: Departamento de Química Física I, Facultad C. Químicas, Universidad Complutense, E-28040 Madrid, Spain. Tel.: +34 91394 4304; fax: +34 91394 4135.
E-mail addresses: pando@quim.ucm.es (C. Pando), renuncio@quim.ucm.es (J.A.R. Renuncio).

0896-8446/$ – see front matter © 2010 Elsevier B.V. All rights reserved.
doi:10.1016/j.supflu.2010.09.020

active ingredient found in vegetable leaves using DMF followed by a GAS precipitation to isolate the natural product [9]. DMF is also used as a solvent in polymer solutions when membranes are formed using supercritical carbon dioxide to induce the phase separation [10]. The mutual affinity between the solvent and the antisolvent is a key factor in this application. On the other hand, CO_2-expanded DMF has been also used as reaction media [11,12]. In order to fully understand and design these processes, the measurement and modeling of properties for the CO_2 + organic polar solvent mixtures are required

The physical and thermodynamic properties of CO_2 + DMF mixtures have been the subject of several investigations. Chang et al. [13] measured solubilities of CO_2 in DMF and liquid densities from 290.8 to 310.1 K at pressures up to 7.82 MPa. Kordikowski et al. [14] reported isothermal vapor–liquid equilibria (VLE, bubble points), liquid densities and volume expansions at 298.15, 303.15 and 313.15 K. Duran-Valencia et al. [15] measured the isothermal VLE data (bubble and dew points) at 293.95, 313.05 and 338.05 K. Byun et al. [16] reported isothermal VLE data (mostly bubble points) and values for the mixture critical parameters in the 318.2–398.2 K temperature interval and found that the critical locus is a type I in the Scott and van Konynenburg classification [17]. The phase diagrams in the critical region were first predicted by van der Waals using his equation of state. Zúñiga-Moreno and Galicia-Luna [18] measured compressed liquid densities and excess volumes in the 313.2–362.7 K interval at pressures up to 25 MPa. Modeling of these VLE data has been carried out using cubic equations of state (EOS) that are derived directly from the van der Waals equation. Chang et al. used the Patel–Teja EOS [19] and Kordikowski et al., Duran-Valencia et al. and Byun et al. used the Peng–Robinson EOS [20].

To the best of our knowledge, no attention has been paid to the heat evolved when supercritical CO_2 dissolves into the liquid DMF. The excess molar enthalpies (H_m^E) at these conditions can be quite high and must be considered in order to understand and optimize supercritical fluid applications. In a previous study [21], H_m^E values for CO_2 + *N*-methyl-2-pyrrolidone (NMP) mixtures were reported at 313.15 and 338.15 K and 9.48, 15.00 and 20.00 MPa. NMP is another organic polar solvent frequently used in the SAS and GAS micronizations and in the formation of polymeric membranes. Exothermic H_m^E values were observed at all the conditions of temperature and pressure studied. The lowest H_m^E values ($\approx -4500\ J\ mol^{-1}$) were observed for mixtures at 338.15 K and 9.48 MPa. These thermal effects were shown to play an important role in supercritical antisolvent micronizations using NMP.

In this paper, we report excess molar enthalpies for the binary system CO_2 + DMF under conditions of temperature and pressure typically used in supercritical CO_2 applications: 313.15 and 323.15 K and 9.00, 12.00, 15.00 and 18.00 MPa as well as 333.15 K and 9.00 and 15.00 MPa. Using concepts introduced and developed by van der Waals, these H_m^E data will be analyzed taking into account molecular interactions, phase equilibria and density data, and critical properties. On the other hand, the Peng–Robinson and the Soave–Redlich–Kwong EOS [20,22] will be used to model the literature VLE and critical data together with the excess enthalpy data. The extension of these equations of state to mixtures will be carried out by means of the classical mixing rules first proposed by van der Waals to evaluate the parameters *a* and *b*. Both in the calculations and discussion, the key concepts and modeling tools used in this paper originate from the ideas of van der Waals. As every worker in the field of thermodynamics, we feel very much indebted to his pioneering work and breakthrough contributions. It is an honor for us to participate in this issue commemorating the 100 year anniversary of Johannes Diderik van der Waals Nobel Prize for Physics and to join other colleagues in the homage to this extraordinary scientist.

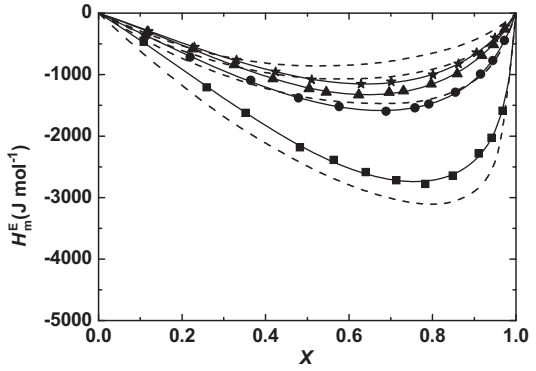

Fig. 1. Excess molar enthalpies, H_m^E, for the binary system [CO_2 (x) + *N*,*N*-dimethylformamide ($1-x$)] versus CO_2 mole fraction at 313.15 K and: (■) 9.00 MPa; (●) 12.00 MPa; (▲) 15.00 MPa; (★) 18.00 MPa; (—), calculated using Eq. (4) and coefficients given in Table 2; (- - -), calculated using the Peng–Robinson EOS [20] and values for the binary parameters k_{12} and δ_{12} given in Table 4.

2. Experimental

The materials employed were CO_2 (Air Liquide 99.98 mol% pure) and DMF (Sigma–Aldrich, 99.8 mol% pure). Commercial materials were used without further purification.

An isothermal high-pressure flow calorimeter (Hart Scientific model 7501) was used to perform H_m^E measurements. The calorimeter was first described by Christensen et al. [23] and the experimental procedure is described elsewhere [21]. The reactants were pumped into the calorimetric cell by two thermostatted pumps (ISCO, model LC-2600) at constant flow rates. The temperature of the pumps, 313.15 K, was controlled within ±0.02 K. Volume flow rates were selected to cover the entire concentration range. For each pump, the uncertainty in the volume flow rate was obtained by a previous calibration. The calorimetric cell was located into a silicon bath in which temperature was controlled within ±0.001 K. A Peltier cooling device and a pulsed heater kept the cell under isothermal conditions. The pulse energy was determined by a heater calibration. The pressure was measured using a calibrated pressure transducer (Lucas Schaevitz, model P721-0001). A back-pressure regulator located outside the calorimeter kept the pressure within ±0.01 MPa.

All runs were made in the steady-state fixed composition mode. Measurements were carried out at total volume flow rates of 0.0014 and 0.0028 $cm^3\ s^{-1}$. The volume flow rates were converted to molar flow rates using the densities and molar masses. CO_2 densities at the temperature and pressure of the pumps were obtained from NIST [24]. DMF densities were obtained from data reported by Zúñiga-Moreno and Galicia-Luna [18]. Since densities are affected by temperature and pressure changes, the error in molar flow rates was derived taking into account contributions from variations in volume flow rates, pressure, and pumps temperature. The mole fraction precision is based on the error in molar flow rates and was estimated to be better than ±0.001. The error in H_m^E was obtained taking into account contributions from molar flow rates, pulse energy and frequency and was estimated to be ±1% or at least $\pm 1\ J\ mol^{-1}$.

3. Experimental results

H_m^E data for the binary system [CO_2 (x) + DMF ($1-x$)] were determined at 313.15 and 323.15 K and 9.00, 12.00, 15.00 and 18.00 MPa as well at 333.15 K and 9.00 and 15.00 MPa over the entire composition range and are given in Table 1. Figs. 1–3 show plots of H_m^E versus CO_2 mole fraction at 313.15, 323.15 and 333.15 K, respectively. For comparison purposes the same scale has been used for H_m^E in

Table 1
Excess molar enthalpy, H_m^E, for the binary system [CO_2 (x) + DMF ($1-x$)].

x	H_m^E (J mol^{-1})	x	H_m^E (J mol^{-1})	x	H_m^E (J mol^{-1})
313.15 K and 9.00 MPa					
0.108	−465	0.564	−2390	0.848	−2643
0.259	−1209	0.640	−2586	0.911	−2284
0.352	−1622	0.713	−2719	0.942	−2028
0.483	−2181	0.782	−2779	0.968	−1587
313.15 K and 12.00 MPa					
0.114	−368	0.577	−1520	0.855	−1287
0.219	−716	0.689	−1597	0.915	−991
0.365	−1094	0.758	−1542	0.944	−771
0.479	−1380	0.791	−1478	0.973	−443
313.15 K and 15.00 MPa					
0.117	−303	0.545	−1285	0.859	−985
0.225	−583	0.623	−1329	0.918	−690
0.325	−839	0.696	−1290	0.946	−512
0.418	−1066	0.731	−1265	0.973	−259
0.504	−1228	0.797	−1152		
313.15 K and 18.00 MPa					
0.120	−294	0.511	−1086	0.862	−824
0.230	−554	0.629	−1154	0.906	−644
0.331	−763	0.701	−1116	0.950	−405
0.424	−958	0.801	−1002	0.974	−223
323.15 K and 9.00 MPa					
0.108	−789	0.564	−3592	0.911	−2592
0.210	−1535	0.640	−3935	0.942	−1817
0.306	−2163	0.713	−4106	0.971	−940
0.397	−2756	0.782	−4185		
0.483	−3241	0.848	−4158		
323.15 K and 12.00 MPa					
0.114	−408	0.577	−2026	0.915	−1543
0.219	−812	0.653	−2126	0.944	−1274
0.318	−1175	0.724	−2161	0.973	−769
0.410	−1551	0.791	−2100		
0.496	−1831	0.855	−1898		
323.15 K and 15.00 MPa					
0.117	−361	0.545	−1468	0.918	−906
0.225	−684	0.660	−1551	0.946	−674
0.325	−980	0.731	−1527	0.973	−388
0.418	−1177	0.797	−1431		
0.488	−1372	0.859	−1248		
323.15 K and 18.00 MPa					
0.120	−313	0.591	−1270	0.920	−638
0.230	−606	0.666	−1299	0.950	−462
0.331	−833	0.736	−1252	0.974	−248
0.424	−1018	0.801	−1121		
0.494	−1151	0.862	−939		
333.15 K and 9.00 MPa					
0.108	−881	0.483	−3566	0.782	−3478
0.210	−1672	0.564	−3996	0.848	−2383
0.306	−2427	0.640	−4315	0.911	−1365
0.397	−3039	0.713	−4526	0.942	−893
333.15 K and 15.00 MPa					
0.117	−487	0.585	−1877	0.918	−1203
0.225	−864	0.696	−1955	0.946	−928
0.325	−1189	0.764	−1909	0.973	−512
0.418	−1468	0.810	−1789		
0.504	−1717	0.859	−1586		

these plots. At each condition of temperature and pressure, excess molar enthalpies are exothermic and exhibit minima in the CO_2-rich region. Minima values range from −1154 J mol^{-1} at 313.15 K and 18.00 MPa to −4526 J mol^{-1} at 333.15 K and 9.00 MPa. For a given mole fraction, mixtures become less exothermic as pressure increases or temperature decreases. On the other hand, a linear section is observed in the H_m^E versus CO_2 mole fraction plot at 9.00 MPa and 323.15 and 333.15 K. H_m^E varies linearly with CO_2 mole fraction in the two-phase region where a gaseous and a liquid mixture of fixed compositions, for a given condition of temperature and pressure, are in equilibrium. Since a mixture of global composition x consists of amounts of substance n_l of liquid mixture of composition x_l and n_v of vapor mixture of composition x_v, the excess molar enthalpy in the two-phase region may be expressed as

$$H_m^E = H_{m,l}^E n_l + H_{m,v}^E n_v \quad (1)$$

where $H_{m,l}^E$ is the excess molar enthalpy of the liquid mixture, and $H_{m,v}^E$ is the excess molar enthalpy of the vapor mixture. Both $H_{m,l}^E$ and $H_{m,v}^E$ have as initial states the carbon dioxide and DMF entering the calorimeter. Therefore, the contributions to the enthalpy due to changes of state are included in $H_{m,l}^E$ and $H_{m,v}^E$. Values of n_l and n_v are related to the mole fractions x_l, x_v and x by the relations:

$$\begin{aligned} x_l n_l + x_v n_v &= x(n_l + n_v) \\ (1-x_l) n_l + (1-x_v) n_v &= (1-x)(n_l + n_v) \end{aligned} \quad (2)$$

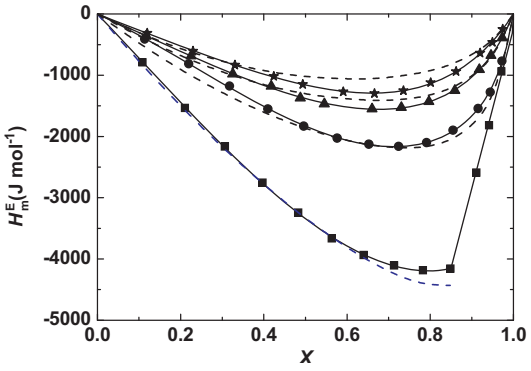

Fig. 2. Excess molar enthalpies, H_m^E, for the binary system [CO_2 (x) + *N*,*N*-dimethylformamide (1 − x)] versus CO_2 mole fraction at 323.15 K and: (■) 9.00 MPa; (●) 12.00 MPa; (▲) 15.00 MPa; (⋆) 18.00 MPa; (—), calculated using Eq. (4) and coefficients given in Table 2; (- - -), calculated using the Peng–Robinson EOS [20] and values for the binary parameters k_{12} and δ_{12} given in Table 4.

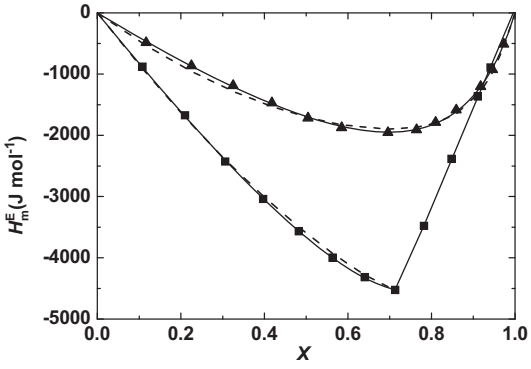

Fig. 3. Excess molar enthalpies, H_m^E, for the binary system [CO_2 (x) + *N*,*N*-dimethylformamide (1 − x)] versus CO_2 mole fraction at 333.15 K and: (■) 9.00 MPa; (▲) 15.00 MPa; (—), calculated using Eq. (4) and coefficients given in Table 2; (- - -), calculated using the Peng–Robinson EOS [20] and values for the binary parameters k_{12} and δ_{12} given in Table 4.

Based on Eqs. (1) and (2) and taking into account that for 1 mol of mixture $n_l + n_v = 1$, the excess molar enthalpy may be expressed as

$$H_m^E = H_{m,v}^E + \frac{x - x_v}{x_l - x_v}(H_{m,l}^E - H_{m,v}^E) \quad (3)$$

Since $H_{m,l}^E$, $H_{m,v}^E$, x_l and x_v have constant values for each isotherm, the second member of Eq. (3) is a first-degree polynomial in x. When $x = x_l$, $H_m^E = H_{m,l}^E$ and when $x = x_v$, $H_m^E = H_{m,v}^E$. Therefore, the liquid and vapor-phase compositions are shown to correspond to the x coordinates of the beginning and the end of the linear sections shown in Figs. 2 and 3. A considerable amount of DMF is present in the liquid mixture but only a very small amount is dissolved in the vapor phase; the CO_2 vapor-phase composition is very close to one and cannot be established from the calorimetric measurements. The linear sections at 323.15 and 333.15 K and 9.00 MPa are in agreement with isothermal VLE data previously reported for CO_2 + DMF by Kordikowski et al., Duran-Valencia et al. and Byun et al. [14–16]. As could be expected from the phase equilibria data and may be observed in Figs. 1–3, two-phase regions do not appear when the pressure is raised from 9.00 to 12.00, 15.00 or 18.00 MPa at the three temperatures studied. Similar trends in the variation of H_m^E with temperature and pressure were observed for the CO_2 + *N*-methyl-2-pyrrolidone mixtures at 313.15 and 338.15 K in the 9.48–20.00 MPa pressure range [21].

H_m^E data for [CO_2 (x) + DMF (1 − x)] were fitted to a (n, m) Padé function given by

$$H_m^E = x(1-x)\frac{\sum_{i=0}^{n} A_i(2x-1)^i}{1 + \sum_{j=1}^{m} B_j(2x-1)^j} \quad (4)$$

where A_i and B_j are adjustable coefficients. A least-square procedure was used to minimize deviations between experimental and calculated excess molar enthalpies. For those conditions of temperature and pressure where phase-splitting occurs, two different sets of coefficients are used to represent data in the two-phase and one-phase region, respectively. In the linear section, a (1, 2) Padé function with fixed values for the denominator coefficients, $B_1 = 0$ and $B_2 = -1$, may be used in order to keep the weight factor $x(1 - x)$. This results in a first-degree polynomial in the composition variable; the slope is $A_1/2$ and the zero intercept is $(A_0 - A_1)/4$. The H_m^E representation using Eq. (4) is shown in Figs. 1–3. Table 2 lists values for the coefficients A_i and B_j and the standard deviation between experimental and calculated H_m^E values at 313.15 and 323.15 K and 9.00, 12.00, 15.00 and 18.00 MPa and 333.15 K and 9.00 and 15.00 MPa. The beginning of the linear sections shown in Table 2 at 9.00 MPa and 323.15 and 333.15 K provides the value for the liquid-phase composition in the two-phase region.

4. Calculation of the phase equilibria and the critical locus using a cubic equation of state

The Peng–Robinson and the Soave–Redlich–Kwong EOS [20,22] were used to correlate the isothermal VLE data reported by Duran-Valencia et al. at 293.95, 313.05 and 338.05 K [15]. These are the most comprehensive sets of VLE data found in the literature for this system and include a good description of both liquid and vapor phase compositions. The equation-of state parameters a and b were evaluated for the mixtures using the classical mixing rules given by

Table 2
Coefficients A_i and B_j and standard deviation, σ, for least-squares representation of H_m^E (J mol^{-1}) for [CO_2 (x) + DMF (1 − x)] at 313.15, 323.15 K and 333.15 K using Eq. (4).

T (K)	P (MPa)	Interval	A_0	A_1	A_2	A_3	B_1	B_2	σ
313.15	9.00	$0 \le x \le 1$	−8871.76	1313.48	1998.24	–	−0.94369	–	7.6
	12.00	$0 \le x \le 1$	−5652.54	1102.22	945.15	–	−0.81944	–	3.1
	15.00	$0 \le x \le 1$	−4842.21	976.61	1617.01	–	−0.81600	–	3.4
	18.00	$0 \le x \le 1$	−4246.99	738.28	937.22	5.70	−0.73901	–	2.5
323.15	9.00	$0 \le x \le 0.848$	−13368.24	2973.08	2268.22	–	−0.98209	–	4.6
		$0.848 \le x \le 1$	−52953.53	51970.61	–	–	0	−1	23
	12.00	$0 \le x \le 1$	−7318.19	426.10	2210.92	–	−0.83108	−0.05328	4.3
	15.00	$0 \le x \le 1$	−5516.23	539.98	855.15	–	−0.75408	–	3.3
	18.00	$0 \le x \le 1$	−4635.05	−730.27	–	–	−0.47876	–	2.4
333.15	9.00	$0 \le x \le 0.713$	−14660.71	614.57	–	–	−0.81603	–	5.2
		$0.713 \le x \le 1$	−32248.60	32535.42	–	–	0	−1	5.9
	15.00	$0 \le x \le 1$	−6765.07	−284.02	–	–	−0.70723	–	4.6

Table 3
Correlation and prediction of VLE data for the CO_2 + DMF system at 293.95, 313.05 and 338.05 K [15] using the Peng–Robinson and the Soave–Redlich–Kwong EOS: binary parameters k_{12} and δ_{12}, standard deviation between experimental and calculated CO_2 compositions, σ, and standard deviation between experimental and calculated total pressure, σ_P.

T (K)	Peng–Robinson correlation				Soave–Redlich–Kwong correlation			
	k_{12}	δ_{12}	σ	σ_P (MPa)	k_{12}	δ_{12}	σ	σ_P (MPa)
293.95	0.0470	0.0025	0.012	0.042	0.0412	−0.0013	0.014	0.053
313.05	0.0228	−0.0269	0.024	0.20	0.0004	0.0196	0.062	0.60
338.05	0.0473	−0.0102	0.006	0.071	0.0471	−0.0086	0.006	0.077
	Prediction using the 313.05 K set of parameters							
	Peng–Robinson				Soave–Redlich–Kwong			
	k_{12}	δ_{12}	σ	σ_P (MPa)	k_{12}	δ_{12}	σ	σ_P (MPa)
293.95	0.0228	−0.0269	0.026	0.13	0.0004	0.0196	0.061	0.39
338.05	0.0228	−0.0269	0.027	0.37	0.0004	0.0196	0.061	0.93

the equations:

$$a = \sum_i \sum_j x_i x_j a_{ij}; \quad a_{ij} = (a_{ii}a_{jj})^{1/2}(1 - k_{ij})$$
$$b = \sum_i \sum_j x_i x_j b_{ij}; \quad b_{ij} = \frac{(b_{ii} + b_{jj})}{2}(1 - \delta_{ij}) \tag{5}$$

where $k_{ij} = k_{ji}$ and $\delta_{ij} = \delta_{ij}$ are binary interaction parameters.

Values for the pure component parameters a and b were calculated using the acentric factor and the critical constants values given by Poling et al. [2] for carbon dioxide and those given by Perry and Green for DMF [25]. The PE 2000 program developed by G. Brunner and coworkers was used in this calculation [26]. Table 3 lists for each temperature values adopted by the binary interaction parameters k_{12} and δ_{12}, values for the standard deviation between experimental and calculated CO_2 compositions, σ, and values for the standard deviation between experimental and calculated total pressures, σ_P. Maximum total pressures at 293.95, 313.05 and 338.05 K are 5.13, 7.51 and 11.51 MPa, respectively. Values of k_{12} and δ_{12} obtained at 313.05 K were also used to predict VLE data at 293.05 and 338.05 K. For both correlations and predictions, lower deviations were obtained by means of the Peng–Robinson EOS. This equation together with the 313.05 K set of binary parameters provides a good description of VLE at the three temperatures studied and was also used to predict the CO_2 + DMF critical locus using the procedure described by Heidemann and Khalil [27]. Fig. 4 shows the P, T projection of the critical locus, the conditions of temperature and pressure for the experimental H_m^E data reported in this paper and the experimental critical points reported by Byun et al. [16] for the mixture. CO_2 mole fraction values for the critical data range from 0.994 at 318.2 K to 0.898 at 398.2 K. The type I critical curve was obtained by means of the Peng–Robinson EOS [20] used in conjunction with the classical mixing rules and the 313.05 K set of binary parameters given in Table 3. This EOS provided a better description of the mixture critical data than that of the Soave–Redlich–Kwong EOS [22].

5. Calculation and discussion of the excess molar enthalpies

The large effects of pressure and temperature on the excess molar enthalpy values are related to changes in molecular interactions and the state and densities of the pure components and their mixtures. At the conditions of H_m^E measurements, DMF is a liquid and its density does not change to a great extent with temperature and pressure in the intervals considered in this paper. However, carbon dioxide is a supercritical fluid that may be either a high-density (liquid-like) fluid or a low-density (gas-like) fluid. Table 4 lists the densities of the pure components obtained from the sources described in Section 2. The state of the mixtures may be established using Fig. 4 and Byun et al. critical data [16]. When carbon dioxide and DMF are mixed at 313.15 K and 9.00 MPa, carbon dioxide is a gas-like fluid and the resulting mixtures are mostly liquid. Byun et al. data indicate that fluid mixtures are confined to a very narrow mole fraction range in the carbon dioxide rich region. These negative H_m^E values are a consequence of two contributions: (a) changes in molecular interactions due to the disruption of the DMF structure by the carbon dioxide and the new DMF–CO_2 interactions, and (b) the CO_2 change of state from that of a gas-like fluid to that of liquid mixture component. The latter is the so-called fluid condensation effect that has been reported for other similar mixtures [21]. When the pressure is increased at this temperature, CO_2 density rises considerably and the fluid condensation effect

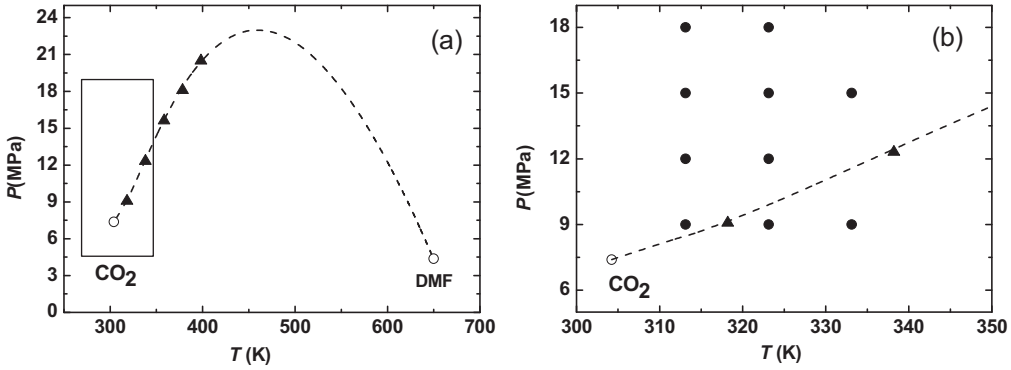

Fig. 4. P, T projection of the CO_2 + DMF critical locus showing (a) the CO_2 and DMF critical points (○), the critical temperatures and pressures reported by Byun et al. [16] (▲), the critical line calculated by means of the Peng–Robinson EOS [20] and the 313.05 K binary interaction parameters given in Table 3 (- - -) and (b) the (P, T) coordinates where experimental H_m^E data were taken in this study (●).

Table 4
Carbon dioxide and *N*,*N*-dimethylformamide experimental densities [18,24] and prediction and correlation of H_m^E data for their binary mixtures at 313.15, 323.15 and 333.15 K using the Peng–Robinson and the Soave–Redlich–Kwong EOS: binary parameters k_{12} and δ_{12}, standard deviation between experimental and correlated binary excess enthalpies, σ_{cor} (J mol^{-1}), and standard deviation between experimental and predicted binary excess enthalpies, σ_{pre} (J mol^{-1}).

T (K)	P (MPa)	ρ_{CO_2} (g cm^{-3})	ρ_{DMF} (g cm^{-3})	Soave–Redlich–Kwong				Peng–Robinson			
				k_{12}	δ_{12}	σ_{cor}	σ_{pre}	k_{12}	δ_{12}	σ_{cor}	σ_{pre}
313.15	9.00	0.4855	0.9356	0.1150	0.0656	350	910	0.1206	0.0693	360	420
	12.00	0.7178	0.9375			70	550			70	260
	15.00	0.7802	0.9394			150	420			160	350
	18.00	0.8195	0.9412			190	330			200	370
323.15	9.00	0.2850	0.9263	0.1017	0.0531	140	690	0.1057	0.0554	120	280
	12.00	0.5847	0.9283			110	630			120	240
	15.00	0.6998	0.9303			78	490			74	270
	18.00	0.7571	0.9322			130	420			130	300
333.15	9.00	0.2354	0.9171	0.0992	0.0547	32	450	0.1040	0.0577	38	340
	15.00	0.6041	0.9212			55	520			53	260

becomes negligible. The intermolecular-interactions contribution to H_m^E may be expected to remain approximately the same at a given temperature in this range of pressure. As a consequence, values of H_m^E at 313.15 K become much less exothermic as pressures rises.

When carbon dioxide and DMF are mixed at 323.15 or 333.15 K and 9.00 MPa, carbon dioxide is a gas-like fluid and its density is much lower than that at 313.15 K and 9.00 MPa. The resulting mixtures are liquid or a gaseous and a liquid mixture in equilibrium. The fluid condensation effect becomes very important and mixtures show extremely exothermic mixing: minimum H_m^E values of −4185 and −4526 J mol^{-1} are reached at 323.15 and 333.15 K, respectively. As the pressure is increased at 323.15 or 333.15 K, CO_2 densities sharply increase and H_m^E values become less exothermic.

The excess molar enthalpies of CO_2 + DMF were also calculated using Peng–Robinson and the Soave–Redlich–Kwong EOS [20,22] and the classical mixing rules. The excess molar enthalpy for a binary mixture is given by

$$H_m^E = H_m^R(\text{mixture}) - \sum_i x_i H_{m,i}^R \quad (6)$$

where H_m^R is the residual molar enthalpy of the mixture and $H_{m,i}^R$ is that of pure components. The residual molar enthalpy is given by

$$H_m^R = RT(z-1) + \int_\infty^V \left[T\left(\frac{\partial P}{\partial T}\right)_V - P \right] dV \quad (7)$$

where z is the compressibility factor. H_m^E data taken in the one-phase region at 313.15, 323.15 and 333.15 K were predicted using the binary interactions parameters obtained from VLE data taken at 313.05 K. H_m^E data were also simultaneously correlated using Eqs. (5)–(7). As was already discussed in Section 2, the uncertainties in temperature, pressure and composition are smaller than those of the excess molar enthalpies and a least square-procedure was used to minimize relative deviations between experimental and calculated H_m^E. Table 4 lists values adopted by the binary interaction parameters k_{12} and δ_{12} and values for the standard deviation between experimental and correlated binary excess enthalpies, σ_{cor}, and the standard deviation between experimental and predicted binary excess enthalpies, σ_{pre}, for each condition of temperature and pressure. Values for k_{12} and δ_{12} are higher than those obtained in VLE data correlations. Values for σ_{cor} are of similar magnitude for the two equations of state used. However, values obtained for σ_{pre} are considerable smaller when the Peng–Robinson EOS is used. A comparison of values for σ_{cor} and σ_{pre} and the maximum absolute value of H_m^E for each condition of temperature and pressure indicates that relative deviations are larger at 313.15 K. Both predictions and correlations become more accurate as temperature increases. This may be also observed in Figs. 1–3 where results from the Peng–Robinson EOS correlation are shown. Values for k_{12} and δ_{12} reported in Table 4 at 313.15, 323.15 and 333.15 K may be used to calculate H_m^E at each temperature in the 9.00–18.00 MPa or 9.00–15.00 MPa pressure intervals.

6. Conclusions

Excess molar enthalpies for mixtures of supercritical CO_2 and DMF were measured at T = 313.15, 323.15 and 333.15 K in the 9.00–18.00 MPa pressure range over the entire composition range. The CO_2 + DMF system presents immiscibility at 323.15 and 333.15 K and 9.00 MPa; in this range H_m^E varies linearly with mole fraction due to vapor–liquid equilibria. The effects of pressure and temperature on the excess molar enthalpy are large. Excess molar enthalpies are exothermic at all the conditions of temperature and pressure studied and become extremely exothermic (minimum H_m^E values of −4185 and −4526 J mol^{-1}) when low-density supercritical carbon dioxide is mixed with the liquid DMF and the resulting mixture is a liquid or a gaseous and a liquid mixture in equilibrium.

The Peng–Robinson and the Soave–Redlich–Kwong EOS [20,22] were used in conjunction with the classical mixing rules to correlate VLE data for CO_2 + DMF at 293.95, 313.05 and 338.05 K [15]. The best results were obtained for the Peng–Robinson EOS. Using the 313.05 K set of parameters, this equation was shown to provide a simultaneous and accurate description of VLE and critical data for the CO_2 + DMF system. On the other hand, predictions of excess molar enthalpies using the Peng–Robinson EOS and the 313.05 K set of parameters are considerably more accurate than those obtained using the Soave–Redlich–Kwong EOS. H_m^E data may be also correlated by means of the cubic EOS. Using the higher values thus obtained for the k_{12} and δ_{12} interaction parameters, excess molar enthalpies may be calculated at temperatures and pressures in the T = (313.15–333.15) K and P = (9.00–18.00) MPa intervals. As temperature increases both predictions and correlations become more accurate.

Acknowledgements

We gratefully acknowledge the financial support of the Santander-Universidad Complutense de Madrid, research project PR34/07-15789 and the Spanish Ministry of Education and Science (MEC), research project CTQ2009-09707. F.Z. thanks the E.U. for its support through an Erasmus Mundus University II predoctoral grant.

References

[1] E.J. Beckmann, Supercritical and near-critical CO_2 in green chemical synthesis and processing, J. Supercritical Fluids 28 (2004) 121–191.

[2] B.E. Poling, J.M. Prausnitz, J.P. OïConnell, The Properties of Gases and Liquids, McGraw-Hill International Editions, Singapore, 2001.
[3] Y. Marcus, Introduction to Liquid-state Chemistry, Wiley Interscience, London, 1977.
[4] E. Reverchon, Supercritical antisolvent precipitation of micro- and nano-particles, J. Supercritical Fluids 15 (1999) 1–21.
[5] J. Jung, M. Perrut, Particle design using supercritical fluids: literature and patent survey, J. Supercritical Fluids 20 (2001) 179–219.
[6] S.M. Pourmortazavi, S.S. Hajimirsadeghi, Application of supercritical carbon dioxide in energetic materials processes: a review, Industrial and Engineering Chemistry Research 44 (2005) 6523–6533.
[7] C.-K. Kim, B.-C. Lee, Y.-W. Lee, H.S. Kim, Solvent effect on particle morphology in recrystallization of HMX (cyclotetramethylenetetranitramine), Korean J. Chemical Engineering 26 (2009) 1125–1129.
[8] L. He, X. Zheng, Q. Xu, Modification of carbon nanotubes using poly(vynilidene fluoride) with assistance of supercritical carbon dioxide: the impact of the solvent, J. Physical Chemistry 114 (2010) 5257–5262.
[9] M. Charoenchaitrakool, W. Trisilanum, P. Srinopakhun, Application of gas anti-solvent process to the recovery of andrographolide from *Andrographis paniculatanees*, Korean J. Chemical Engineering 27 (2010) 950–954.
[10] M. Temtem, T. Casimiro, A. Aguiar-Ricardo, Solvent power and despressurization effects in the formation of polysulfone membranes with CO_2-assisted phase inversion method, J. Membrane Science 283 (2006) 244–252.
[11] S. Chanfreau, P. Cognet, S. Camy, J.-S. Condoret, Electrocarboxilation in supercritical CO_2 and CO_2-expanded liquids, J. Supercritical Fluids 46 (2008) 156–162.
[12] Y. Du, D.-L. Kong, H.-Y. Wang, F. Cai, J.-S. Tian, J.-Q. Wang, L.-N. He, Sn-catalyzed synthesis of propylene carbonate from propylene glycol and CO_2 under supercritical conditions, J. Molecular Catalysis A: Chemical 241 (2005) 233–237.
[13] C.J. Chang, C.-Y. Chen, H.-C. Lin, Solubilities of carbon dioxide and nitrous oxide in cyclohexanone, toluene, and *N*,*N*-dimethylformamide at elevated pressures, J. Chemical and Engineering Data 40 (1995) 850–855.
[14] A Kordikowski, A.P. Schenk, R.M. Van Nielen, C.J. Peters, Volume expansions and vapor–liquid equilibria of binary mixtures of a variety of polar solvents and certain near-critical solvents, J. Supercritical Fluids 8 (1995) 205–216.
[15] C. Duran-Valencia, A. Valtz, L.A. Galicia-Luna, D. Richon, Isothermal vapor–liquid equilibria of the carbon dioxide (CO_2)–*N*,*N*-dimethylformamide (DMF) system at temperatures from 293.95 K to 338.05 K and pressures up to 12 MPa, J. Chemical and Engineering Data 46 (2001) 1589–1592.
[16] H.-S. Byun, N.-H. Kim, C. Kwak, Measurements and modeling of high-pressure phase behavior of binary CO_2–amides systems, Fluid Phase Equilibria 208 (2003) 53–68.
[17] R.L. Scott, P.H. van Konynenburg, Van der Waals and related models for hydrocarbon mixtures, Discussion of the Faraday Society 49 (1970) 87–97.
[18] A. Zúñiga-Moreno, L.A. Galicia-Luna, Compressed liquid densities and excess volumes for the binary system CO_2 + *N*,*N*-dimethylformamide (DMF) system at temperatures from (313 to 363) K and pressures up to 25 MPa, J. Chemical and Engineering Data 50 (2005) 1224–1233.
[19] N.C. Patel, A.S. Teja, A new cubic equation of state for fluids and fluid mixtures, Chemical Engineering Science 37 (1982) 463–473.
[20] D.Y. Peng, D.B. Robinson, A new two-constant equation of state, Industrial and Engineering Chemistry Fundamentals 15 (1976) 59–64.
[21] M.J. Dávila, A. Cabañas, C. Pando, Excess molar enthalpies for binary mixtures related to supercritical antisolvent precipitation: carbon dioxide + *N*-methyl-2-pyrrolidone, J. Supercritical Fluids 42 (2007) 172–179.
[22] G. Soave, Equilibrium constants from a modified Redlich–Kwong equation of state, Chemical Engineering Science 27 (1972) 1197–1203.
[23] J.J. Christensen, L.D. Hansen, R.M. Izatt, D.J. Eatough, R.M. Hart, Isothermal flow calorimeter, Review of Scientific Instruments 47 (1976) 730–734.
[24] NIST Standard Reference Database Number 69, which can be accessed electronically through the NIST Chemistry Web Book. Available from: http://webbook.nist.gov/chemistry/.
[25] R. Perry, D.W. Green, Perry's Chemical Engineers' Handbook, 7th ed., Mc Graw Hill, New York, 1997.
[26] O. Pfohl, S. Petkov, G. Brunner, PE 2000. Available from: www.tu-harburg.de/v8/gruppe-prof-smirnova/veroeffentlichungen/pe-2000/download.html.
[27] R.A. Heidemann, A.M. Khalil, The calculation of critical points, AIChE J. 26 (1980) 767–779.

J. of Supercritical Fluids 60 (2011) 45–50

Contents lists available at ScienceDirect

The Journal of Supercritical Fluids

journal homepage: www.elsevier.com/locate/supflu

Role of excess molar enthalpies in supercritical antisolvent micronizations using dimethylsulfoxide as the polar solvent

Fouad Zahran, Jacobo Morère, Albertina Cabañas, Juan A.R. Renuncio, Concepción Pando*

Dpto. de Química Física I, Universidad Complutense, E-28040 Madrid, Spain

ARTICLE INFO

Article history:
Received 10 December 2010
Received in revised form 24 January 2011
Accepted 16 February 2011

Keywords:
Supercritical carbon dioxide
Dimethylsulfoxide
Excess molar enthalpies
Supercritical antisolvent precipitation
Phase equilibria

ABSTRACT

The role of excess molar enthalpies (H_m^E) in the supercritical antisolvent (SAS) micronizations using dimethylsulfoxide (DMSO) as the polar solvent was investigated. Excess molar enthalpies for CO_2 + DMSO mixtures were measured using an isothermal high-pressure flow calorimeter under conditions of temperature and pressure typically used in SAS micronizations. In most cases, mixtures showed very exothermic mixing. A local temperature increase can be expected in the precipitation chamber as a consequence of the heat evolved when CO_2 dissolves in DMSO. Based on the H_m^E measurements, local temperature increases were calculated and shown to explain immiscibility of CO_2 and DMSO and agglomerated or irregular particles for average temperature and pressure conditions where complete miscibility and uniform particles could have been expected. H_m^E data were also discussed in terms of molecular interactions, phase equilibria, density and critical parameters previously reported for CO_2 + DMSO.

1. Introduction

Supercritical antisolvent (SAS) micronization has been extensively used during the last years to obtain micro and nanoparticles with controlled particle size and morphology [1–4]. This approach is based on the relatively low solvent power of CO_2 for solutes such as polymers, pharmaceutical compounds, explosives or colorants and its good miscibility with many polar organic solvents. Typical solvents used are acetone, dimethylsulfoxide, *N*,*N*-dimethylformamide, dichloromethane and *N*-methyl-2-pyrrolidone. Supercritical carbon dioxide is used as an antisolvent: upon CO_2 solution, the liquid experiences a volumetric expansion and becomes a bad solvent for the solute that precipitates from the organic solution. The role of phase equilibria, jet mixing and mass transfer in these micronizations has been analyzed and several authors have pointed out that the phase behavior of CO_2 + organic solvent is one of the crucial factors governing the morphology and the mean size of particles obtained in the SAS process [5–10]. Consequently, the high-pressure phase behavior and volumetric expansion of these mixtures have received considerable attention. However, no much attention has been paid to the heat evolved when supercritical CO_2 dissolves into the organic solvent. To the best of our knowledge, only Dukhin et al. [11,12] have taken into account these heats or mixing or excess molar enthalpies (H_m^E) that can be quite high at these conditions. Thus, thermal effects during this process have an effect on the phase separation path and must be considered in order to fully understand SAS processes and optimize micronization conditions. Since CO_2 is fed into the precipitation chamber at a flow rate much higher than that of the solution and the solute concentration is very low, the contribution to H_m^E due to solute interactions may be neglected and the thermal effect in SAS experiments can be considered mainly due to the formation of CO_2 + organic solvent mixtures very rich in carbon dioxide ($x \geq 0.95$). In a previous study [13], H_m^E values for CO_2 + *N*-methyl-2-pyrrolidone mixtures were measured at our laboratory at 313.15 and 338.15 K and 9.48, 15.00 and 20.00 MPa and the relation between thermal effects and phase behavior and coalescence phenomena observed in SAS micronization of several antibiotics was discussed. More recently, similar effects were observed for CO_2 + acetone and CO_2 + *N*,*N*-dimethylformamide mixtures [14,15]. In this paper, we report excess molar enthalpies for the binary system CO_2 + DMSO under conditions of temperature and pressure typically used in supercritical CO_2 applications: 313.15 and 323.15 K and 9.00, 12.00, 15.00 and 18.00 MPa as well as 333.15 K and 9.00 and 15.00 MPa. These data will be analyzed in terms of molecular interactions, phase equilibria and density data, and their role in the supercritical antisolvent micronization will be discussed.

Dimethylsulfoxide (DMSO) is an organic solvent with a relatively high dipolar moment (3.8 D [16]) that is able to dissolve a large variety of products. DMSO has been frequently used as a solvent in SAS precipitation [1–5] and as a cosolvent to improve CO_2 solution of drugs such as eflucimibe [17]. Raveendran and

* Corresponding author at: Departamento de Química Física I, Facultad C. Químicas, Universidad Complutense, E-28040 Madrid, Spain. Tel.: +34 91394 4304; fax: +34 91394 4135.
E-mail address: pando@quim.ucm.es (C. Pando).

0896-8446/$ – see front matter © 2011 Elsevier B.V. All rights reserved.
doi:10.1016/j.supflu.2011.02.015

Wallen [18] have chosen CO_2 + DMSO as a model system to study CO_2–Lewis base complexes and solvation in supercritical CO_2 for the sulfonyl group. Ab initio calculations were performed and the interaction energy, geometry and other molecular properties of the CO_2–DMSO complex were calculated and compared to those of complexes formed by formaldehyde, acetaldehyde, acetic acid and methyl acetate. Results indicate that the S=O bond plays a key role in the CO_2–DMSO complex and explain the high miscibility of DMSO in CO_2. On the other hand, the physical and thermodynamic properties of CO_2 + DMSO mixtures have been the subject of numerous investigations and densities, viscosities, critical parameters and phase equilibria and volumetric expansion data are available in the literature [19–28]. Andreatta et al. [26] discussed the type of critical locus in the Scott and van Konynenburg classification [29]. According to them CO_2 + DMSO belongs either to type III or IV in this classification; more data in the lower temperature range are required to reach a definitive conclusion. Other investigations were carried out for ternary mixtures formed by CO_2, DMSO and H_2O [22,26], dextran [30], yttrium acetate [5] or cefonicid [6]. The presence of a third component such as water or dextran that interacts with carbon dioxide modifies the phase diagram. In the case of solutes such as yttrium acetate or the antibiotic cefonicid that interact weakly with carbon dioxide the ternary phase diagram for the low solute concentration usually employed in SAS is coincident with the binary one in the CO_2-rich region which is the region for mixtures involved in SAS. These phase equilibria data for the CO_2 + DMSO system will be used to interpret the excess molar enthalpies reported in this paper, and their relevance in morphologies observed in some supercritical antisolvent micronizations will be analyzed.

2. Experimental

The materials employed were CO_2 (Air Liquide 99.98 mol% pure) and DMSO (Fluka, ≥99.9 mol% pure). Commercial materials were used without further purification.

An isothermal high-pressure flow calorimeter (Hart Scientific model 7501) was used to perform H_m^E measurements. The calorimeter was first described by Christensen et al. [31] and the experimental procedure is described elsewhere [13]. The reactants were pumped into the calorimetric cell by two thermostated pumps (ISCO, model LC-2600) at constant flow rates. Volume flow rates were selected to cover the entire concentration range. Temperature of the pumps was controlled within ±0.02 K. For each pump, the uncertainty in the volume flow rate was obtained by a previous calibration. The calorimetric cell was located into a silicon bath in which temperature was controlled within ±0.001 K. A Peltier cooling device and a pulsed heater kept the cell under isothermal conditions. The pulse energy was determined by a heater calibration. The pressure was measured using a calibrated pressure transducer (Lucas Schaevitz, model P721-0001). A back-pressure regulator located outside the calorimeter kept the pressure within ±0.01 MPa.

All runs were made in the steady-state fixed composition mode. Measurements were carried out at total volume flow rates of 0.0014 and 0.0028 $cm^3\ s^{-1}$. These values were chosen to cover the entire mole fraction range by combining adequate values for the flow rates of the two pumps. Also, the coincidence of the experimental results obtained using different total flow rates is an indication of equilibrium conditions in the calorimeter. The volume flow rates were converted to molar flow rates using the densities and molar masses. CO_2 densities at the temperature and pressure of the pumps were obtained from NIST [32]. DMSO densities were obtained from the Tait equation provided by Czeslik and Jonas [33]. Since densities are affected by temperature and pressure changes, the uncertainty in molar flow rates was derived taking into account contributions from variations in volume flow rates, pressure, and pumps temperature. The mole fraction uncertainty is based on the molar flow rates uncertainty and was estimated to be better than ±0.001. The uncertainty in H_m^E was obtained taking into account contributions from molar flow rates, pulse energy and frequency and was estimated to be ±1%.

Table 1
Excess molar enthalpy, H_m^E, for the binary system [CO_2 (x) + DMSO ($1-x$)].

x	H_m^E (J mol^{-1})	x	H_m^E (J mol^{-1})	x	H_m^E (J mol^{-1})
313.15 K and 9.00 MPa					
0.151	−407	0.516	−1376	0.828	−1974
0.220	−570	0.567	−1444	0.901	−1712
0.286	−829	0.616	−1582	0.968	−1083
0.348	−936	0.706	−1774		
0.407	−1127	0.748	−1876		
313.15 K and 12.00 MPa					
0.156	−241	0.557	−946	0.740	−1113
0.286	−451	0.597	−1002	0.773	−1109
0.384	−653	0.634	−1059	0.865	−934
0.430	−772	0.671	−1095	0.933	−662
313.15 K and 15.00 MPa					
0.063	−78	0.474	−614	0.740	−921
0.156	−221	0.516	−675	0.773	−905
0.286	−415	0.557	−759	0.865	−626
0.384	−516	0.671	−900	0.933	−374
313.15 K and 18.00 MPa					
0.063	−182	0.421	−755	0.805	−856
0.122	−303	0.483	−825	0.865	−709
0.156	−346	0.597	−890	0.949	−406
0.212	−408	0.634	−914		
0.306	−589	0.706	−952		
323.15 K and 9.00 MPa					
0.095	−473	0.429	−2885	0.682	−3658
0.168	−968	0.567	−3709	0.720	−3292
0.302	−2077	0.606	−3905	0.828	−2067
0.362	−2453	0.644	−3765	0.913	−1007
323.15 K and 12.00 MPa					
0.102	−287	0.381	−1169	0.700	−1997
0.180	−517	0.433	−1325	0.771	−1912
0.247	−769	0.547	−1659	0.840	−1782
0.320	−1005	0.625	−1852	0.919	−1159
323.15 K and 15.00 MPa					
0.115	−262	0.392	−1015	0.709	−1468
0.187	−469	0.477	−1167	0.779	−1321
0.255	−616	0.558	−1367	0.846	−1208
0.329	−774	0.635	−1410	0.922	−757
323.15 K and 18.00 MPa					
0.109	−163	0.399	−752	0.715	−1088
0.191	−348	0.468	−849	0.784	−1060
0.261	−457	0.566	−996	0.850	−873
0.336	−681	0.643	−1098	0.924	−538
333.15 K and 9.00 MPa					
0.095	−720	0.426	−3366	0.756	−1860
0.168	−1370	0.487	−3755	0.828	−1306
0.232	−2428	0.527	−3576	0.913	−660
0.308	−2077	0.606	−2979		
0.362	−2858	0.682	−2339		
333.15 K and 15.00 MPa					
0.106	−387	0.392	−1124	0.709	−1780
0.187	−565	0.461	−1276	0.779	−1680
0.255	−801	0.558	−1535	0.846	−1478
0.329	−956	0.635	−1712	0.922	−1060

3. Results and discussion

H_m^E data for the binary system [CO_2 (x) + DMSO (1–x)] were determined at 313.15 and 323.15 K and 9.00, 12.00, 15.00 and 18.00 MPa as well at 333.15 K and 9.00 and 15.00 MPa over the entire composition range and are given in Table 1. Fig. 1(a–d) shows plots of H_m^E vs CO_2 mole fraction at 9.00, 12.00, 15.00 and 18.00 MPa, respectively. At each condition of temperature and pressure in the 12.00–18.00 MPa pressure range, excess molar enthalpies are

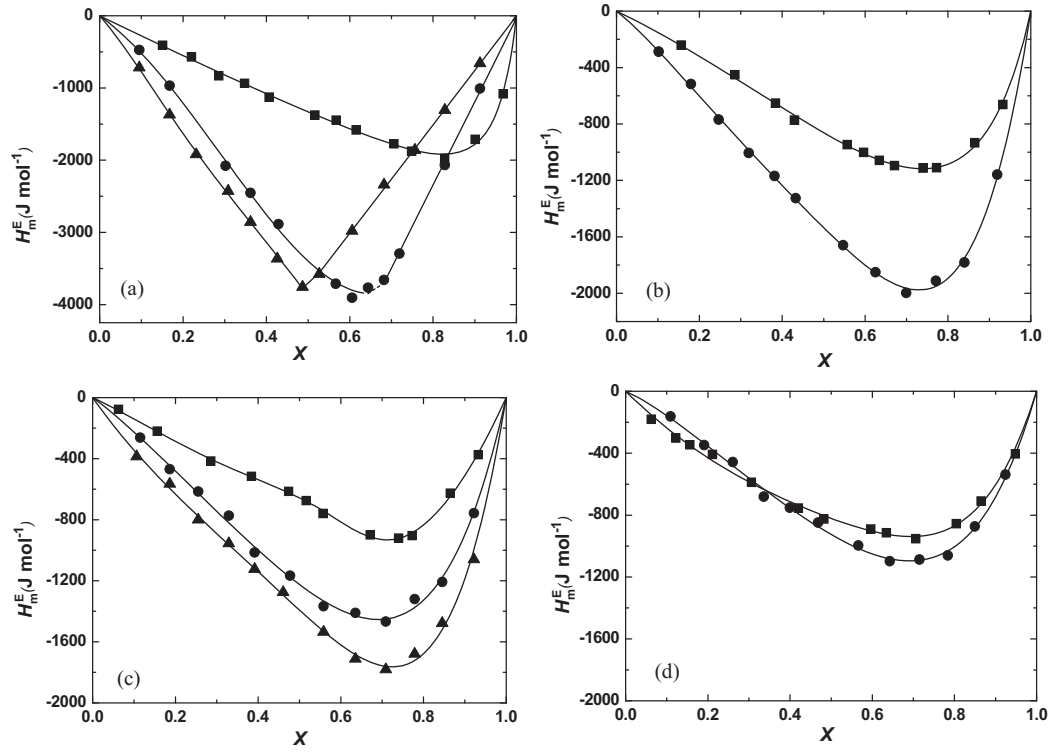

Fig. 1. Excess molar enthalpies, H_m^E, for the binary system [CO_2(x) + dimethylsulfoxide ($1-x$)] vs CO_2 mole fraction at (a) 9.00 MPa, (b) 12.00 MPa, (c) 15.00 MPa, (d) 18.00 MPa and: (■) 313.15 K; (●) 323.15 K; (▲) 333.15 K; (—), calculated using Eq. (3) and coefficients given in Table 2.

exothermic and exhibit minima in the CO_2-rich region. For a given mole fraction and pressure, most mixtures become increasingly exothermic as the temperature increases. Minimum values range from $-900\,J\,mol^{-1}$ to $-2000\,J\,mol^{-1}$. The effect of temperature becomes less pronounced when the pressure is increased to 18.00 MPa: H_m^E values obtained at this pressure and 313.15 or 323.15 K are very similar.

At 9.00 MPa mixtures show very exothermic mixing: a minimum of $-2000\,J\,mol^{-1}$ is already observed at 313.15 K and minima of approximately $-4000\,J\,mol^{-1}$ are observed at the higher temperatures of 323.15 and 333.15 K. On the other hand, a linear section is observed in the H_m^E vs CO_2 mole fraction plot at 9.00 MPa and 323.15 and 333.15 K. H_m^E varies linearly with CO_2 mole fraction in the two-phase region where a gaseous and a liquid mixture of fixed compositions, for a given condition of temperature and pressure, are in equilibrium. For a mixture of global composition x, the enthalpy effect in the two-phase region is the sum of two contributions due to the n_l mol of liquid mixture of composition x_l and n_v mol of vapor mixture of composition x_v,

$$H_m^E = H_{m,l}^E\, n_l + H_{m,v}^E\, n_v \tag{1}$$

where $H_{m,l}^E$ is the excess molar enthalpy of the liquid mixture, and $H_{m,v}^E$ is the excess molar enthalpy of the vapor mixture. Based on the relations among n_l, n_v, x, x_l and x_v [13], Eq. (1) may be rewritten as:

$$H_m^E = H_{m,v}^E + \frac{x - x_v}{x_l - x_v}(H_{m,l}^E - H_{m,v}^E) \tag{2}$$

Since $H_{m,l}^E$, $H_{m,v}^E$, x_l and x_v have constant values for each isotherm/isobar, the second member of Eq. (2) is a first-degree polynomial in x. When $x = x_l$, $H_m^E = H_{m,l}^E$ and when $x = x_v$, $H_m^E = H_{m,v}^E$. Therefore, the liquid and vapor-phase compositions are shown to correspond to the x coordinates of the beginning and the end of the linear sections shown in Fig. 1(a). A considerable amount of DMSO is present in the liquid mixture but only a very small amount is dissolved in the vapor phase; the CO_2 vapor-phase composition is very close to one and cannot be established from the calorimetric measurements.

The linear sections at 323.15 and 333.15 K and 9.00 MPa are in agreement with the isothermal vapor–liquid equilibrium and critical data previously reported for CO_2 + DMSO by González et al. and Chiu et al. [21,27] shown in Fig. 2. As could be expected from the

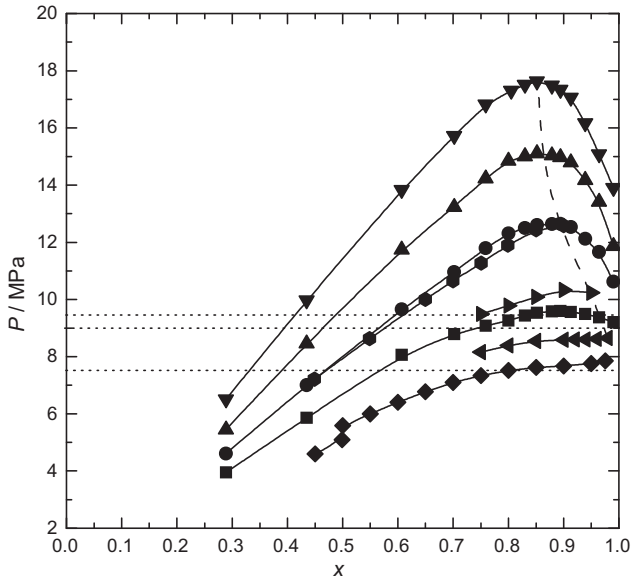

Fig. 2. Isothermal vapor–liquid equilibrium and critical data for the binary system [CO_2(x) + dimethylsulfoxide ($1-x$)] reported by González et al. [21]: (◆), 309.41 K; (◄) 314.49 K; (►), 321.28 K; (⬢) 328.94 K, and Chiu et al. [27]: (■) 318.15 K; (●) 328.95 K; (▲) 338.15 K; (▼) 348.15 K, critical line (– – –), and pressure conditions of SAS experiments carried out by Reverchon et al. [5] at 313.15 K using DMSO (· · · ·).

Table 2
Coefficients A_i and B_j and standard deviation, σ, for least-squares representation of H_m^E (J mol^{-1}) for [CO_2 (x) + DMSO (1 − x)] at 313.15, 323.15 and 333.15 K using Eq. (3).

T (K)	P (MPa)	Interval	A_0	A_1	A_2	A_3	A_4	B_1	B_2	σ (J mol^{-1})
313.15	9.00	$0 \le x \le 1$	−5312.55	−207.75	−382.21	−278.96	–	−0.88	–	14
	12.00	$0 \le x \le 1$	−3446.04	−1094.14	–	–	–	−0.65	–	5.4
	15.00	$0 \le x \le 1$	−2590.39	2702.41	−8778.49	−5693.33	919.34	−1.97	3.28	36
	18.00	$0 \le x \le 1$	−3283.77	−1956.63	−2161.30	−926.08	–	–	–	8.3
323.15	9.00	$0 \le x \le 0.644$	−13580.0	−10768.6	−1231.86	–	–	–	–	23
		$0.644 \le x \le 1$	−23178.3	23026.0	–	–	–	0	−1	21
	12.00	$0 \le x \le 1$	−6139.87	−5765.40	−4605.59	−2682.20	–	–	–	5.9
	15.00	$0 \le x \le 1$	−4897.54	−4061.67	−2098.72	−957.17	–	–	–	8.5
	18.00	$0 \le x \le 1$	−3700.18	−3029.32	−1524.31	−981.35	–	–	–	6.3
333.15	9.00	$0 \le x \le 0.487$	−15482.3	−14968.4	−16795.0	−10968.9	–	–	–	13
		$0.487 \le x \le 1$	−15060.2	15043.7	–	–	–	0	−1	11
	15.00	$0 \le x \le 1$	−5568.42	−4929.65	−4592.05	−1418.29	–	–	–	9.0

phase equilibria data and may be observed in Fig. 1(b)–(d), two-phase regions do not appear when the pressure is raised from 9.00 to 12.00, 15.00 or 18.00 MPa at the three temperatures studied.

H_m^E data for [CO_2 (x) + DMSO (1–x)] were fitted to a (n, m) Padé function given by

$$H_m^E = x(1-x)\frac{\sum_{i=0}^{n} A_i(2x-1)^i}{1+\sum_{j=1}^{m} B_j(2x-1)^j} \quad (3)$$

where A_i and B_j are adjustable coefficients. A least-square procedure was used to minimize deviations between experimental and calculated excess molar enthalpies. For those conditions of temperature and pressure where phase-splitting occurs, two different sets of coefficients are used to represent data in the two-phase and one-phase region, respectively. In the linear section, a (1, 2) Padé function with fixed values for the denominator coefficients, $B_1 = 0$ and $B_2 = -1$, may be used in order to keep the weight factor $x(1-x)$. This results in a first-degree polynomial in the composition variable; the slope is $A_1/2$ and the zero intercept is $(A_0 - A_1)/4$. The H_m^E representation using Eq. (3) is shown in Fig. 1. Table 2 lists values for the coefficients A_i and B_j and the standard deviation between experimental and calculated H_m^E values at 313.15 and 323.15 K and 9.00, 12.00, 15.00 and 18.00 MPa and 333.15 K and 9.00 and 15.00 MPa. The beginning of the linear sections shown in Table 2 at 9.00 MPa and 323.15 and 333.15 K provides the value for the liquid-phase composition in the two-phase region.

In a typical SAS experiment supercritical CO_2 is preliminarily fed to the precipitation chamber at constant flow rate. Then the liquid solvent is fed also at constant flow rate in order to obtain steady state operating conditions. Afterwards, DMSO is replaced by the liquid solution and precipitation starts. The concentration of solutes in the DMSO solution is low and the CO_2/solution flow ratio is very high. As has been already pointed out, when the solute has little interaction with carbon dioxide the ternary phase diagram for the low solute concentrations usually employed in SAS is coincident with the binary one in the CO_2-rich region which is the region for mixtures involved in SAS. Therefore, the mixtures formed in the precipitation chamber may be treated as binary CO_2 + organic solvent systems. In general, nanoparticles are obtained when the precipitation is carried out in the supercritical region. The uniformity of the resulting products becomes worse when the precipitation conditions approach the critical locus. Irregular micro-scale aggregated particles are formed in the vapor region and both dense cake and spherical clusters are produced in the vapor–liquid region [5–10]. The heat evolved when the supercritical CO_2 dissolves into the organic solution has an important role in the phase behavior. The temperature control in the precipitation chamber is not very precise and the local temperature increase may lead to T and P conditions where phase splitting takes place. Since CO_2 is fed into the chamber at a flow rate much higher than that of the solution and the solute concentration is very low, the contribution to H_m^E due to solute interactions may be neglected and the thermal effect in SAS experiments can be considered mainly due to the formation of CO_2 + DMSO mixtures very rich in carbon dioxide ($x \ge 0.95$). Consequently, the temperature increase ΔT may be estimated using the H_m^E data reported in this paper. Since carbon dioxide is the predominant component in these mixtures, its isobaric heat capacity [34] was used to calculate the local temperature increase assuming an adiabatic process and using Eq. (3) to evaluate the heat evolved when a mol of mixture is formed for two composition values: $x = 0.95$ and 0.98. Values for ΔT thus obtained are shown in Table 3 and they help to explain immiscibility observed in SAS micronizations for temperature and pressure conditions where complete miscibility could have been expected for CO_2 and DMSO. As a consequence the particles morphologies do not correspond to those expected in a supercritical phase.

Reverchon et al. [5] used DMSO as a solvent in the SAS precipitation of yttrium acetate at 313.15, 323.15 and 333.15 K, pressures up to 16.0 MPa and $x = 0.98$. A windowed vessel was used to observe the phase behavior of the CO_2 + DMSO mixtures and the liquid jet formation and evolution. According to González et al. [21] the critical temperature and pressure for $x = 0.98$ are 314.9 K and 8.65 MPa. At 313.15 K and 1.36 wt% of YAc in DMSO, Reverchon et al. reported two phases and agglomerated nanoparticles at 7.5 MPa, two phases and a mixture of nanoparticles and microparticles at 9.0 MPa, one phase and balloon-like particles at 9.5 MPa and one phase and uniform nanoparticles from 10 to 15 MPa. An inspection of Fig. 2 indicates that one phase should have been observed already at 9.00 MPa. However, the temperature increase of 2.9 K shown in Table 3 for these x, P and T conditions explains the immiscibility observed for mixtures formed in the SAS experiments and a particle morphology that does not correspond to the uniform nanoparticles expected in a supercritical phase. As the pressure rises for this

Table 3
Carbon dioxide and dimethylsulfoxide experimental densities[a,b] and estimated temperature increments at mixing in the x interval 0.95–0.98.

T (K)	P (MPa)	ρ_{CO_2} (g cm^{-3})	ρ_{DMSO} (g cm^{-3})	ΔT (K)
313.15	9.00	0.4855	1.0851	5.2–2.9
	12.00	0.7178	1.0867	2.7–1.3
	15.00	0.7802	1.0882	2.3–1.0
	18.00	0.8195	1.0898	3.1–1.5
323.15	9.00	0.2850	1.0753	3.3–1.4
	12.00	0.5847	1.0769	5.1–2.2
	15.00	0.6998	1.0786	3.9–1.7
	18.00	0.7571	1.0801	3.4–1.5
333.15	9.00	0.2354	1.0658	3.5–1.4
	15.00	0.6041	1.0695	4.7–2.0

[a] Ref. [32].
[b] Ref. [33].

condition of temperature, the heat evolved upon mixing and the local temperature increase are of smaller magnitude and the phase behavior is not affected. Similar effects are observed for experiments carried out by Reverchon et al. at 323.15 and 333.15 K [5].

Chang et al. used DMSO as a solvent in the SAS precipitation of α-chymotrypsin [7] and lysozyme [8] at 308.15, 318.15, 328.15 and 338.15 K and pressures up to 20 MPa. In both cases agglomerated or irregular particles are obtained at pressures below 10 MPa when the considerable heat evolved may lead to a local temperature increase in the precipitator. The very exothermic H_m^E values correlate with T and P conditions where micronization is less successful. The solubility of both proteins in CO_2 and its concentration in the solution are very low and the binary phase diagram shown in Fig. 2 may be used to discuss results. For instance, in the case of lysozyme at 308.15 K for identical values of lysozyme concentration, capillary size, and CO_2 and solution flow rates irregular nanoparticles are obtained at 8.5, 10, and 12 MPa and uniform nanoparticles are obtained at 15 and 20 MPa. At this temperature one phase is already expected at 8.5 MPa and at 10 and 12 MPa particle morphologies should correspond to the uniform nanoparticles expected for the supercritical region well above the critical boundary. Of course, there are other factors that may simultaneously influence the particle morphology but the heat evolved upon mixing CO_2 and the polar solvent is shown to play an important role. As was already mentioned, the effect of the heat of mixing in SAS was first introduced by Dukhin et al. [11,12] in their study of the dynamic interfacial tension (DIT) near a critical point of the CO_2 + polar solvent mixtures. A new nonisothermic DIT mode was introduced and shown to contribute to the jet stability in the case of exothermic mixing. There are several studies such as those of Dukhin et al. [12], Reverchon et al. [10], Petit-Gas et al. [35] or Tenorio et al. [36] aimed at the understanding of SAS fundamental mechanisms. High-pressure phase equilibria, hydrodynamics and mass transfer must be simultaneously taken into account and their interrelation has to be elucidated. In these studies, the different regimes are classified according to the experimental conditions location with respect to the mixture critical point (MCP): subcritical conditions, near above the MCP and far above the MCP. Two time scales, one for the complete disappearance of the interfacial tension and another for the time of the jet break-up were shown to compete [10]. In this paper, the heat evolved upon mixing is shown to modify the experimental conditions location with respect to the MCP causing a change of regime. Thus, these H_m^E data for CO_2 + DMSO and those previously obtained for binary mixtures formed by CO_2 and *N*-methyl-2-pyrrolidone, acetone or *N*,*N*-dimethylformamide may contribute to a better understanding of the fundamental aspects of SAS micronizations. On the other hand, excess enthalpy data could be also useful when CO_2-expanded solvents are used as reaction media [37,38].

The large effects of pressure and temperature on the excess molar enthalpy values are related to changes in molecular interactions and the state and densities of the pure components and their mixtures. Table 3 lists the densities of the pure components obtained from the sources described in Section 2. At the conditions of H_m^E measurements, DMSO is a liquid and its density does not change to a great extent with temperature and pressure in the intervals considered in this paper. However, carbon dioxide is a supercritical fluid that may be either a high-density (liquid-like) fluid or a low-density (gas-like) fluid. When carbon dioxide and DMSO are mixed at 313.15 K and 9.00 MPa, carbon dioxide is a gas-like fluid and the resulting mixtures are mostly liquid. González et al. and Chiu et al. critical data [21,27] indicate that fluid mixtures are confined to a very narrow mole fraction range in the carbon dioxide rich region. These negative H_m^E values are a consequence of two contributions: (a) changes in molecular interactions due to the disruption of the DMSO structure by carbon dioxide and the formation of the DMSO–CO_2 complexes, and (b) the CO_2 change of state from that of a gas-like fluid to that of liquid mixture component. The latter is the so-called fluid condensation effect that has been reported for other similar mixtures [13–15]. When the pressure is increased at 313.15 K, CO_2 density rises considerably and the fluid condensation effect becomes negligible. The intermolecular-interactions contribution to H_m^E may be expected to remain approximately the same at a given temperature in this range of pressure. As a consequence, values of H_m^E at 313.15 K become much less exothermic as pressures rises.

When carbon dioxide and DMSO are mixed at 323.15 or 333.15 K and 9.00 MPa, carbon dioxide is a gas-like fluid; its density is much lower than that at 313.15 K and 9.00 MPa. The resulting mixtures are liquid or a gaseous and a liquid mixture in equilibrium. The fluid condensation effect becomes very important and mixtures show extremely exothermic mixing: minimum H_m^E values of −3905 and −3755 J mol^{-1} are reached at 323.15 and 333.15 K, respectively. As the pressure is increased at 323.15 or 333.15 K, CO_2 densities sharply increase and H_m^E values become less exothermic.

4. Conclusions

Excess molar enthalpies for mixtures of supercritical CO_2 and DMSO were measured at T = 313.15, 323.15 and 333.15 K in the 9.00–18.00 MPa pressure range over the entire composition range. The CO_2 + DMSO system presents immiscibility at 323.15 and 333.15 K and 9.00 MPa; in this range H_m^E varies linearly with mole fraction due to vapor–liquid equilibria. The effects of pressure and temperature on the excess molar enthalpy are large. Excess molar enthalpies are exothermic at all the conditions of temperature and pressure studied and become extremely exothermic (minimum H_m^E values of −3905 and −3755 J mol^{-1}) when low-density supercritical carbon dioxide is mixed with the liquid DMSO and the resulting mixture is a liquid or a gaseous and a liquid mixture in equilibrium.

These heat of mixing data are used to establish thermal effects in SAS experiments. The local temperature increases thus produced in the precipitation chamber are shown to modify the phase separation path and the particle morphology. Therefore, these thermal effects must be taken into account in SAS design and modeling. In order to avoid the modification of phase behavior for a given micronization temperature, it may be recommended to work at a pressure at least 1 or 1.5 MPa above the estimated critical pressure for the binary mixture CO_2 + DMSO.

Acknowledgements

We gratefully acknowledge the financial support of the Santander-Universidad Complutense de Madrid, research project PR34/07-15789 and the Spanish Ministry of Science and Innovation (MICINN), research project CTQ2010-16940. F.Z. thanks the E.U. for its support through an Erasmus Mundus University II predoctoral grant.

References

[1] E. Reverchon, Supercritical antisolvent precipitation of micro- and nanoparticles, J. Supercritical Fluids 15 (1999) 1–21.
[2] J. Jung, M. Perrut, Particle design using supercritical fluids: literature and patent survey, J. Supercritical Fluids 20 (2001) 179–219.
[3] A. Shariati, C.J. Peters, Recent developments in particle design using supercritical fluids, Current Opinion in Solid State and Materials Science 7 (2003) 371–383.
[4] S.-D. Yeo, E. Kiran, Formation of polymer particles with supercritical fluids: a review, J. Supercritical Fluids 34 (2005) 287–308.
[5] E. Reverchon, G. Caputo, I. De Marco, Role of phase behavior and atomization in the supercritical antisolvent precipitation, Industrial and Engineering Chemistry Research 42 (2003) 6406–6414.
[6] E. Reverchon, I. De Marco, E. Torino, Nanoparticles production by supercritical antisolvent precipitation: a general interpretation, J. Supercritical Fluids 43 (2007) 126–138.

[7] S.C. Chang, M.J. Lee, H.M. Lin, The influence of phase behaviour on the morphology of protein α-chymotrypsin prepared via a supercritical anti-solvent process, J. Supercritical Fluids 44 (2008) 219–229.
[8] S.C. Chang, M.J. Lee, H.M. Lin, Role of phase behavior in micronization of lysozyme via a supercritical anti-solvent process, Chemical Engineering J. 139 (2008) 416–425.
[9] A. Martín, M.J. Cocero, Micronization processes with supercritical fluids: fundamentals and mechanisms, Advanced Drug Delivery Reviews 60 (2008) 339–350.
[10] E. Reverchon, E. Torino, S. Dowy, A. Brauer, A. Leipertz, Interactions of phase equilibria, jet fluid dynamics and mass transfer during supercritical antisolvent micronization, Chemical Engineering J. 156 (2010) 446–458.
[11] S.S Dukhin, C. Zhu, R. Dave, R. Pfeffer, J.J. Luo, F. Chávez, Y. Shen, Dynamical interfacial tension near critical point of a solvent-antisolvent mixture and laminar jet stabilization, Colloids and Surfaces A. Physicochemical and Engineering Aspects 229 (2003) 181–189.
[12] S.S. Dukhin, Y. Shen, R. Dave, R. Pfeffer, Droplet mass transfer, intradroplet nucleation and submicron particle production in two-phase flow of solvent-supercritical antisolvent emulsion, Colloids and Surfaces A. Physicochemical and Engineering Aspects 261 (2005) 163–176.
[13] M.J. Dávila, A. Cabañas, C. Pando, Excess molar enthalpies for binary mixtures related to supercritical antisolvent precipitation: carbon dioxide + *N*-metil-2-pirrolidone, J. Supercritical Fluids 42 (2007) 172–179.
[14] F. Zahran, C. Pando, J.A.R. Renuncio, A. Cabañas, Excess molar enthalpies of CO_2 + acetone at pressures from (9.00 to 18.00) MPa and temperatures from (313.15 to 333.15) K, J. Chemical Engineering Data 55 (2010) 3649–3654.
[15] F. Zahran, C. Pando, A. Cabañas, J.A.R. Renuncio, Measurements and modeling of high-pressure excess molar enthalpies and isothermal vapor–liquid equilibria of the carbon dioxide + *N*,*N*-dimethylformamide system, J. Supercritical Fluids 55 (2010) 566–572.
[16] A.L McClellan, Tables of Experimental Dipole Moments, Rahara Entrerprises, El Cerrito, 1974.
[17] M. Sauceau, J.-J. Letourneau, B. Freiss, Solubility of eflucimibe in supercritical carbon dioxide with or without a co-solvent, D. Richon, J. Fages, J. Supercritical Fluids 31 (2004) 133–140.
[18] P. Raveendran, S.L. Wallen, Cooperative C–H···O hydrogen bonding in CO_2 – Lewis base complexes: implications for solvation in supercritical CO_2, J. American Chemical Society 124 (2001) 12590–12599.
[19] S.-D. Yeo, P.G. Debenedetti, M. Radosz, H.-W. Schmidt, Supercritical Antisolvent process for substituted para-linked aromatic polyamides: phase equilibrium and morphology study, Macromolecules 26 (1993) 6207–6210.
[20] A. Kordikowski, A.P. Schenk, R.M. Van Nielen, C.J. Peters, Volume expansions and vapor–liquid equilibria of binary mixtures of a variety of polar solvents and certain near-critical solvents, J. Supercritical Fluids 8 (1995) 205–216.
[21] A.V. González, R. Tufeu, P. Subra, High-pressure vapor–liquid equilibrium for the binary systems carbon dioxide + dimethyl sulfoxide and carbon dioxide + dichloromethane, J. Chemical and Engineering Data 47 (2002) 492–495.
[22] N. Elvassore, A. Bertucco, V. Di Noto, On-line monitoring of volume expansion in gas antisolvent processes by UV–Vis spectroscopy, J. Chemical and Engineering Data 47 (2002) 223–227.
[23] C.-W. Lee, Ch.-Y. Jung, H.-S. Byun, High-pressure phase behavior of carbon dioxide + 1-methyl-2-pyrrolidinone and carbon dioxide + 1-ethyl-2-pyrrolidinone systems, J. Chemical and Engineering Data 49 (2004) 53–57.
[24] R. Rajasingam, L. Lioe, Q.T. Pham, F.P. Lucien, Solubility of carbon dioxide in dimethylsulfoxide and *N*-methyl-2-pyrrolidone at elevated pressure, J. Supercritical Fluids 31 (2004) 227–234.
[25] M.J. Lazzaroni, D. Bush, J.S. Brown, C.A. Eckert, High-pressure vapor–liquid equilibria of some carbon dioxide + organic binary systems, J. Chemical and Engineering Data 50 (2005) 60–65.
[26] A.E. Andreatta, L.J. Florusse, S.B. Bottini, C.J. Peters, Phase-equilibria of dimethyl sulfoxide (DMSO) + carbon dioxide and DMSO + carbon dioxide + water mixtures, J. Supercritical Fluids 42 (2007) 60–68.
[27] H.-Y. Chiu, R.-F. Jung, M.-J. Lee, H.-M. Lin, Vapor–liquid phase equilibrium behaviour of mixtures containing supercritical carbon dioxide near critical region, J. Supercritical Fluids 44 (2008) 273–278.
[28] C. Brice, E. Rodier, J.J. Letourneau, J. Fages, Development and Characterization techniques of thermodynamic and physical properties applied to the CO_2-DMSO mixture, International J. Chemical Reactor Engineering 7 (2009) A46.
[29] R.L. Scott, P.H. van Konynenburg, Van der Waals and related models for hydrocarbon mixtures, Discussions of the Faraday Society 49 (1970) 87–97.
[30] Y. Pérez de Diego, F.E. Wubbolts, G.J. Witkamp, Th.W. de Loos, P.J. Jansens, Measurements of the phase behaviour of the system dextran/DMSO/CO_2 at high pressures, J. Supercritical Fluids 35 (2005) 1–9.
[31] J.J. Christensen, L.D. Hansen, R.M. Izatt, D.J. Eatough, R.M. Hart, Isothermal flow calorimeter, Review of Scientific Instruments 47 (1976) 730–734.
[32] Thermophysical Properties of Fluid Systems, National Institute of Standards and Technologies. Available from http://webbook.nist.gov/chemistry/fluid/.
[33] C. Czeslik, J. Jonas, Effect of pressure on local order in liquid dimethyl sulfoxide, J. Physical Chemistry A 103 (1999) 3222–3227.
[34] R. Span, W. Wagner, A new equation of state for carbon dioxide covering the fluid region from the triple-point temperature to 1100 K and pressures up to 800 MPa, J. Physical and Chemical Reference Data 25 (1996) 1509–1596.
[35] T. Petit-Gas, O. Boutin, I. Raspo, E. Badens, Role of hydrodynamics in supercritical antisolvent processes, J. Supercritical Fluids 51 (2009) 248–255.
[36] A. Tenorio, P. Jaeger, M.D. Gordillo, C.M. Pereyra, E.J. Martínez de la Ossa, On the selection of limiting hydrodynamic conditions for the supercritical antisolvent (SAS) process, Industrial and Engineering Chemistry Research 48 (2009) 9224–9232.
[37] G. Musie, M. Wei, B. Subramaniam, D.H. Busch, Catalytic oxidations in carbon dioxide-based media, including novel CO_2-expanded phases, Coordination Chemistry Reviews 789 (2001) 219–221.
[38] R. Glässer, J. Williardt, D. Bush, M.J. Lazzaroni, C.A. Eckert, Application of high-pressure phase equilibria to the selective oxidation of alcohols over supported platinum catalysts in supercritical carbon dioxide, in: C.-J. Liu, R.G. Mallinson, M. Aresta (Eds.), Utilization of Greenhouse Gases, American Chemical Society, Washington, DC, 2003, pp. 352–364.

J. Chem. Thermodynamics xxx (2012) xxx–xxx

Contents lists available at SciVerse ScienceDirect

J. Chem. Thermodynamics

journal homepage: www.elsevier.com/locate/jct

Excess molar enthalpies for mixtures of supercritical CO_2 and ethyl acetate and their role in supercritical fluid applications

Fouad Zahran, Concepción Pando *, Juan A.R. Renuncio, Albertina Cabañas

Dpto. de Química Física I, Universidad Complutense, E-28040 Madrid, Spain

ARTICLE INFO

Article history:
Received 20 July 2011
Received in revised form 30 January 2012
Accepted 3 February 2012
Available online xxxx

Keywords:
Supercritical carbon dioxide
Ethyl acetate
Excess molar enthalpies
Carbon dioxide-expanded solvent
Supercritical antisolvent precipitation

ABSTRACT

Mixtures of supercritical CO_2 and ethyl acetate (EA) are very often involved in supercritical fluid applications and their thermodynamic properties are required to understand and design these processes. Excess molar enthalpies (H^E_m) for (CO_2 + EA) mixtures were measured using an isothermal high-pressure flow calorimeter under conditions of temperature and pressure typically used in supercritical processes: pressures from (9.00 to 18.00) MPa and temperatures from (313.15 to 333.15) K. Mixtures showed exothermic mixing; excess molar enthalpies exhibited a minimum in the CO_2-rich region. The effects of pressure and temperature on the excess molar enthalpy of (CO_2 + EA) are large. The most exothermic H^E_m values were observed for a coincident CO_2 mole fraction value of 0.737 at T/K = (323.15 and 333.15) and P/MPa = 9.00: (−4489 and −4407) J · mol^{-1}, respectively. Two-phase splitting was observed in the CO_2-rich region at T/K = 333.15 and P/MPa = 9.00; in this region H^E_m varies linearly with CO_2 mole fraction. For a given mole fraction and temperature, mixtures become more exothermic as pressure decreases. These trends were analyzed in terms of molecular interactions, phase equilibria, density and critical parameters previously reported for (CO_2 + EA). Excess molar enthalpies here reported were correlated using the Soave–Redlich–Kwong and Peng–Robinson equations of state, and the classical mixing rule with two binary interaction parameters. The influence of the thermal effects on the phase behavior of (CO_2 + EA) mixtures formed in supercritical antisolvent precipitation experiments was discussed.

1. Introduction

The mixtures formed by supercritical carbon dioxide and organic solvents such as ethyl ethanoate (ethyl acetate, EA) have received considerable attention in the recent past due to the advantages of CO_2 over conventional organic solvents and its numerous technological applications. Carbon dioxide is the most commonly used supercritical fluid since it is non-toxic, low cost, non-flammable and allows operation at low temperatures and moderate pressures (T_c = 304.1 K, P_c = 7.38 MPa [1]). Mixtures formed by supercritical CO_2 and EA are used in the micronization of solutes such as polymers, pharmaceuticals, superconductors, explosives and colorants. The so-called supercritical antisolvent precipitation (SAS) [2–5] is a well established technique based on using supercritical carbon dioxide as an anti-solvent to induce controlled precipitation of solutes from their organic solvent solutions. Thanks to the relatively low solvent power of CO_2 for these solutes and its good miscibility with many organic solvents, when the supercritical fluid dissolves in the organic solvent the liquid experiences a volumetric expansion and becomes a bad solvent for the solute that precipitates from the solution in micro and nanoparticles. Using this technique, Miguel *et al.* [6] and De Zordi *et al.* [7] have recently recrystallized lutein and piroxicam from their ethyl acetate solutions and Chen *et al.* [8] have precipitated 3,5-diprenyl-4-hydroxycinnamic acid from the ethyl acetate solutions of Brazilian propolis. (CO_2 + EA) mixtures are also involved in other supercritical or near critical crystallization processes such as the gas antisolvent (GAS) and the Depressurization of an Expanded Liquid Organic Solution (DELOS) techniques [9,10]. On the other hand, CO_2-expanded EA is also used as reaction media [11,12].

The physical and thermodynamic properties of the (CO_2 + organic solvent) mixtures are required to understand and design these supercritical fluid applications. Consequently, the high-pressure density and phase behavior, and the volumetric expansion of (CO_2 + EA) mixtures have received considerable attention in the last years [13–22]. However, no much attention has been paid to the heat evolved when supercritical CO_2 dissolves into the organic

Abbreviations: EA, ethyl acetate; DMSO, dimethylsulfoxide; SAS, supercritical antisolvent precipitation; GAS, gas antisolvent; DELOS, Depressurization of an Expanded Liquid Organic Solution; VLE, (vapor + liquid) equilibrium; SRK, Soave–Redlich–Kwong; PR, Peng–Robinson.

* Corresponding author. Address: Departamento de Química Física I, Facultad C. Químicas, Universidad Complutense, E-28040 Madrid, Spain. Tel.: +34 91394 4304; fax: +34 91394 4135.

E-mail address: pando@quim.ucm.es (C. Pando).

0021-9614/$ - see front matter © 2012 Published by Elsevier Ltd.
doi:10.1016/j.jct.2012.02.034

solvent. To the best of our knowledge, the excess molar enthalpies (H^E_m) for the (CO_2 + EA) mixtures have not been reported so far. H^E_m values at the conditions of temperature and pressure typically used in supercritical fluid applications can be quite high. Thus, thermal effects during these processes have an effect on the phase separation path and must be considered in order to optimize precipitation and reaction conditions. In this paper, we report excess molar enthalpies for the binary system (CO_2 + EA) under the following conditions of temperature and pressure: T/K = (313.15 and 323.15) and P/MPa = (9.00, 12.00, 15.00, and 18.00) as well as T/K = 333.15 and P/MPa = (9.00 and 15.00). Under these conditions carbon dioxide is a supercritical fluid that is mixed with the liquid ethyl acetate (T_c = 523.2 K, P_c = 3.83 MPa [1]). Depending upon temperature, pressure and mole fraction, the resulting mixtures may be liquid, fluid or a liquid and a vapor mixture in equilibrium. The excess enthalpy data for mixtures of CO_2 and EA will be analyzed in terms of molecular interactions, phase equilibria and density data, and critical parameters. The influence of these thermal effects on the phase behavior of mixtures formed in the precipitation chamber in SAS experiments will be examined.

2. Experimental

The materials employed were CO_2 (Air Liquide, mole fraction 0.9998) and ethyl ethanoate (Sigma–Aldrich, mole fraction ⩾ 0.999). Commercial materials were used without further purification.

An isothermal high-pressure flow calorimeter (Hart Scientific model 7501) was used to perform H^E_m measurements. The calorimeter was first described by Christensen *et al.* [23] and the experimental procedure is described elsewhere [24]. The reactants were pumped into the calorimetric cell by two thermostated syringe pumps (model: LC-2600, ISCO) at constant flow rates. Temperature of the pumps was controlled within ±0.02 K. Volume flow rates were selected to cover the entire concentration range. For each pump, the uncertainty in the volume flow rate was obtained by a previous calibration. The flow rate stability was ±1% over the total volume of the cylinder. The calorimetric cell was located into a silicon bath in which temperature was controlled within ±0.001 K. A Peltier cooling device and a pulsed heater kept the cell under isothermal conditions. The pulse energy was determined by a previous heater calibration based on the Joule effect. The pressure was measured using a calibrated pressure transducer (Lucas Schaevitz, model P721-0001). A back-pressure regulator located outside the calorimeter kept the pressure within ±0.01 MPa.

All runs were made in the steady-state fixed composition mode. Measurements at all the P and T conditions studied were carried out at total volume flow rates of (0.0014 and 0.0028) $cm^3 \cdot s^{-1}$. The CO_2 mole fraction range is covered by combining adequate values for the flow rates of the two pumps at these total volume flow rates. Also, the coincidence within the experimental error of results obtained using different total flow rates is an indication of equilibrium conditions in the calorimeter. The volume flow rates were converted to molar flow rates using the densities and molar masses. CO_2 densities at the temperature and pressure of the pumps were obtained from NIST webbook [25]. EA densities were obtained from the Tait equation provided by Smith *et al.* [16]. Since densities are affected by temperature and pressure changes, the error in molar flow rates was derived taking into account contributions from variations in volume flow rates, pressure, and pumps temperature. The mole fraction precision is based on the error in molar flow rates and was estimated to be better than ±0.001. The error in H^E_m was obtained taking into account contributions from molar flow rates, pulse energy and frequency and was estimated to be ±0.01 $|H^E_m|$ J · mol^{-1}. Periodically, H^E_m values obtained using this calorimeter for the {ethanol (1) + H_2O (2)} system at 323.15 K and 15.00 MPa were compared to those previously reported by Ott *et al.* [26]. This set of data has been proposed as a reference for isothermal dilution and flow calorimeters [27].

3. Results and discussion

H^E_m data for the binary system {CO_2 (1) + EA (2)} were determined at T/K = (313.15 and 323.15) and P/MPa = (9.00, 12.00, 15.00, and 18.00) as well as at T/K = 333.15 and P/MPa = (9.00 and 15.00) over the entire composition range and are given in table 1. Figures 1 to 3 show plots of H^E_m *vs* CO_2 mole fraction at T/K = (313.15, 323.15, and 333.15), respectively. For comparison

TABLE 1
Excess molar enthalpy, H^E_m, for the binary system {CO_2 (1) + EA (2)}.[a]

x_1	H^E_m/(J · mol^{-1})	x_1	H^E_m/(J · mol^{-1})	x_1	H^E_m/(J · mol^{-1})
T = 313.15 K and P = 9.00 MPa					
0.087	−453	0.462	−2196	0.814	−2983
0.172	−947	0.542	−2524	0.889	−2660
0.256	−1361	0.660	−2861	0.926	−2262
0.381	−1924	0.737	−3042	0.963	−1584
T = 313.15 K and P = 12.00 MPa					
0.123	−419	0.519	−1288	0.806	−1265
0.235	−776	0.599	−1368	0.866	−1099
0.338	−1015	0.673	−1403	0.949	−669
0.432	−1166	0.742	−1349	0.975	−371
T = 313.15 K and P = 15.00 MPa					
0.132	−362	0.539	−1148	0.818	−948
0.250	−632	0.618	−1194	0.875	−762
0.356	−871	0.724	−1151	0.927	−518
0.452	−1013	0.788	−1023	0.953	−375
T = 313.15 K and P = 18.00 MPa					
0.071	−258	0.463	−938	0.825	−754
0.137	−424	0.550	−990	0.880	−607
0.259	−693	0.629	−1005	0.931	−414
0.367	−843	0.700	−942	0.955	−312
T = 323.15 K and P = 9.00 MPa					
0.087	−881	0.502	−3724	0.814	−4313
0.172	−1586	0.582	−4136	0.889	−3349
0.256	−2202	0.660	−4455	0.926	−2290
0.421	−3338	0.737	−4489	0.963	−1153
T = 323.15 K and P = 12.00 MPa					
0.123	−640	0.559	−1986	0.866	−1691
0.235	−1136	0.636	−2047	0.922	−1373
0.338	−1486	0.742	−2044	0.949	−1133
0.432	−1737	0.806	−1902	0.975	−651
T = 323.15 K and P = 15.00 MPa					
0.132	−454	0.539	−1281	0.818	−1192
0.250	−730	0.655	−1357	0.875	−1046
0.369	−987	0.724	−1341	0.927	−734
0.452	−1141	0.757	−1315	0.953	−553
T = 323.15 K and P = 18.00 MPa					
0.071	−282	0.550	−1090	0.880	−768
0.137	−456	0.629	−1147	0.931	−518
0.259	−713	0.70	−1117	0.955	−387
0.367	−899	0.796	−1005		
0.463	−1008	0.853	−843		
T = 333.15 K and P = 9.00 MPa					
0.087	−863	0.421	−3609	0.814	−4150
0.172	−1798	0.542	−4148	0.889	−3388
0.257	−2551	0.660	−4356	0.926	−2228
0.339	−3119	0.737	−4407	0.963	−1077
T = 333.15 K and P = 15.00 MPa					
0.132	−565	0.539	−1560	0.818	−1574
0.250	−949	0.618	−1656	0.875	−1337
0.356	−1244	0.690	−1705	0.927	−942
0.452	−1433	0.757	−1679	0.953	−756

[a] Standard uncertainties u are $u(T)$ = 0.001 K, $u(P)$ = 0.01 MPa, $u(x)$ = 0.001 and $u(H^E_m)$ = 0.01 | H^E_m |.

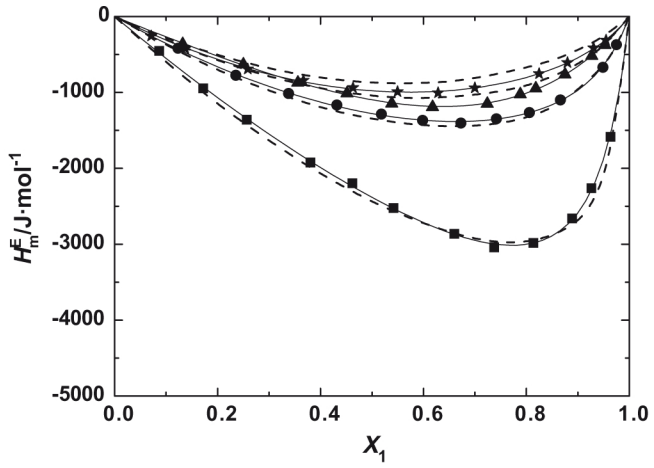

FIGURE 1. Excess molar enthalpies, H^E_m, for the binary system {CO_2 (1) + EA (2)} at T/K = 313.15 and pressures of: ■, 9.00 MPa; ●, 12.00 MPa; ▲, 15.00 MPa; ★, 18.00 MPa; —, calculated using equation (3) and coefficients given in table 2; ---, calculated using the Soave–Redlich–Kwong equation of state [30].

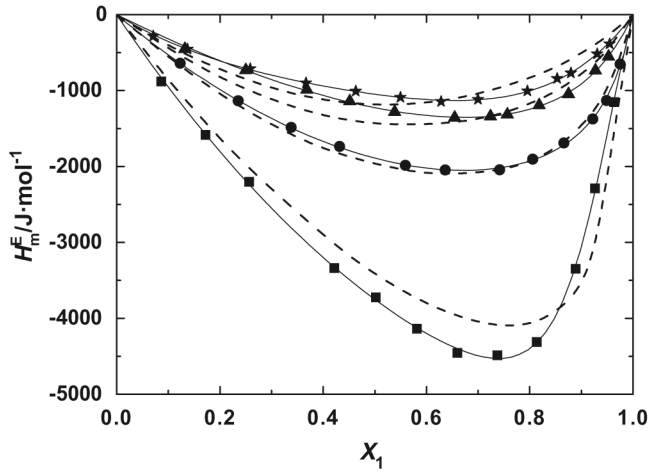

FIGURE 2. Excess molar enthalpies, H^E_m, for the binary system {CO_2 (1) + EA (2) at T/K = 323.15 and pressures of: ■, 9.00 MPa; ●, 12.00 MPa; ▲, 15.00 MPa; ★, 18.00 MPa; —, calculated using equation (3) and coefficients given in table 2; ---, calculated using the Soave–Redlich–Kwong equation of state [30].

purposes the same scale has been used for H^E_m in figures 1 to 3. Mixtures always showed exothermic mixing. For a given mole fraction and temperature, mixtures become increasingly exothermic as the pressure decreases. At each condition of temperature and pressure, excess molar enthalpies exhibit a minimum in the CO_2-rich region. For a given mole fraction and pressure, as the temperature increases from (313.15 to 323.15) K mixtures show more exothermic mixing. However, H^E_m values are slightly affected when temperature increases from (323.15 to 333.15) K at a given mole fraction and pressure. The most exothermic H^E_m values were observed at P/MPa = 9.00 and T/K = (323.15 and 333.15). Minimum values of (−4489 and −4407) J · mol^{-1} are reached, respectively, at these two temperatures for mixtures with a coincident CO_2 mole fraction value of 0.737. On the other hand, a linear section is observed in the H^E_m *vs* CO_2 mole fraction plot at P/MPa = 9.00 and T/K = 333.15 for $x_1 \geqslant 0.889$. H^E_m varies linearly with CO_2 mole fraction due to the appearance of a two-phase region where a gaseous and a liquid mixture of fixed compositions, for a given condition of temperature and pressure, are in equilibrium. For a mixture of global composition x_1, the enthalpy effect in the two-phase region

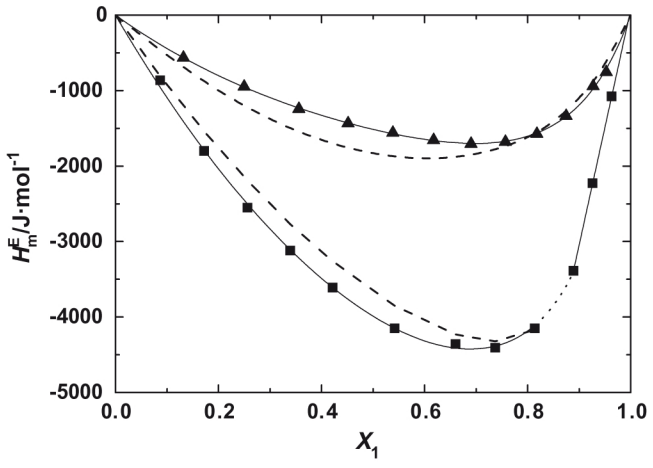

FIGURE 3. Excess molar enthalpies, H^E_m, for the binary system {CO_2 (1) + EA (2)} at T/K = 333.15 and pressures of: ■, 9.00 MPa; ▲, 15.00 MPa; —, calculated using equation (3) and coefficients given in table 2; ---, calculated using the Soave–Redlich–Kwong equation of state [30].

is the sum of two contributions due to the n_l mol of liquid mixture of CO_2 composition x_l and n_v mol of vapor mixture of CO_2 composition x_v,

$$H^E_m = H^E_{m,l} n_l + H^E_{m,v} n_v, \quad (1)$$

where $H^E_{m,l}$ is the excess molar enthalpy of the liquid mixture and $H^E_{m,v}$ is the excess molar enthalpy of the vapor mixture. Equation (1) may be rewritten as [24]

$$H^E_m = H^E_{m,v} + \frac{x_1 - x_v}{x_l - x_v}(H^E_{m,l} - H^E_{m,v}). \quad (2)$$

Since $H^E_{m,l}$, $H^E_{m,v}$, x_l and x_v have constant values for each isotherm, the second member of equation (2) is a first-degree polynomial in x_1. When $x_1 = x_l$, $H^E_m = H^E_{m,l}$ and when $x_1 = x_v$, $H^E_m = H^E_{m,v}$. Therefore, the liquid and vapor-phase compositions are shown to correspond to the x coordinates of the beginning and the end of the linear section shown in figure 3. A considerable amount of EA may be present in the liquid mixture but only a very small amount is dissolved in the vapor phase; the CO_2 vapor-phase composition is very close to one and cannot be established from the calorimetric measurements.

H^E_m data for {CO_2 (1) + EA (2)} were fitted to a (n,m) Padé function given by

$$H^E_m/\mathrm{J\cdot mol^{-1}} = x_1(1-x_1)\frac{\sum_{i=0}^{n} A_i(2x_1-1)^i}{1+\sum_{j=1}^{m} B_j(2x_1-1)^j}, \quad (3)$$

where A_i and B_j are adjustable coefficients. A least-square procedure was used to minimize deviations between experimental and calculated excess molar enthalpies. For those conditions of temperature and pressure where phase-splitting occurs, two different sets of coefficients are used to represent data in the two-phase and one-phase region, respectively. In the linear section, a (1,2) Padé function with fixed values for the denominator coefficients, $B_1 = 0$ and $B_2 = -1$, may be used in order to keep the weight factor $x_1(1 - x_1)$. This results in a first-degree polynomial in the composition variable; the slope is $A_1/2$ and the zero intercept is $(A_0 - A_1)/4$. The H^E_m representation using equation (3) is shown in figures 1 to 3. Table 2 lists values for the coefficients A_i and B_j and the standard deviation between experimental and calculated H^E_m values. A value of 0.88 was determined for the CO_2 liquid-phase composition from the intersection of the two correlation functions describing the excess enthalpies in terms of mole fraction in the two-phase and the

Please cite this article in press as: F. Zahran et al., J. Chem. Thermodyn. (2012), doi:10.1016/j.jct.2012.02.034

TABLE 2
Coefficients A_i and B_j and standard deviation,[a] , for least-squares representation of H^E_m for {CO_2 (1) + EA (2) at T/K = (313.15, 323.15, and 333.15) using equation (3).

T/K	P/MPa	Interval	A_0	A_1	A_2	B_1	B_2	σ/(J · mol^{-1})
313.15	9.00	$0 \leqslant x_1 \leqslant 1$	−9528.7	884.04	−198.31	−0.86070	0	7.3
	12.00	$0 \leqslant x_1 \leqslant 1$	−5114.2	1789.8	0	−0.82319	0	3.5
	15.00	$0 \leqslant x_1 \leqslant 1$	−4386.4	−470.50	0	−0.43247	0	3.2
	18.00	$0 \leqslant x_1 \leqslant 1$	−3913.4	2163.9	0	−0.79778	0	3.9
323.15	9.00	$0 \leqslant x_1 \leqslant 1$	−15003	−17974	−5653.0	−1.8692	0.96932	10
	12.00	$0 \leqslant x_1 \leqslant 1$	−7560.7	3081.1	0	−0.87691	0	5.2
	15.00	$0 \leqslant x_1 \leqslant 1$	−4902.9	930.50	0	−0.73669	0	4.3
	18.00	$0 \leqslant x_1 \leqslant 1$	−4195.5	−704.97	−1787.1	−0.26853	0	3.6
333.15	9.00	$0 \leqslant x_1 \leqslant 0.88$[a]	−15947	−12825	7772.0	−0.30466	−1.0901	10
		0.88[a] $\leqslant x_1 \leqslant 1$	−62015	62294	0	0	−1	0.1
	15.00	$0 \leqslant x_1 \leqslant 1$	−6055.4	721.63	−1352.5	−0.65253	0	5.1

[a] Standard uncertainty of the liquid phase composition in the two-phase region $u(x) = 0.01$.

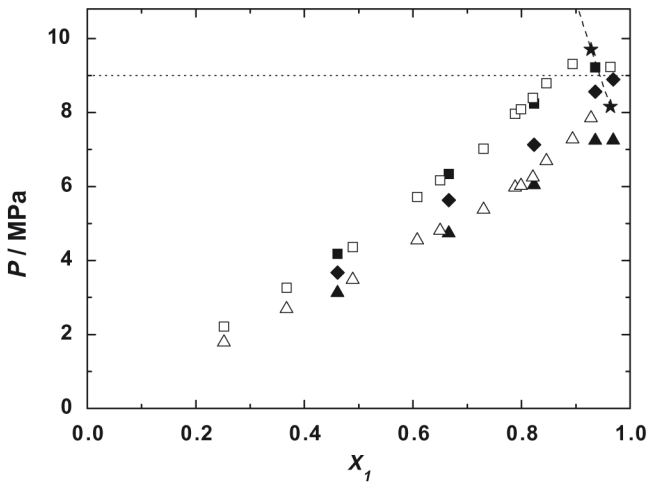

FIGURE 4. Isothermal (vapor + liquid) equilibrium for the binary system {CO_2 (1) + EA (2)} reported by Byun *et al.* [19] (Δ, 313.15 K; □, 333.15 K) and Borges *et al.* [21] (▲, 313.15 K; ♦, 323.15 K; ■, 333.15 K), pressure condition of H^E_m measurements (···), and critical line (---) based on critical data reported by Byun *et al.* [19] (★).

one-phase sections at T/K = 333.15 and P/MPa = 9.00. This value indicates the beginning of the linear section shown in table 2.

Figure 4 shows the isothermal (vapor + liquid) equilibria (VLE) and critical data reported by Byun *et al.* [19] and Borges *et al.* [21] for {CO_2 (1) + EA (2)}. There is good agreement between the VLE data taken by these authors and data previously reported by Chrisochoou *et al.* [14], Kordikowski *et al.* [15], Tian *et al.* [18] and Kato *et al.* [20]. Data reported by Wagner and Pavlícek [13] and da Silva *et al.* [17] disagree with those obtained by the other authors. For the sake of clarity, we have chosen the data recently reported by Byun *et al.* and Borges *et al.* to represent the VLE data at (313.15, 323.15, and 333.15) K. On the other hand, Byun et al. also reported critical parameters for (CO_2 + EA). The value obtained for the liquid phase composition at T/K = 333.15 and P/MPa = 9.00 is in agreement with the VLE data shown in figure 4. According to these data, a two-phase region confined to x_1 values close to one should have been also observed at T/K = 323.15 and P/MPa = 9.00. Usually, the beginning of the two-phase region is denoted by an abrupt change in the curvature of the H^E_m *vs* x_1 plot as those observed for the {CO_2 (1) + *N*,*N*-dimethylformamide (2)} at T/K = (332.15, 333.15) and P/MPa = 9.00 [28]. This change does not appear at T/K = 323.15 and P/MPa = 9.00 and a two-phase region cannot be established from calorimetric measurements at these conditions of temperature and pressure.

The excess molar enthalpies of {CO_2 (1) + EA (2)} were also calculated using the Soave–Redlich–Kwong (SRK) [29] and Peng–Robinson (PR) equations of state [30]. The excess molar enthalpy for a binary mixture is given by

$$H^E_m = H^R_m(\text{mixture}) - \sum_i x_i H^R_{m,i}, \tag{4}$$

where H^R_m is the residual molar enthalpy of the mixture and $H^R_{m,i}$ is that of the pure components. The residual molar enthalpy is given by

$$H^R_m = RT(z-1) + \int_\infty^V \left[T\left(\frac{\partial P}{\partial T}\right)_V - P \right] dV, \tag{5}$$

where z is the compressibility factor. The equation-of state parameters a and b were evaluated for the mixtures using the classical mixing rule given by the equations:

$$a = \sum_i \sum_j x_i x_j a_{ij}; \quad a_{ij} = (a_{ii}a_{jj})^{1/2}(1-k_{ij})$$
$$b = \sum_i \sum_j x_i x_j b_{ij}; \quad b_{ij} = \frac{(b_{ii}+b_{jj})}{2}(1-\delta_{ij}), \tag{6}$$

where $k_{ij} = k_{ji}$ and $\delta_{ij} = \delta_{ij}$ are binary interaction parameters. Values for the pure component parameters a and b were calculated using the acentric factor and the critical constants values given by Poling *et al.* [1]. H^E_m data taken in the one-phase region at each of the three temperatures considered were simultaneously correlated using equations (4)–(6). As was already discussed in Section 2, the uncertainties in temperature, pressure and composition are smaller than those of the excess molar enthalpies and a least square-procedure was used to minimize relative deviations between experimental and calculated H^E_m. Table 3 lists values adopted by the binary interaction parameters k_{12} and δ_{12} and values for the standard deviation between experimental and calculated binary excess enthalpies, σ, for each condition of temperature and pressure. Both the SRK and the PR correlate satisfactorily the excess molar enthalpies. Since most σ values are slightly lower for the SRK equation, results shown in figures 1 to 3 were obtained using this equation of state.

The large effects of pressure and temperature on the excess molar enthalpy values are related to changes in the state and densities of the pure components and their mixtures. The critical data reported by Byun *et al.* [19] for the (CO_2 + EA) system up to T/K = 373.15 and all the high-pressure phase equilibria data [13–15,17–21] point out a type I diagram in the classification of Scott and van Konynenburg [31]. Figure 5 shows the *P*, *T* projection of (CO_2 + EA) critical locus based on Byun *et al.* data and the conditions of temperature and pressure for the experimental H^E_m data reported in this paper. The state of the mixtures formed in the calorimeter (liquid, fluid, two-phase) may be established using this figure and taking into account the critical composition and

TABLE 3
Densities of carbon dioxide and EA, estimated temperature increments in the SAS precipitation chamber, and binary parameters k_{12} and δ_{12} and standard deviation between experimental and calculated excess enthalpies, σ, for the {CO_2 (1) + EA (2)} correlation of H^E_m using the SRK and PR equations of state.

T/K	P/MPa	ρ/(g · cm^{-3})		ΔT/K[c]	SRK			PR		
		CO_2[a]	EA[b]		k_{12}	δ_{12}	σ/(J · mol^{-1})	k_{12}	δ_{12}	σ/(J · mol^{-1})
313.15	9	0.4855	0.9356	7.1	0.0745	0.0658	120	0.0783	0.0688	130
	12	0.7178	0.9375	3.4			57			55
	15	0.7802	0.9394	3.2			61			66
	18	0.8195	0.9412	3.1			76			83
323.15	9	0.2850	0.9263	8.3	0.1291	0.1166	250	0.1273	0.1154	260
	12	0.5847	0.9283	6.7			70			70
	15	0.6998	0.9303	4.3			160			150
	18	0.7571	0.9322	3.4			130			130
333.15	9	0.2354	0.9171	13	0.1239	0.1190	210	0.1211	0.1174	220
	15	0.6041	0.9212	5.0			190			190

[a] Reference [25]. Standard uncertainty $u(\rho) = 0.00005$ g · cm^{-3}.
[b] Reference [16]. Standard uncertainty $u(\rho) = 0.00005$ g · cm^{-3}.
[c] For a mixture with $x_1 = 0.95$.

vapor-liquid equilibrium data. At the conditions of H^E_m measurements, EA is a liquid and its density does not change to a great extent with temperature and pressure [16]. However, carbon dioxide may be either a high-density (liquid-like) fluid or a low-density (gas-like) fluid. Densities of both components are listed in table 3. When carbon dioxide and EA are mixed at T/K = 313.15 and pressures greater than 9.00 MPa, carbon dioxide is a liquid-like fluid and the resulting mixtures are mostly liquid. Critical data indicate that fluid mixtures are confined to a very narrow mole fraction range where $x_1 > 0.964$. H^E_m values are moderately exothermic. The change-of state contribution to H^E_m is small and excess molar enthalpy values may be considered mainly the result of the molecular interaction contribution to H^E_m. EA presents a solvent structure dominated by dipole–dipole interactions (μ = 1.9 D [1]) that is disrupted upon mixing with carbon dioxide leading to an endothermic contribution to H^E_m. Moderately exothermic enthalpies are the result of a balance between the endothermic contribution and an exothermic one due to strong EA–CO_2 interactions. Aida *et al.* [22] carried out molecular dynamics simulations and found that the EA carbonyl atom attracts very strongly CO_2 molecules. The molecular interaction contribution to H^E_m may be expected to change only slightly with temperature and pressure in the intervals considered in this study. Mixing at T/K = 313.15 and P/MPa = 9.00 becomes considerably more exothermic as a result of combining a gas-like carbon dioxide with a liquid EA to obtain liquid mixtures. The contribution to H^E_m due to intermolecular interactions is combined with another exothermic contribution due to the CO_2 change of state from that of a gas-like fluid to that of liquid mixture component. This fluid condensation effect is even more pronounced at a temperature of (323.15 or 333.15) K and a pressure of 9.00 MPa when EA is mixed with a fluid of very low density and the resulting mixtures are a liquid or a gaseous and a liquid mixture in equilibrium. Fluid mixtures are also confined to a narrow mole fraction range at these conditions of temperature and pressure. Minimum values of (−4489 and −4407) J · mol^{-1} are reached for $x_1 = 0.737$ at P/MPa = 9.00 MPa and T/K = (323.15 and 333.15), respectively. As the pressure is increased from (9.00 to 18.00) MPa at a temperature of (323.15 or 333.15) K, carbon dioxide density increases reaching values typical of a liquid and mixing becomes much less exothermic than that observed at the same temperature and P/MPa = 9.00.

Similar values of H^E_m and similar trends for the variation of this magnitude with mole fraction, temperature, and pressure were observed for other (CO_2 + organic solvent) mixtures previously studied at our laboratory [24,28,32,33] under conditions of temperature and pressure typically used in supercritical CO_2 applications. The solvents considered were *N*-methyl-2-pyrrolidone, *N*,*N*-dimethylformamide, acetone and dimethylsulfoxide. The variations observed may be attributed to the type of critical diagram and differences in intermolecular interactions. However, the magnitude of the fluid condensation contribution may be expected to be similar for the different solvents at a given temperature and pressure.

Several authors [4–6,34–37] have pointed out that the phase behavior of (CO_2 + organic solvent) is one of the crucial factors governing the morphology and the mean size of particles obtained in the SAS process. The presence of the solute can induce modifications in the phase diagram. This is the case of polymers; however, when the solute has little interaction with carbon dioxide the ternary phase diagram for the low solute concentrations usually employed in SAS is coincident with the binary one in the CO_2-rich region which is the region for mixtures involved in SAS [35]. Therefore, the mixtures formed in the precipitation chamber may be treated as binary (CO_2 + organic solvent) systems. In general, nanoparticles are obtained when the precipitation is carried out in the supercritical region. The uniformity of the resulting products becomes worse when the precipitation conditions approach the critical locus. Irregular micro-scale aggregated particles are formed in the vapor region and both dense cake and spherical clusters are produced in the vapor–liquid region [5,6,34–37]. The heat evolved when the supercritical CO_2 dissolves into the organic solution has an important role in the phase behavior. Typically, 500 cm^3 precipitation chambers are used and there is not stirring throughout the experiment. The temperature control in these chambers is not very precise and a local temperature increase may be expected. As a consequence T and P conditions are reached where phase splitting takes place. Since CO_2 is fed into the chamber at a flow rate much higher than that of the solution and the solute concentration is very low, the contribution to H^E_m due to solute interactions may be neglected and the thermal effect in SAS experiments can be considered mainly due to the formation of (CO_2 + EA) mixtures very rich in carbon dioxide ($x_1 \geqslant 0.95$). Consequently, the temperature increase ΔT may be estimated using the H^E_m data reported in this paper. Since carbon dioxide is the predominant component in these mixtures, its isobaric heat capacity [38] was used to calculate the local temperature increase assuming an adiabatic process and using equation (3) to evaluate the heat evolved when a mol of mixture of composition $x_1 = 0.95$ is formed. Values for ΔT thus obtained are shown in table 3. An examination of these values together with literature vapor-liquid equilibrium data shown in figure 4 indicates how the heat evolved upon mixing affects the phase behavior. For instance, at $x_1 = 0.95$, P/MPa = 9.00 and

Please cite this article in press as: F. Zahran et al., J. Chem. Thermodyn. (2012), doi:10.1016/j.jct.2012.02.034

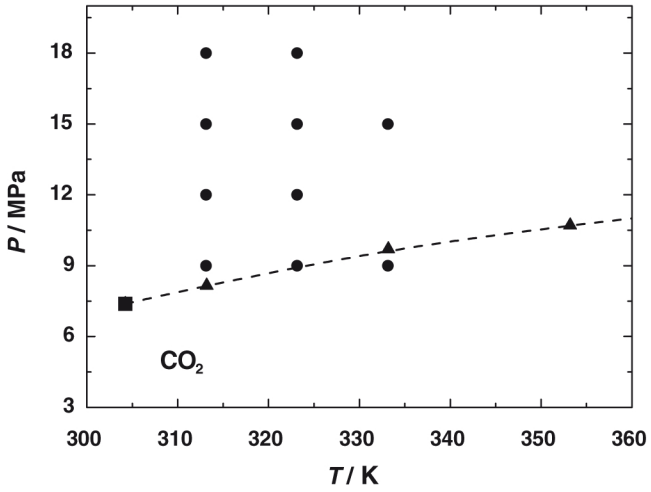

FIGURE 5. *P*, *T* projection of the {CO_2 (1) + EA (2)} critical curve showing the critical point of carbon dioxide, ■; ---, locus based on data reported by Byun *et al.* [19], ▲, and the (*P*, *T*) coordinates where experimental data were taken, •.

T/K = 313.15 or 323.15 carbon dioxide and EA are completely miscible. However, a 8.3 K local temperature increase at *T*/K = 323.15 and *P*/MPa = 9.00 would induce immiscibility because the new isotherm is close to that shown in figure 4 at *T*/K = 333.15 K. The 7.1 K local temperature increase at *T*/K = 313.15 and *P*/MPa = 9.00 would approach precipitation conditions to the critical locus or even induce immiscibility for the CO_2-rich mixtures formed in the SAS experiments. In both cases the particle morphology would not correspond to that expected in a supercritical phase.

The enthalpy effect on the phase equilibria has been clearly shown in SAS micronizations using dimethylsulfoxide (DMSO) as the polar solvent. Reverchon *et al.* [34] precipitated YAc from its DMSO solutions using CO_2 as the antisolvent agent at (313.15, 323.15, and 333.15) K, x_1 = 0.98 and pressures up to 16.0 MPa. A windowed vessel was used to observe the phase behavior of the {CO_2 (1) + DMSO (2)} mixtures formed in the precipitation chamber. Immiscibility was observed for initial temperature and pressure conditions where one supercritical phase was expected according to the phase equilibria data available for this system. By measuring the excess molar enthalpies for (CO_2 + DMSO) mixtures at these *T* and *P* conditions and carrying out ΔT calculations similar to those above described, we have shown that Reverchon *et al.* phase equilibria observations are a consequence of temperature increases due to the enthalpy effect [33].

4. Conclusions

Excess molar enthalpies for mixtures of supercritical CO_2 and EA were measured under conditions of temperature and pressure typically used in supercritical CO_2 applications: *T*/K = (313.15 and 323.15) and *P*/MPa = (9.00, 12.00, 15.00, and 18.00) as well as *T*/K = 333.15 and *P*/MPa = (9.00 and 15.00). The (CO_2 + EA) system presents immiscibility at *T*/K = 333.15 and *P*/MPa = 9.00 for CO_2-rich mixtures; in this range H^E_m varies linearly with mole fraction due to (vapor + liquid) equilibria.

The effects of pressure and temperature on the excess molar enthalpy are large. H^E_m values are exothermic at all the conditions of temperature and pressure studied and become extremely exothermic when low-density supercritical carbon dioxide is mixed with the liquid EA and the resulting mixture is a liquid or a gaseous and a liquid mixture in equilibrium.

Excess molar enthalpies for (CO_2 + EA) can be correlated using the SRK and PR equations of state and the classical mixing rule with two adjustable binary parameters for each temperature.

Thermal effects in SAS experiments are shown to modify the phase behavior of (CO_2 + EA) mixtures formed in the precipitation chamber thus affecting the morphology of the particles.

Acknowledgements

We gratefully acknowledge the financial support of the Spanish Ministry of Science and Innovation (MICINN), research project CTQ2010-16940. F.Z. thanks the E.U. for its support through an Erasmus Mundus University II predoctoral grant.

References

[1] B.E. Poling, J.M. Prausnitz, J. P. O'Connell, The Properties of Gases and Liquids, fifth ed., McGraw-Hill International Editions, Singapore, 2001.
[2] E. Reverchon, J. Supercrit. Fluids 15 (1999) 1–21.
[3] A. Shariati, C.J. Peters, Curr. Opin. Solid State Mater. Sci. 7 (2003) 371–383.
[4] A. Martín, M.J. Cocero, Adv. Drug Delivery Rev. 60 (2008) 339350.
[5] E. Reverchon, E. Torino, S. Dowy, A. Brauer, A. Leipertz, Chem. Eng. J. 156 (2010) 446–458.
[6] F. Miguel, A. Martín, F. Mattea, M.J. Cocero, Chem. Eng. Process. 47 (2008) 1594–1602.
[7] N. De Zordi, I. Kikic, M. Moneghini, D. Solinas, J. Supercrit. Fluids 55 (2010) 340–347.
[8] C.R. Chen, C.T. Shen, J.J. Wu, H.L. Yang, S.L. Hsu, C.M. Chang, J. Supercrit. Fluids 50 (2009) 176–182.
[9] P. Subra-Paternault, C. Roy, D. Vrel, A. Vega-Gonzalez, C. Domingo, J. Cryst. Growth 309 (2007) 76–85.
[10] S. Sala, E. Elizondo, E. Moreno, T. Calvet, M.A. Cuevas-Diarte, N. Ventosa, J. Veciana, Cryst. Growth Des. 10 (2010) 1226–1232.
[11] M. Wei, G.T. Musie, D.H. Busch, B. Subramaniam, J. Am. Chem. Soc. 124 (2002) 2513–2517.
[12] K. Nishi, Y. Morikawa, R. Misumi, M. Kaminoyama, Chem. Eng. Sci. 60 (2005) 2419–2426.
[13] Z. Wagner, J. Pavlícek, Fluid Phase Equilib. 97 (1994) 119–126.
[14] A. Chrisochoou, K. Schaber, U. Bolz, Fluid Phase Equilib. 108 (1995) 1–14.
[15] A. Kordikowski, A.P. Schenk, R.M. Van Nielen, C.J. Peters, J. Supercrit. Fluids 8 (1995) 205–216.
[16] R.L. Smith, T. Yamaguchi, T. Sato, H. Suzuki, K. Arai, J. Supercrit. Fluids 13 (1998) 29–36.
[17] M.V. da Silva, D. Barbosa, P.O. Ferreira, J. Mendonça, Fluid Phase Equilib. 175 (2000) 19–33.
[18] Y.L. Tian, H.G. Zhu, Y. Xue, Z.H. Liu, L. Yin, J. Chem. Eng. Data 49 (2004) 1554–1559.
[19] H.S. Byun, M.Y. Choi, J.S. Lim, J. Supercrit. Fluids 37 (2006) 323–332.
[20] M. Kato, D. Kodama, M. Sato, K. Sugiyama, J. Chem. Eng. Data 51 (2006) 1031–1034.
[21] G.R. Borges, A. Junges, E. Franceschi, F.C. Corazza, M.L. Corazza, J.V. Oliveira, C. Dariva, J. Chem. Eng. Data 52 (2007) 1437–1441.
[22] T. Aida, T. Aizawa, M. Kanakubo, H. Nanjo, J. Supercrit. Fluids 55 (2010) 56–61.
[23] J.J. Christensen, L.D. Hansen, R.M. Izatt, D.J. Eatough, R.M. Hart, Rev. Sci. Instrum. 47 (1976) 730–734.
[24] M.J. Dávila, A. Cabañas, C. Pando, J. Supercrit. Fluids 42 (2007) 172–179.
[25] NIST Standard Reference Database Number 69, which can be accessed electronically through the NIST Chemistry Web Book (http://webbook.nist.gov/chemistry/).
[26] J.B. Ott, G.V. Cornett, C.E. Stouffer, B.F. Woodfield, C. Guanquan, J.J. Christensen, J. Chem. Thermodyn. 18 (1986) 867–875.
[27] R. Sabbah, A. Xu, J.S. Chickos, M.L. Planas-Leitão, M.V. Roux, L.A. Torres, Thermochim. Acta 331 (1999) 93204.
[28] F. Zahran, C. Pando, A. Cabañas, J.A.R. Renuncio, J. Supercrit. Fluids 55 (2010) 566–572.
[29] D.Y. Peng, D.B. Robinson, Ind. Eng. Chem. Fundam. 15 (1976) 59–64.
[30] G. Soave, Chem. Eng. Sci. 27 (1972) 1197–1203.
[31] R.L. Scott, P.H. van Konynenburg, Discuss. Faraday Soc. 49 (1970) 87–97.
[32] F. Zahran, C. Pando, J.A.R. Renuncio, A. Cabañas, J. Chem. Eng. Data 55 (2010) 3649–3654.
[33] F. Zahran, J. Morère, A. Cabañas, C. Pando, J.A.R. Renuncio, J. Supercrit. Fluids 60 (2011) 45–50.
[34] E. Reverchon, G. Caputo, I. De Marco, Ind. Eng. Chem. Res. 42 (2003) 6406–6414.
[35] E. Reverchon, I. De Marco, E. Torino, J. Supercrit. Fluids 43 (2007) 126–138.
[36] S.C. Chang, M.J. Lee, H.M. Lin, J. Supercrit. Fluids 44 (2008) 219–229.
[37] S.C. Chang, M.J. Lee, H.M. Lin, Chem. Eng. J. 139 (2008) 416–425.
[38] R. Span, W. Wagner, J. Phys. Chem. Ref. Data 25 (1996) 1509–1596.

Please cite this article in press as: F. Zahran et al., J. Chem. Thermodyn. (2012), doi:10.1016/j.jct.2012.02.034

Chapter 5. Supercritical Antisolvent Micronization of Pharmaceuticals

Supercritical Antisolvent Micronization of Pharmaceuticals

Micronization is the process of reducing the average diameter of a solid material particle. Modern methods use supercritical fluids in the micronization process. The most widely applied techniques are the SAS method (Supercritical Anti-Solvent), the RESS process (Rapid Expansion of Supercritical Solutions), and the PGSS method (Particles from Gas Saturated Solutions) that have been previously described (chapter one). In this work we have chosen the SAS method to micronize different pharmaceutical compounds. In the first place, a laboratory scale SAS apparatus was assembled (chapter three). In the next sections the validation of this SAS apparatus is described using a system previously studied in the literature as well as the micronization of some pharmaceutical active ingredients.

5.1. Validation of SAS Apparatus: Micronization of Yttrium Acetate

The micronization of yttrium acetate, YAc, has been chosen to validate our SAS equipment. YAc is widely used in the electrotechnical industry as a precursor for high-temperature superconductors. Reverchon et al. have micronized YAc from yttrium acetate/dimethyl sulfoxide (DMSO) mixtures using supercritical CO_2 as the antisolvent [1-5]. SAS micronization of YAc was performed to improve its properties; submicronic particles act as points of nucleation of the pining centers in the high-temperature superconductors. YAc micronization experiments performed by Reverchon et al. [1-2] were used as a starting point in this work and as a reference for the validation of our equipment. In the first article [1], these authors found that the volumetric expansion of the liquid carrier controls the morphology of the particles produced by SAS, whereas the solution concentration controls the particle size (PS) and particle size distribution (PSD) of the precipitate. Furthermore, YAc nanoparticles were successfully produced by SAS, obtaining mean diameters down to 100 nm. In the second article [2], they confirmed that SAS micronization is a highly versatile process capable of generating particles of various dimensions and morphologies depending on the operating conditions. They also demonstrated that it is possible to obtain microparticles of YAc with mean diameters from 0.28 to 50 μm by simply changing the operating pressure and/or temperature and that the near-critical region can be used to confer larger dimensions and different morphologies to precipitated particles. In reference [3] results obtained previously at 40 °C and 15.0 MPa are compared. In reference [4] attention is focused on the expanded microparticles morphology. Results from previous studies are discussed together with those obtained at temperatures of 43 and 65 °C and a pressure of 15.0 MPa, and at a

temperature of 60 °C and pressures of 12.0, 12.5 and 13.5 MPa. In the most recent paper [5], additional experiments were carried out at 40 °C and several values of pressures for the correlation of fluid dynamics with particle morphology.

As previously pointed out, the prerequisites for a successful SAS precipitation are the high solubility of the organic solvent in the supercritical carbon dioxide (SC-CO_2) as well as the low solubility of the solute to be precipitated in SC-CO_2. When the solvent has high solubility in SC-CO_2, its solvent power for the solute reduces faster in the presence of SC-CO_2. Therefore, supersaturation happens sooner and smaller particles are formed. On other hand, the solute must have a very low solubility in SC-CO_2 at the working conditions in order to avoid the redissolution of the solute by SC-CO_2 and be a good candidate for SAS.

The morphology of the particles obtained by SAS is greatly influenced by the phase diagram of the system. Working at the one-phase supercritical region usually gives uniform particles with a narrow particle size distribution while working at the multiphase region results in particle coalescence and non uniform particles. The presence of a solute, third component, may or may not modify the binary CO_2 + organic solvent system. For example, in the case of dextran that interacts with carbon dioxide the pseudo-binary phase diagram, the ternary phase diagram at low concentration of the solute, differs to a great extent from the binary phase diagram [6]. On the contrary, for ionic solutes such as cefonicid that interact weakly with carbon dioxide the ternary phase diagram for the low solution concentration, usually employed in SAS, is coincident with the binary one in the CO_2-rich region which is the region for mixtures involved in SAS. As was explained in the introduction chapter, Reverchon et al. used a view cell to confirm this coincidence for the CO_2 + DMSO + cefonicid system [3]. The same behavior as cefonicid may be expected for the YAc salt.

As was mentioned in chapter four, Andreatta et al. [7] discussed the type of critical locus for CO_2 + DMSO in the Scott and van Konynenburg classification [8]. According to them, this system belongs either to type III or IV in this classification; more data in the lower temperature range are required to reach a definitive conclusion. This discussion is however irrelevant for the conditions currently used in SAS experiments. To this end, it is enough to consider the vapor-liquid critical line and the isothermal vapor-liquid equilibrium (VLE) data for CO_2 + DMSO shown in Fig. 4.8 of this thesis. Fig 4.8 also shows how the immiscibility region becomes larger as the temperature increases.

These phase equilibria data for the CO_2 + dimethylsulfoxide system were used to understand the different morphologies observed in YAc supercritical antisolvent micronizations. Taking into account the mixture critical line for the binary system CO_2 + DMSO, four different sets of experimental conditions have been chosen to validate our SAS apparatus. The temperature and pressure values for these experiments are listed in table 5.1.

Table 5.1 Temperature and pressure experimental conditions of the SAS micronization of YAc using DMSO.

Experiment	**Conditions**	
	***T* (°C)**	***P* (MPa)**
1	40	11
2	60	14
3	60	15
4	60	20

The other experimental conditions were 2 % concentration for the YAc solution, 1 mL/min solution flow rate, 15 g/min CO_2 flow rate and drying time required to fill 3 times the precipitation chamber. The solution concentration in all the SAS experiments of this thesis is expressed as mass of solute per 100 mL of solution. The nozzle diameter was 100 μm in all the experiments. These solution and CO_2 flow rates lead to a value of 0.96 for the CO_2 mole fraction in the CO_2 + DMSO mixtures formed in the precipitation chamber.

The materials employed were CO_2 (Air Liquide 99.98 mol% pure), DMSO (Fluka, ≥ 99.9 mol % pure) and yttrium (III) acetate hydrate (Aldrich ≥ 99.9 mol % pure). The experiments (1-4) were carried out in the one-phase supercritical region for CO_2 + dimethyl sulfoxide (DMSO). In particular, experiment (2) was carried out very close to the mixture critical point to see the thermal effects in the mixing process between SC-CO_2 and DMSO that takes place in the SAS precipitation chamber. Fig. 5.1 shows the image of the untreated YAc.

Fig. 5.1 Image of untreated YAc.

The SEM images of YAc precipitated in experiments 1-4 are shown in Figs. 5.2 - 5.5. In experiments 1, 3 and 4 discrete nanoparticles with a spherical morphology have been obtained. In some images particles appear slightly aggregated or connected, which is attributed to the incomplete removal of the solvent at the washing step. On the contrary, in experiment 2, aggregated particles forming a block have been found. The different morphology of the precipitate at these conditions will be explained later.

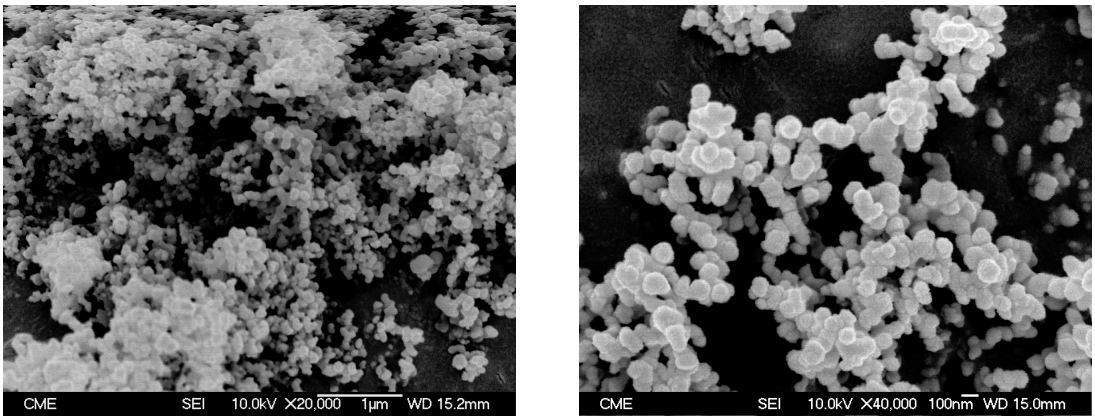

Fig. 5.2 SEM images of the YAc precipitated at 40 °C and 11 MPa (Exp. 1).

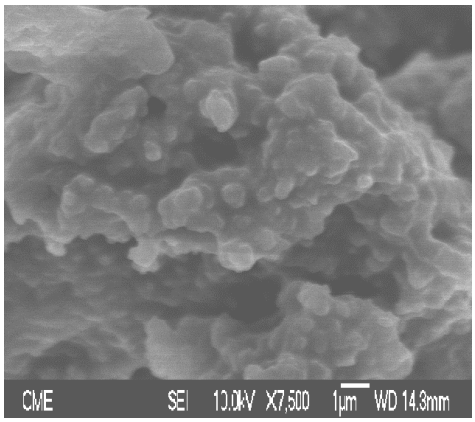

Fig. 5.3 SEM images of the YAc precipitated at 60 °C and 14 MPa (Exp. 2).

A slightly decrease in the mean particle size was observed with the increase of the pressure. This effect can be seen in Fig. 5.4 and Fig 5.5, where the SEM images of the precipitated YAc are shown for the experiments performed at 60 °C and 15 and 20 MPa, respectively.

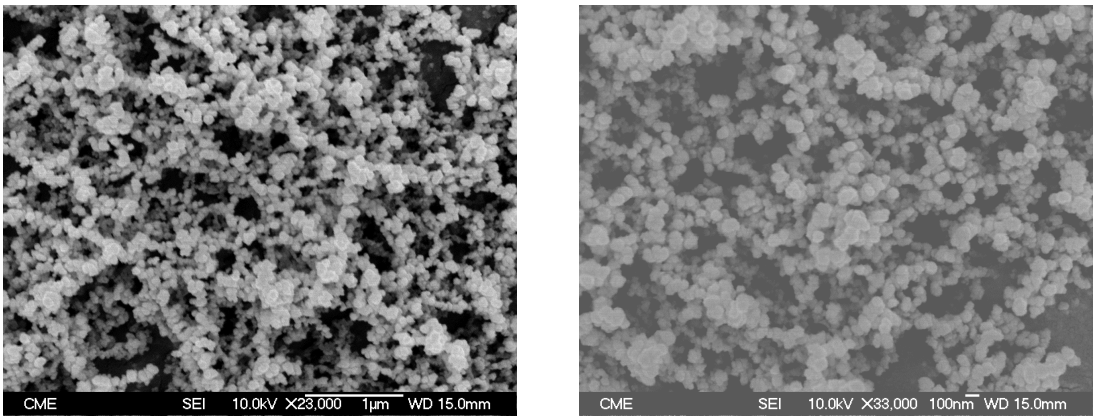

Fig. 5.4 SEM images of the YAc precipitated at 60 °C and 15 MPa (Exp. 3).

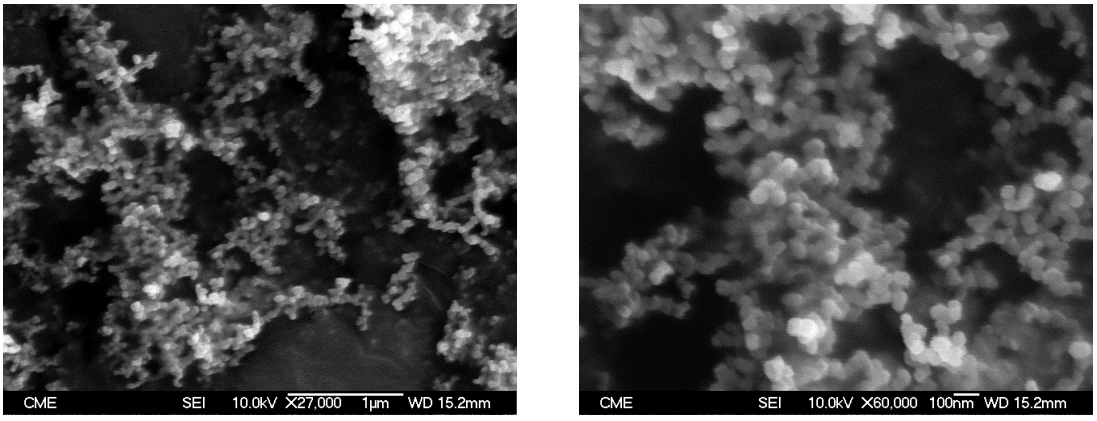

Fig. 5.5 SEM images of the YAc precipitated at 60 °C and 20 MPa (Exp. 4).

Fig. 5.6 shows the mean particle size (PS) and particle size distribution calculated following the procedure described in chapter three. As pointed out, it can be observed how with increasing pressure the particle size and its standard deviation (SD) decrease and the particle size distribution becomes narrower. Particles precipitated in experiment 1 at a lower *T* and *P* yield larger particles with a wider PSD. Our results will be compared to those obtained by Reverchon et al. in 2003 [2] because the conditions of temperature and pressure are the same or very close to those used in our study.

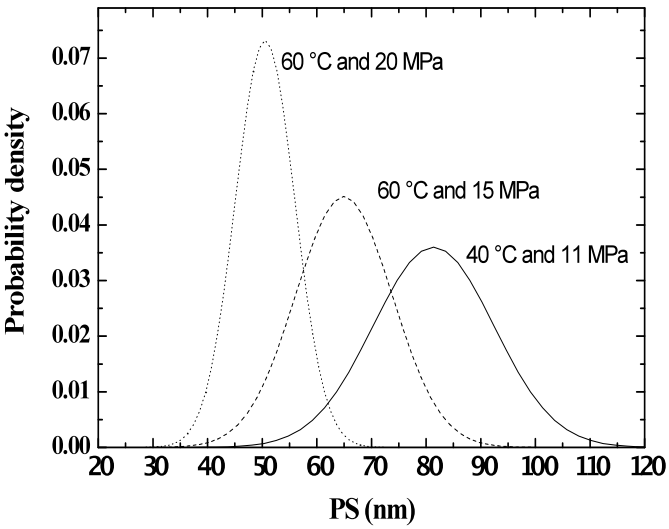

	PS (nm)	SD (nm)
Exp 1	80	11
Exp 2	Aggregation	
Exp 3	65	9
Exp 4	50	5

Fig. 5.6 Probability density as a function of particle size for experiments 1, 3 and 4.

As previously mentioned the other experimental conditions used in this study were: 2 % concentration for the YAc solution, 1 mL/min solution flow rate and 15 g/min CO_2 flow rate. These flow rates lead to a value of 0.96 for the CO_2 mole fraction. The obtained powder is dried at a time equal to 3 times the time required to completely fill the 500 mL precipitation chamber (between 60 and 120 min). All over this study, the nozzle used is always the same and it has a diameter of 100 μm. On the other hand, those of Reverchon et al. [2] were: 1.36 % concentration for the YAc solution, 10 mL/min solution flow rate, 300 g/min CO_2 flow rate, drying time 90 min for a 500 mL precipitator and nozzle diameter of 60 μm. The much larger flow rates used by Reverchon are however not often used in most SAS experiments. These flow rates also lead to a value of 0.98 for the CO_2 mole fraction in the CO_2 + DMSO mixtures formed in the precipitation chamber. Tables 5.2a-b show the results obtained in this work and those obtained previously by Reverchon et al.

Table 5.2a Results obtained in this study for SAS micronization of YAc.

Experiment	**Conditions**		**PS (nm)**	**Morphology**	**ΔT (°C) (x = 0.96)**
	***T* (°C)**	***P* (MPa)**			
1	40	11	80	nanoparticles	3.2
2	60	14	-	aggregated	3.7
3	60	15	65	nanoparticles	3.8
4	60	20	50	nanoparticles	-

Table 5.2b Results obtained by Reverchon et al [2].

Conditions		**PS (nm)**	**Morphology**
***T* (°C)**	***P* (MPa)**		
40	9	400	nano/microparticles
40	10	80	nanoparticles
40	11	90	nanoparticles
40	12	170	nanoparticles
40	15	100	nanoparticles
60	14	3000-10000	balloons
60	16	100-2000	nano + balloons

Our results are in agreement with those obtained by Reverchon et al., although smaller particles have been obtained in similar conditions of temperature and pressure. For example, at 40 °C and 11 MPa the mean PS obtained by Reverchon et al. [2] is 90 nm but in our case it is 80 nm. Therefore, our SAS apparatus may be considered suitable for SAS micronizations.

Moreover, particle morphology is shown to depend on phase equilibrium for CO_2 + dimethyl sulfoxide. In this work, we have studied the thermal effects in the mixing process between SC-CO_2 and DMSO that takes place in the SAS precipitation chamber [9]. Mixing process may cause a local increase of T in the chamber which also affects phase separation. According to the procedure described in chapter four, the temperature increments inside the precipitation chamber, ΔT, can be estimated at 0.96 CO_2 mole fraction. Values of 3.2, 3.7 and 3.8 degrees are obtained for experiments 1, 2 and 3, respectively. ΔT can not be estimated for experiment 4 due to the lack of experimental excess enthalpy values at 60 °C and 20 MPa. The 3.8 degrees increment in experiment 3 at 60 °C brings the P condition closer to the higher pressure of the phase boundary at 64 °C. A similar ΔT increment in experiment 2 carried out at a lower pressure leads to phase splitting. The P and T conditions for experiment 2 will correspond to the two-phase region at 64 °C where aggregated particles are obtained. Fig. 5.7 shows a scheme of the vapor-liquid equilibrium data at 60 °C and 64 °C, the positions of the working conditions and the morphologies of the particles.

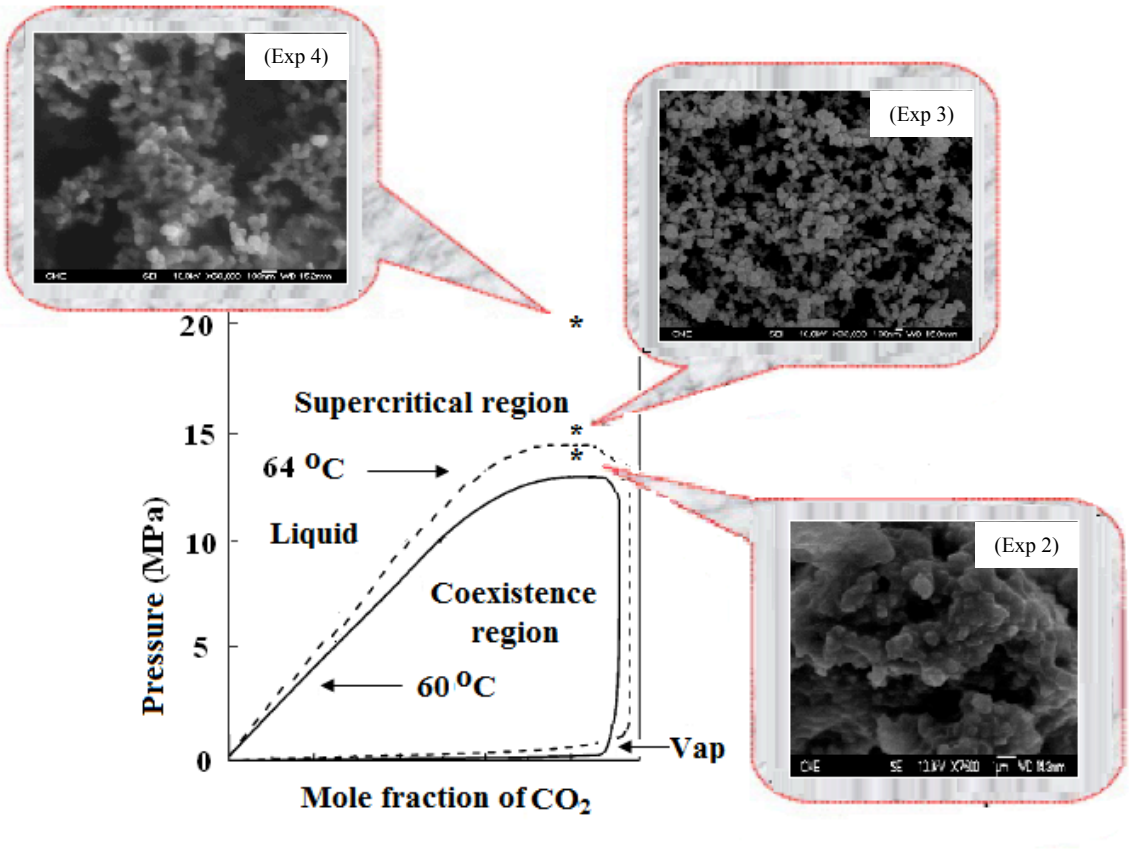

Fig. 5.7 Particles morphology and phase diagram at 60 °C and 64 °C. Phase boundaries are based on data shown in Fig. 4.8.

The local temperature increment at the precipitation chamber is attributed to the mixing of the SC-CO_2 and DMSO and provokes that exp.2 was performed in the two phase region instead of the one phase supercritical region as originally planned. Similarly Reverchon et al. [2] obtained at the same temperature and pressure conditions large balloons 3000-10000 nm. Although the reason of their unsuccessful micronization was not explained by Reverchon et al. [2], we believe that local thermal effect at these conditions could explain it.

Finally, from all the previous, we can say that we have assembled a SAS apparatus that can be applied for micronization of a wide category of solutes. This study shows that the process arrangement and the apparatus strongly influence the final product properties. The binary phase diagram of the binary system CO_2 + organic solvent and the heat of mixing strongly affect the morphology of the micronized particles.

5.2. Micronization of 5-Fluorouracil

5-Fluorouracil, 5-FU, is commercialized under the brand names Adrucil, Carac, Efudix, Efudex and Fluoroplex. It is a pyrimidine analog drug used in the treatment of several types of cancer.

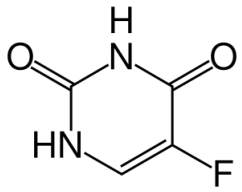

5-fluoro-1*H*-pyrimidine-2,4-dione, IUPAC name of 5-FU

The chemotherapy agent 5-FU has been in used against cancer for about 40 years. It acts in several ways, but principally as a thymidylate synthase inhibitor. Interrupting the action of this enzyme blocks the synthesis of the pyrimidine thymidine, which is a nucleotide required for DNA replication. Thymidylate synthase methylates deoxyuridine monophosphate (dUMP) into thymidine monophosphate (dTMP). Administration of 5-FU causes a scarcity in dTMP, so rapidly dividing cancerous cells undergo cell death via thymineless death [10].

5.2.1. Literature Review and Design of Experiments

Guney and Akgerman have measured the solubilities of 5-fluorouracil in SC-CO_2 at pressures ranging from 11 to 21 MPa and at temperature values of 35 °C and 55 °C and found them to vary from 3.72 x 10^{-7} to 2.86 x 10^{-6} in weight fraction [11]. Suleiman et al. have measured the solubilities of 5-FU at pressures ranging from 10 to 30 MPa and temperatures ranging from 35 to 55 °C and found them to vary from 3.60 x 10^{-6} to 1.46 x 10^{-5} in mole fraction [12]. Furthermore 5-FU is soluble in a variety of solvent such as methanol, acetone, dichloromethane, so on, which are highly soluble in SC-CO_2. These properties make 5-FU a good candidate for SAS micronization; carbon dioxide acts as antisolvent.

Kalantarian et al. have recently precipitated 5-FU using SAS from methanol, methanol-dichloromethane, methanol-acetone, and methanol-ethanol mixtures [13]. The conditions of the experiments included pressures of 10 and 15 MPa, temperature of 40 °C, a solution flow rate of 1 mL/min, and CO_2 flow rate of 20 mL/min. The particles were characterized physicochemically before and after the process for their morphology and crystallinity. In spite of differences in size, the particles after precipitation were not very different regarding their morphology. The resulting particles were of a regular shape, partly spherical, and appeared to have a smooth surface. They reported that marked changes in the physicochemical properties

of the produced particles were possible by using different solvents or mixture of solvents in the supercritical processing of 5-FU. They found that acetone and dichloromethane increase the solubility of methanol in SC-CO_2 resulting in a reduction of the particle size of the precipitated particles, in addition to a change in the morphologic properties of the particles. Generally, when a solvent has a higher solubility in SC-CO_2; its solvent power reduces faster in the presence of SC-CO_2. Therefore, supersaturation happens sooner and smaller particles are formed. In agreement to this statement, the particles produced from methanol alone had a mean size of 2970 nm while the particles produced from methanol-acetone had sizes of 730-980 nm depending on the amount of acetone. With dichloromethane the particles size reached 250-440 nm depending on the amount of dichloromethane. Particles exhibit a relatively smooth surface and a narrow particle size distribution.

Kalantarian et al. have also used the GAS and SAS methods to co-precipitate 5-FU as a hydrophilic antitumor drug and poly lactide-co-glycolide (PLGA) as a biodegradable polymer with the aim of forming sustained-release matrices [14]. They used acetone and methanol/dichloromethane mixtures. The process conditions were mild and non-aqueous, so the hydrophilic drug incorporated in the PLGA had good stability during the process. With more 5-FU loading in the produced microparticles, drug release was faster and the amount of burst release was greater. The rapid release probably represented the release of drug-loaded microparticles with a high ratio of 5-FU and lower polymer molecular weight. Particles with 4.9% 5-FU and PLGA with high molecular weight showed the slowest drug release.

Chen et al. have successfully prepared 5-FU-SiO_2-PLLA drug-polymer microcapsules (< 0.5 μm) with a core-shell structure in a modified SEDS process, in which an 'injector' was employed in the particles suspension delivery system [15]. The 5-FU-SiO_2 particle suspension in a solution of PLLA in dichloromethane and supercritical CO_2 were sprayed together through the coaxial nozzle into the high-pressure vessel. The supercritical CO_2 was used as both anti-solvent for its chemical properties and 'spray enhancer' by mechanical effect. This study demonstrated that the modified SEDS process could be used to produce drug-polymer microcapsules with a core-shell structure, high encapsulation efficiency and sustained drug release effect.

In view of the results obtained from validating our SAS apparatus and the solubility data available for DMSO in SC-CO_2, dimethyl sulfoxide was chosen as a solvent for the

micronization of 5-FU. The CO_2 and DMSO are the same materials used in the micronization of YAc. 5-FU was supplied from Sigma-Aldrich (≥ 99 mol % pure).

As mentioned in chapter three, the factors to consider in the SAS process are: the concentration of the solution (C), the temperature (T), the pressure (P), the solution flow rate (Q_L), the supercritical CO_2 flow rate (Q_{CO2}), the drying time (t), and the nozzle diameter ($Ø_n$). In our study, the drying time and the nozzle diameter are kept constant at 3 times the time required to fill the precipitation chamber and 100 μm, respectively. In order to minimize the number of experiments, the fractional factorial design was employed. Among all possible fractional factorial design, the design 2^{5-2} was selected. As a result, we generated eight different combinations of signs for the five factors as shown in table 5.3. as deeply explained in chapter three.

Table 5.3 The Fractional Factorial 2^{5-2} Design.

Run	C (1)	T (2)	P(3)	Q_L (4=12)	Q_{CO2} (5=13)
1	-	-	-	+	+
2	+	-	-	-	-
3	-	+	-	-	+
4	+	+	-	+	-
5	-	-	+	+	-
6	+	-	+	-	+
7	-	+	+	-	-
8	+	+	+	+	+

The generated combinations are eight different trails (25, 2, 19, 12, 13, 22, 7 and 32) out of the full factorial design at two levels 2^5 given by Yates order [16]. Thus, the design is a fraction of ¼ of the full 2^5 design. Details above the allied factors and the procedure to generate table 5.3 were given in the methodology chapter.

Table 5.4 shows the level identification for CO_2 + DMSO + 5-FU system. The low level of concentration was set to obtain a sufficient amount of precipitate for subsequent analysis; the high level was limited by the saturation of the solution at room temperature.

Table 5.4 Level Identification of the Factors.

Factor	Unit	Labels	Low Level (-)	High Level (+)
Concentration	%	C	1	2
Temperature	°C	T	40	50
Pressure	MPa	P	15	18
Solution flow rate	mL/min	Q_L	1	1.4
CO_2 flow rate ($x \geq 0.96$)	g/min	Q_{CO2}	15	20

The two levels of temperature and pressure were chosen mainly on the basis of isothermal vapor–liquid equilibrium and critical data for CO_2 + DMSO shown in Fig. 4.8, to work in the supercritical region. 5-FU may be expected to interact weakly with CO_2. Therefore, the binary phase diagram for CO_2 + DMSO shown in Fig. 4.8 may be used to establish the temperature and pressure conditions for SAS experiments. The lower temperature and lower pressure were chosen aiming to stay within the one phase supercritical region; the upper values for temperature and pressure were chosen based on reducing energy costs and previous studies. Flow rate limits were chosen to obtain CO_2 mole fractions ≥ 0.96, in the carbon dioxide- rich region, considering the limitation of ours SAS apparatus.

The alias structure determines which effects are confounded with each other. MINITAB 15 SOFTWARE [17] was used to generate the simplified alias structure that is shown in tables 5.5.

Table 5.5 The Simplified Alias Structure.

Concentration	Effect l_1 = 1 + 24 + 35 = 1
Temperature	Effect l_2 = 2 + 14 = 2
Pressure	Effect l_3 = 3 + 15 = 3
Solution flow rate	Effect l_4 = 4 + 12 = 4
Supercritical CO_2 flow rate	Effect l_5 = 5 + 13 = 5

In table 5.3 the effect (contrast) in each column is due to both the main variables (C, T, P, Q_L and Q_{CO2}) and the effects of the interactions shown in table 5.5. For screening purposes, the interactions between two factors were also considered negligible [18], so the effect value l_i is caused only by the main factor, by other words, concentration for column 1, temperature for column 2, and so on.

5.2.2. SEM Images. Particle size and Response and Contrast Calculation

The mean particle size and particle morphology obtained from SEM images were used as a response to evaluate the process performance.

Fig. 5.8 shows an optical image of the 5-FU commercial powder and its SEM image. SEM images of untreated 5-FU exhibits granulated particles with a mean particle size > 100 μm.

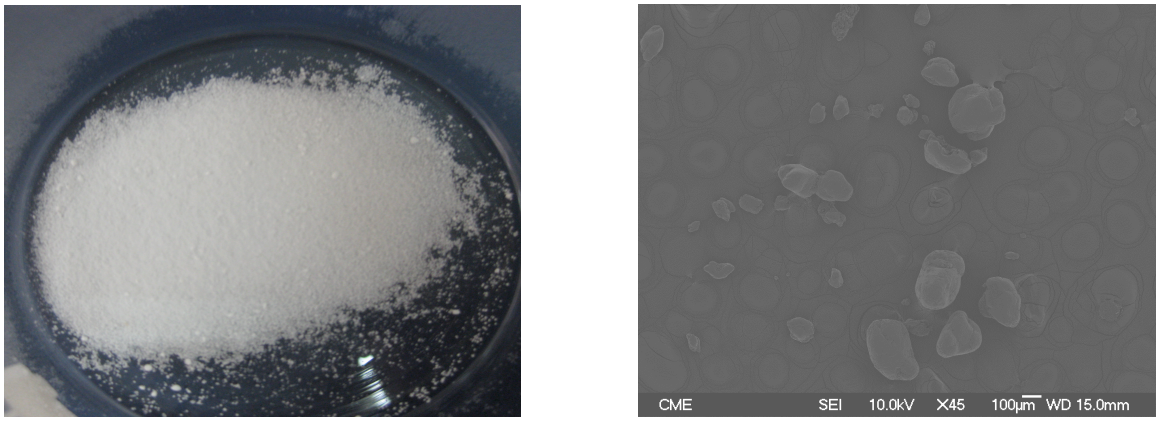

Fig. 5.8 Images of untreated 5-FU.

SEM images of the 5-FU precipitated are shown next in Figs. 5.9-12. Conditions of the precipitation experiments are given in tables 5.3 and 5.4. All experiments of the design matrix were carried out following the same experimental procedure. In every case the precipitation was successful and fluffy powders were obtained. SEM images reveled, however, that six of the eight experiments (1, 2, 5, 6, 7 and 8) led to a successful micronization of 5-fluorouracil. On the other hand, the micronization was unsuccessful for runs 3 and 4 were much larger particles of regular shape were obtained. SEM images of micronized 5-fluorouracil samples show the formation of elongated particles with a distributed mean particle size in range of 216-670 nm and standard deviation within the range of 65-220 nm, respectively.

The effect of 5-FU concentration in the liquid solution has been studied at temperatures of 40 °C and 50 °C and pressures of 15 and 18 MPa. With the exception of the experiment at 50 °C and 15 MPa, small particles have been obtained at all concentrations.

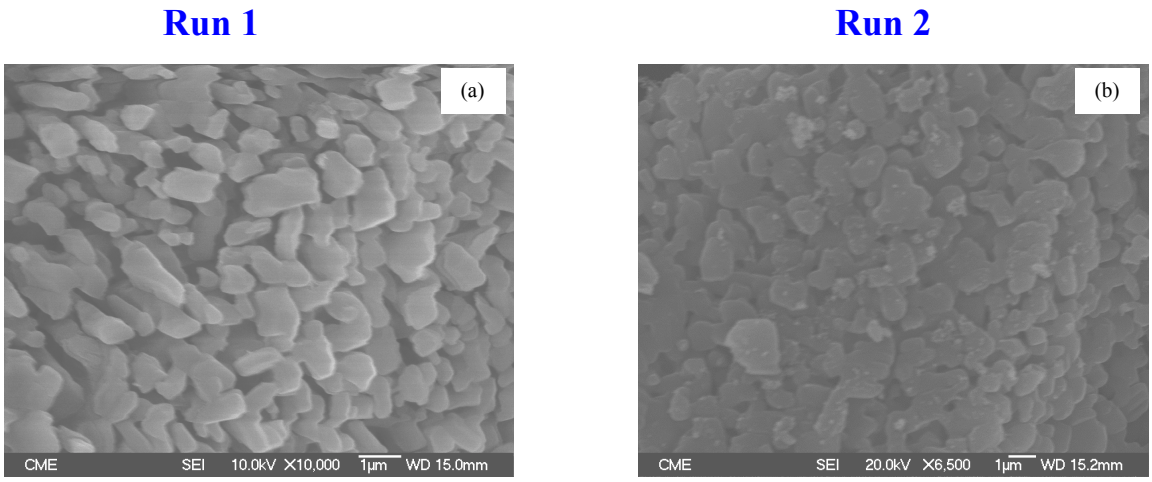

Fig. 5.9 SEM images of SAS 5-FU obtained at 40 °C, 15 MPa and concentrations of 1 (a) and 2% (b).

Fig. 5.9 compares particles obtained at 40 °C and 15 MPa using two different concentrations. Notice that the magnification is lower in the SEM image of run 2, showing how larger particles are obtained at the higher concentration. In runs 3 and 4 carried out at 50 °C and 15 MPa and concentrations of 1 and 2%, respectively, much larger crystals exhibiting a thin bar shape are obtained as shown in Fig 5.10.

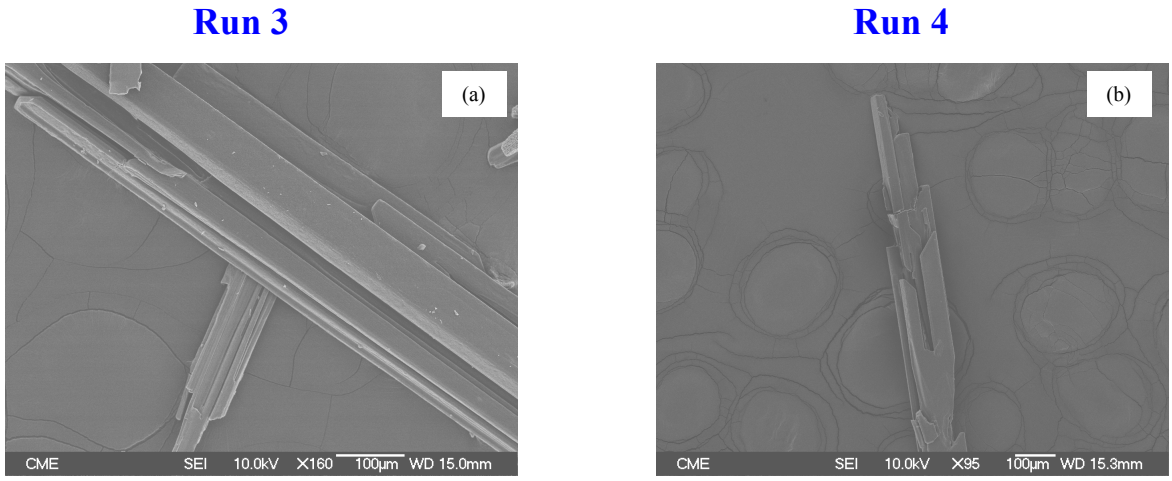

Fig. 5.10 SEM images of SAS 5-FU obtained at 50 °C, 15 MPa and concentrations of 1 (a) and 2% (b).

The precipitations performed at 50 °C and 15 MPa were successful but not the micronizations and very large particles were obtained at these conditions. The reasons for that are not completely understood but it may be attributed to the influence of 5-FU on the phase diagram of the CO_2 + DMSO binary system which could result in phase splitting.

The effect of pressure on the particles morphology was studied at 40 °C and 15 and 18 MPa. As shown in Fig 5.9 and Fig 5.11 for runs 1, 2, 5 and 6 carried out at 40 °C, for a given concentration the particle size decreases as the pressure increases.

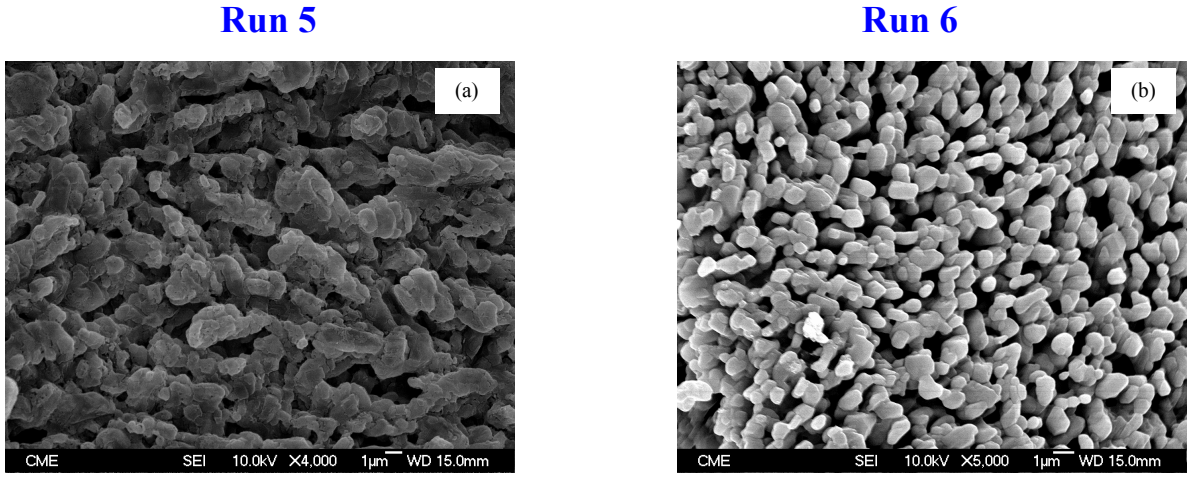

Fig. 5.11 SEM images of SAS 5-FU obtained at 40 °C, 18 MPa and concentrations of 1 (a) and 2% (b).

The effect of temperature on the particles morphology was studied at 18 MPa and 40 and 50 °C. As shown in Fig 5.11 and Fig 5.12 for runs 5, 6, 7 and 8 carried out at 18 MPa, the mean particle size decreases as the temperature increases for a given concentration (images given at different magnification).

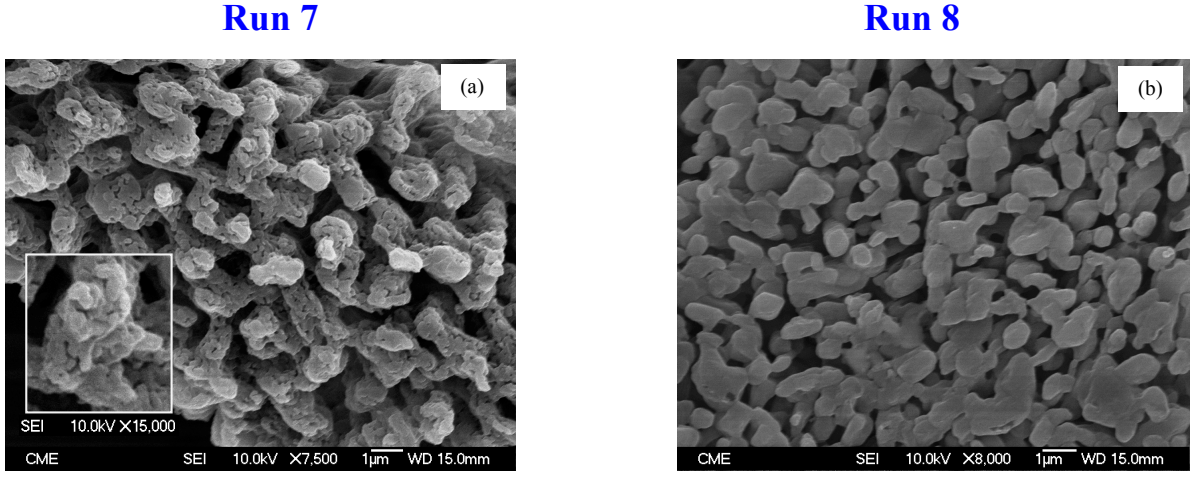

Fig. 5.12 SEM images of SAS 5-FU obtained at 50 °C, 18 MPa and concentrations of 1 (a) and 2% (b).

SEM images for runs 1, 2, 5-8 show that the particle size increases as the 5-FU concentration increases at a given temperature and pressure. However at highest pressure and lowest concentration at both 40 and 50 °C, run 5 and 7, the elongated particles start to be aggregated and from what look like a porous structure. Particle size distribution at every

condition were obtained from the analysis of the SEM images following the procedure described in chapter three and are shown in Fig. 5.13. These data were used as the response to evaluate the parameters that affect performance of the SAS process.

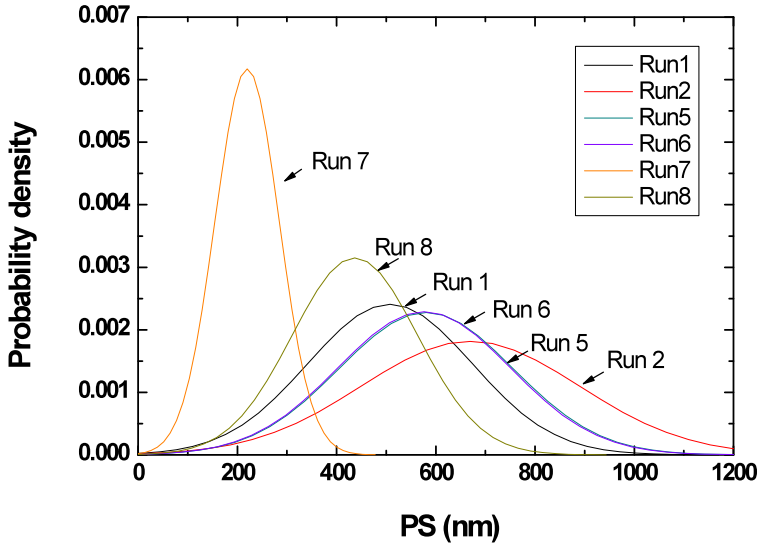

Fig. 5.13 Probability density as a function of particle size for 5-FU SAS micronization.

Table 5.6 shows again the fractional factorial design matrix with values for the particle size and the standard deviation obtained from the SEM images.

Table 5.6 The Fractional Factorial 2^{5-2} Design with Response and Contrast.

Run	*C* (1)	*T* (2)	*P*(3)	Q_L	Q_{CO2}	Response	
						Mean PS (nm)	SD (nm)
1	-	-	-	+	+	508	170
2	+	-	-	-	-	670	220
3	-	+	-	-	+	-	-
4	+	+	-	+	-	-	-
5	-	-	+	+	-	580	180
6	+	-	+	-	+	576	170
7	-	+	+	-	-	216	65
8	+	+	+	+	+	436	130
Mean effect, Contrast, l_i							
PS,nm	94.5	-420.5	157	15	13.5		
SD	28.5	-135.5	39	2.5	2		

The mean effect, l_i, of each column was calculated using equation (3.44) as it was explained in chapter three.

Three key factors with major effect on the particle size were identified. In order of decreasing importance, these are temperature, pressure and concentration.

As shown in Fig. 5.13, the smallest particle sizes with the narrowest particle distribution are obtained in run 7 while the largest particle sizes with a very broad particle distribution are obtained in run 2.

Fig. 5.14 shows the effect of the different factors on the particle size. It confirms that temperature and pressure have the highest influence in the particle size. The order of importance of the factors for particle size and morphology can be summarized in view of their mean effect as following

$$T > P > C >> Q_L > Q_{CO2}$$

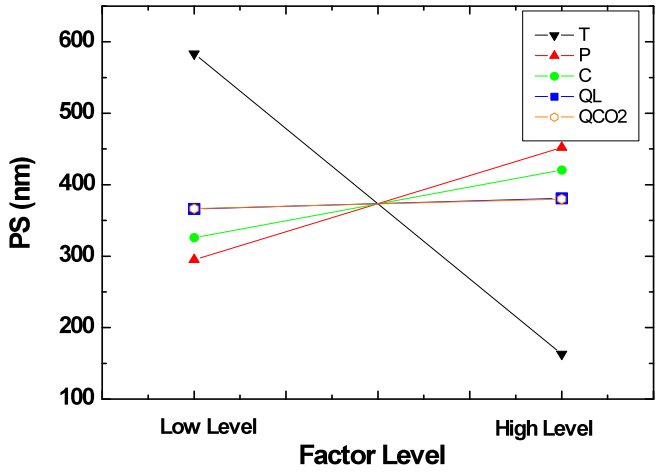

Fig. 5.14 Effect of the different factors on particles size for 5-FU SAS micronization.

Thermal effects for the conditions of temperature and pressure used are moderate. Temperature increases inside the precipitation chamber were calculated using the procedure described in chapter four. Values of 1.9 and 2.6 degrees were obtained for experiments at 40 °C and 15 and 18 MPa, respectively, and values of 3.2 and 2.8 degrees for experiments carried out at 50 °C and 15 and 18 MPa, respectively. These moderate increases together with the pressure values that are much higher than those shown for the phase boundaries at x = 0.96 and 40 °C and 50 °C in Fig. 4.8, exclude the possibility of a phase separation such as that described in the YAc micronization at 60 °C and 14 MPa.

Best conditions for the 5-FU micronization were those of run 7: the concentration of the solution (C = 1%), the temperature (T = 50 °C), the pressure (P = 18 MPa), the solution flow rate (Q_L = 1 mL/min), the supercritical CO_2 flow rate (Q_{CO2} = 15 g/min), the drying time (t = 3 Volume), and the nozzle diameter ($Ø_n$ = 100 µm) which result in the smallest mean particle size of 216 nm. In comparison to previous report, the particle size and morphology of 5-FU precipitated in this work are similar to those obtained by Kalantarian et al. [14]. In their study, best results were obtained for particles precipitated from methanol-dichloromethane 50:50 exhibiting a mean particle size of 248 nm.

5.2.3. Characterization of 5-FU using X-ray Diffraction

The crystallinity of the precipitated particles has been evaluated using X-ray diffraction powder (XRD). Samples were scanned over the range of 10-50 degrees 2θ. Fig 5.15 compares the XRD patterns of the untreated and SAS processed 5-FU.

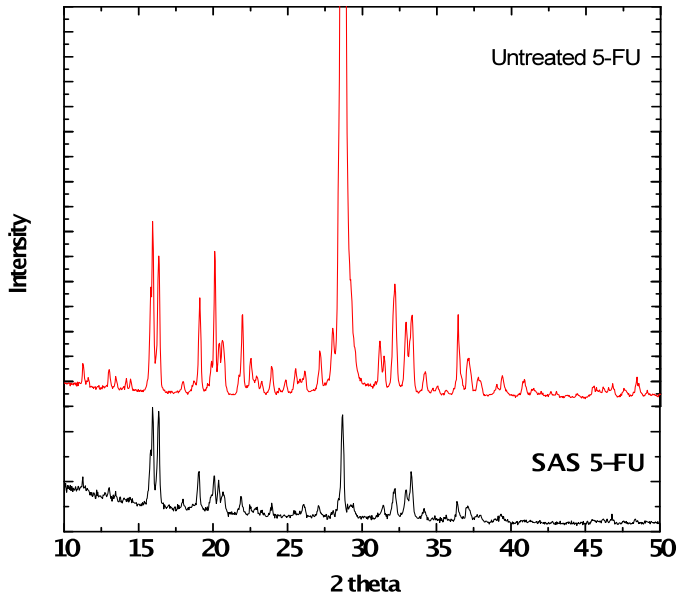

Fig. 5.15 XRD patterns of untreated 5-FU and SAS Processed 5-FU obtained at 50 °C and 18 MPa and concentrations of 1%.

The XRD pattern of the untreated 5-FU exhibits a very intense peak at 28.7 degree. The high intensity of this peak suggests a preferred orientation of the untreated drug at this position. On the other hand, the preferred orientation disappeared in the XRD pattern of the SAS precipitated 5-FU and that may be attributed to a decrease of crystallinity during SAS precipitation of 5-FU from DMSO with respect to the untreated drug. Kalantarian et al. [14] observed the preferred orientation in the XRD patterns of both the untreated and the

precipitated 5-FU from methanol/dichloromethane. The differences in crystallinity between the sample precipitated from DMSO and that obtained by Kalantarian et al. [14] using acetone and dichloromethane may be attributed to the difference in polarity of the solvents used in the SAS precipitation.

5.3. Micronization of Diflunisal

Diflunisal is a non-steroidal anti-inflammatory drug (NSAID). It was first sold under the brand name Dolobid, marketed by Merck & Co., but generic versions are now widely available.

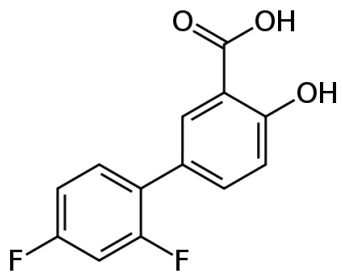

2,4-difluoro-4-hydroxybiphenyl-3-carboxylic acid, IUPAC name of diflunisal.

Diflunisal is a salicylic acid derivative used to relieve pain, tenderness, swelling and stiffness caused by osteoarthritis (arthritis caused by a breakdown of the lining of the joints) and rheumatoid arthritis (arthritis caused by swelling of the lining of the joints). Diflunisal is also used to relieve mild to moderate pain from other causes. Like all NSAIDs, diflunisal acts by inhibiting the production of prostaglandins, hormones which are involved in inflammation and pain [19-21].

A comparison of the pharmacological profile of diflunisal with that of some well-known anti-inflammatory agents such as such as aspirin, ibuprofen and indomethacin has shown that diflunisal is more potent and less toxic than these drugs [22].

5.3.1. Literature Review and Design of Experiments

The low solubility of the target substance in supercritical carbon dioxide is essential for the development of the supercritical antisolvent precipitation. Coimbra et al. [23] have measured the solubility of diflunisal in supercritical CO_2 at 308.2, 318.2, and 328.2 K from 9.0 to 25.0 MPa using a static analytical method. Experimental solubilities were found to be between 0.54×10^{-6} and 8.07×10^{-6} in terms of diflunisal mole fraction. The obtained experimental

solubility data were successfully correlated by the Peng-Robinson cubic EOS and using the classical van der Waals mixing rules. Therefore, diflunisal has a very low solubility in supercritical carbon dioxide and could be precipitated in principle by SAS.

The wide applications of diflunisal, its low solubility in supercritical carbon dioxide and the lack of literature on the SAS micronization of this drug, made diflunisal our next target for micronization. In view of the results obtained from the micronization of YAc and 5-FU, DMSO was chosen in the first place as a solvent for the micronization of diflunisal. Preliminary experiments carried out at conditions similar to those employed in the YAc and 5-FU SAS experiments showed that DMSO is not a suitable solvent for the SAS micronization of diflunisal because of the re-dissolution of the precipitated drug due to the high solubility of diflunisal in DMSO.

On the other hand, the phase behavior available for CO_2 + acetone [24-29], in addition to the excess molar enthalpies of CO_2 + acetone mixtures [30] reported in this thesis made acetone a good candidate as a solvent for the micronization of diflunisal. Preliminary SAS experiments carried out using acetone were successful to precipitate diflunisal.

In this study, the materials employed were: acetone (Sigma-Aldrich, ≥ 99 mol % pure) and diflunisal (Sigma- Aldrich, analytical standard). The CO_2 and DMSO are the same materials used in the micronization of YAc.

For the choice of the temperature and pressure conditions of the SAS micronization of diflunisal, the isothermal vapor-liquid equilibrium (VLE) data of the binary system CO_2 + acetone have to be taken into account. Fig. 5.16 shows the vapor-liquid equilibrium data for this system at 40 and 50 °C. This system presents a type I diagram in the classification of Scott and van Konynenburg [8]. Details of the critical locus can be found in Fig. 4 of reference [30].

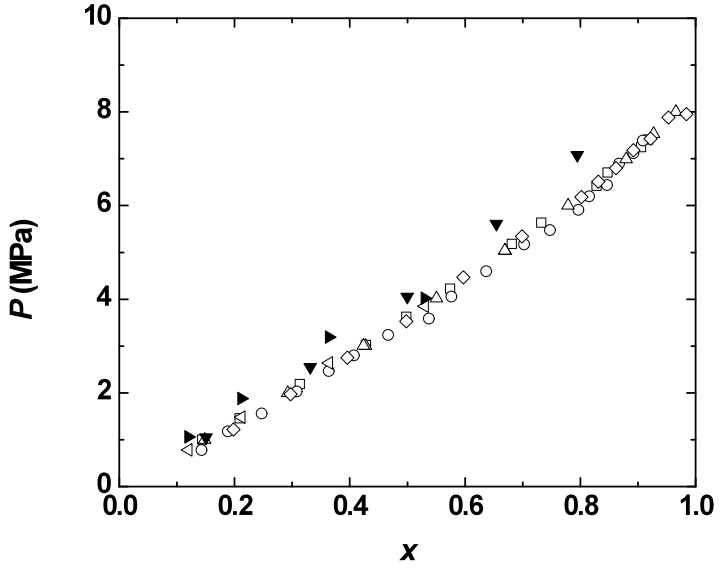

Fig. 5.16 Isothermal vapor–liquid equilibrium for [CO_2(*x*) + acetone (1-*x*)] reported by Katayama et al. [24]: (□) 40 °C, Day et al. [25] : (○) 40 °C, Adrian and Maurer [26]: (Δ) 40 °C, Bamberger and Maurer [27] : (▼) 50 °C, Chiu et al. [28] : (◊) 40 °C, and Stievano and Elvassore [29] : (◁) 40 °C; (►) 50 °C.

Table 5.7 shows the temperature, pressure experimental conditions and the estimated temperature increments for CO_2 + acetone at a temperature of 40 °C and pressures of 9, 12 and 15 MPa.

Table 5.7 The temperature, pressure and concentration experimental conditions along with the temperature increments for SAS micronization of diflunisal from acetone solutions.

Experiment	**Conditions**			**Δ*T* (°C) (*x* = 0.96)**
	***T* (°C)**	**Conc. (%)**	***P*/ MPa**	
1	40	2	9	5.5
2		2	12	2.0
3		4		
4		4	15	2.2

The other experimental conditions were 1 mL/min solution flow rate, 15 g/min CO_2 flow rate, drying time required to fill 3 times the precipitation chamber. The liquid and CO_2 flow rates lead to a value of 0.96 for the CO_2 mole fraction in the CO_2 + acetone mixtures formed in the precipitation chamber.

In this thesis, we have studied the thermal effects in the mixing process between SC-CO_2 and acetone that take place in the SAS precipitation chamber [30]. Mixing process may cause a local increase in T in the chamber which also affects phase separation. According to the procedure described in chapter four the temperature increments inside the precipitation chamber, ΔT, can be estimated at 0.96 CO_2 mole fraction. Values of 5.5, 2.0, 2.0 and 2.2 are obtained for experiments 1, 2, 3 and 4, respectively. Since the P and T conditions are not close to the mixture critical point, the 5.5, 2.0 or 2.2 degrees increments have no effect on the phase boundaries. Fig. 5.16 indicates that the CO_2 + acetone mixtures formed in the precipitation chamber at these conditions are indeed supercritical.

5.3.2. SEM Images. Influence of SAS Parameters

Fig. 5.17 shows the optical and SEM images of the commercial drug. The untreated diflunisal exhibits a high crystallinity.

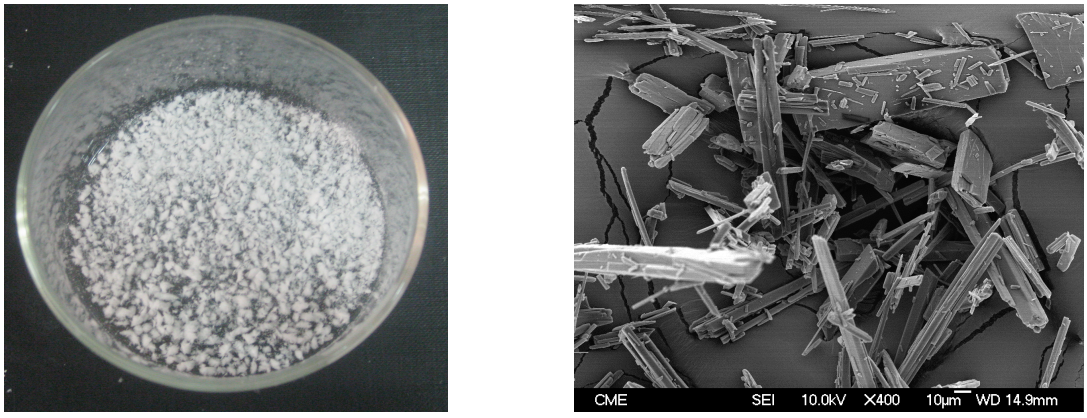

Fig. 5.17 Images of untreated diflunisal.

Large thin bars of a crystalline material were observed in the SEM images of the untreated drug. SEM images of the SAS precipitated diflunisal in experiments 1-4 are shown in Figs. 5.18-5.20. In every experiment, similar thin and very long crystalline particles forming laminar sticks were observed. The sticks are bound together like the branches of a tree. The width of the sticks ranges from 2-10 µm at all conditions.

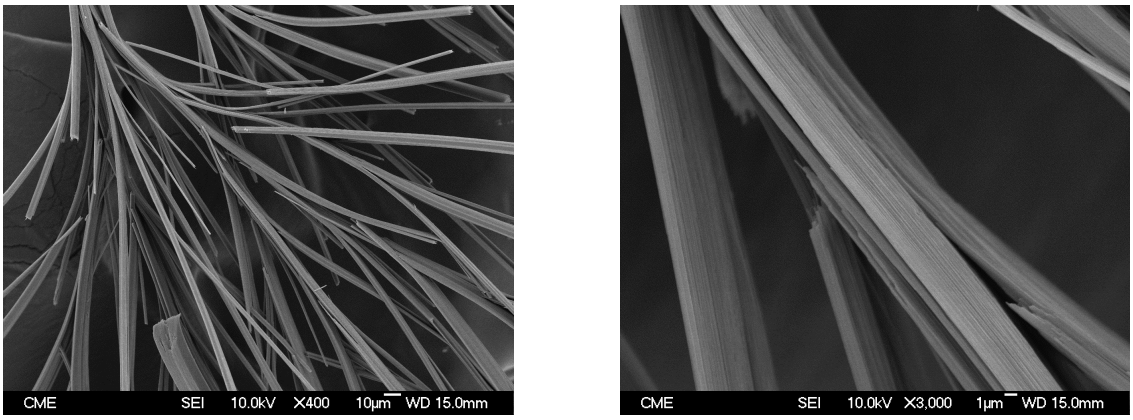

Fig. 5.18 SEM images of SAS diflunisal obtained at 40 °C, 9 MPa and concentration of 2%.

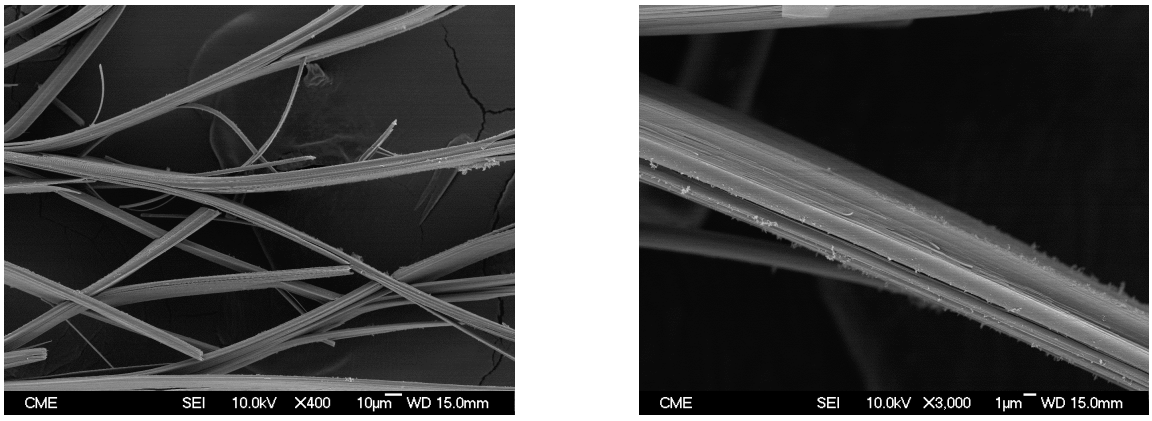

Fig. 5.19 SEM images of SAS diflunisal obtained at 40 °C, 12 MPa and concentration of 2%.

SEM images of the SAS precipitated diflunisal at a temperature of 40 °C, pressures ranging from 9 to 15 MPa and concentrations of 2 and 4% show that the different conditions do not lead to significant changes in the crystallinity of diflunisal.

The effect of pressure on the particles morphology was studied at a temperature of 40 °C and pressures of 9 and 12 MPa. As shown in Fig 5.18 and Fig 5.19, the material precipitated is very similar in both cases but for a given concentration, the width of the sticks decreases slightly as the pressure increases.

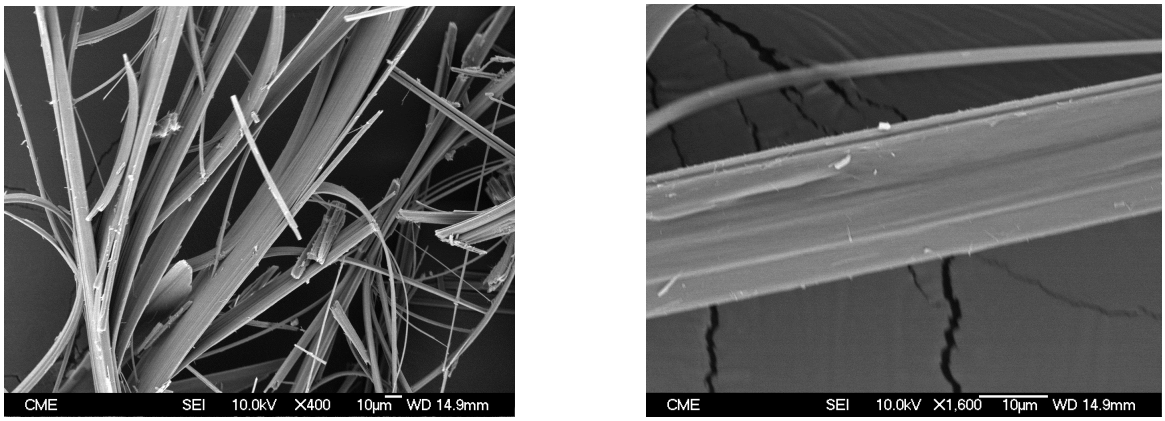

Fig. 5.20 SEM images of SAS diflunisal obtained at 40 °C, 12 MPa and concentration of 4%.

The effect of the concentration of the solution on the morphology of SAS precipitated diflunisal was studied at solution concentrations of 2 % and 4 % at 40 °C and 12 MPa. As shown in Fig. 5.19 and Fig. 5.20, the material precipitated in both cases is very similar but crystals are slightly wider at the highest concentration. By increasing the pressure up to 15 MPa at 40 °C and 4 %, slightly thinner bars are observed again as shown in Fig. 5.21. The effect of both concentration and pressure on the morphology of the precipitate for this compound is very weak.

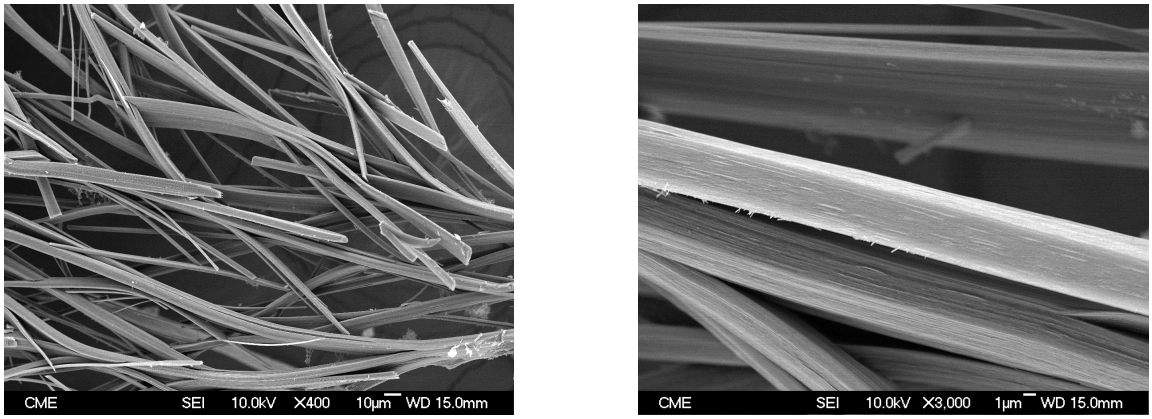

Fig. 5.21 Images of SAS diflunisal obtained at 40 °C, 15 MPa and concentration of 4%.

As it was already mentioned in chapter one, SAS can be used to generate an amorphous drug by co-precipitation with a polymer such as polyvinylpyrrolidone (PVP). Since diflunisal is a crystalline drug, the co-precipitation of diflunisal with PVP is thought to be an effective method to improve the amorphousness of the drug. Because of the poor solubility of PVP in acetone, a mixture of good and poor polymer solvents was used in the co-precipitation process. DCM was chosen to be the good polymer solvent along with acetone as a poor polymer solvent and an acetone/DCM mixture (80:20, v/v %) was used. Dichloromethane

(Scharlau, ≥ 99.8 mol % pure) was used. The reasons for this solvent mixture will be further explained in the 5.4.2. section.

To have a complete understanding for the influence of PVP on the crystallinity of diflunisal, a mixture of acetone/DCM (80:20, v/v %), the same mixture used to precipitate PVP as will be discussed later, was used to precipitate the drug alone at a temperature of 35 °C and pressure of 14 MPa. The other experimental conditions were 2% solution concentration, 1 mL/min solution flow rate, 20 g/min CO_2 flow rate, drying time required to fill 3 times the precipitation chamber. The liquid and CO_2 flow rates lead to a value of ≥ 0.96 for the CO_2 mole fraction in the mixtures formed in the precipitation chamber. Fig. 5.22 shows VLE data for the CO_2 + DCM system at temperatures close to those used in the SAS experiments.

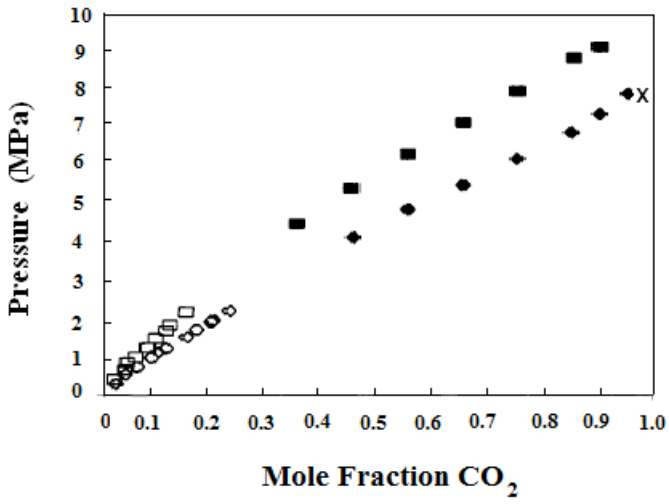

Fig. 5.22 Isothermal vapor–liquid equilibrium and critical data for [CO_2(*x*) + DCM (1-*x*)] reported by Vonderheiden et al. [31] : (◊) 37.5 °C; (□) 54.5 °C, Gonzalez et al. [32]: (♦) 38 °C; (■) 50 °C and Reaves et al. [33]: (x) critical point; 38.5 °C.

Unfortunately, there is not phase equilibrium data available in the literature for the ternary system CO_2 + acetone + DCM. Both the binary CO_2 + DCM and CO_2 + acetone systems display a type I diagram [32]. In view of the similarity of phase behavior for the CO_2 + DCM and CO_2 + acetone systems, we can expect the CO_2 + acetone + DCM system to behave in a similar way to that described in chapter one for the CO_2 + hexane + methanol mixtures. At 35 °C and 14 MPa we can expect temperature increases in the precipitation chamber similar to those obtained for CO_2 + acetone mixtures. Nevertheless, the mixture formed will be supercritical because the *P* and *T* conditions are not close to the mixtures critical point.

As shown in Fig. 5.23 the SEM images of the precipitated diflunisal from acetone/DCM (80:20, v/v) exhibit the same trend observed during the precipitation from acetone alone. A bundle of thin bars like branches of a tree is observed.

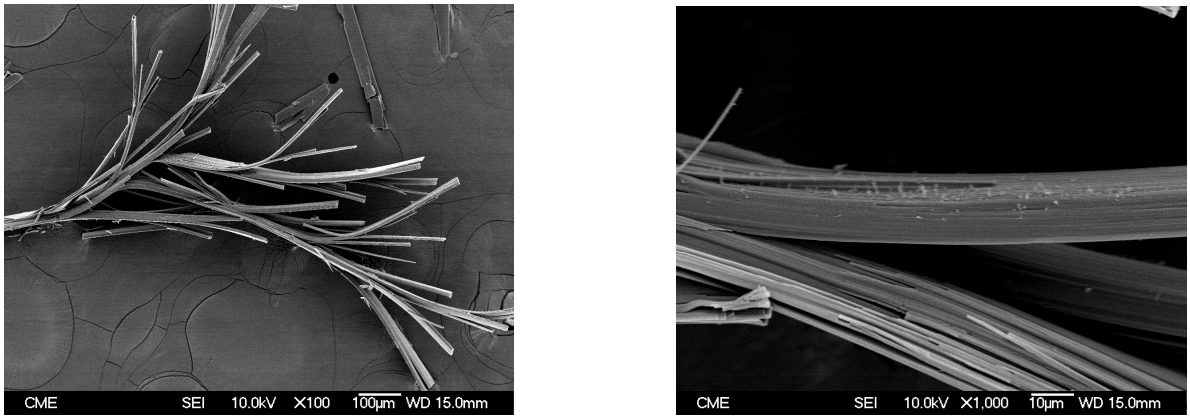

Fig. 5.23 SEM images of SAS diflunisal obtained at 35 °C, 14 MPa and concentration of 2%.

SEM images of the SAS precipitated diflunisal from acetone/dichloromethane at 35 °C and 14 MPa show that there is no change in the morphology of diflunisal in comparison with that obtained from acetone alone. This solute does not seem to be very sensitive to the precipitation conditions, nor to the solvent during SAS.

5.3.3. Characterization of Diflunisal using X-ray Diffraction and Differential Scanning Calorimetry

Polymorphism is defined as the ability of a molecule to adopt more than one crystalline form. This phenomenon occurs widely among organic compounds where several crystal packing possibilities exist via variations in intermolecular hydrogen bonding of functional groups. Different packing arrangements of organic molecules result in different physical properties such as melting point, solubility, hardness, and density. Diflunisal was reported, on the basis of powder X-ray data, to have at least four polymorphic crystal forms of which only one crystal structure has been solved [34]. Cotton and Hux [35] described the existence of three nonsolvated polymorphs. Martínez-Ohárriz et al. [36] reported the existence of a fourth form, IV, and gave the experimental conditions for crystallizing each polymorph together with their IR spectra and powder X-ray diffraction (XRD) patterns. Briefly, polymorphs I, III, and IV of diflunisal were prepared by dissolving with continuous stirring an adequate amount of drug in, respectively, chloroform, ethanol, and toluene and warming the solution in a water bath to 60 °C. The undissolved drug was filtered off and the resultant saturated solution was then cooled in a refrigerator set at 6 °C. The obtained crystals were separated by filtering

under reduced pressure and dried over P_2O_5 at room temperature. For the preparation of form II, distilled water was added to the ethanolic or methanolic saturated solution of the drug at room temperature to initiate crystallization, and then the solution was allowed to cool. Fig. 5.24 shows the XRD patterns of the polymorphs of diflunisal. Martínez-Ohárriz et al. [36] found that precipitation of diflunisal from the more polar solvent led to the type II polymorph. On the other hand, precipitation from the less polar solvent led to type IV polymorph.

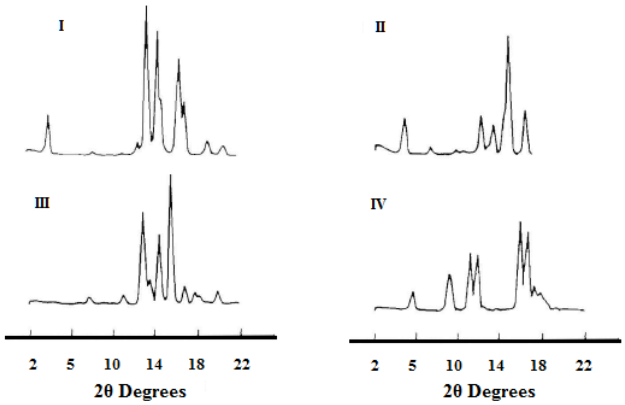

Fig. 5.24 X-ray diffraction patterns of the polymorphs of diflunisal, Martínez-Ohárriz et al. [36]

The polymorphism of the precipitated particles and untreated diflunisal has been examined using X-ray powder diffraction system. The XRD patterns of the original substance and SAS processed diflunisal over the range of 5-50 degrees 2θ are shown in Fig. 5.25.

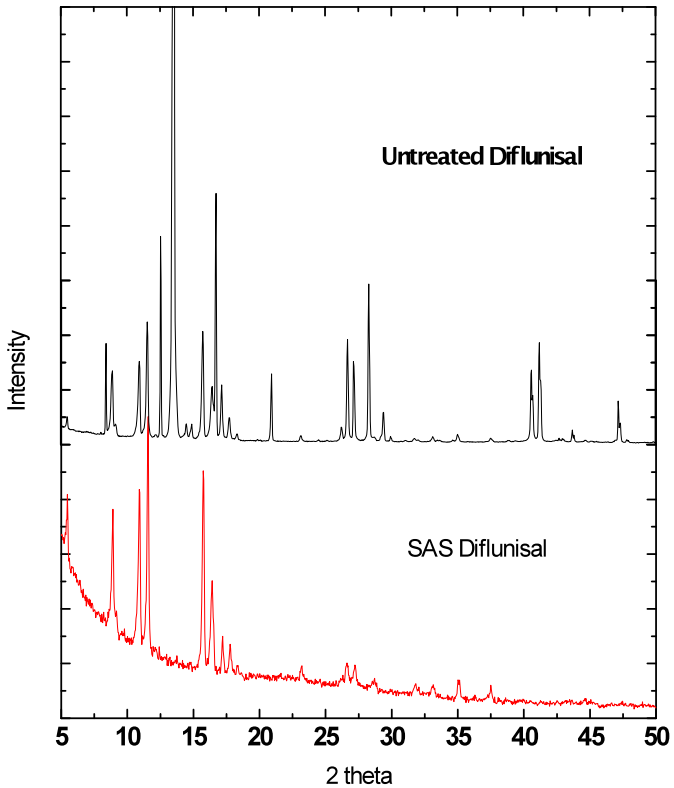

Fig. 5.25 XRD patterns of untreated and SAS diflunisal obtained at 35 °C, 14 MPa and concentration of 2%.

The XRD patterns of the original substance and SAS processed diflunisal are different, which means that the polymorphism of diflunisal is changed through the SAS process. Confusion exists in the literature regarding the nomenclature and identity of the polymorphic forms of diflunisal, but a comparison of the patterns of Fig. 5.25 with the powder diffraction data published by Martínez-Ohárriz et al. [36] reveals that the precipitated drug exhibits form IV. The XRD pattern for the untreated diflunisal is similar to form II but not actually the same suggesting that it is composed of a mixture of polymorphs. The untreated diflunisal is an analytical standard material and the history of the recrystallization processes is unknown; this could explain why its XRD pattern exhibits a mixture of different polymorphs.

For further characterization of the samples, differential scanning calorimetry (DSC) was performed. The thermograms curves of the solids prior and after precipitation are shown in Fig. 5.26. The thermal behavior was studied by heating 5 mg of the sample at a scan rate of 5 °C/min in a covered sample aluminum pan with a hole under nitrogen gas flow, and the investigation was carried out over the temperature range -20 to 250 °C.

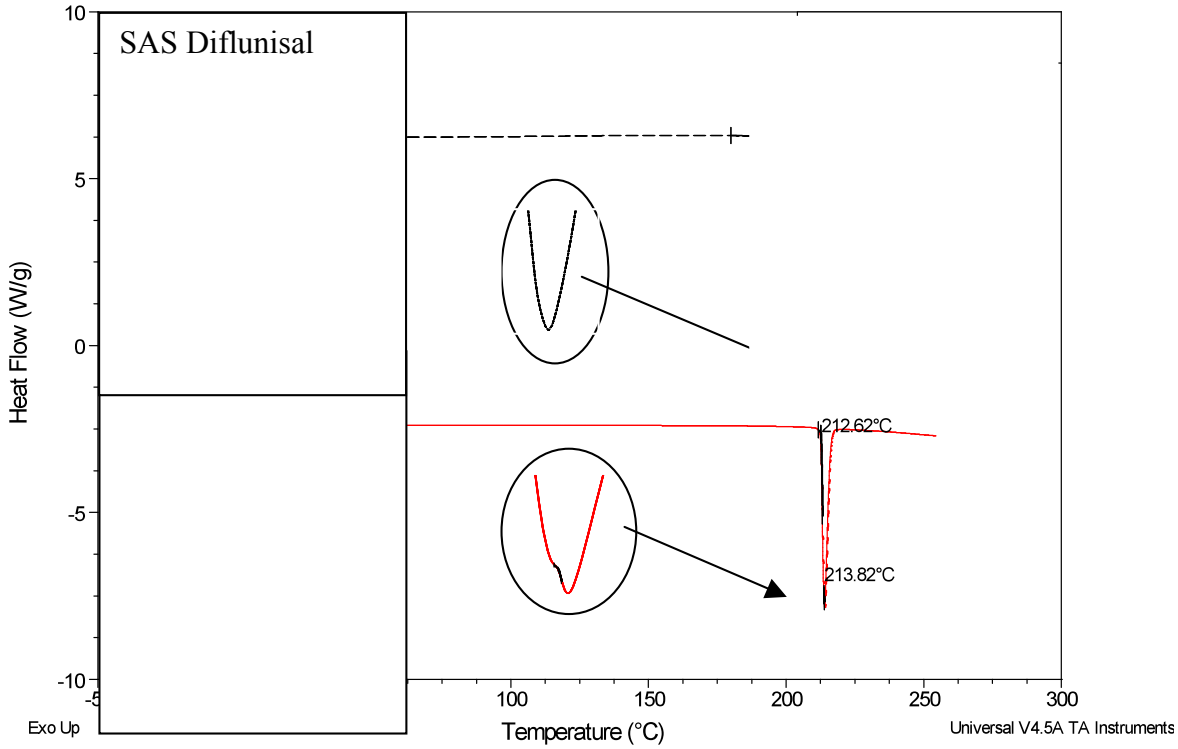

Fig. 5.26 DSC thermograms of untreated and SAS processed diflunisal obtained at 35 °C, 14 MPa and concentration of 2%.

The melting point was measured as the point of intersection between the baseline and the linear section of the ascending endothermic curve. The DSC thermograms show that the untreated diflunisal has a splitted peak with two melting points at 216.62 and 213.82 °C which confirm the presence of more than one polymorph. On the contrary, the SAS diflunisal exhibits a single sharp peak at 212.63 °C peak corresponding to the melting point of form IV.

5.3.4. Dissolution Profiles of Diflunisal

The major objective of scientists in the pharmaceutical industry is to improve the bioavailability, stability of the active pharmaceutical ingredients and its convenience to the patient. Bioavailability means the rate and extent to which the active substance or therapeutic moiety is absorbed from a pharmaceutical form and becomes available at the site of action. The bioavailability of an orally administered drug depends on its solubility in aqueous media over the pH range of 1.0–7.5 and the rate of mass transfer across biological membranes [37].

Martínez-Ohárriz et al. [36] studied the dissolution properties of the different polymorphic forms by determining the intrinsic dissolution rate. They found that the dissolution rates of crystalline forms in a phosphate buffer solution of pH 5 are in the sequence: form I > form II > form III > form IV. Rodríguez-Espinosa et al. [38] studied the dissolution profile of diflunisal form II in a buffer solution at pH 5. They found that 10 % of the drug was dissolved within 1 hour. The dissolved amount increased to 20 % after 2 hours, reaching 30 % at 3 hours.

The dissolution profile of the diflunisal samples precipitated by SAS was followed by UV-VIS spectroscopy. The absorption spectrum of diflunisal at 25 mg/L solution in a phosphate buffer solution of pH 7.4 is shown in Fig. 5.27. The spectrum shows two broad bands at 275 and 306 nm which can be related to the two aromatic rings of the molecule.

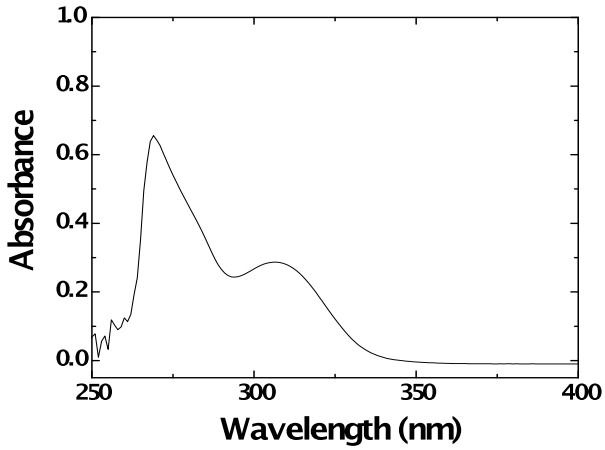

Fig. 5.27 Ultraviolet absorption spectrum of a 25 mg/L solution of diflunisal in the dissolution medium.

According to Brittain et al. [39], the free rotation that would exist in solution about the bond connecting the difluorobenzene and salicylate groups leads to energy states associated with each aromatic ring. Therefore, the corresponding transitions would be decoupled from each other and could be separately observed in the absorption spectrum.

Thus, the band observed at 275 nm is most likely due to absorbance associated with the difluorobenzene group, and the band observed at 306 nm would then be associated with absorbance in the salicylate group. The most intense band at of 275 nm was then used to perform the calibration curve of diflunisal, Fig. 5.28.

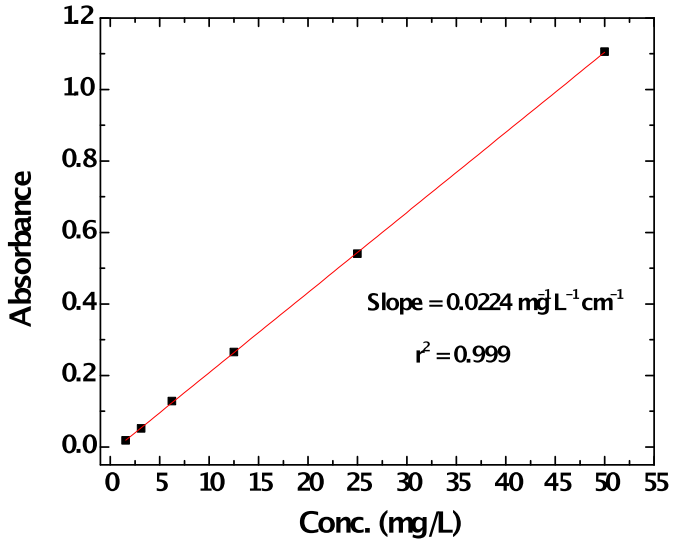

Fig. 5.28 Calibration curve of diflunisal performed at 275 nm.

According to the Lambert-Beer law, the absorbance of the solution, A, is linearly related to the concentration of the solute obeying the following equation:

$$A = acl \tag{5.1}$$

where a is the absorption coefficient in $mg^{-1}\ L^{-1}\ cm^{-1}$, c is the concentration in $mg^{-1}\ L^{-1}$ of the solute and l is the path length = 1 cm.

By fitting the absorbance versus concentration to a straight line, the absorption coefficient can be determined from the slope and it was found to be 0.0224 $mg^{-1}\ L^{-1}\ cm^{-1}$.

The dissolution profile of the untreated and SAS processed diflunisal from acetone/DCM at 35 °C, 14 MPa and concentration of 2% was studied using the rotating disk method described by Nogami et al. [40]. This method presents a constant area during the time scale of this experiment and yielded evidence of a zero-order kinetic process. Dissolution tests were carried out in a pH 7.4 phosphate buffer medium (0.01 M phosphate buffer). A hydraulic press at 5000 kg/cm^2 was used to prepare compressed disks in similar fashion to those used for IR spectroscopy by the conventional procedure; 100 mg of the diflunisal powder were used in each case. Then the compressed tablet was added to 1 L of the buffer solution thermostated at 37 °C. A vertical stirrer with 100 rpm speed was used to improve the diffusivity of the drug into the solution by generating a continuous fluid motion. Aliquots of 5 mL were taken up to 480 min at regular time intervals and were analyzed for the drug content using a UV/VIS spectrophotometer. The volume of the solution was kept constant by adding 5 mL of the phosphate buffer solution each time those samples were withdrawn. Dissolution profiles are shown in Fig. 5.29.

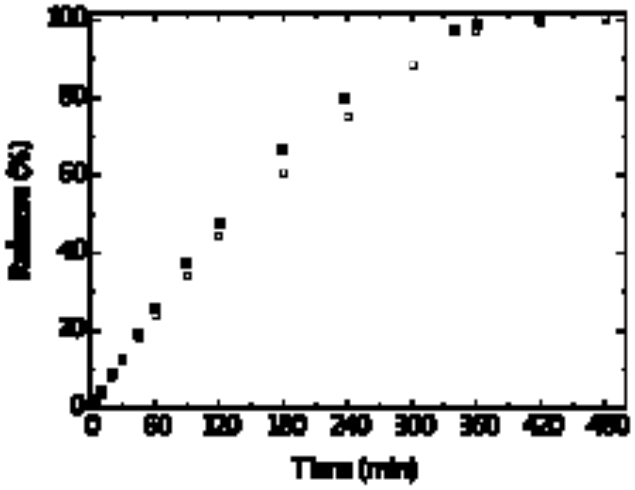

Fig. 5.29 Dissolution profiles of untreated diflunisal (□) and SAS processed diflunisal (■) obtained at 35 °C, 14 MPa and concentration of 2%.

The dissolution profile of the untreated and SAS processed diflunisal from acetone/DCM obtained at 35 °C, 14 MPa and concentration of 2% is represented in terms of the drug release percentage calculated as follows:

$$\text{Release (\%)} = \frac{C_t}{C_{100\%}} * 100 \tag{5.2}$$

where C_t is the concentration of the solution at time t and $C_{100\%}$ is the concentration of the solution at complete dissolution.

By applying the Lambert- Beer law given in Eq. (5.1), the release (%) can be easily obtained

$$\text{Release (\%)} = \frac{A_t}{A_{100\%}} * 100 \tag{5.3}$$

where A_t is the absorbance of the solution at time t, $A_{100\%}$ is the absorbance of the solution at complete dissolution of the disk.

The drug release (%) of the untreated and SAS processed diflunisal are very close to each other especially in the first and last hours. The SAS processed diflunisal exhibited a slightly higher dissolution rate compared to untreated drug. Approximately 24 % and 26 % of the untreated and the SAS processed drug, respectively, were dissolved within 1 hour and these values increased up to 44 % and 48 %, respectively, after 2 hours. The percentage release as a function of time exhibits a linear behavior ($r > 0.99$) for both diflunisal samples in the first two hours. This linear tendency was lost with time as a result of partial dissolution of the disk losing the zero-order kinetics. Approximately 99 % of the solid material was dissolved in both cases after 6 hours. The slight difference in solubility of both materials is most likely due to the different polymorphic forms. In the next section the co-precipitation process and its influence on the solubility and amorphousness of diflunisal is described in detail.

5.4. Amorphization of Diflunisal by Co-precipitation with Polyvinylpyrrolidone

In cases where low solubility limits permeability of the crystalline drug, the amorphous form may have an advantage in improving dissolution properties. There are a number of different methods to generate amorphous drug substances such as solvent deposition [41], co-grinding [42], melt extrusion [43], spray drying [44], melt quenching [45] and melt adsorption [46]. However, some of these applications may be difficult due to the thermal and deposition instability of drug during melting, which often poses a major problem [47, 48]. Hancock and Parks [49] reported that the experimental solubilities of amorphous solids are at least 2–4 times greater than their crystalline counterparts.

One of the possible methods to enhance the dissolution properties is the co-precipitation of the poorly soluble drug with a water soluble polymer. Polyvinylpyrrolidone polymer, also commonly called polyvidone or povidone, is a water-soluble linear polymer made from the monomer *N*-vinylpyrrolidone which is used in large number of pharmaceutical formulations including gastrointestinal pharmaceutical preparations. It offers enhancement of dissolution rate and bioavailability of drugs with low aqueous solubility.

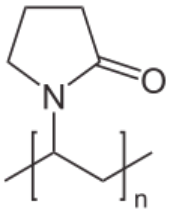

Poly[1-(2-oxo-1-pyrrolidinyl)ethylene], IUPAC name of PVP.

PVP can be purchased with different *K*-values number (*K*-10, *K*-15, *K*-25, *K*-30, *K*-90, *K*-360, etc), which is based on viscosity measurements [50]. As mentioned in the introduction, polymers with different *K*-values have different molecular weight and glass transition temperature. The influence of two different types of PVP polymer on the physicochemical properties of diflunisal was investigated, PVP *K*-10 of average $\overline{M}_w$ = 10,000 and PVP *K*-30 of average $\overline{M}_w$ = 40,000.

5.4.1. Literature Review

The possibility of improving the solubility and bioavailability based on the co-precipitation of the poorly soluble drug with PVP using supercritical antisolvent technology is very attractive and was already discussed in chapter one [37, 51-55]. Lim et al. [51] have investigated the feasibility of using supercritical antisolvent co-precipitation process to influence the crystallinity or amorphous character of a crystalline non-steroidal anti-inflammatory drug, indomethacin (IDMC), for solubility enhancement. They were able to co-precipitate the IDMC with PVP *K*-360 from acetone/DCM at 85 bar and 35 °C using supercritical carbon dioxide as antisolvent. Drug to polymer ratios of 85:15, 50:50 and 20:80 were used. They revealed that it was technically feasible to generate amorphous indomethacin by co-precipitation with minimum 50 wt. % PVP polymer using SAS. Also they demonstrated that the amorphousness increases as the PVP content increases. The drug kinetic dissolution of the amorphous form of SAS IDMC co-precipitated with PVP has been enhanced as compared to its pure crystalline form and physical blends of IDMC-PVP. Spherical particles having mean diameters in the nano range were obtained at 20:80 drug to polymer ratio.

Majerik et al. [37] aimed to improve the bioavailability of oxeglitazar, an orally administered poorly water soluble active substance used in the treatment of type II diabetes, using a SAS process. Oxeglitazar was co-precipitated at 80 bar and 35 °C with various polymeric excipients: polyoxyethylene–polyoxypropylene block copolymers (Poloxamer 188 and 407), polyethylene glycol (PEG 8000) and polyvinylpyrrolidone (PVP *K*-17) from six

different solvents: ethanol, tetrahydrofuran, dichloromethane, chloroform, *N*-methyl-2-pyrrolidone, dimethyl sulfoxide and two binary solvent mixtures: ethanol/tetrahydrofuran (50:50, v/v %) and ethanol/chloroform (50:50, v/v %). SAS formulations of oxeglitazar–PEG 8000, Poloxamer 188 and 407 contained acicular drug crystals that were partly embedded in polymeric spheres, while experiments with PVP *K*-17 resulted in quasi amorphous solid dispersions with high density. In spite of their morphology, SAS formulations exhibited significantly faster dissolution rates compared to those of the raw drug and physical mixtures. Similar results were obtained when the co-precipitation of oxeglitazar and Poloxamer 407 was performed. More than double amount of the active substance was dissolved after 5 min from the Poloxamer 407 and PVP *K*-17 formulations in comparison with the unprocessed drug. In addition, SAS prepared Poloxamer 407 formulation from DCM solution exhibited high polymorphic purity and low residual solvent content.

Badens et al. [52] aimed to improve the dissolution kinetics of oxeglitazar using supercritical antisolvent and spray-freezing (SF) techniques. In the SF experiments the feed solution was injected into liquid nitrogen, a freeze-drying step, through a capillary nozzle located just above the surface of the cryogenic medium resulting in precipitation of particles. Oxeglitazar was formulated with various excipients, including: Poloxamer 188 and 407, polyethylene glycol (PEG) 8000 and polyvinylpyrrolidone (PVP *K*-17) in a 1:1 weight ratio at 80 bar and 35 °C. Dichloromethane, chloroform, and a binary co-solvent system of chloroform/ethanol (50:50, v/v %) were tested in SAS. In the SF process, *tert*-butanol was used as solvent. SAS and SF processed formulations exhibited enhanced dissolution rates. Within 5 min, the amount of dissolved drug varied from 31.6 to 64.3 % for SAS and from 77.9 to 96.9 % for freeze-dried formulations while only 30.5 % was dissolved from the raw drug. However, a part from the oxeglitazar/PVP *K*-17 solid dispersion prepared by SAS still exhibited high crystallinity and particle showed acicular shape. On the contrary, freeze-dried formulations consisted of porous spherical particles with high amorphous content (94.2–100%).

Wu et al. [53] succeeded to prepare solid dispersions of the poorly water-soluble drug piroxicam in polyvinylpyrrolidone (PVP *K*-25) by precipitation with compressed antisolvent (PCA) and spray drying techniques. Methylene chloride was used as a solvent and the working conditions were 9.65 MPa and 25 °C for PCA. Piroxicam was found amorphously dispersed in both solid dispersion systems with a drug to polymer weight ratio of 1:4.

Spherical particles having mean diameters of 1- 5 μm were obtained. IR-spectra data indicated the formation of hydrogen bonding between the drug and the polymer. Both precipitation techniques evaluated led to higher dissolution rates of piroxicam. By comparison, PCA-processed solid dispersions showed distinctly superior performance. Piroxicam dissolved completely within the first 5 min and the dissolution rate within the first 15 min was at least 20 times faster than that of the raw drug.

Uzun et al. [54] used supercritical fluid gas antisolvent method (GAS) to co-precipitate cefuroxime axetil amorphous (CFA, antibiotic) and PVP *K*-30 for preparing drug–polymer composite particles. Solutions of CFA and PVP *K*-30 in methanol with overall concentrations of 50 - 150 mg/mL and drug / polymer ratios of 1/1 - 1/4 were sprayed into the CO_2 at 7 – 20 MPa and 35 - 50 °C with drug + polymer solution injection rates of 0.85 and 2.5 mL/min. Spherical particles having mean diameters of 1.88 - 3.97 μm were obtained. Mean particle size was not affected significantly with the change of process parameters; it was only affected by pressure change. On the other hand, particle size distribution was affected by pressure, temperature, drug + polymer solution injection rate and concentration. The drug release rate of SAS co-precipitated CFA–PVP (1/1) particles was almost 10 times slower than that of the pure drug alone. However, the drug release percentage increased with increasing the PVP content. The drug release rate of SAS co-precipitated particles was faster than that of the pure CFA.

Corrigan and Crean [55] successfully prepared micro-crystalline hydrocortisone–PVP composites using the supercritical fluid gas antisolvent method. Analysis indicated that hydrocortisone–PVP systems were more crystalline than the corresponding systems prepared by spray drying. Systems prepared by the GAS method were more similar in physicochemical properties to the co-precipitates prepared by conventional solvent evaporation. In addition, GAS hydrocortisone–PVP composites had dissolution rates lower than those of the corresponding systems prepared by the other processing methods but equivalent to those of the physical mixtures.

PVP has a poor solubility in acetone, the first solvent chosen to micronize diflunisal, but it is very soluble in ethanol. Preliminary SAS precipitation experiments of polyvinylpyrrolidone from ethanol (Panreac, ≥ 99.9 mol % pure) at pressures of 8 and 12 MPa, temperatures of 35 and 40°C and PVP *K*-30 solution concentrations of 2% and 5% (CO_2 mole fraction ≥ 0.96)

were carried out. The SAS precipitation was unsuccessful because of the high solubility of the polymer in ethanol which redissolves any precipitated particles.

Gokhale et al. [56] have developed a new SAS process for the formation of polymer particles which utilizes a mixture of thermodynamically good and poor polymer solvents and enables one to manipulate the particle size and morphology by varying the good-to-poor solvent ratio. Experiments were conducted on PVP polymer of molecular weights 1,300,000 (*K*-90) and 360,000 (*K*-60) dissolved in binary mixtures of DCM (a good solvent) and acetone (a poor solvent) for micro-nozzles diameters from 10 μm to 127 μm, jet velocities ranging from 0.3 m/s to 20 m/s, and CO_2 pressures from 79 bar to 120 bar. They found that by increasing the acetone content of the acetone /DCM solvent mixtures, the size of the polymer particles is reduced from several hundreds to several tens of nanometers and their surface rugosity is practically eliminated. Based on these results, a mixture of thermodynamically good (DCM) and poor polymer solvents (acetone) was chosen in this thesis as a solvent for the SAS precipitation of PVP. To minimize the particle size of the precipitated particles, a mixture of acetone/DCM (80:20, v/v %) was used in this study. Gokhale et al. [56] concluded that the operation at a chamber pressure slightly above the critical points of CO_2 + acetone (Fig. 5.16) and CO_2 + DCM (Fig. 5.22) binary systems, favors a narrow particle size distribution.

5.4.2. Co-precipitation of Diflunisal with PVP *K*-10. SEM images

To have a clear image of the influence of PVP on diflunisal, PVP *K*-10 was precipitated alone from acetone/DCM (80:20, v/v %) at 35 °C and 8.5 MPa. PVP *K*-10 was supplied from Fluka. The other experimental conditions were solution concentration of 2 %, 1 mL/min solution flow rate, 20 g/min CO_2 flow rate, drying time required to fill 3 times the precipitation chamber and nozzle diameter of 100 μm. The liquid and CO_2 flow rates lead to a value of 0.97 for the CO_2 mole fraction in mixtures formed in the precipitation chamber. SEM images of PVP *K*-10 thus obtained are shown in Fig. 5.30. SEM images of SAS precipitated PVP *K*-10 reveal that the sample is formed by spherical nanoparticles.

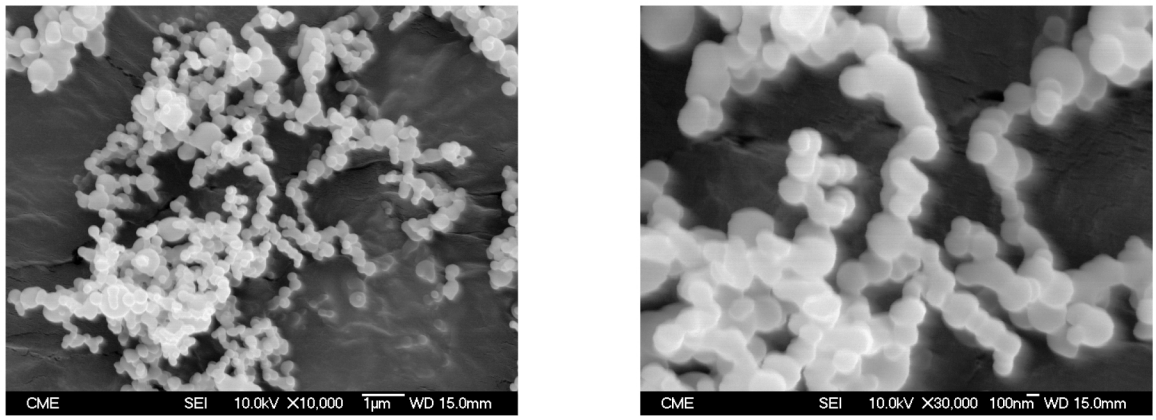

Fig. 5.30 SEM images of SAS PVP *K*-10 obtained at 35 °C, 8.5 MPa and concentration of 2%.

Analysis of the SEM images shows that the mean particle size of the precipitated polymer particles was 230 nm with standard deviation of 80 nm. Fig. 5.31 shows the particle size distribution of the precipitated polymer.

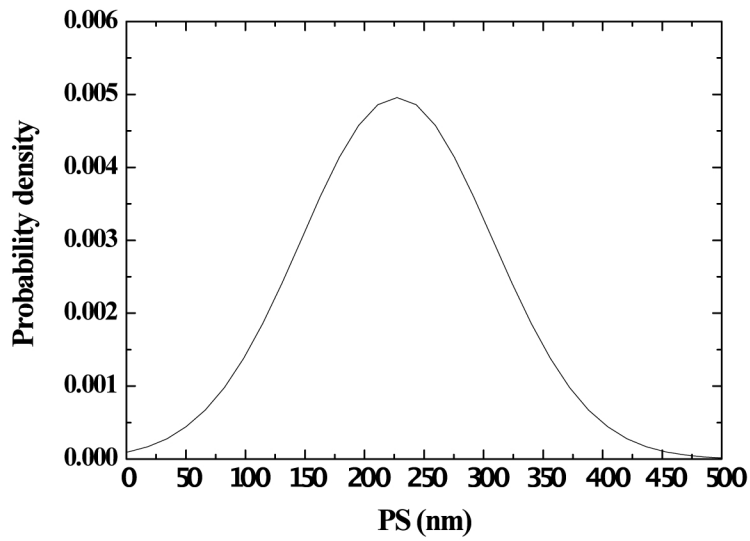

Fig. 5.31 Probability density of SAS PVP *K*-10 as a function of particle size.

Because of the successful micronization of PVP *K*-10 and diflunisal by SAS in the acetone/DCM mixture, the co-precipitation of both materials was carried out. Diflunisal was co-precipitated with PVP *K*-10 at a fixed weight ratio of (50:50) from acetone/DCM (80:20, v/v %) at different conditions. The experimental conditions are summarized in table 5.8. The presence of the polymer along with the target drug in the mixture of solvents makes the phase diagram of the system more complicated and the choice of the precipitation conditions cannot be based just in the binary CO_2 + organic solvent phase diagram. Therefore, a wide range of

temperature and pressure conditions and two different CO_2 mole fractions were attempted for the co-precipitation of diflunisal with PVP.

Table 5.8 Experimental conditions utilized in the co-precipitation of diflunisal with PVP *K*-10 at a weight ratio of (50:50) from acetone/DCM.

Exp.	*T* (°C)	Conc. (%)	*P* (MPa)	CO_2 flow rates (g/min)	Solution flow rate (mL/min)	Mole fraction
1	35	2	8.5	20	1	0.97
2	35	4	8.5			
3	35	4	9			
4	35	4	12			
5	35	2	15			
6	40	2	9			
7	40	4	9			
8	35	4	8	10	3	0.84
9	35	4	9			
10	35	4	10			
11	35	4	12			

The drying time was the time required to fill 3 times the precipitation chamber and it was ranged from (60- 120 min).

Experiments 1, 2, and 3, carried out at 0.97 CO_2 mole fraction and a temperature of 35 °C, pressure from 8 to 9 MPa and solution concentrations of 2 and 4 %, showed the formation of a viscous solution at the bottom of the precipitation chamber. In addition experiment 8, carried out at 0.84 CO_2 mole fraction and a temperature of 35 °C, pressure of 8 MPa and solution concentration of 4 %, showed the same result. These *T* and *P* conditions are very close to the critical conditions of both CO_2 + acetone and CO_2 + DCM. The fact that no precipitate was

obtained when carrying out the precipitation near the critical points of the CO_2 + organic solvent binary system may be attributed to the precipitation from a multi-phase region.

In experiment 9, a slight increase in pressure from 8 to 9 MPa with respect to experiment 8 led to a successful precipitation. Fig. 5.31 shows the SEM images of the SAS precipitated diflunisal + PVP *K*-10 co-precipitate obtained at experiment 9.

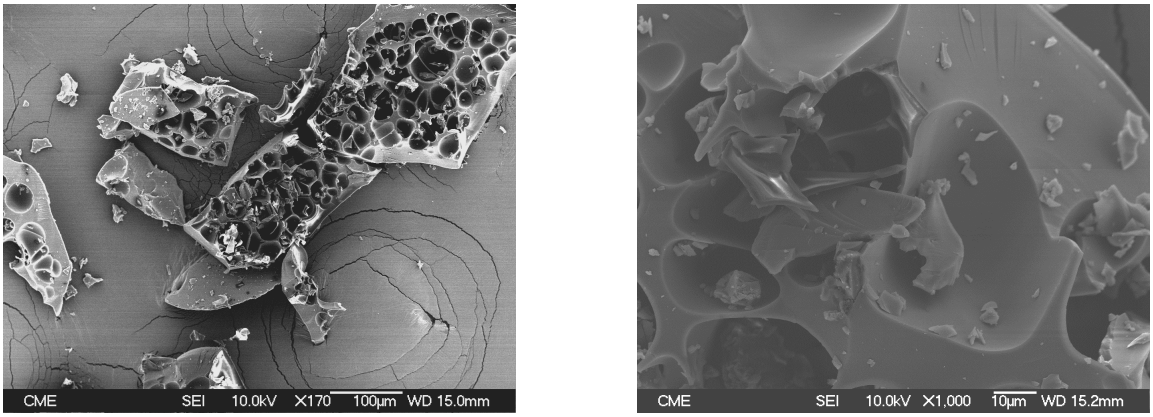

Fig. 5.31 SEM images of diflunisal + PVP *K*-10 co-precipitate obtained at 35 °C, 9 MPa, concentration of 4% and 0.84 CO_2 mole fraction (Exp. 9).

The morphology of the co-precipitated particles is completely different in comparison with the pure diflunisal and pure PVP precipitated previously. The SEM micrographs of the co-precipitate exhibit large porous blocks with smaller particles at the surface and in the holes. However, working at the same conditions of experiment 9 but at higher CO_2 mole fraction of 0.97 in experiment 3, a viscous solution as that previously mentioned was obtained. The large change observed with CO_2 concentration in this case may be related to the complicate phase diagram of the five-component mixture.

The effect of increasing temperature from 35 to 40 °C was studied in experiments 3 and 7. In this case, a very sticky precipitate was formed at 40 °C at the frit and it may be attributed to the plasticization of the PVP polymer at higher temperatures. Even after decreasing the solution concentration to 2 % at the same conditions (experiment 6) a sticky precipitate was observed.

The influence of pressure on the co-precipitated diflunisal + PVP *K*-10 was studied at a temperature of 35 °C and solution concentration of 4 % varying the pressure from 9 to 12

MPa at 0.84 CO_2 mole fraction (experiments 9, 10 and 11). The co-precipitates obtained at these conditions are shown in Fig. 5.31- 5.33.

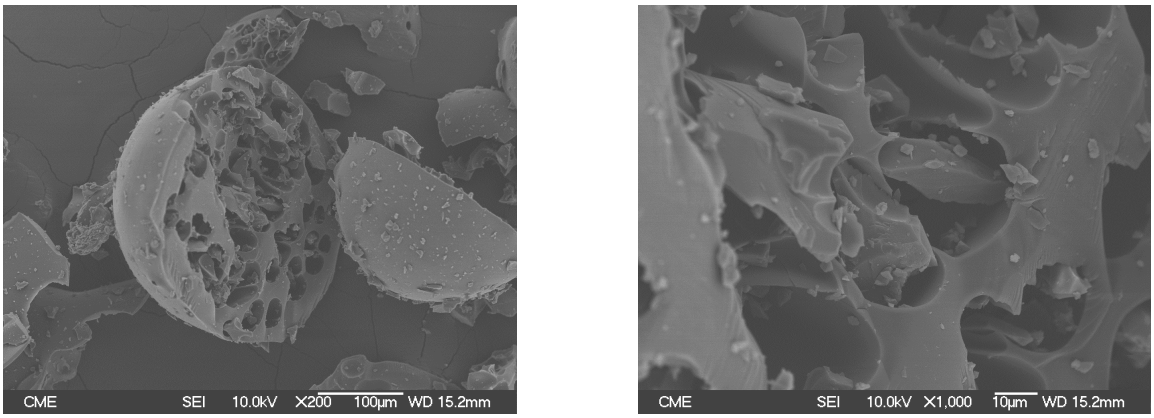

Fig. 5.32 SEM images of diflunisal + PVP *K*-10 co-precipitate obtained at 35 °C, 10 MPa, concentration of 4% and 0.84 CO_2 mole fraction (Exp. 10).

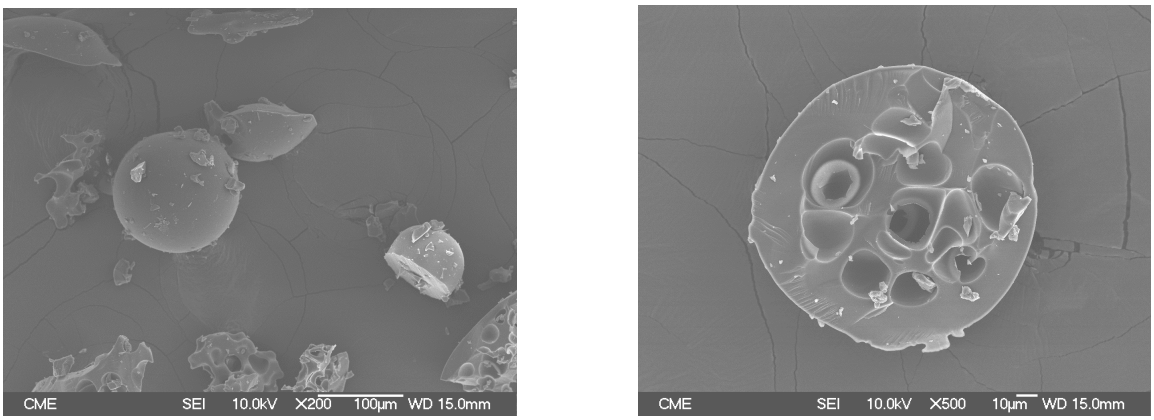

Fig. 5.33 SEM images of diflunisal + PVP *K*-10 co-precipitate obtained at 35 °C, 12 MPa, concentration of 4% and 0.84 CO_2 mole fraction (Exp. 11).

Comparing the SEM micrographs obtained at 10 and 12 MPa with those obtained at 9 MPa at the same temperature and mole fraction, the co-precipitates at the higher pressures have a more regular morphology with very large spherical particles. Porosity of the particles at these conditions however is slightly lower. The size of the spherical balloons obtained decreases with increasing the pressure. The mean size of the porous balloons obtained at 10 MPa was 100 µm while it was 60 µm at 12 MPa.

In addition, experiment 4 was carried out at a higher CO_2 mole fraction of 0.97 and at the same conditions of experiment 11 described previously. Fig. 5.34 shows the diflunisal + PVP *K*-10 co-precipitate obtained.

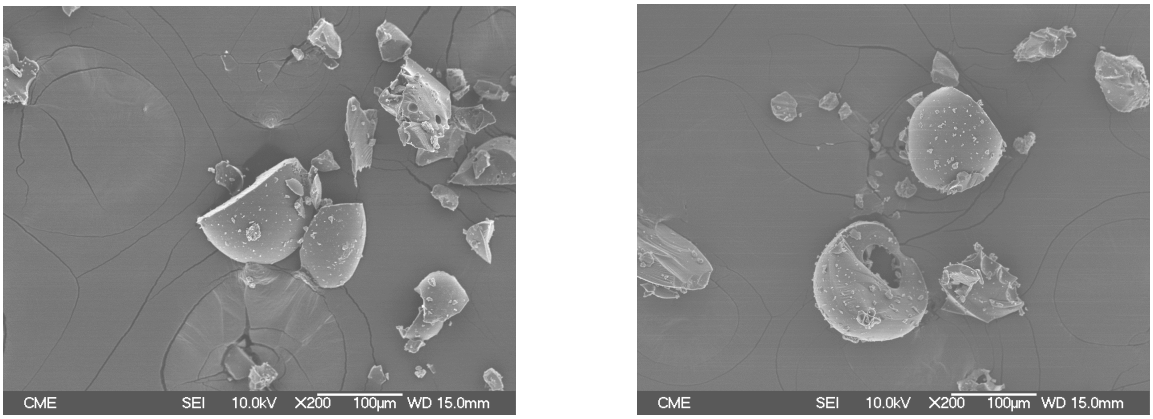

Fig. 5.34 SEM images of diflunisal + PVP *K*-10 co-precipitate obtained at 35 °C, 12 MPa, concentration of 4% and 0.97 CO_2 mole fraction (Exp. 4).

Spherical balloons were obtained with a slightly smaller mean size of 50 µm with respect to those obtained at 0.84 CO_2 mole fraction in experiment 11. In view of these results, the following experiments were performed at the higher CO_2 mole fraction.

As indicated in table 5.8, experiment 5 was carried out at 0.97 CO_2 mole fraction, 35 °C, 15 MPa and solution concentration of 2 %. Fig. 5.35 (a-b) shows the SEM images of diflunisal + PVP *K*-10 co-precipitate obtained at 15 MPa at two different magnifications.

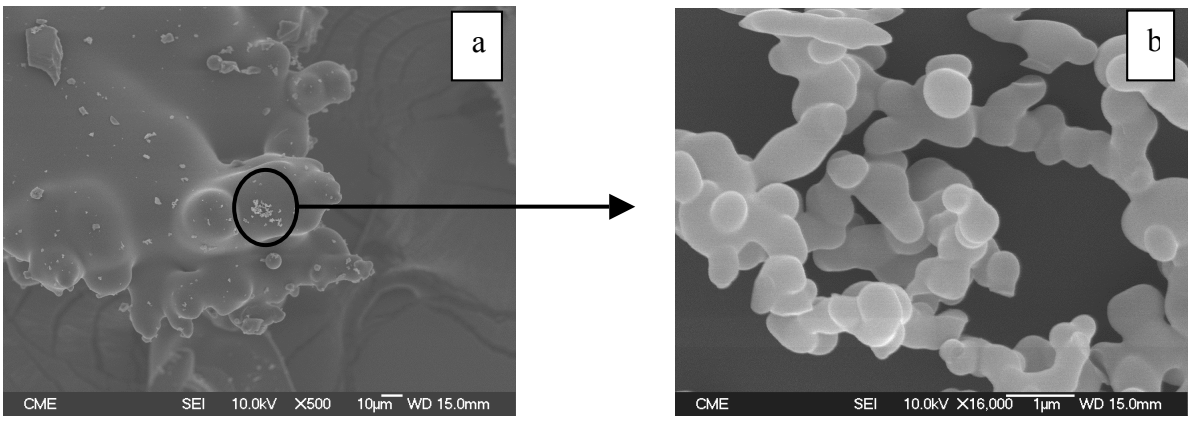

Fig. 5.35 SEM images of diflunisal + PVP *K*-10 co-precipitate obtained at 35 °C, 15 MPa, concentration of 2% and 0.97 CO_2 mole fraction (Exp. 5).

By increasing the pressure up to 15 MPa, a fluffy powder was also obtained. However, SEM images revealed that the particles precipitated forming a block, Fig. 5.35a. This coalescence of particles may be attributed to plasticization of PVP in the CO_2 mixture at high pressure. The SEM image at a higher magnification, Fig. 5.35b, showed the presence of nanoparticles spread on the surface.

Although results of the co-precipitation of diflunisal and PVP *K*-10 are not very encouraging, it is very important to underline that the crystallinity of the diflunisal disappeared in the co-precipitate in contrast to that of the pure diflunisal precipitated from the same solvent mixture. Therefore, the dissolution rate of the composite material in comparison to the raw drug is expected to increase. However, further increase of pressure in the precipitation chamber to 15 MPa results in particle coalescence.

5.4.3. Co-precipitation of Diflunisal with PVP *K*-30. SEM images

It is well known that the plasticizing effect of CO_2 on polymers decreases with increasing polymer molecular weight, therefore to avoid particle coalescence we decided to use PVP *K*-30 in the co-precipitation. PVP *K*-30 has a molecular weight 4 times higher than PVP *K*-10. In view of the experimental conditions previously discussed, the temperature of 35 °C, pressure of 12 MPa, solution concentration of 4 % and a value of 0.97 CO_2 mole fraction were chosen to be the starting experimental conditions. Co-precipitation of PVP *K*-30 and diflunisal was carried out at a weight ratio of (50:50) from acetone/DCM (80:20, v/v %). PVP *K*-30 was supplied from Fluka. The experimental conditions are described in table 5.9. Two different solution concentrations of 2 and 4% and pressures up to 14 MPa were tested.

Table 5.9 Experimental conditions utilized in the co-precipitation of diflunisal with PVP *K*-30 at a weight ratio of (50:50) from acetone/DCM.

Exp.	*T* (°C)	Conc. (%)	*P* (MPa)	CO_2 flow rates (g/min)	Solution flow rate (mL/min)	Mole fraction
12	35	4	12	20	1	0.97
13	35	2	12			
14	35	2	14			

The drying time was the time required to fill 3 times the precipitation chamber and it was ranged from (50- 60 min).

The influence of the polymer molecular weight in the co-precipitate was studied by comparison of experiments 4 and 12. Fig. 5.34 and 5.36 show the SEM images of diflunisal + PVP co-precipitate obtained by using PVP *K*-10 and *K*-30, respectively. All the other experimental conditions are coincident. Much better results were obtained using PVP *K*-30 and small nanoparticles were obtained.

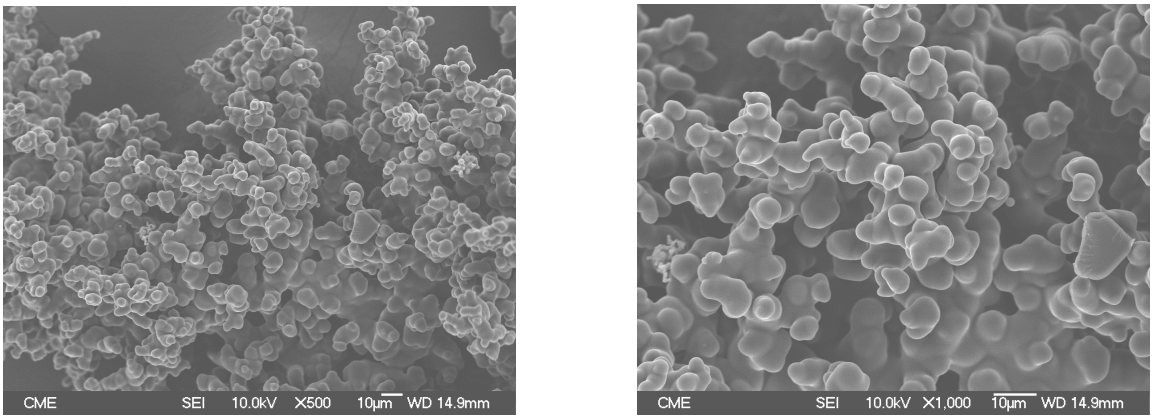

Fig. 5.36 SEM images of diflunisal + PVP *K*-30 co-precipitate obtained at 35 °C, 12 MPa, concentration of 4% and 0.97 CO_2 mole fraction (Exp. 12).

As observed previously, the crystallinity of the diflunisal disappeared during the co-precipitation with PVP *K*-30 with respect to the SAS precipitated diflunisal from the same solvent mixture. SEM micrographs of the diflunisal + PVP *K*-30 co-precipitate exhibit spherical microparticles slightly aggregated. The mean particle size of the diflunisal + PVP *K*-30 co-precipitate is at least 5 times smaller than that of the co-precipitate obtained using PVP *K*-10. The polymer molecular weight was found to have a profound effect on the mean particle size. The increase of the polymer molecular weight results in an important decrease in the particle size.

SEM images obtained from experiment 13 carried out at a temperature of 35 °C, a pressure of 12 MPa, solution concentration of 2 % and a value of 0.97 CO_2 mole fraction are shown in Fig. 5.37.

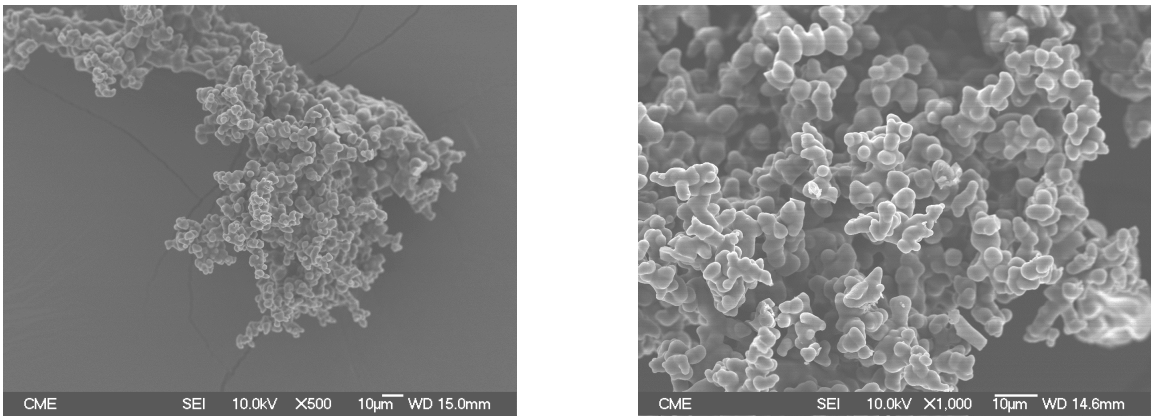

Fig. 5.37 SEM images of diflunisal + PVP *K*-30 co-precipitate obtained at 35 °C, 12 MPa, concentration of 2% and 0.97 CO_2 mole fraction (Exp. 13).

A decrease in solution concentration from 4 to 2 % also resulted in a decrease in the co-precipitate particle size as shown in Fig. 5.36 and 5.37. A smaller particle size was observed in this case in comparison with that obtained in experiment 12.

As mentioned before in many parts of this study, in SAS process, the particle size generally decreases with increasing pressure. However, the increase of pressure in the co-precipitation of diflunisal + PVP *K*-10 up to 15 MPa resulted in particle coalescence. Therefore, a pressure of 14 MPa at the same condition of experiment 13 was tested to see the influence of a further increase in pressure on the mean particle size of the drug + PVP *K*-30 polymer co-precipitate. SEM images of the diflunisal + PVP *K*-30 co-precipitate obtained at 35 °C, 14 MPa, concentration of 2 % and 0.97 CO_2 mole fraction are presented in Fig. 5.38.

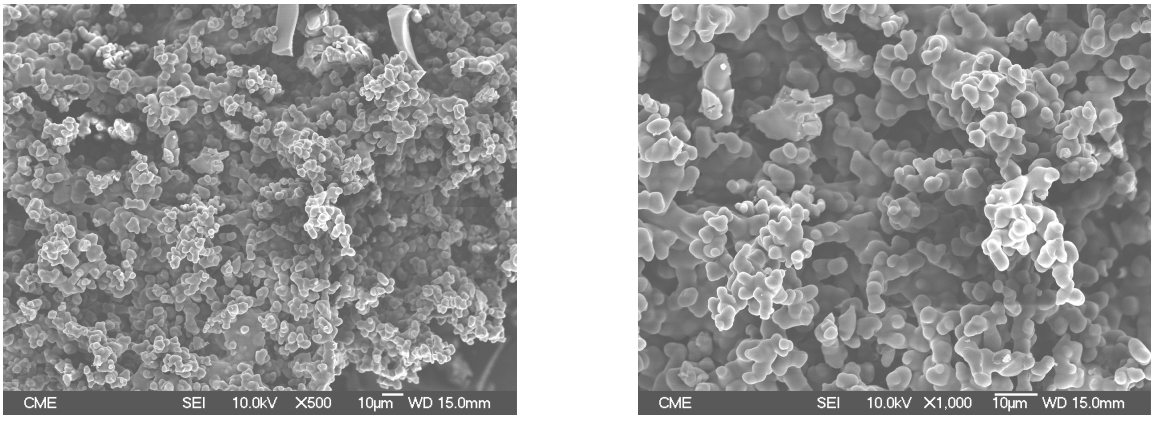

Fig. 5.38 SEM images of diflunisal + PVP *K*-30 co-precipitate obtained at 35 °C, 14 MPa, concentration of 2% and 0.97 CO_2 mole fraction (Exp. 14).

At these concentrations spherical particles are also obtained. Particle size is slightly smaller than that observed at the lower pressure. The mean particle size of the diflunisal + PVP *K*-30 was found to decrease slightly with increasing the pressure of the precipitation chamber up to 14 MPa without coalescence with respect to particles obtained at experiment 13 and experiment 5. For the larger molecular weight PVP *K*-30, the effect of the supercritical CO_2 + solvent mixture into the polymer is not noticeable and as in previous experiments, slightly smaller particle are obtained at the highest pressure.

For comparison, PVP *K*-30 was precipitated alone from acetone/DCM (80:20, v/v %) at a temperature of 35 °C, pressure of 14 MPa and solution concentration of 2%. The other experimental conditions were 1 mL/min solution flow rate, 20 g/min CO_2 flow rate, drying time 60 min and nozzle diameter of 100 μm. The liquid and CO_2 flow rates lead to a value of 0.97 for the CO_2 mole fraction in mixtures formed in the precipitation chamber. SEM images of PVP *K*-30 thus obtained are shown in Fig. 5.39. The SAS precipitated PVP *K*-30 exhibits spherical nanoparticles smaller than those obtained for PVP *K*-10.

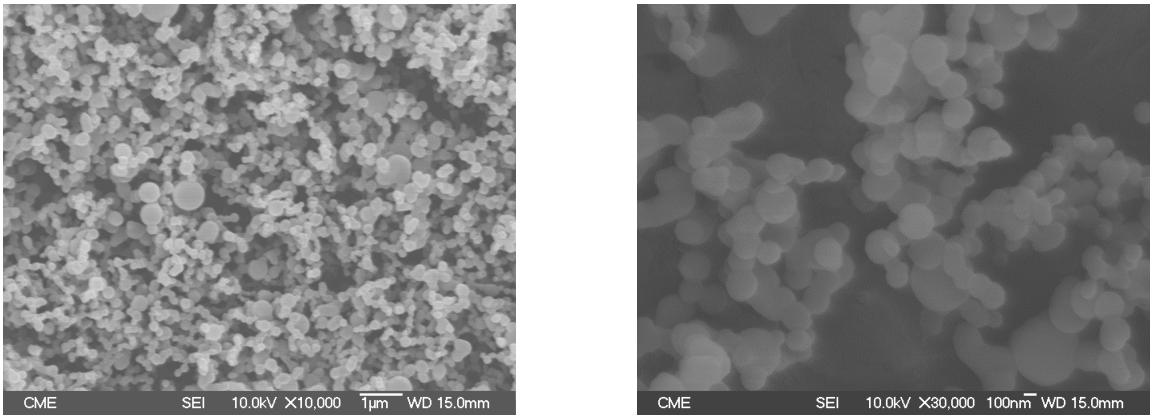

Fig. 5.39 SEM images of SAS PVP *K*-30 obtained at 35 °C, 14 MPa and concentration of 2%.

The mean particle size of the precipitated polymer was 210 nm with standard deviation of 90 nm. Fig. 5.40 shows the particle size distribution of the precipitated polymer.

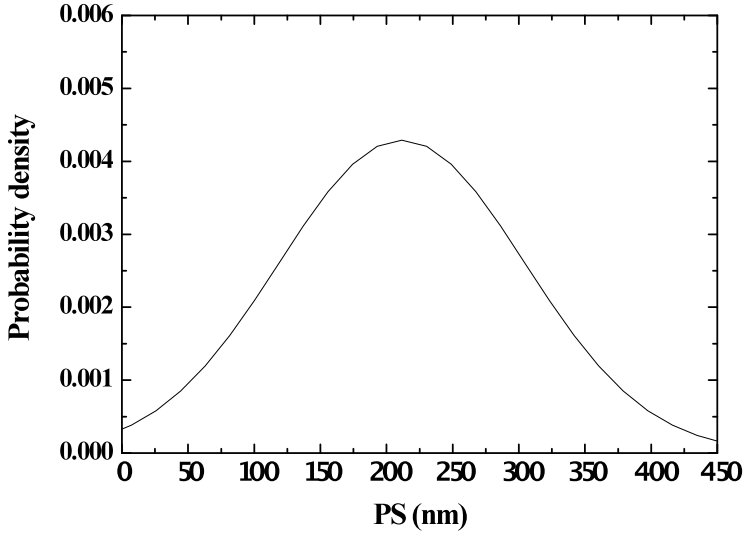

Fig. 5.40 Probability density of SAS PVP *K*-30 as a function of particle size.

The influence of the drug: polymer weight ratio on the properties of the diflunisal + PVP *K*-30 co-precipitates from acetone/DCM (80:20, v/v %) was studied at three different drug to polymer weight % ratios of 75:25, 50:50 and 25:75 at a temperature of 35 °C, a pressure of 14 MPa, solution concentration of 2 % and a value of 0.97 CO_2 mole fraction. The experimental conditions are described in table 5.10.

Table 5.10 Experimental conditions utilized in the co-precipitation of diflunisal with PVP *K*-30 at different drug: polymer ratios from acetone/DCM (80:20, v/v %).

Exp.	***T* (°C)**	**Conc. (%)**	***P* (MPa)**	**Weight ratio**	**CO_2 flow rates (g/min)**	**Solution flow rate (mL/min)**	**Mole fraction**
15	35	2	14	75:25	20	1	0.97
14	35	2	14	50:50			
16	35	2	14	25:75			

The drying time was the time required to fill 3 times the precipitation chamber (close to 60 min). The co-precipitates obtained at the three different drug: polymer ratios are shown in Figs. 5.38, 5.41 and 5.42.

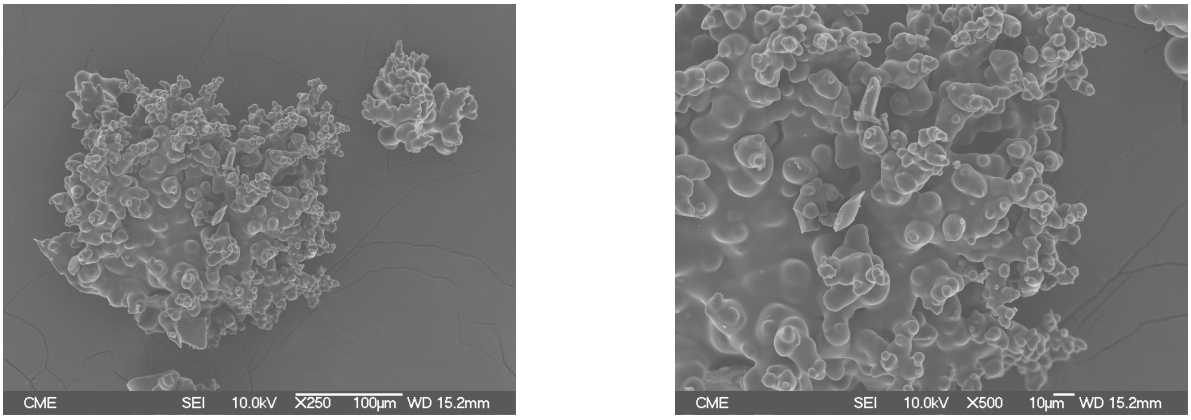

Fig. 5.41 SEM images of diflunisal + PVP *K*-30 co-precipitate obtained at (75:25, drug: polymer wt. %) (Exp.15). Other conditions are the same as Exp.14.

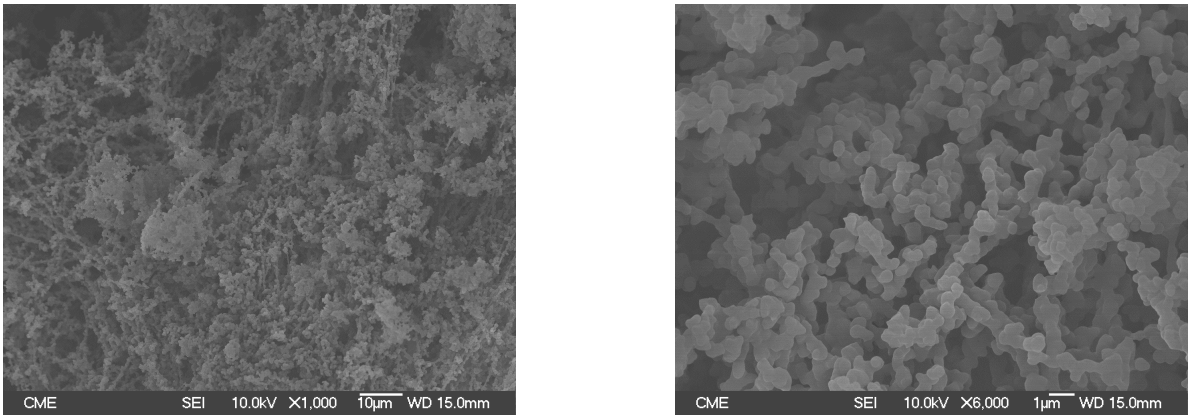

Fig. 5.42 SEM images of diflunisal + PVP *K*-30 co-precipitate obtained at (25:75, drug: polymer wt. %) (Exp.16). Other conditions are the same as Exp.14.

The crystallinity of the diflunisal disappeared in the co-precipitate even at the lowest polymer content. The co-precipitate obtained at experiment 15 showed spherical particles with mean particle size less than 10 µm that are highly aggregated forming a block. On the other hand, the co-precipitate obtained at 25:75, drug: polymer wt. % showed loose spherical particles of mean particle size of 460 nm with very little aggregation with respect to those obtained at 50:50, drug: polymer wt. %. SEM images presented in Figs. 5.38, 5.41 and 5.42 demonstrate how the aggregation and the mean particle size decrease with an increase of the polymer content. The trend observed is in agreement with that described by Lim et al. [51] for the co-precipitation of IDMC with PVP *K*-360 from acetone/DCM at 85 bar and 35 °C using supercritical carbon dioxide as antisolvent at drug to polymer ratios of 85:15, 50:50 and 20:80.

5.4.4. Characterization of Diflunisal-PVP K-30 Co-precipitates

The diflunisal + PVP K-30 composites obtained from acetone/DCM (80:20, v/v %) at three different drug to polymer ratios of 75:25, 50:50 and 25:75 at a temperature of 35 °C, pressure of 14 MPa, solution concentration of 2 % and a value of 0.97 CO_2 mole fraction (experiments 14-16) were characterized further using XRD, FTIR and DSC as well as the dissolution profile in comparison with the pure drug.

5.4.4.1. Characterization Using X-ray Diffraction

X-ray powder diffraction was performed for the pure materials and the SAS co-precipitates at the three weight ratios obtained from acetone/DCM to investigate the state of the drug (amorphous or crystalline). The crystallinity of materials is indicated by the presence of sharp peaks that are absent in the case of amorphous state. Samples were scanned over the range of 5-50 degrees 2θ as shown in Fig 5.43.

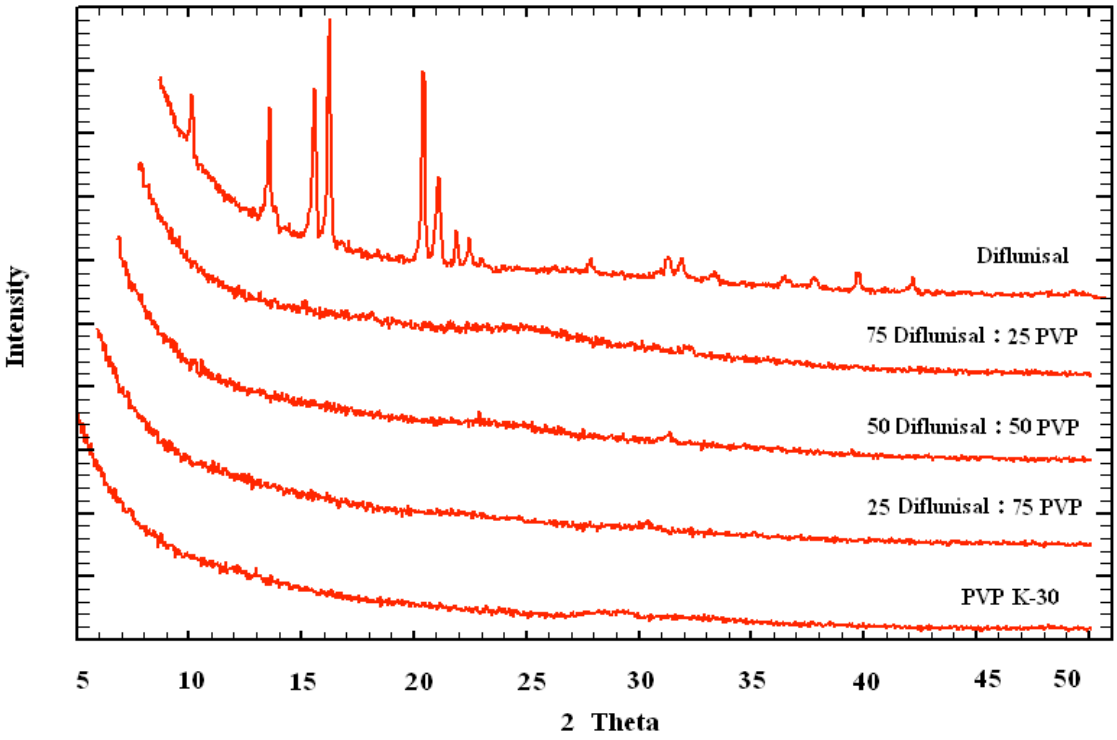

Fig. 5.43 XRD pattern of diflunisal, PVP *K*-30, and three diflunisal + PVP *K*-30 composites obtained by SAS at 35 °C, 14 MPa, concentration of 2% and 0.97 CO_2 mole fraction.

XRD patterns show that the SAS processed diflunisal is a crystalline material while the SAS precipitated PVP *K*-30 is an amorphous material. The crystallinity of the diflunisal disappears in the co-precipitate with PVP *K*-30 in comparison with SAS precipitated diflunisal from the same solvent mixture. The amorphousness of the co-precipitates did not

change when the PVP *K*-30 content was increased from 25 % to 75 %. The inhibitory effect of the polymer on the crystallinity of the diflunisal may be attributed to the interaction of the drug with the PVP polymer resulting in a change in the molecular mobility of the drug, ultimately leading to an amorphous form of diflunisal.

5.4.4.2. Characterization Using Infrared Spectroscopy

The nature and extent of interactions between diflunisal and the PVP *K*-30 polymeric carrier in the solid state are examined by FTIR spectrometer. Mixing of two the components at the molecular level will cause changes in the oscillating dipole of the molecules. This will manifest itself as changes in the frequency and bandwidth of interacting groups in the spectrum. FTIR spectra have been recorded for diflunisal, PVP *K*-30, and the three diflunisal + PVP *K*-30 composites obtained at 35 °C and 14 MPa over the range of 4000-450 cm^{-1} as shown in Fig 5.44. For comparison purposes, the FTIR- spectra were expanded in the 2000-600 cm^{-1} range.

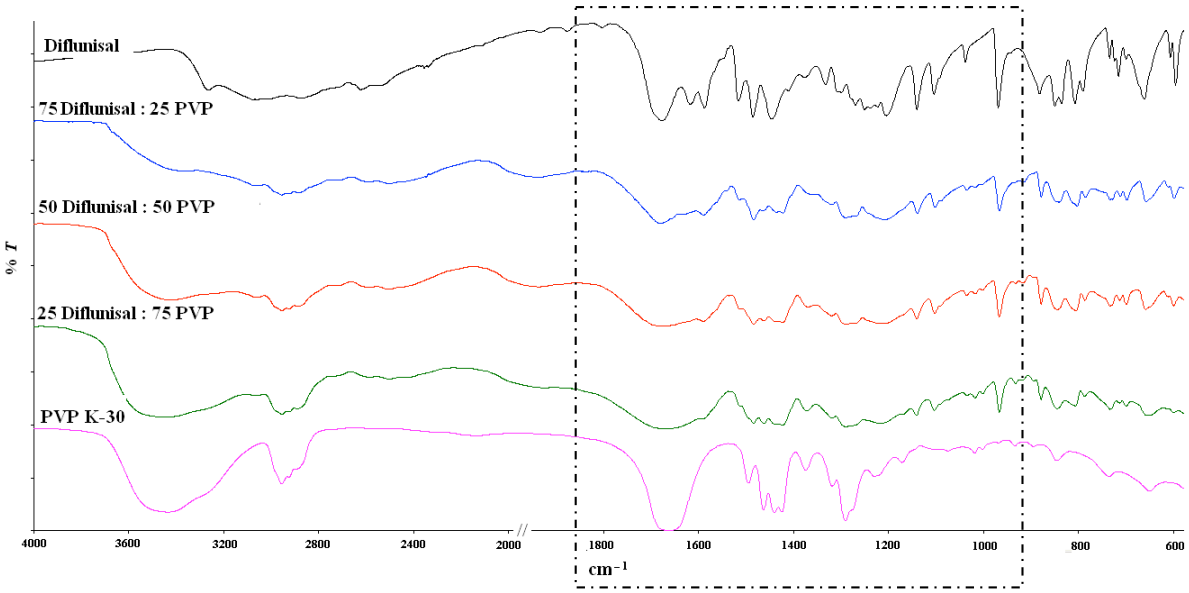

Fig. 5.44 FTIR-spectrum of diflunisal, PVP *K*-30, and three diflunisal + PVP *K*-30 composites obtained by SAS at 35 °C, 14 MPa, concentration of 2% and 0.97 CO_2 mole fraction.

The functional groups in the FTIR-spectrum showed band shifts and broadening compared to the spectra of the pure drug and PVP *K*-30 which may be attributed to the interaction of the functional groups. PVP is capable of forming H-bond either through the nitrogen or the carbonyl group on the pyrole ring. However, the steric hindrance prevents the lone pair of nitrogen to participate in the intermolecular interactions, thus making the carbonyl group more favorable for H-bonding [57]. On the other hand, diflunisal is capable of forming H-

bond either through the fluor, the carbonyl group, the hydroxyl group or carboxylic O-H group.

In the region of 4000-2000 cm^{-1} diflunisal exhibits a band at about 3400–3200 cm^{-1} due to the stretching of the carboxylic O-H group which is subjected to intermolecular hydrogen bonding. The aromatic C-H stretch interferes with the O-H band and a broad multiplet peak at about 3200–2800 cm^{-1} is observed. In the same region, the PVP polymer shows two broad bands one of them is split, the first centered at 3500 cm^{-1} and could be attributed to the presence of water due to the high hydrophilicity of the polymer, and the second at about 3100-2900 cm^{-1} is related to the aliphatic C-H stretch. In the carbonyl frequency region, the drug shows a strong band at 1690 cm^{-1} associated with the CO stretch in the carboxylic group, while the polymer gives a broad strong band (1660 cm^{-1}) due to the CO stretch in the cyclic amide. The broadening of the band corresponding to the diflunisal carbonyl group (1690 cm^{-1}) in the three diflunisal + PVP *K*-30 composites suggests the formation of intermolecular hydrogen bonding between the diflunisal and PVP *K*-30. In the low-frequency region (1600–600 cm^{-1}) the bands observed in the three co-precipitates belong to both the polymer and the drug, but some bands of diflunisal and the polymer have either disappeared or reduced their intensity significantly. For example, the C-H aliphatic bending vibration of the polymer (1260 cm^{-1}) has almost disappeared; this could be attributed to steric hindrance resulting from the interaction between the drug and the PVP through the carbonyl group of the polymer. The C-F bending vibration of the polymer (1000-900 cm^{-1}) has also reduced its intensity. All these results might indicate that a significant change in the total symmetry of the drug molecule in the solid polymer matrix has occurred in the co-precipitates.

5.4.4.3. Characterization Using Differential Scanning Calorimetry and Thermogravimetric Analysis (TGA)

In order to get further evidence of the possible interaction of diflunisal with PVP and to understand better the structure of the co-precipitates, DSC and TGA studies of SAS co-precipitated diflunisal + PVP *K*-30 from acetone/DCM (80:20, v/v %) as well as the pure materials were performed from room temperature to 500 °C at a heating rate of 5 °C/min using open aluminum crucibles. This study was carried out using a simultaneous DSC and TGA device, the so-called SDT apparatus.

The DSC thermograms of the pure materials and the three co-precipitates are shown in Fig. 5.45. Comparison of the DSC diffractograms gives an idea about the crystallinity of the drug in composites. The thermal behavior was studied by heating 10 mg of the sample at a scan rate of 5 °C/min in an open sample aluminum pan and the investigation was carried out over the temperature range 25 to 500 °C.

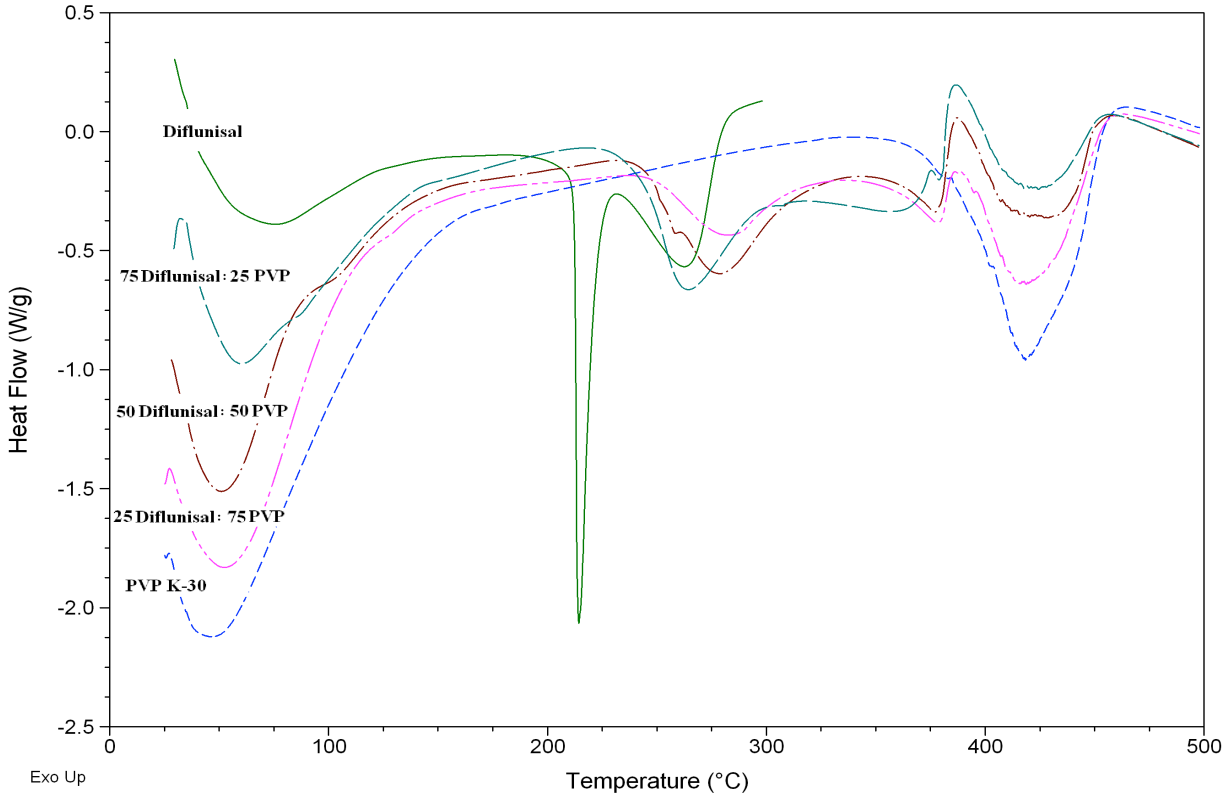

Fig. 5.45 DSC thermograms of diflunisal, PVP *K*-30, and three diflunisal + PVP *K*-30 composites obtained by SAS at 35 °C, 14 MPa, concentration of 2% and 0.97 CO_2 mole fraction.

The DSC thermogram of the pure diflunisal has three peaks. Although diflunisal is not hydrophilic, a broad peak appeared at about 50-75 °C which could be attributed to the presence of traces of moisture in the housing furnace of the SDT device and working in an open aluminum pan. This peak did not appear in the thermogram obtained by the DSC apparatus for the same sample, Fig. 5.26. The second one is a very sharp endothermic peak at 212.46 °C that represents the melting point of the drug. This point was determined using the same criteria as that used in the determination of the melting point of the raw drug. The third one appears at 270 °C and it is due to the complete decomposition of the drug. On the other hand, the thermal behavior of the polymer is that expected for a hygroscopic and amorphous substance. An extreme endothermal effect is shown in the 25-75 °C range due to polymer dehydration. Then, one could expect to see the glass transition of the PVP polymer as

mentioned previously in the introduction chapter. The glass transition temperature of the PVP polymer can be estimated using the *K*-value and it was found for PVP *K*-30 to be 164 °C. However, the presence of a large amount of water in the polymer hinders the glass transition temperature which could not be observed in the DSC. The polymer only showed a second peak associated to its decomposition at 415 °C. In addition, the co-precipitates thermograms resembled that of the pure polymer; the melting point of the drug at 212 °C is not observed which confirms the destruction of the crystalline state of the drug in the solid polymer matrix. Furthermore, the hygroscopic property of the amorphous polymer appeared as a highly endothermic peak in 25-75 °C. The endothermic effect due to the dehydration of the polymer with heating is increased with increasing PVP *K*-30 content. For the composite materials the broad band due to the loss of water also showed a shoulder at 75-125 °C which shifted to a higher temperature as the concentration of PVP increased. This may suggests the presence of water molecules in the composite material in a different form to that found in PVP and that found in pure diflunisal. The three co-precipitates showed two decomposition peaks one attributed to the drug and the other one attributed to the polymer. The broadening in the decomposition peak of the drug and the polymer could be attributed to the intermolecular interaction between diflunisal and PVP *K*-30. Furthermore, there was a clear shift of the decomposition temperature of the drug with increasing the concentration of the polymer at higher temperatures which also supports the strong interaction between diflunisal and the PVP *K*-30.

The glass transition temperatures of the pure materials and the drug in the co-precipitate obtained at drug to polymer ratio 50:50 were examined using differential scanning calorimetry. The thermal behavior was studied by heating 5 mg of the sample at a scan rate of 5 °C/min in a covered sample aluminum pan with a hole under nitrogen gas flow. The DSC thermograms of SAS processed diflunisal, PVP *K*-30 and co-precipitate are shown in Fig. 5.46. The investigation was performed in two heating ramps. The first ramp was carried out over the temperature range -20 to 125 °C to eliminate the interference of dehydration peak then the sample was equilibrated at -20 °C. After that the second heating ramp was started at the same heating rate and ended at 250 °C. Fig. 5.46 represents the DSC thermograms of the second ramps only.

Glass transition peaks appeared at 99.13 °C and 175.73 °C in the DSC thermograms of the the 50:50 co-precipitate and pure polymer, respectively. On the other hand, this peak did not appear in the DSC thermogram of the pure drug. The sharp endothermic peak that represents

the melting point of the drug did not appear in the DSC thermograms of the 50:50 co-precipitate; this is a further evidence of the amorphization of diflunisal by co-precipitation with PVP *K*-30.

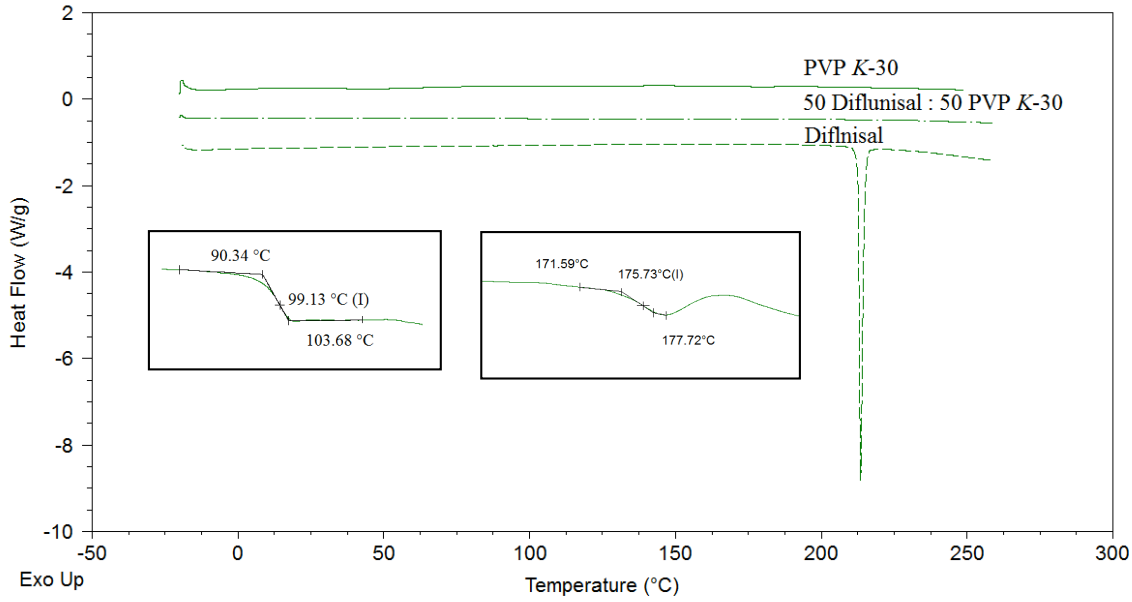

Fig. 5.46 DSC thermograms of diflunisal, PVP *K*-30, and 50 diflunisal : 50 PVP *K*-30 composite obtained by SAS at 35 °C, 14 MPa, concentration of 2% and 0.97 CO_2 mole fraction.

Thermogravimetric Analysis curves of the pure materials and the three co-precipitates were obtained simultaneously with the DSC thermograms at the same working conditions as shown in Fig. 5.47. TGA measures the amount and rate of change in the weight of a material as a function of temperature or time in a controlled atmosphere. Measurements were carried out primarily to determine the composition of the materials and to predict their thermal stability at temperatures up to 500 °C. TGA curves of the SAS processed diflunisal and PVP *K*-30 exhibited 2.2 % and 9.4 % weight loss, respectively, in the 25-75 °C range due to the dehydration of the pure materials. The decomposition of the pure drug started very early in comparison to the decomposition of the polymer. Diflunisal started to decompose at 180 °C and almost decomposed at 290°C forming a yellow solid residue while PVP *K*-30 started to decompose at 350 °C and almost decomposed at 460 °C forming a black solid residue.

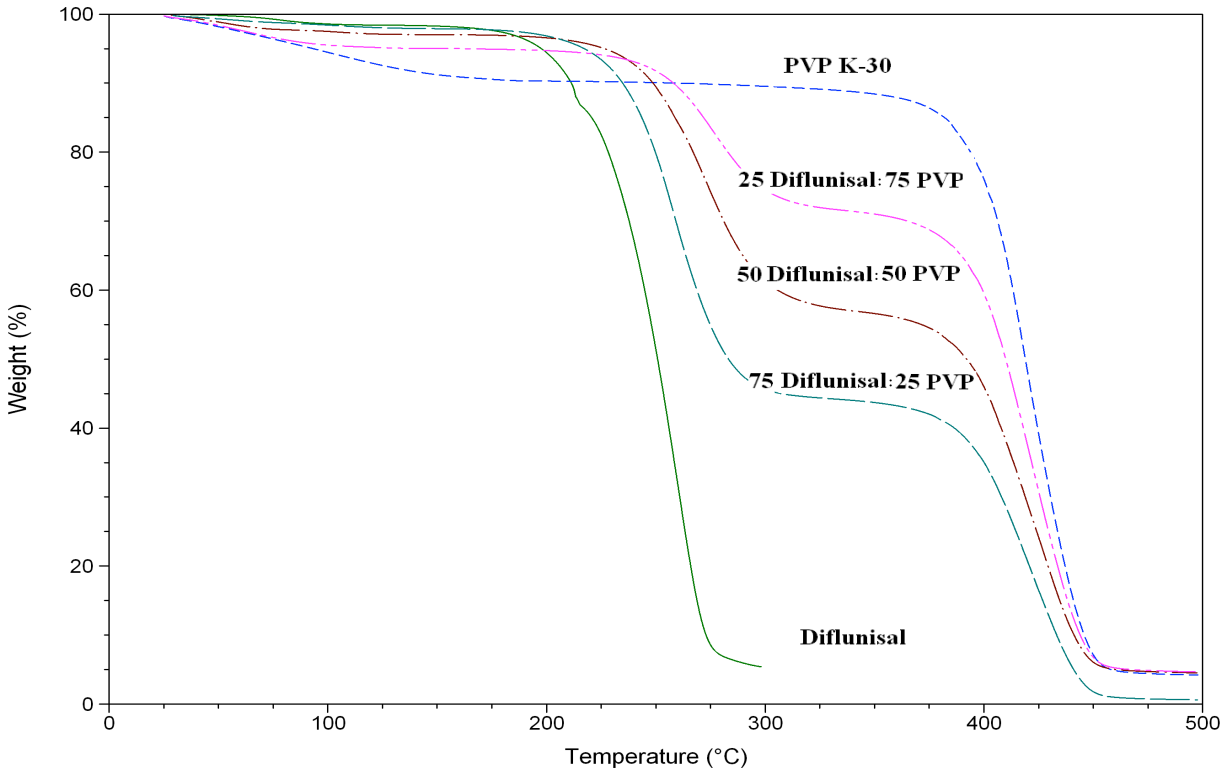

Fig. 5.47 TGA curves of diflunisal, PVP *K*-30, and three diflunisal + PVP *K*-30 composites obtained by SAS at 35 °C, 14 MPa, concentration of 2% and 0.97 CO_2 mole fraction.

TGA curves of the three composites showed that the rate of decomposition decreased with increasing the polymer content and that the compositions of the SAS co-precipitates were close to the feed compositions. TGA curves of the diflunisal + PVP K-30 composites obtained at drug to polymer ratios of 75:25, 50:50 and 25:75 showed weight loss of 1.6 %, 2.8 % and 4.6 %, respectively, in 25-75 °C range due to dehydration of composites. The decomposition process of the co-precipitates took place in two steps. The first step started at a temperature very close to the starting decomposition temperature of the drug and the second one started also very close to that of the polymer. From the weight losses of TGA drug to polymer weight ratios of 61.6:38.4, 45.3:54.7 and 25.5:74.5 were obtained. The co-precipitates almost decomposed completely at 460 °C forming a black solid residue similar to that of PVP *K*-30.

The results obtained from XRD, IR, DSC and TGA, indicated that the crystallinity of diflunisal disappeared with the co-precipitation process which could be attributed to the incorporation of the drug within the polymer at a molecular level. Generally the dissolution rate of an amorphous substance is faster than the crystalline one; therefore, the dissolution rate of the co-precipitates in comparison to the raw drug is expected to increase.

There is an agreement between the results obtained in this study and those given in the literature for the influence of the PVP polymer on drug crystallinity. The disappearance of drug crystallinity by the co-precipitation with the PVP polymer found in this study was previously reported [37, 51-55]. In addition, in this work amorphous diflunisal was generated by co-precipitation with only 25 wt. % PVP polymer while 50 wt. % PVP was used to generate amorphous drug by Majerik et al. [37], Lim et al. [51], Badens et al. [52] and Uzun et al. [54]; 60 wt. % PVP by Corrigan and Crean [55] and 80 wt. % PVP by Wu et al. [53]. As to the co-precipitate morphology, our results are better than those reported by Majerik et al. [37] and Badens et al. [52], who did not obtained spherical particles. This could be attributed to the intermolecular bonding between the PVP polymer and the drug; with increasing the intermolecular bonding, the amorphous co-precipitates form at lower PVP content. Furthermore, for a given drug to polymer ratio, the mean particle sizes obtained in this study are smaller than those obtained by Uzun et al. [54]; Corrigan and Crean [55] and close to that obtained by Lim et al. [51] and Wu et al. [53].

5.4.5. Dissolution Profiles of Co-precipitates

The dissolution profiles of the diflunisal + PVP *K*-30 composites obtained at drug to polymer ratios of 75:25, 50:50 and 25:75 from acetone/DCM at 35 °C, 14 MPa and concentration of 2% were studied. Dissolution tests were carried out following the same procedure described in the dissolution experiments of the untreated and SAS processed diflunisal. Aliquots of 5 mL were taken at 5 to 90 min at regular time intervals and were analyzed using a UV/VIS spectrophotometer. Dissolution profiles are shown in Fig. 5.48.

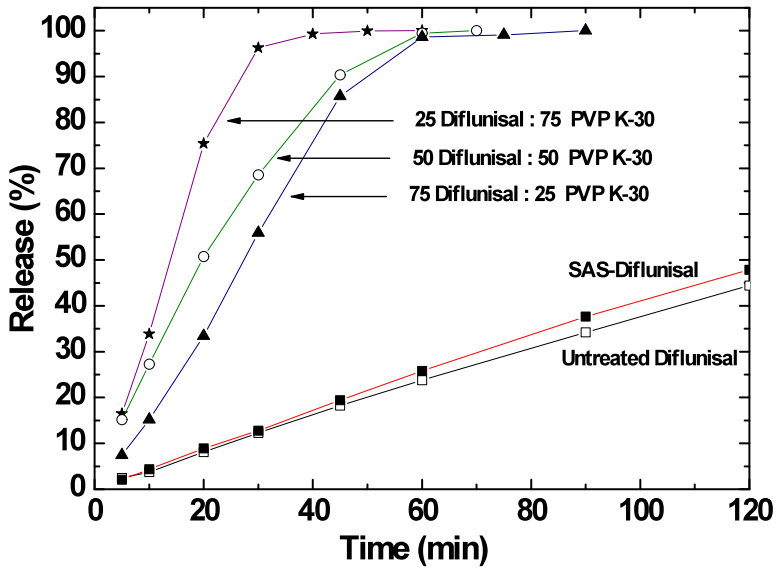

Fig. 5.48 Dissolution profile of diflunisal + PVP *K*-30 co-precipitates obtained at 35 °C, 14 MPa and concentration of 2% in comparison with the untreated and SAS processed diflunisal dissolution profiles.

For comparison purposes, untreated and SAS processed diflunisal profiles are also shown here. All the dissolution rates of the diflunisal + PVP *K*-30 co-precipitates are higher than those of the untreated and SAS processed diflunisal. For a given time, the drug release increased with increasing PVP *K*-30 content; the highest dissolution rate was observed in the 25 diflunisal: 75 PVP *K*-30 co-precipitate. After 10 min, the percentage drug release of diflunisal + PVP *K*-30 composites obtained at drug to polymer ratios of 75:25, 50:50 and 25:75 were approximately 7 %, 15 % and 34 %, respectively, and these values increased up to 15 %, 27 % and 75 %, respectively, after 20 min. On the other hand, approximately 4 % and 4 % of the untreated and the SAS processed drug, respectively, were dissolved within 10 min and these values increased up to 8 % and 9 %, respectively, after 20 min. As previously mentioned, the linear tendency of the dissolution rate was lost with time as a result of partial dissolution of the disk losing the zero-order kinetics. Approximately 75 % of the drug was dissolved after 20-30 min for diflunisal + PVP *K*-30 composites. Furthermore, approximately 99 % of the drug was dissolved after 40 min for 25:75 diflunisal + PVP *K*-30 composite. The improvement of the dissolution rate of diflunisal by co-precipitation with PVP *K*-30 is in agreement with the data obtained by Rodríguez-Espinosa et al. [38] for diflunisal + PVP *K*-30 co-precipitate obtained by solid dispersion technique. They studied the dissolution kinetics of diflunisal form II, drug-polymer physical mixture (70:30 wt %) and three solid dispersions obtained by dissolving diflunisal at diflunisal: PVP weight ratios of 80:20, 70:30 and 50:50 as shown in Fig. 5.49.

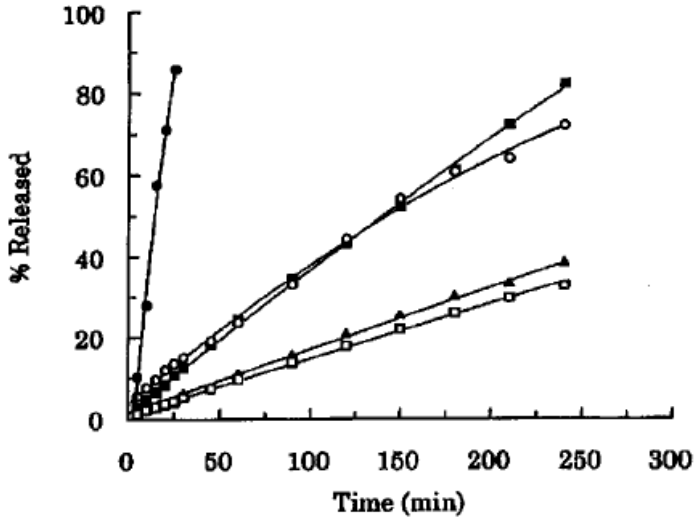

Fig. 5.49 Dissolution profile of diflunisal form II (□), physical mixture 70:30 (▲), co-precipitate 70:30 (○), co-precipitate 80:20 (■) and co-precipitate 50:50 (●) [38].

Rodríguez-Espinosa et al. [38] found that the dissolution rates of the co-precipitates were faster than those of the physical mixture and the pure drug. The dissolution rate of the co-

precipitates increased with an increase of the PVP content. However, dissolution rate of the co-precipitate obtained at 70:30 drug to polymer ratio was slower than that obtained at 80:20 drug to polymer ratio. The dissolution rate obtained at 50:50 drug to polymer ratio surprisingly high in comparison to the other ratios.

For a given time, the percentage drug release of the co-precipitates obtained by SAS in this study are higher than those obtained by Rodríguez-Espinosa et al. [38] using the conventional technique for a similar drug to polymer ratio as shown in Fig. 5.48 and Fig. 5.49. However, the drug percentage release of the drug to polymer ratio 50:50 obtained in our work is slightly lower than the highest value obtained by Rodríguez-Espinosa et al. [38].

Furthermore, the improvement of the dissolution rate of the pure drug by co-precipitation with the PVP water soluble polymer is in agreement with the data reported by Majerik et al. [37], Lim et al. [51], Badens et al. [52], Wu et al. [53], Uzun et al. [54] and Corrigan and Crean [55].

Finally, the experiments showed that there are no large changes in the crystallinity of diflunisal with the different working conditions. The crystallinity of diflunisal disappeared in the co-precipitate with PVP *K*-10 or PVP *K*-30 in all studied ratios. The best results were obtained from PVP *K*-30 at 35 °C, 14 MPa, 2% solution concentration and 0.97 CO_2 mole fraction. The dissolution rate of diflunisal is improved by co-precipitation with the polymer. Enhancement of the dissolution rate could be attributed to the inhibition of the drug crystallization. This is mostly due to PVP surface adsorption and efficient steric hindrance for nucleation and crystal growth [58, 59]. The dissolution rates demonstrate the potential of using PVP as a suitable “amorphous inducing and stabilizing” agent for a poorly water-soluble drug such as diflunisal to improve the bioavailability using SAS process.

References:

[1] E. Reverchon, G. D. Porta, A. D. Trolio and S. Pace, Supercritical Antisolvent Precipitation of Nanoparticles of Superconductor Precursors, *Ind. Eng. Chem. Res.* 37 (1998) 952–958.

[2] E. Reverchon, G. C., and I. De Marco, Role of Phase Behavior and Atomization in the Supercritical Antisolvent Precipitation, *Ind. Eng. Chem. Res.*42 (2003) 6406–6414.

[3] E. Reverchon, I. De Marco and E. Torino, Nanoparticles production by supercritical antisolvent precipitation: A general interpretation, *J. Supercrit. Fluids* 43 (2007) 126–138.

[4] E. Reverchon, I. De Marco, R. Adami and G. Caputo, Expanded micro-particles by supercritical antisolvent precipitation: Interpretation of results, *J. Supercrit. Fluids* 44 (2008) 98–108.

[5] E. Reverchon, E. Torino, S. Dowy, A. Braeuer and A. Leipertz, Interactions of phase equilibria, jet fluid dynamics and mass transfer during supercritical antisolvent micronization, *Chem. Eng. J.* 156 (2010) 446–458.

[6] Y. P. de Diego, F.E. Wubbolts, G. J. Witkamp, Th. W. de Loos, P. J. Jansens, Measurements of the phase behaviour of the system dextran/DMSO/CO_2 at high pressures, *J. Supercrit. Fluids* 35 (2005) 1–9.

[7] A. E. Andreatta, L. J. Florusse, S. B. Bottini, C. J. Peters, Phase-equilibria of dimethyl sulfoxide (DMSO) + carbon dioxide and DMSO + carbon dioxide + water mixtures, *J. Supercrit. Fluids* 42 (2007) 60–68.

[8] R. L. Scott, P. H. van Konynenburg, Van der Waals and related models for hydrocarbon mixtures, *Discuss. Faraday Soc.* 49 (1970) 87–97.

[9] F. Zahran, J. Morère, A. Cabañas, J. A.R. Renuncio and C. Pando, Role of excess molar enthalpies in supercritical antisolvent micronizations using dimethyl sulfoxide as the polar solvent, *J. Supercrit. Fluids* 60 (2011) 45– 50.

[10] D. B. Longley, D. P. Harkin and P. G. Johnston, 5-Fluorouracil: mechanisms of action and clinical strategies, *Nat. Rev. Cancer* 3 (2003) 330–338.

[11] O. Guney and A. Akgerman, Solubilities of 5-Fluorouracil and β-Estradiol in Supercritical Carbon Dioxide, *J. Chem. Eng. Data* 45 (2000) 1049–1052.

[12] D. Suleiman, L. A. Estévez, J. C. Pulido, J. E. García, and C. Mojica, Solubility of Anti-Inflammatory, Anti-Cancer, and Anti-HIV Drugs in Supercritical Carbon Dioxide, *J. Chem. Eng. Data* 50 (2005) 1234–1241.

[13] P. Kalantarian, A. R. Najafabadi, I. Haririan, A. Vatanara, Y. Yamini, M. Darabi and K. Gilani, Preparation of 5-fluorouracil nanoparticles by supercritical antisolvents for pulmonary delivery, *Int. J. Nanomed.*, 5 (2010) 763–770.

[14] P. Kalantarian, I. Haririan, A. R. Najafabadi, M. A. Shokrgozar and A. Vatanara, Entrapment of 5-fluorouracil into PLGA matrices using supercritical antisolvent processes, *J. Pharm. Pharmacol*., 63 (2011) 500–506.

[15] A.-Z. Chen, Y. Li, D. Chen, J.-Y. Hu, Development of core-shell microcapsules by a novel supercritical CO_2 process, *J. Mater Sci: Mater Med* 20 (2009) 751–758.

[16] G. E. P. Box, W. G. Hunter and J. S. Hunter, Statistics for Experimenters. An Introduction to Design, Data Analysis and Model Building; 2nd Ed., J. Wiley and Sons: New York, (1993).

[17] MINITAB 15 SOFTWARE. Available from: http://www.minitab.com/en-US/products/minitab/free-trial.aspx?langType=1033

[18] J. Antony, Design of Experiments for Engineers and Scientists. Elsevier Science & Technology Books, Amsterdam : Butterworth-Heinemann, (2003).

[19] T. Y. Shen. Chemical and pharmacological properties of diflunisal. *Pharmacother.* 3 (1983) 3S–8S.

[20] R. O. Davies. Review of the animal and clinical pharmacology of diflunisal. *Pharmacother.* 3 (1983) 9S-22S.

[21] J. L. Wallace. Prostaglandins, NSAIDs, and Gastric Mucosal Protection: Why Doesn't the Stomach Digest Itself?, *Physiol. Rev.* 88 (2008) 1547–1565 .

[22] J. Hannah, W. V. Ruyle, H. Jones, A. R. Matzuk, K. W. Kelly, B. E. Witzel, W. J. Holtz, R. A. Houser and T. Y. Shen. Novel analgesic-antiinflammatory salicylates, *J. Med. Chem.* 21 (1978) 1093–1100.

[23] P. Coimbra, D. Fernandes, M. H. Gil, and H. C. de Sousa, Solubility of Diflunisal in Supercritical Carbon Dioxide, *J. Chem. Eng. Data* 53 (2008) 1990–1995.

[24] T. Katayama, K. Ohgaki, G. G. Maekawa, T. Nagano. Isothermal vapour-liquid equilibria of acetone-carbon dioxide and methanol-carbon dioxide at high pressures. *J. Chem. Eng. Jpn.* 8 (1975) 89–92.

[25] C. Y. Day, C. J. Chang, C. Y. Chen. Phase equilibrium of ethanol + CO_2 and acetone + CO_2 at elevated pressures. *J. Chem. Eng. Data* 41 (1996) 839–843.

[26] T. Adrian and G. Maurer. Solubility of carbon dioxide in acetone and propionic acid at temperatures between 298 and 333 K, *J. Chem. Eng. Data* 42 (1997) 668–672.

[27] A. Bamberger and G. Maurer. High-pressure (vapour-liquid) equilibria in carbon dioxide + acetone or 2-propanol) at temperatures from 293 to 333 K, *J. Chem. Thermodyn.* 32 (2000) 685–700.

[28] H. Y. Chiu, M. J. Lee, H. Lin. Vapor-liquid phase boundaries of binary mixtures of carbon dioxide with ethanol and acetone. *J. Chem. Eng. Data* 53 (2008) 2393–2402.

[29] M. Stievano and N. Elvassore, High-pressure density and vapor-liquid equilibrium for the binary systems carbon dioxide-ethanol, carbon dioxide-acetone and carbon dioxide-dichloromethane*, J. Supercrit. Fluids* 33 (2005) 7–14.

[30] F. Zahran, C. Pando, J. A. R. Renuncio, and A. Cabañas. Excess Molar Enthalpies of CO_2 + Acetone at Pressures from (9.00 to 18.00) MPa and Temperatures from (313.15 to 333.15) K, *J. Chem. Eng. Data* 55 (2010) 3649–3654.

[31] F. H. Vonderheiden and J. W. Eldridge. The System Carbon Dioxide-Methylene Chloride. Solubility, Vapor Pressure, Liquid Density, and Activity Coefficients, *J. Chem. Eng. Data* 8 (1963) 20–21.

[32] A. V. Gonzalez, R. Tufeu, and P. Subra. High-Pressure Vapor−Liquid Equilibrium for the Binary Systems Carbon Dioxide + Dimethyl Sulfoxide and Carbon Dioxide + Dichloromethane, *J. Chem. Eng. Data* 47 (2002) 492-495.

[33] J. T. Reaves, T. G. Aron and C. B. Roberts. Critical Properties of Dilute Carbon Dioxide + Entrainer and Ethane + Entrainer Mixtures. J. *Chem. Eng. Data* 43 (1998) 683–686.

[34] Y. B. Kim and I. Y. Park. Disordered Crystal Structure of Diflunisal, *J. Kor. Pharm. Sci.* 26 (1996) 55-59.

[35] M. L. Cotton and R. A. Hux. Diflunisal, *Anal. Profiles Drug Subs.* 14 (1985) 491–526.

[36] M. C. Martinez-Oharriz, C. Martin, M. M. Goni, C. Rodriguez-Espinosa, M. C.T. De Ilarduya-Apaolaza and M. Sanchez. Polymorphism of Diflunisal: Isolation and Solid-State Characteristics of a New Crystal F orm, *J. Pharm. Sci.* 83 (1994) 174–177.

[37] V. Majerik, G. Charbit, E. Badens, G. Horváth, L. Szokonya, N. Bosc and E. Teillaud. Bioavailability enhancement of an active substance by supercritical antisolvent precipitation, *J. Supercrit. Fluids* 40 (2007) 101–110.

[38] C. Rodriguez-Espinosa, M. C. Martínez-Ohárriz, C. Martín, M. M. Goñi, I. Vélaz, M. Sánchez. Dissolution kinetics for coprecipitates of diflunisal with PVP K30, *Eur. J. Drug Metab.Pharmokinet.*, 23 (1998) 109–112.

[39] H. G. Brittain, B. J. Elder, P. K. Isbester and A. H. Salerno. Solid-State Fluorescence Studies of Some Polymorphs of Diflunisal, *Pharm. Res.* 22 (2005) 999–1006.

[40] J. Nogami, T. Nagai and A. Suzuki. Studies on powdered preparations. XVII. Dissolution rate of sulfonamides by rotating disk method, *Chem. Pharm. Bull.*1966, 14 (1966) 329–338.

[41] K. Y. Yang, R. Glemza and C. I. Jarowski. Effects of amorphous silicon dioxides on drug dissolution, *J. Pharma. Sci*. 68 (1979) 560– 565.

[42] B. Deepak and H. Bogner. Amorphization of indomethacin by co-grinding with neusilin US2: amorphization kinetics, physical stability and mechanism, *Pharm. Res.* 23 (2006) 2317–2325.

[43] S Yusuke, F. Makiko, S. Yuka, Y. Ryusuke, F. Shinji, N. Sayaka, M. Yuya, K. Naoya, Y. Masaki, O. Kiyohisa and W. Yoshiteru. The preparation of solid dispersion powder of indomethacin with crospovidone using a twin-screw extruder or kneader, *Int. J. Pharm.* 365 (2009) 53–60.

[44] E. Yonemochi, S. Kitahara, S. Maeda, S. Yamamura, T. Oguchi and K. Yamamoto. Physicochemical properties of amorphous clarithromycin obtained by grinding and spray drying, *Eur. J. Pharm. Sci.* 7 (1999) 331–338.

[45] F. Usui, M. Ikeda, T. Isobe and M. Senna. Stability of amorphous indomethacin compounded with silica, *Int. J. Pharm.*226 (2001) 81–91.

[46] M. Kinoshita, K. Baba, A. Nagayasu, K. Yamabe, T. Shimooka, Y. Takeichi, M. Azuma, H. Houchi and K. Minakuchi. Improvement of solubility and oral bioavailability of a poorly water soluble drug, TAS-301, by its melt-adsorption on a porous calcium silicate, *J. Pharm. Sci.* 91 (2002) 362– 370.

[47] M. P. Summers and R. P. Enever. Preparation and properties of solid dispersion system containing citric acid and primidone, *J. Pharm. Sci.* 65 (1976) 1613–1617.

[48] J. L. Ford, A. F. Stewart and M. H. Rubinstein. The assay and stability of chloroprooamide in solid dispersion with urea, *J. Pharmacol*. 31 (1979) 726–729.

[49] B.C. Hancock and M. Parks, What is the true solubility advantage for amorphous pharmaceuticals, *Pharm. Res.* 17 (2000) 397–404.

[50] W. Scholtan. Molecular weight determination of PVP by means of ultracentrifuge and viscosity, *Makromol. Chem.* 7 (1952) 209–235.

[51] R. T. Y. Lim, W. K. Ng and R. B. H. Tan. Amorphization of pharmaceutical compound by co-precipitation using supercritical anti-solvent (SAS) process (Part I), *J. Supercrit. Fluids* 53 (2010) 179–184.

[52] E. Badens, V. Majerik, G. Horváth, L. Szokonya, N. Bosc, E. Teillaud and G.Charbit. Comparison of solid dispersions produced by supercritical antisolvent and spray-freezing technologies, *Int. J. Pharm.* 377 (2009) 25–34.

[53] K. Wu, J. Li, W. Wang, D. A. Winstead. Formation and characterization of solid dispersions of piroxicam and polyvinylpyrrolidone using spray drying and precipitation with compressed antisolvent, *J. Pharm. Sci.* 98 (2009) 2422–2431.

[54] I. N. Uzun, O. Sipahigil and S. Dincer. Coprecipitation of Cefuroxime Axetil–PVP composite microparticles by batch supercritical antisolvent process, *J. Supercrit. Fluids* 55 (2011) 1059–1069.

[55] O. I. Corrigan and A. M. Crean. Comparative physicochemical properties of hydrocortisone-PVP composites prepared using supercritical carbon dioxide by the GAS anti-solvent recrystallization process, by coprecipitation and by spray drying, *Int. J. Pharm.* 245 (2002) 75–82.

[56] A. Gokhale, B. Khusid , R. N. Dave and R. Pfeffer. Effect of solvent strength and operating pressure on the formation of submicrometer polymer particles in supercritical microjets, *J. Supercrit. Fluids* 43 (2007) 341–356.

[57] M. C. Martínez-Ohárriz, C. Rodríguez-Espinosa, C. Martín, M. M. Goñi, M. C. Tros-Ilarduya and M. Sánchez. Solid Dispersions of Diflunisal–PVP: Polymorphic and Amorphous States of the Drug, *Drug Dev. Ind. Pharm.* 28 (2002) 717–725.

[58] M. Yoshioka, B. C. Hancock and G. Zografi. Inhibition of indomethacin crystallization in poly(vinylpyrrolidone) coprecipitates, *J. Pharm. Sci.* 84(1995) 983–986.

[59] M. Savva, V. P. Torchilin and L. Huang. Effect of polyvinyl pyrrolidone on the thermal phase transition of 1, 2 dipalmitoyl-sn-glycero-3-phosphocholine bilayer, *J. Colloid Interface Sci.*, 217 (1999) 160–165.

Chapter 6. Summary and Conclusions

Summary and Conclusions

This thesis deals with the micronization of solids using supercritical fluids. The reasons for this study are twofold: the need for further study of supercritical antisolvent (SAS) processes in order to correctly design and scale-up them and the need for further development of pharmaceuticals micronizations. The role of excess molar enthalpies in the SAS micronization and the SAS micronization of some pharmaceuticals were studied.

Chapter 1. Introduction

The first part of this work is an introduction about supercritical fluids (SCFs) followed by a description of the production of microparticles using SCFs. Next, the fundamentals of supercritical antisolvent (SAS) precipitation and its application in the field of pharmaceuticals are summarized.

Chapter 2. Objectives This chapter describes the objectives of the thesis.

Chapter 3. Methodology

The high-pressure isothermal flow calorimeter used to measure the excess molar enthalpies (H_m^E) for the CO_2 + organic solvent systems is described. The calculation of phase equilibria, excess enthalpy and critical locus using an equation of state (EOS) is explained. A detailed account of the SAS apparatus built in this thesis is given. The design of experiment (DOE) strategy and the methods employed for particle characterization are described.

Chapter 4. Thermal Effects in the Supercritical Antisolvent Micronizations

In the first step, the excess molar enthalpy data for the CO_2 + organic solvent systems were determined under the conditions of temperature and pressure usually employed in SAS micronizations. In a second step, the interaction between the excess enthalpies and phase equilibria in the SAS precipitation chamber was elucidated. The solvents acetone (Ac), *N*,*N*-dimethylformamide (DMF), dimethylsulfoxide (DMSO) and ethyl acetate (EA) were studied. This part of the thesis has been the subject of four publications which are included in chapter four.

The conditions for temperature and pressure were 313.15 and 323.15 K and 9.00, 12.00, 15.00 and 18.00 MPa as well as 333.15 K and 9.00 and 15.00 MPa. Similar trends for the

variation of H_m^E with mole fraction, temperature and pressure were observed for all the CO_2 + organic solvent systems studied. In most cases, mixtures showed very exothermic mixing. H_m^E minimum values may be as low as –4500 J mol^{-1}. For most conditions of temperature and pressure, excess molar enthalpies exhibited this minimum in the CO_2 rich region. At certain conditions, linear sections in the representation of H_m^E versus carbon dioxide mole fraction were observed due to the appearance of a two phase region in which a gaseous and a liquid mixture of fixed composition are at equilibrium. The liquid and the vapor-phase compositions are shown to correspond to the *x* coordinates of the beginning and end of the linear sections. The composition values thus obtained were compared with the VLE data from the literature.

The effects of temperature and pressure on H_m^E are large. For a given system and mole fraction, in general, mixtures become less exothermic as pressure increases or temperature decreases. The effect of the nature of the organic solvent depends on the conditions of temperature and pressure. For instance, CO_2 + EA mixtures are the most exothermic ones at the three temperatures studied and 9.00 MPa. However, at the other pressures studied they exhibit values intermediate between those observed for the other systems studied.

Excess molar enthalpies for CO_2 + Ac, DMF or EA were accurately correlated using the Peng-Robinson and Soave-Redlich-Kwong equations of state, and the classical mixing rule with two adjustable binary parameters for each temperature. Excess molar enthalpies could not be correlated for the CO_2 + DMSO system; this could be related to the complex critical behavior exhibited by this system. Furthermore, in the case of the CO_2 + DMF system, the Peng-Robinson and the Soave-Redlich-Kwong EOS were used in conjunction with the classical mixing rules to provide a simultaneous and accurate description of vapor-liquid equilibrium (VLE) and critical data for the system and to predict excess molar enthalpies. Best results were obtained using the Peng-Robinson EOS.

The trends of the excess enthalpies with temperature and pressure were analyzed in terms of molecular interactions, phase equilibria, density and critical parameters previously reported for CO_2 + organic solvent. A literature search was carried out and the available information about CO_2 + acetone, DMF, DMSO or EA systems was gathered. These systems have been the subject of numerous investigations due to their relation to supercritical fluid applications.

The excess molar enthalpy is shown to be the sum of two contributions. One contribution is associated to changes in molecular interactions due to the disruption of the organic solvent liquid structure by carbon dioxide and the formation of complexes among CO_2 and the organic solvent molecules. The second contribution to H_m^E is due to the carbon dioxide change of state from that of a gas-like or liquid-like fluid to that of a liquid mixture component. These two contributions were referred as the molecular interactions contribution and the change-of-state contribution, respectively.

Acetone, DMF, DMSO and EA are unassociated solvents but all of them present high dipolar moments and solvent structures dominated by dipole-dipole interactions. On the other hand, carbon dioxide does have a relatively large quadrupole moment. The high dipolar moments lead to highly structured liquids with relatively high densities. The solvent structure is disrupted upon mixing with carbon dioxide leading to an endothermic contribution to H_m^E. Moderately exothermic enthalpies are the result of a balance between the endothermic contribution and an exothermic one due to strong organic solvent- CO_2 interactions. This is the molecular interaction contribution to H_m^E that may be expected to change only slightly with temperature and pressure.

In order to analyze the change of state contribution to H_m^E we need to consider the state and densities of the pure components and those of the mixtures formed in the calorimeter. The organic solvents are liquid at the conditions of temperature and pressure of the experiments. Their density values vary slightly with temperature and pressure. However, the state and density of carbon dioxide differ to a great extent from one (P, T) coordinate to another. Carbon dioxide is a supercritical fluid that may be either a high-density (liquid-like) fluid or a low-density (gas-like) fluid.

The state of the mixtures formed in the calorimeter (liquid, fluid, two-phase) may be established by examining the situation of the (P, T) coordinate with respect to the system critical locus and taking into account the critical composition and the vapor-liquid equilibrium data. The CO_2 + acetone, CO_2 + DMF and CO_2 + EA systems exhibit type I critical behavior in the classification of Scott and van Konynenburg; their complete critical locus were calculated using the available critical data. The critical behavior of the CO_2 + DMSO system is more complicate; it belongs either to type III or IV in the Scott and van Konynenburg classification.

The fluid carbon dioxide mixes with the liquid solvent forming a liquid mixture or the gaseous and liquid mixtures in equilibrium. As a consequence of the CO_2 change of state, this contribution to the excess enthalpy is exothermic and becomes increasingly exothermic when low-density CO_2 is mixed. This effect is sometimes called the fluid condensation effect. When carbon dioxide enters the calorimeter as a liquid-like fluid, the change-of-state contribution to H_m^E is small and excess molar enthalpy values may be considered mainly the result of the molecular interactions contribution to H_m^E. When carbon dioxide enters the calorimeter as a gas-like fluid, the fluid condensation effect is very pronounced and the change-of-state contribution to H_m^E is extremely exothermic. As a result, the excess molar enthalpy may reach values of – 4500 J mol^{-1}.

For a given temperature, pressure and mole fraction the variations due to the organic solvent nature observed may be attributed to the type of critical diagram and differences in intermolecular interactions in the pure liquid and the mixtures. These differences lead to varying values for the molecular interaction contribution to H_m^E. However, the magnitude of the change-of-state contribution can be expected to be similar for the different solvents at a given temperature, pressure and mole fraction when no phase equilibria are involved.

Mixtures formed by supercritical CO_2 and an organic solvent are involved in several supercritical processes other than SAS. The excess enthalpy data reported in this thesis may be used to model or optimize these processes. However, the aim of this study was to understand the interaction between phase equilibria and excess enthalpies during SAS experiments.

As was already pointed out, the phase behavior of the CO_2 + organic solvent is one of the crucial factors governing the morphology and the mean size of particles obtained in the SAS process. The presence of the solute can induce modifications in the phase diagram. This is the case of polymers; however, when the solute has little interaction with carbon dioxide the ternary phase diagram for the low solute concentrations usually employed in SAS is coincident with the binary one in the CO_2-rich region which is the region for mixtures involved in SAS. Therefore, the mixtures formed in the precipitation chamber may be treated as binary CO_2 + organic solvent systems. The heat evolved when the supercritical CO_2 dissolves into the organic solution has an important role in the phase behavior. The temperature control in the precipitation chamber is not very precise and a local temperature

increase may be expected. As a consequence, if the precipitation starts at T and P conditions of complete miscibility for the CO_2 + organic solvent system, phase splitting may take place in a short time.

Since CO_2 is fed into the chamber at a flow rate much higher than that of the solution and the solute concentration is very low, the contribution to H_m^E due to solute interactions may be neglected and the thermal effects in SAS experiments can be considered mainly due to the formation of CO_2 + organic solvent mixtures very rich in carbon dioxide ($x \geq 0.95$). Assuming an adiabatic process and using the heat capacity of pure CO_2, the H_m^E measured have been used to estimate the temperature increments in the precipitation chamber. These estimations allowed to explain the unexpected morphology of the precipitates obtained at certain conditions.

The enthalpy effect on the phase equilibria has been clearly shown in SAS micronizations from the literature using a windowed vessel and DMSO as the polar solvent. By modifying the phase equilibria, excess molar enthalpies will influence the particle precipitation mechanism. There are other factors that may simultaneously influence the particle morphology but the heat evolved upon mixing CO_2 and the polar solvent is shown to play an important role.

Chapter 5. Supercritical Antisolvent Micronizations of Pharmaceuticals

- **Validation of SAS Apparatus: Micronization of Yttrium Acetate**

The micronization of yttrium acetate (YAc) from dimethylsulfoxide was chosen to validate the SAS equipment built at our laboratory. Precipitation experiments were performed at temperatures of 40 and 60 °C and pressures ranging from 11 to 20 MPa. Concentration of YAc in DMSO was kept constant at 2%. The phase equilibria data for the CO_2 + DMSO system were used to understand the different morphologies observed in YAc micronizations. SEM images of YAc precipitated at condition of complete solubility of CO_2 + DMSO showed discrete or slightly aggregated nanoparticles with a spherical morphology. On the contrary, working in the two phase region resulted in aggregated particles forming a block. A decrease in the mean particle size was observed with the increase of the pressure. To establish if the precipitation conditions are in the one or two phase region, the phase equilibria and the excess enthalpies for CO_2 + DMSO should be taken into account as the mixing process may cause a local increase in T in the chamber which also affects phase separation. Thus at 60 °C and 14

MPa mixing of DMSO and CO_2 is highly exothermic and causes a local temperature increase of ≈ 4°C leading to phase splitting. Then the *P* and the new *T*, 64 °C, conditions will correspond to the two-phase region where aggregated particles are obtained.

Our results for the YAc micronization are in agreement with those previosly reported by Reverchon et al. This equipment has been used for the micronization of 5-fluorouracil, diflunisal, and the co-precipitation of diflunisal with polyvinylpyrrolidone (PVP).

- **Micronization of 5-Fluorouracil**

5-Fluorouracil (5-FU) is a pyrimidine analog drug used in the treatment of several types of cancer. This compound is soluble in DMSO but has a very low solubility in CO_2. Dimethyl sulfoxide was chosen as a solvent for the micronization of 5-FU. The factors that could affect the SAS process are: the concentration of the solution (*C*), the temperature (*T*), the pressure (*P*), the solution flow rate (Q_L), the supercritical CO_2 flow rate (Q_{CO2}), the drying time (*t*), and the nozzle diameter ($Ø_n$). In our study, the drying time and the nozzle diameter were kept constant at 3 times the time required to fill the precipitation chamber and 100 μm, respectively. In order to decrease the number of experiments the DOE methodology was applied and the 2^{5-2} fractional factorial design was employed reducing the number of experiments to eight. The value of the CO_2 mole fraction was ≥ 0.96. The mean particle size and particle morphology obtained from SEM images were used as a response to evaluate the process performance.

SEM images of untreated 5-FU exhibits granulated particles with a mean particle size > 100 μm. Precipitation experiments were carried out at 40, 50 °C; 15, 18 MPa; and concentrations of 1 or 2 (%). SEM images of the 5-FU precipitated revealed that six of the eight experiments (1, 2, 5, 6, 7 and 8) led to a successful micronization of 5-fluorouracil. Elongated particles with a distributed mean particle sizes in the range of 216-670 nm were obtained. On the other hand, the micronization was unsuccessful for experiments 3 and 4 where much larger particles of regular shape were obtained.

For a given concentration, the mean particle size decreased as the pressure and the temperature increased. The order of importance of the factors for particle size and morphology can be summarized in view of their mean effect as follows

$$T > P > C >> Q_L > Q_{CO2}$$

Best conditions for the 5-FU micronization were those of experiment 7: C = 1%, T = 50 °C, P = 18 MPa, Q_L = 1 mL/min and Q_{CO2} = 15 g/min which resulted in the smallest mean particle size of 216 nm.

The crystallinity of the precipitated particles was evaluated using powder X-ray diffraction (XRD). The XRD pattern of the untreated 5-FU exhibited a very intense peak at 28.7 degree which suggested a preferred orientation of the untreated drug at this position. On the other hand, the preferred orientation disappeared in the XRD pattern of the SAS precipitated 5-FU and that may be attributed to a decrease of crystallinity during SAS precipitation of 5-FU from DMSO with respect to the untreated drug.

- **Micronization of Diflunisal**

Diflunisal is a non-steroidal anti-inflammatory drug that is very soluble in DMSO and scarcely soluble in CO_2. However, preliminary experiments carried out at conditions similar to those employed in the YAc and 5-FU SAS experiments showed that DMSO is not a suitable solvent for the SAS micronization of diflunisal. On the other hand, SAS experiments using acetone were successful. Precipitation experiments were performed at 40 °C; and 9, 12 and 15 MPa and concentrations of 2 and 4%. Temperature increments inside the precipitation chamber, ΔT, were estimated to be up to 5.5 degrees. Since the P and T conditions are not close to the mixture critical point, the temperature increment does not lead to phase splitting.

Large thin bars of a crystalline material were observed in the SEM images of the commercial diflunisal. In every SAS precipitation SEM images show similar thin and very long crystalline particles forming laminar sticks. The sticks are bound together like the branches of a tree. The width of the sticks ranged from 2 to 10 μm at all operating conditions. SEM images showed that the different conditions do not lead to significant changes in the crystallinity and morphology of diflunisal. Furthermore, SAS precipitation of diflunisal from acetone/dichloromethane (DCM) mixture (80:20, v/v %) gave similar results to those obtained from acetone alone. Precipitation of pure diflunisal did not seem to be very sensitive to the precipitation conditions, nor to the solvent.

Diflunisal was reported to have at least four polymorphic crystal forms. The XRD patterns of the original substance and the SAS processed diflunisal were different, indicating that the polymorphism of diflunisal is changed through the SAS process. The precipitated drug

exhibits form IV. The XRD pattern for the untreated diflunisal suggested that it is composed of a mixture of polymorphs. Furthermore, the DSC thermograms showed that the untreated diflunisal has a splitted peak with two melting points at 216.62 and 213.82 °C which confirmed the presence of more than one polymorph. On the contrary, the SAS diflunisal exhibited a single sharp peak at 212.63 °C peak corresponding to the melting point of form IV.

- **Amorphization of Diflunisal by Co-precipitation with PVP**

The SAS co-precipitation of diflunisal with PVP was thought to be an effective method to improve the drug amorphousness. The influence of two different types of PVP polymer on the physicochemical properties of diflunisal was investigated. PVP *K*-10 ($\overline{M}_w$ = 10,000) and PVP *K*-30 ($\overline{M}_w$ = 40,000) were used. Preliminary SAS precipitation of polyvinylpyrrolidone from ethanol at pressures of 8 and 12 MPa, temperatures of 35 and 40°C, and PVP solution concentrations of 2% and 5% (CO_2 mole fraction ≥ 0.96) were unsuccessful. Because of the poor solubility of PVP in acetone, a mixture of good and poor polymer solvents was utilized in the co-precipitation process. DCM was chosen to be the good polymer solvent along with acetone as a poor polymer solvent and an acetone/DCM mixture (80:20, v/v %) was used.

First, PVP *K*-10 was precipitated alone from acetone/DCM (80:20, v/v %) at 35 °C, 9 MPa, a solution concentration of 2% and a value of 0.97 for the CO_2 mole fraction. Spherical nanoparticles were obtained with 230 nm mean particle size. Diflunisal was then co-precipitated with PVP *K*-10 at a drug : polymer weight ratio of (50:50) at 35 and 40 °C, pressures ranging from 8 to 15 MPa, solution concentrations of 2 and 4 % and at two different CO_2 mole fractions of 0.84 and 0.97. At 35 °C, viscous solutions were obtained at pressures ranging from 8 to 9 MPa. By increasing temperature slightly to 40 °C, sticky precipitates were observed. Working at higher pressures up to 12 MPa at 35 °C resulted in the formation of porous spherical balloons, whose size decreased as pressure increased. However, further increase of pressure up to 15 MPa resulted in coalescence of particles. Nevertheless, it was clear that the crystallinity of the diflunisal disappeared in the co-precipitate in comparison with the SAS precipitated diflunisal from the same solvent mixture.

Second, PVP *K*-30 was used at the same experimental conditions. Much better results were obtained which could be attributed to the fact that the plasticizing effect of CO_2 on polymers decreased with increasing polymer molecular weight. As observed with PVP *K*-10, the

crystallinity of the diflunisal disappeared during the co-precipitation with PVP *K*-30 with respect to the SAS precipitated diflunisal from the same solvent mixture. The mean particle size of the diflunisal + PVP *K*-30 co-precipitate is at least 5 times smaller than that of the co-precipitate obtained using PVP *K*-10. The increase of the polymer molecular weight resulted in an important decrease in the particle size.

For comparison, PVP *K*-30 was precipitated alone from acetone/DCM (80:20, v/v %) at 35 °C, 14 MPa and a solution concentration of 2 %. SEM images exhibited spherical nanoparticles with mean particle size of 210 nm.

The influence of the drug: polymer weight ratio on the properties of the diflunisal + PVP *K*-30 co-precipitates from acetone/DCM (80:20, v/v %) was studied at three different drug to polymer weight ratios of 75:25, 50:50 and 25:75 at a temperature of 35 °C, a pressure of 14 MPa, a solution concentration of 2 % and a value of 0.97 for CO_2 mole fraction. The crystallinity of the diflunisal disappeared in the co-precipitate even with the lowest polymer content. The 75:25 co-precipitate consists of spherical particles with mean particle size less than 10 μm that are highly aggregated forming a block. On the other hand, the 25:75 co-precipitate showed loose spherical particles of mean particle size of 460 nm with very little aggregation with respect to that obtained at 50:50.

The diflunisal + PVP *K*-30 composites at the three different drug to polymer ratios were characterized further using XRD, FTIR and DSC as well as the dissolution profile in comparison with the pure drug. XRD patterns show that the SAS processed diflunisal is a crystalline material while the SAS precipitated PVP *K*-30 is an amorphous material. The crystallinity of the diflunisal disappeared in the co-precipitates. The amorphousness of the co-precipitates did not change when the PVP *K*-30 content was increased from 25 % to 75 %. The inhibitory effect of the polymer on the crystallinity of the diflunisal may be attributed to the interaction of the drug with the PVP resulting in a change in the molecular mobility of the drug, ultimately leading to an amorphous form of diflunisal. FTIR-spectrum showed band shifts and broadening compared to the spectra of the pure drug and PVP *K*-30 which may be attributed to the interaction of the functional groups. The broadening of the band corresponding to the diflunisal carbonyl group (1690 cm^{-1}) in the three co-precipitates suggested the formation of intermolecular hydrogen bonding between the diflunisal and PVP

K-30. All these results might indicate that a significant change in the total symmetry of the drug molecule in the solid polymer matrix has occurred in the co-precipitates.

In order to get further evidence of the interaction of diflunisal with PVP and to understand better the structure of the co-precipitates, DSC and TGA studies were performed. In the DSC thermogram of the composite materials, a broad band due to the loss of water showed a shoulder at 75-125 °C which shifted to a higher temperature as the concentration of the PVP increased. This may suggested the presence of water molecules in the composite material in a different form to that found in PVP and in pure diflunisal. The three co-precipitates showed two decomposition peaks one attributed to the drug and the other one attributed to the polymer. Furthermore, there was a clear shift of the decomposition temperature of the drug with increasing the concentration of the polymer at higher temperatures which also supported the strong interaction between diflunisal and the PVP *K*-30. TGA curves of the three composites showed that the compositions of the SAS co-precipitates were close to the feed compositions. In addition, the decomposition process of the co-precipitates took place in two steps. The first step started at a temperature very close to the starting decomposition temperature of the drug and the second one started also very close to that of the polymer.

The results obtained from XRD, IR, DSC and TGA, indicated that the crystallinity of the diflunisal disappeared with the co-precipitation process which suggests the incorporation of the drug within the polymer at a molecular level.

Dissolution tests using the rotating disk method were carried out in a simulated intestinal fluid (phosphate buffer pH 7.4) for the pure drug, the untreated drug and the three co-precipitated materials obtained at drug to polymer ratios of 75:25, 50:50 and 25:75. The dissolution profiles were followed by UV-VIS spectroscopy at 275 nm. All the dissolution rates of the diflunisal + PVP *K*-30 co-precipitates were higher than those of the untreated and SAS processed diflunisal. For a given time, the drug release increased with increasing PVP *K*-30 content; the highest dissolution rate was observed in the 75 % PVP *K*-30 co-precipitate. Approximately 75 % of the drug was dissolved after 20-30 min for diflunisal + PVP *K*-30 composites.

The properties of our co-precipitates compare favorably with those of other drug-PVP co-precipitates obtained by SAS and GAS and with the diflunisal-PVP *K*-30 physical mixture

and solid dispersions reported in the literature. Two key aspects should be underlined: the good morphology and small size of the composites obtained in this study, and the faster dissolution rates that demonstrate the potential of using PVP as an agent to induce amorphousness and stabilization of a poorly water-soluble drug such as diflunisal.

Resumen

Resumen[a]

A continuación se incluye un resumen de esta tesis en español, a fin de dar cumplimiento al artículo 4.3 de la normativa UCM sobre la admisión a trámite de la tesis doctoral. Dicho artículo establece que, en el caso de tesis doctorales redactadas en otra lengua como el inglés, "se deberá presentar un amplio resumen en español que incluya, al menos, la introducción, objetivos, conclusiones y aportaciones fundamentales de la tesis doctoral".

Introducción

1.1. Fluidos Supercríticos

Los fluidos supercríticos (SCFs) son sustancias puras o mezclas a una temperatura y presión superiores a sus coordenadas críticas. La densidad es la principal característica diferenciadora de un fluido supercrítico; el comportamiento del fluido puede modularse pasando desde el de un líquido a alta presión al de un gas a baja presión.

El dióxido de carbono es el fluido supercrítico más utilizado porque no es tóxico, ni inflamable y tiene una temperatura y presión crítica moderadas. La Fig. 1.1 muestra el diagrama de fases presión-temperatura del dióxido de carbono. En el diagrama se muestran las condiciones donde coexisten dos fases junto con áreas donde sólo existe una fase y el punto en que el coexisten tres fases, el denominado punto triple. También se muestra la presión crítica (P_c) y la temperatura crítica (T_c); la región del fluido supercrítico se extiende por encima de P_c y T_c. Si en esta área se reduce la presión o la temperatura la sustancia pasará a estar en las regiones de vapor o líquida, respectivamente, sin que haya tenido lugar ningún cambio de fase. El dióxido de carbono tiene una temperatura crítica de 304.12 K y una presión crítica de 7.37 MPa [2].

La Tabla 1.1 muestra las masas molares y las temperaturas, presiones y densidades críticas de varios compuestos utilizados como fluidos supercríticos. Como puede verse, las moléculas más ligeras tienden a tener temperaturas críticas más bajas y densidades críticas más altas que las moléculas de masa molecular más alta.

[a] Para evitar duplicidades, las figuras, tablas y referencias bibliográficas citadas en este resumen se encuentran en la versión en inglés que constituye el resto de la memoria.

Las presiones críticas de la mayor parte de sustancias varían de 3 a 6 MPa. La presencia de enlaces de hidrógeno o la polaridad de las moléculas conducen a un aumento de la temperatura o presión crítica del compuesto. Aunque en los procesos supercríticos pueden emplearse una gran variedad de compuestos, las sustancias más comunes como el dióxido de carbono, los hidrocarburos ligeros y el agua son las que han recibido más atención.

1.1.1. Propiedades de los Fluidos Supercríticos

En la tabla 1.2 se comparan las propiedades de los fluidos supercríticos con las habituales de los gases y los líquidos. Las propiedades termofísicas de los SCF incluyen densidades similares a las de los líquidos, viscosidades similares a las de los gases y difusividades muy superiores a las de los líquidos.

La densidad es un factor muy importante a la hora de determinar la solubilidad de diferentes compuestos en un fluido. Un SCF de densidad alta tiene una capacidad como disolvente similar a la de los disolventes líquidos. Por otra parte, los SCFs tienen en comparación con los líquidos una viscosidad relativamente baja y unos valores de la difusividad que les permiten penetrar en las matrices sólidas. Estas propiedades favorecen la transferencia de masa de un soluto en el seno de un SCF con respecto al seno de un líquido. La transferencia de calor también está favorecida en un SCF porque los SCFs tienen valores de la conductividad térmica altos en comparación con los de los gases aunque sean inferiores a los de los líquidos. Además, la baja tensión superficial del SCF hace que el fluido pueda penetrar en los materiales porosos.

Como resultado de esta combinación de propiedades, los SCFs son sustancias muy interesantes para aplicaciones tecnológicas tales como la extracción, el tratamiento y fabricación de materiales, la micronización de sólidos y como medios de reacción. La ciencia y tecnología de fluidos supercríticos es un área en creciente desarrollo.

Una de las propiedades más importantes es la solubilidad de los diferentes materiales en el fluido. Esta solubilidad tiende a aumentar al aumentar la densidad del fluido a temperatura constante. En la Fig. 1.2 se muestra como varía la densidad del dióxido de carbono en función de la temperatura y la presión.

A una temperatura por debajo de la temperatura crítica ($T < T_c$), como 280 K, al aumentar la presión, la densidad del dióxido de carbono gas aumente. Si se aumenta más la presión se produce separación de fases o equilibrio líquido-vapor representado por una línea discontinua. Si se aumenta la temperatura a 300 K, el CO_2 se comprime y condensa en un líquido menos denso; si embargo, el equilibrio líquido-vapor persiste. En el punto crítico las dos fases se transforman en una fase de fluido supercrítico. A temperaturas inferiores a T_c, se requiere un gran aumento de la presión para que la densidad se eleve un poco. Sin embargo, en la región supercrítica cerca del punto crítico una pequeña modificación de la presión trae consigo un gran cambio en la densidad; así se puede modular la densidad y otra propiedades. Un pequeño aumento de presión en el dióxido de carbono a 310 K ($T > T_c$) causa un gran aumento de la densidad de la fase supercrítica. A temperaturas más altas el fluido empieza a comportarse como un gas.

Muchos gases a presión son realmente fluidos supercríticos. Por ejemplo, el nitrógeno tiene constantes críticas de 126.2 K y 3.4 MPa. Por tanto, el nitrógeno (o el aire comprimido) en una botella de gases por encima de esta presión es realmente un fluido supercrítico. A temperatura ambiente, se comporta como un gas, similar al CO_2 a temperaturas ≥ 400 K.

1.1.2 Diagramas de Fase de Mezclas Formadas por Fluidos Supercríticos

Se ha definido un fluido supercrítico como una sustancia a una temperatura y presión superiores a sus coordenadas críticas. La misma definición es válida para un compuesto puro y una mezcla. Generalmente se estudian en primer lugar las mezclas binarias, para pasar a las ternarias y mezclas de orden superior. Esta estrategia nos permite usar nuestro conocimiento de las mezclas con dos o tres componentes en el estudio de mezclas multicomponentes.

Lejos del punto crítico los diagramas P-x y T-x de una mezcla binaria son fáciles de comprender. Sin embargo cuando las condiciones de temperatura o presión se acercan al punto crítico de uno de los componentes, se obtienen diagramas de fase como el mostrado en la Fig. 1.3 para el sistema CO_2 + pentano a 344 K [4].

A la presión de 5 MPa, la intersección de una paralela al eje de abcisas con la curva superior proporciona el valor de la fracción molar del CO_2 en la fase líquida rica en pentano (x_1) mientras que la intersección de esta línea con la curva inferior proporciona el valor de la fracción molar del CO_2 en la fase de vapor rica en CO_2 (y_1). Estas son las composiciones de

las mezclas líquida y vapor en equilibrio a 344 K y 5 MPa. Cada pareja de valores de la composición obtenidos así para una presión dada describen posible estados de equilibrio líquido-vapor para este sistema. Al aumentar la presión, los valores de x_1 e y_1 se aproximan. A la presión de 9.5 MPa, las dos curvas confluyen, el valor coincidente de x_1 e y_1 es la composición de la mezcla con coordenadas críticas 344 K y 9.5 MPa. Para obtener otras coordenadas críticas *P*, *T*, *x* de este sistema es necesario representar diagramas similares a los de la Fig. 1.3 a otras temperaturas. El conjunto de coordenadas crítica *P*, *T*, *x* obtenido define el denominado locus crítico de este sistema concreto. Por tanto hace falta un diagrama tridimensional P-T-x para describir el comportamiento crítico de un sistema binario. La Fig. 1.4 muestra este diagrama para un sistema como el CO_2 + pentano. Este es el comportamiento crítico más sencillo. C_1 y C_2 son los puntos críticos del CO_2 y el pentano, respectivamente. Las líneas continúas A-C_1 y B-C_2 representan las curvas de presión de vapor de ambos componentes puros. La línea de trazos que conecta C_1 y C_2 es el locus crítico del sistema CO_2 + pentano. Las dos superficies que describen la fase líquida y la fase vapor están delimitadas por las curvas A-C_1, B-C_2 y C_1-C_2. En la Fig. 1.4 también se muestran algunas secciones isotermas e isobaras comprendidas entre las superficies de las fases líquida y vapor. Estas secciones originan los diagramas bidimensionales P-x y T-x mostrados a la izquierda en la Fig. 1.4. La Fig. 1.5 muestra los diagramas P-T a *x* constante (isopletas) del sistema etano + heptano y la proyección del diagrama de fases tridimensional sobre el plano *PT*.

Generalmente sólo se da la información mostrada en la proyección P-T. Esta proyección de la Fig.1.5 también describe el comportamiento del sistema CO_2 + pentano. En este caso, los puntos del locus próximos a C_1 representan coordenadas críticas de mezclas ricas en CO_2- y los puntos próximos a C_2 corresponden a mezclas ricas en pentano. Esta representación simplificada es la base de la clasificación de Scott y van Konynenburg [5] de los diagramas de fase de sistemas binarios mostrada en la Fig. 1.6.

Scott y van Konynenburg demostraron que casi todos los tipos de equilibrios de fase binarios conocidos (líquido-vapor, líquido-líquido y gas-gas) pueden predecirse usando la ecuación de estado de van der Waals y las reglas de mezcla cuadráticas. Cinco tipos fueron generados usando esta ecuación. Para completar la descripción Street [6] añadió el tipo VI que es poco frecuente. El comportamiento del sistema se clasifica en uno de estos tipos teniendo en cuenta la forma de la línea crítica y la ausencia o presencia de líneas de equilibrio

entre tres fases. Mc Hugh y Krukonis [7] describieron con detalles el aspecto y explicación de los diagramas P-T-x de estos seis tipos. El sistema CO_2 + pentano pertenece al tipo I que está caracterizado por una línea crítica continua que conecta los puntos críticos de los componentes puros C_1 y C_2 y la miscibilidad completa en la fase líquida.

En el tipo II los dos componentes no son completamente miscibles y aparece equilibrio entre tres fases a temperaturas inferiores a los puntos críticos de ambos componentes. Esto sucede en la línea de equilibrio líquido-líquido-vapor (LLV). El punto UCEP indica la temperatura consoluta superior para el equilibrio líquido-líquido (L-L) y es comúnmente conocido por su acrónimo en inglés (upper critical end point). A presiones superiores a la de este punto la fase vapor condensa en una línea de trazos discontinua que representa el equilibrio L-L.

Cuando la inmiscibilidad alcanza temperaturas próximas a la temperatura crítica de uno de los componentes, el diagrama de fases puede ser tipo III. En este caso la línea crítica tiene dos secciones. La sección que comienza en el punto crítico del componente menos volátil (C_2) se extiende hasta presión alta y puede tener un máximo o un mínimo en la temperatura y/o presión. Cuando las temperaturas de esta línea crítica son superiores a la del componente 2, se la denomina línea crítica gas-gas (b). La otra sección del locus crítico está a temperaturas más bajas y conecta el punto crítico del componente más volátil (C_1) y el "upper critical end point" (UCEP) que delimita la línea de equilibrio de tres fases (LLV).

En los tipos IV y V la línea crítica gas-líquido empieza en C_2 y termina en la temperatura consoluta inferior o "lower critical end point" representado por LCEP. Este punto delimita la línea de equilibrio de tres fases LLV que termina en el "upper critical end point" (UCEP) y está conectada al punto crítico del otro componente por la línea crítica VL. En el diagrama tipo IV aparece a bajas temperaturas equilibrio líquido-líquido (LL) similar al del diagrama tipo II.

Generalmente el diagrama es de tipo I cuando los dos componentes del sistema binario tienen una naturaleza química similar. Cuando los componentes difieren el comportamiento se complica y aparecen los tipos II, III, etc. [8]. Por ejemplo, en la serie CO_2 + alcano, el diagrama de fases varía al aumentar la longitud de la cadena. El tipo I lo presentan los

sistemas desde CO_2 + metano a CO_2 + pentano, el tipo II, desde CO_2 + octano a CO_2 + undecano, el tipo III el sistema CO_2+ hexadecano y el tipo IV el sistema CO_2 + tridecano [9].

Finalmente, los diagramas de fase tipo VI se observan para algunos sistemas binarios en los que uno o ambos componentes presentan asociación por enlace de hidrógeno. En este caso hay dos líneas críticas: una línea continua similar a la de los tipos I y II y una línea de equilibrio LLV a bajas temperaturas limitada por los puntos UCEP y LCEP. Este LCEP distingue al tipo VI del tipo II.

La descripción del equilibrio de fases a alta presión no se limita a fases fluidas. En muchas aplicaciones de los SCF está implicada una fase sólida. En esta tesis, se consideran diagramas binarios y ternarios sin intervención de fase sólida. Los diagramas con interferencia de una fase sólida no se describen para no alargar esta introducción.

El locus crítico de un sistema ternario es una superficie que se extiende entre los locus de los tres sistemas binarios relacionados con el ternario. Para sistemas binarios de tipo I esta superficie será continua. En otros casos la superficie crítica presentará discontinuidades pudiendo hacerse muy complicada. El análisis del locus se puede simplificar si se considera al sistema ternario como un conjunto de sistemas pseudobinarios. En la Fig. 1.7 se muestra el locus del sistema ternario CO_2 + hexano + metanol basado en esta simplificación [10]. Las líneas críticas continuas son los locus críticos de los tres sistemas binarios implicados. Los símbolos unidos por líneas de trazos son datos críticos obtenidos para mezclas de CO_2 y una mezcla metanol + hexano de composición fija. En este diagrama el componente pseudobinario es la mezcla hexano + metanol. Cada locus pseudobinario (línea de trazos) empieza en el componente común CO_2 y termina en un punto del locus hexano + metanol. Los sistemas CO_2 + hexano y CO_2 + metanol son tipo I; el sistema metanol + hexano es tipo II.

En los procesos SCF estudiados en esta tesis aparecen dos tipos de sistemas ternarios. El primer tipo está formado por CO_2 como primer componente y dos disolventes orgánicos como segundo y tercer componentes; estos sistemas pueden tratarse de modo similar al descrito para CO_2 + hexano + metanol. En el segundo tipo de sistemas, el primer componente es CO_2, el segundo componente es un disolvente orgánico y el tercero es un sólido que ha sido previamente disuelto en el disolvente orgánico. La naturaleza del sólido es variada:

puede tratarse de un fármaco como la cefonicida o a polímero como el dextrano o la polivinilpirrolidona.

Reverchon et al. [11] han estudiado el efecto de la cefonicida en el diagrama de fases del sistema binario dióxido de carbono + dimetilsulfóxido (DMSO). En la Fig. 1.8 se representa el diagrama P-x para este sistema a 60 ºC, junto con los datos experimentales obtenidos en presencia de cefonicida.

En este estudio se utilizó una celda de observación visual y se encontró que para concentraciones bajas de cefonicida (30 mg/mL) los datos experimentales de equilibrio líquido-vapor (VLE) del ternario CO_2 + DMSO + cefonicida eran similares a los datos del sistema binario CO_2 + DMSO. Por otra parte, a concentraciones superiores de cefonicida (50 mg/mL) los datos de VLE del ternario CO_2 + DMSO + cefonicida diferían de los datos binarios en la zona pobre en CO_2 mientras que en la zona rica en CO_2 los datos de VLE del sistema ternario eran prácticamente coincidentes con los del binario. Las diferencias entre los datos VLE del sistema binario y ternario se reducen al disminuir la concentración del soluto e incrementarse la fracción molar de CO_2. Generalmente, el punto crítico de la mezcla del sistema ternario no coincide con el del sistema binario [11]. Esta coincidencia si se produce cuando la cantidad del tercer componente (cefonicida) es pequeña.

Diego et al. [12] utilizaron una celda de observación visual para estudiar el equilibrio de fases del sistema CO_2 + DMSO + dextrano a presiones en el intervalo de 8-12 MPa y temperaturas comprendidas entre 283.69 y 363.66 K. Las medidas se llevaron a cabo con una concentración constante de CO_2 del 20 % en masa. Se encontró que para concentraciones bajas del polímero (0.1 % en masa) no se observaba equilibrio líquido–líquido. Cuando se aumentó la concentración de dextrano a 0.85 %, se observaron equilibrios líquido-vapor, líquido-líquido y líquido-líquido-vapor. Al aumentar la concentración de dextrano hasta 8 % el equilibrio líquido-líquido apareció a una temperatura más baja. Como el dextrano interacciona con el CO_2 el diagrama de fases pseudobinario, diagrama de fases ternario para bajas concentraciones del soluto, difiere mucho del diagrama binario [12]. Para solutos como la cefonicida que interaccionan débilmente con el CO_2, el diagrama de fases ternario para bajas concentraciones de soluto coincide con el binario al menos en la región rica en CO_2 [11].

El conocimiento de los diagramas de fase es un factor clave para analizar el comportamiento de fases de los sistemas implicados en aplicaciones de los SCFs. Por ejemplo, la solubilidad de un sólido o un líquido en un fluido supercrítico en función de la presión a una temperatura dada se obtiene de diagramas P-x como el de la Fig. 1.3. Los diagramas similares al de la Fig. 1.4 nos ayudarán a encontrar la temperatura y presión crítica de una mezcla binaria. A partir de esta información se puede establecer el estado de la mezcla (líquido, supercrítico, equilibrio líquido-vapor). En los capítulos siguientes se verá que los diagramas de fase son necesarios para entender los fundamentos de los procesos que usan los SCF y para optimizar las condiciones de operación de los mismos. Desafortunadamente, aunque en la bibliografía existen datos para muchos sistemas binarios formados por un fluido supercrítico, los datos para sistemas ternarios y de orden superior son escasos.

1.2. Tecnología basada en los Fluidos Supercríticos

La naturaleza medioambientalmente benigna de los fluidos supercríticos como el dióxido de carbono (SC-CO_2) ha hecho que se haya investigado su uso en aplicaciones diversas relacionadas con la industria alimentaria, procesos químicos, industrias farmacéutica y textil y en la limpieza de componentes valiosos [13-16].

- **Extracción con Fluidos Supercríticos**

La extracción con fluidos supercríticos, conocida por su acrónimo en inglés SFE, se usa mucho en industrias como la petroquímica, química y textil y para producir extractos de gran calidad a partir de materias primas naturales en la industria alimentaria. La aplicación en la industria farmacéutica supone un reto porque sus exigencias de recuperación y reproducibilidad son más rigurosas [13]. SFE puede usarse en la etapa de preparación de muestras para fines analíticos o en gran escala para eliminar de una matriz un componente no deseado (por ejemplo el descafeinado) [17] o para extraer el producto deseado (por ejemplo, aceites esenciales) [18].

- **Cromatografía Supercrítica**

La cromatografía supercrítica, conocida por su acrónimo en inglés SFC, es una técnica analítica usada para separar los componentes de mezclas complejas con un fluido supercrítico (típicamente CO_2) como fase móvil. En la SFC la muestra pasa por medio de CO_2 a través de una columna de separación; la mezcla se separa en bandas debido a la diferente interacción entre cada analito y la fase estacionaria de la columna. Al abandonar la columna las bandas

un detector las identifica y determina sus cantidades [19]. SFC puede utilizarse para separar extractos de alta presión o para purificar mezclas de productos de reacción. También es posible concentrar un extracto eliminando impurezas o sub-productos no deseados. Se puede purificar un polipéptido separando otros péptidos y componentes obtenidos por fermentación. Por ejemplo, la ciclosporina A se puede separar de extractos miceliales purificándola por cristalización [20].

- **Fraccionamiento Mediante Fluidos Supercríticos**

El fraccionamiento de los extractos es una herramienta bien conocida que resulta útil para mejorar la selectividad de la SFE. A veces no es posible evitar la co-extracción de algunas familias de compuestos (con solubilidades diferentes, pero también con diferentes transferencias de masa en el material de partida). En estos casos, es posible llevar a cabo una extracción en etapas incrementando la presión para obtener la extracción fraccionada de los compuestos solubles presentes en la matriz orgánica ordenados por sus solubilidades decrecientes en el disolvente supercrítico. Esta operación permite fraccionar los extractos SCF utilizando varios separadores que trabajan en serie a presiones y temperaturas distintas. A escala industrial se suele trabajar en modo continuo usando CO_2 como disolvente; para aumentar su polaridad frecuentemente se añade como cosolvente etanol. El equipo consiste fundamentalmente en una columna de fraccionamiento por la que fluyen a contracorriente el disolvente supercrítico y el material de partida y secciones de separación. Al contrario que la SFE, este proceso es fácil de operar y puede ser automatizado, con lo que requiere poca mano de obra y tiene bajo coste de operación [21].

- **Reacciones Químicas**

Los fluidos supercríticos ofrecen como medio de reacción la posibilidad de remplazar en las industrias química y farmacéutica a los disolventes orgánicos tradicionales que son dañinos para el medioambiente. Simultáneamente el efecto del disolvente en la reacción se puede controlar y optimizar mejor. Ello está relacionado con las excepcionales propiedades de los SCFs en comparación con las de los líquidos y gases. Los reactivos y el SCF frecuentemente forman una sola fase supercrítica. Los SCF comparten muchas de las ventajas de las reacciones en fase gaseosa como la miscibilidad con otros gases, baja viscosidad, y gran difusividad que mejoran la transferencia de masa y energía y aumentan la velocidad de la reacción. Se han investigado muchos tipos de reacciones químicas, como la oxigenación, hidrogenación y alquilación [22-23].

- **Procesado de Polímeros**

A veces es difícil producir polímeros con distribuciones de masas moleculares estrechas por métodos tradicionales. El parámetro de solubilidad en un fluido supercrítico puede variarse cuidadosa y sistemáticamente modificando la temperatura y presión de modo que pueden fraccionarse materiales según su masa molecular porque la solubilidad varía con ella y con la longitud de cadena. Por tanto se puede someter una mezcla multicomponente a una extracción y fraccionamiento selectivo [13]. Además usando SCFs se pueden producir espumas poliméricas o impregnar un polímero con un buen control de ambos procesos.

- **Recubrimiento y Encapsulado de Partículas**

En aplicaciones farmacéuticas los perfiles de liberación del fármaco son muy importantes. La mayor parte de los principios activos son poco solubles en medios acuosos. Por ello en los últimos años se ha prestado atención al desarrollo de sistemas poliméricos biodegradables para la administración de fármacos con mejores propiedades terapéuticas [24]. Los métodos farmacológicos tradicionales para la producción de micropartículas conteniendo una proteína como material polimérico suelen emplear un disolvente orgánico que puede inactivar el fármaco o dejar residuos del mismo en el producto final. Además no se consigue una gran eficiencia en la encapsulación del fármaco [25]. Se pueden usar los fluidos supercríticos para recubrir las tabletas y partículas de principios activos con el tamaño adecuado. [26].

- **Micronización de Materiales**

Las partículas de pequeño tamaño con dimensiones de distribución definida son importantes en muchas aplicaciones. Por ejemplo, el tamaño de la partícula es un parámetro crucial que determina la velocidad de disolución de un fármaco en un fluido biológico y, por tanto, tiene un efecto importante en su biodisponibilidad. El diseño de partículas es una de las áreas más pujantes entre las aplicaciones de los fluidos supercríticos en las industrias farmacéutica, nutracéutica, cosmética y química [26, 27]. En la siguiente sección se examina más detalladamente la obtención de partículas usando SCFs y, en particular, la técnica por agente antidisolvente supercrítico.

1.3. Producción de Micropartículas usando Fluidos Supercríticos

La morfología, tamaño y distribución de tamaños de las partículas son propiedades clave que deben cumplir ciertos requisitos en conexión con el uso destinado a estos materiales. Las

micro y nanopartículas tienen importancia creciente en la producción de materiales cerámicos avanzados, colorante, explosivos, catalizadores, materiales para recubrimientos, microsensores, polímeros, ingredientes de alimentos y fármacos. Se utilizan varias técnicas de micronización convencionales: trituración, precipitación, "spray drying", "spray freezing" y recristalización por evaporación del disolvente o por agente antidisolvente líquido. Esta última técnica se basa en utilizar dos disolventes líquidos miscibles entre sí. El soluto a micronizar es soluble en el primer disolvente pero no en el segundo. Por tanto la adición del segundo disolvente (antidisolvente) induce la formación de una disolución formada por los dos líquidos y la sobresaturación y precipitación del soluto. Sin embargo la recristalización por evaporación del disolvente o por agente antidisolvente líquido requiere tratamientos posteriores complejos para eliminar completamente los residuos de disolvente. Las otras técnicas también presentan sus propios inconvenientes. Por ejemplo "spray-drying" suele requerir altas temperaturas de trabajo que pueden ocasionar la degradación térmica de materiales sensibles como los fármacos. Además todas las técnicas convencionales comparten el inconveniente del escaso control del tamaño y la distribución de tamaños, generalmente se obtiene un amplio rango de tamaño de partículas [28].

En los últimos años muchos investigadores han superado con éxito las limitaciones de las técnicas convencionales aprovechando las excepcionales propiedades de los fluidos supercríticos. El procesado con SCFs en general y con dióxido de carbono en particular tiene varias ventajas: la no toxicidad y fácil eliminación del disolvente, temperaturas de trabajo moderadas en una atmósfera inerte que evita la degradación del producto y la posibilidad de modular las propiedades del fluido modificando al presión y la temperatura, controlando de ese modo el tamaño de la partícula y/o su morfología. Jung y Perrut [26] revisaron en 2001 las técnicas disponibles para el diseño de partículas usando fluidos supercríticos. Dos años antes Reverchon [29] había revisado las técnicas basadas en la utilización del CO_2 supercrítico como agente antidisolvente. In 2003 Shariati y Peters [30] actualizaron estas revisiones. Mas tarde, otros autores examinaron los avances relativos a distintos tipos de materiales: explosivos (Pourmortazavi y Hajimirsadeghi, 2005 [31]); polímeros (Yeo y Kiran, 2005 [32] y Reverchon et al., 2009 [33]); materiales inorgánicos (Aymonier et al., 2006 [34]); materiales biomédicos (Byrappa et al., 2008 [35] y Okamoto y Danjo, 2008 [36]); ingredientes alimentarios (Weidner, 2009 [37]). Estas técnicas pueden clasificarse en dos grupos; las técnicas no reactivas sólo requieren transformaciones físicas mientras que otras técnicas usan el fluido supercrítico como medio (o simultáneamente como disolvente y

reactivo) para llevar a cabo una reacción en la que se producen partículas. Se pueden obtener micropartículas de un material puro y micropartículas "composite". Estas últimas son muy importantes como fármacos, productos agroquímicos, cosméticos o ingredientes alimentarios; se tratará de ellas en la próxima sección. A continuación se describirán brevemente las técnicas no reactivas más utilizadas.

1.3.1. Micropartículas "Composite"

Muchas formulaciones de fármacos, productos agroquímicos o cosméticos consisten en una sustancia activa encapsulada o embebida en un material de recubrimiento o soporte que les confiere propiedades adicionales. Aunque las micropartículas "composite" tienen estructuras muy variadas se las suele clasificar en microesferas y microcápsulas. Las micoresferas son partículas con geometría irregular en las que la sustancia activa forma agregados o está dispersa a nivel molecular en el seno de la matriz soporte. Las. microcápsulas tienen geometría esférica y están formadas por un núcleo de la sustancia activa rodeado por un recubrimiento sólido polimérico o proteico. Según su tamaño, las micropartículas se clasifican en nano-esferas/cápsulas si son más pequeñas que 1 μm, macro-esferas/cápsulas si son mayores de 1000 μm y micro-esferas/cápsulas si tienen tamaños intermedios.

Gran variedad de materiales como fármacos, enzimas y productos agroquímicos se han preparado como microesferas o microcápsulas. El material de soporte o recubrimiento suele ser un polímero natural o sintético pero también pueden usarse grasas, azúcares y ceras.

Los materiales "composite" o compuestos presentan varias ventajas. En primer lugar, son más fáciles de manejar y de dosificar que las partículas de la sustancia pura. El material elegido como soporte o recubrimiento mejora las propiedades de las mismas y depende del uso que se vaya a dar al material compuesto. Se usa un soporte biodegradable para la liberación controlada del principio activo en el medio (el organismo de un paciente, el suelo de un cultivo agrícola, etc.) Si la sustancia activa puede degradarse, el soporte sirve de

protección frente a los agentes dañinos. Si la sustancia activa es poco soluble en el medio, el soporte facilita su disolución. Este es el caso de numerosos fármacos poco solubles en agua. Si el fármaco es poco soluble en su estado cristalino, su presencia en una forma amorfa en el material compuesto conduce a ventajas adicionales mejorando su solubilidad, velocidad de disolución y biodisponibilidad.

Como ya se ha mencionado existen varias técnicas convencionales para preparar materiales compuestos. Cocero et al. [38] han revisado recientemente estos métodos y los resultantes de la aplicación de tecnologías supercríticas. Estos últimos han sido objeto de numerosas investigaciones en los últimos años; esencialmente son modificaciones de las técnicas usadas para obtener partículas puras. Las ventajas ya mencionadas para el procesado de materiales puros usando SCFs son aplicables en el caso de materiales compuestos. Además los SCFs pueden usarse para modificar las propiedades del soporte (plastificación, hinchado o reducción de la temperatura de fusión en el caso de un polímero) o las interacciones entre el soporte y la sustancia activa. Estas interacciones no se conocen bien; la producción de materiales compuestos todavía es un área de conocimiento empírico.

1.3.2. Expansión Rápida de Disoluciones Supercríticas (RESS)

Val Kukronis [39] fue el primer científico que aplicó los SCFs en la recristalización de materiales sólidos con el objeto de obtener partículas pequeñas con distribuciones estrechas de tamaños. La técnica propuesta se denominó “Rapid Expansion of Supercritical Solutions” (RESS) y se basa en utilizar el fluido supercrítico como disolvente. El material a micronizar se disuelve en el fluido en un extractor (Fig. 1.9). A continuación se produce una despresurización rápida por medio de un nebulizador en una cámara de expansión donde la nucleación del producto conduce a un material muy disperso. Por medio de RESS pueden obtenerse partículas pequeñas con distribuciones estrechas de tamaños a temperaturas moderadas.

Turk [40] ha revisado recientemente las publicaciones sobre esta técnica. RESS tiene la ventaja de no requerir disolventes orgánicos pero su aplicación está limitada a sólidos con una buena solubilidad en dióxido de carbono, que es el fluido más utilizado. La baja solubilidad de las moléculas grandes y polares como los fármacos en CO_2 limita la aplicación de RESS. Si no fuera por esto, RESS sería la técnica a elegir en el diseño de partículas. La coprecipitación también es posible pero tanto la sustancia activa como el soporte tienen que

ser solubles en CO_2. Como RESS es un proceso muy rápido, resulta difícil controlar la morfología y la carga de los "composites". Una posibilidad es precipitar el soporte sobre partículas previamente formadas de la sustancia activa.

1.3.3. Partículas a partir de Disoluciones (o Suspensiones) -Saturadas de Gas (PGSS) y Procesos Afines

Otra técnica supercrítica para diseñar partículas es la denominada "Particles from Gas-saturated Solutions (or Suspensions)" (PGSS). En este proceso el fluido supercrítico se disuelve en un sustrato líquido o en una disolución del sustrato(s) en un disolvente o en una suspensión del sustrato(s) en un disolvente (Fig. 1.10). A continuación la mezcla líquida se despresuriza rápidamente por medio de un nebulizador y se forman partículas sólidas o gotitas dependiendo del tipo de mezcla y las condiciones. Este proceso se basa en la gran solubilidad de los gases comprimidos en líquidos y sólidos como los polímeros en comparación con la baja solubilidad de los mismos en la fase a presión. Se forman partículas de sustancias que no necesitan ser solubles en el fluido supercrítico. PGSS puede aplicarse a suspensiones del sustrato(s) activo en un polímero u otro soporte formándose microesferas "composite".

PGSS también ha sido utilizado para aplicar pinturas u otros recubrimientos como adhesivos. En este proceso hay dificultades para obtener partículas submicrónicas y para controlar las distribuciones del tamaño de las partículas. La coprecipitación es posible; el efecto plastificador y el hinchamiento que acompañan la disolución del CO_2 en el polímero favorecen la incorporación de la sustancia activa. Sin embargo cuando el soporte se usa en fundido, son necesarias temperaturas altas para fundir sustancias como los polímeros semicristalinos usados en algunas aplicaciones.

Afín al proceso PGSS es el proceso denominado "Depressurization of an Expanded Liquid Organic Solution" (DELOS) propuesto por Ventosa et al. [41]. En él, un gas comprimido en un autoclave expande una disolución líquida formada por el soluto a micronizar y un disolvente convencional. En este momento, el gas comprimido actúa como cosolvente y no como antidisolvente. La disolución expandida o mezcla ternaria del soluto, disolvente y gas comprimido se despresuriza reduciendo rápidamente la presión del sistema hasta presión atmosférica en una cámara de expansión. La disolución se evapora y su temperatura

desciende mucho, se produce una sobresaturación y el soluto precipita en forma de partículas pequeñas con una distribución estrecha de tamaños.

1.3.4. Precipitación por Agente Supercrítico Antidisolvente (SAS)

Krukonis et al. [42] fueron los primeros en proponer el uso del dióxido de carbono como agente antidisolvente para inducir la precipitación controlada de solutos a partir de sus disoluciones orgánicas. Este enfoque se basa en la baja solubilidad en CO_2 de solutos como los polímeros o fármacos y la buena miscibilidad del CO_2 con muchos disolventes orgánicos. Este es el proceso denominado precipitación "supercritical antisolvent" (SAS). Se han utilizado distintos dispositivos experimentales y acrónimos: GAS ("gas antisolvent"), PCA ("precipitation by compressed antisolvent"), ASES ("aerosol solvent extraction"), SEDS ("solution enhanced dispersion by supercritical fluid") y SAS ("supercritical antisolvent"). El acrónimo GAS se suele usar para procesos en discontinuo mientras que SAS describe bien a los procesos continuos. Ambos tipos de técnicas se basan en el mismo concepto ilustrado en la Fig. 1.11.

El sólido a precipitar se disuelve en un disolvente orgánico y se mezcla con CO_2 en la cámara de precipitación. Cuando el CO_2 supercrítico se disuelve en el disolvente orgánico, el líquido experimenta una expansión volumétrica y se convierte en un mal disolvente de soluto que precipita en forma de micro y nanopartículas. El tamaño de la partícula se puede modular variando los parámetros del proceso como la presión, temperatura, concentración del soluto, etc. Los parámetros críticos del CO_2 permiten operar a temperaturas moderadas. Además las partículas no tienen restos de disolvente y presentan una distribución estrecha de tamaños. Desde el punto de vista de la Química Sostenible, SAS tiene el inconveniente de usar disolventes orgánicos pero se trabaja a una presión muy inferior a la de RESS. También pueden usarse en SAS inhibidores de la aglomeración o modificadores del hábito del cristal. Como en RESS, es posible producir "composites" coprecipitando simultáneamente la sustancia activa y el soporte o encapsulando partículas formadas previamente. En este caso, se prepara una suspensión de las partículas en una disolución del soporte y este se precipita por SAS. Si se coprecipitan un fármaco y un excipiente polimérico, se pueden modificar fácilmente las proporciones de ambos componentes cambiando sus cantidades relativas en la disolución orgánica.

1.3.5. Reacciones en Medio Supercrítico con Formación de Partículas

Las reacciones en medio supercrítico con formación de partículas han recibido bastante atención como instrumento para sintetizar partículas de materiales cerámicos u óxidos. Al contrario que en los procesos RESS, SAS y PGSS, se utiliza el SCF para llevar a cabo una reacción. Por ejemplo, se disuelven lo precursores en el fluido y se les descompone térmicamente. Tras la despresurización en CO_2, el disolvente vuelve a la fase gaseosa y separándose de las partículas que se obtienen finamente divididas. También se puede llevar a cabo una reacción sol-gel a alta presión y alta temperatura. En la síntesis hidrotérmica se usa un fluido supercrítico simultáneamente como disolvente y reactivo. Para obtener polvos de óxidos, los precursores (sales inorgánicas) se disuelven primero en agua y se introduce la disolución en un reactor operado en condiciones supercríticas. Por cambios de presión y temperatura se modifican las propiedades termodinámicas y de transporte consiguiéndose controlar el crecimiento de los cristales, la morfología y el tamaño y la distribución de tamaños de las partículas. Esta técnica evita etapas de los procesos convencionales como la calcinación pero aún son necesarios el filtrado, lavado y secado. Desafortunadamente, hay que enfrentarse a los problemas de corrosión asociados al uso del agua supercrítica.

1.4. Fundamentos de la Precipitación por Agente Supercrítico Antidisolvente (SAS)

La gran aplicabilidad de SAS ha contribuido a su uso creciente. En los últimos años se han micronizado por este método gran variedad de compuestos como explosivos, polímeros, fármacos, colorantes, catalizadores y compuestos inorgánicos en general. Por lo que respecta a la morfología se han obtenido distintas morfologías para partículas amorfas: nanopartículas con diámetros medios en el intervalo 30-200 nm, micropartículas en el intervalo 0,25-20 μm y micropartículas expandidas (huecas) con diámetros entre 10 y 200 μm. También se han obtenido cristales con distintos hábitos y dimensiones. Debido a estas características, SAS ha sido la técnica elegida en esta tesis.

La precipitación SAS incluye varias etapas:

- Usando una bomba de alta presión se introduce CO_2 supercrítico en la cámara de precipitación a un flujo constante. Se introduce el disolvente o directamente la disolución también a flujo constante alcanzándose el estado estacionario y una proporción fluido/disolvente adecuada. La cámara se calienta y se controlan la temperatura y la presión.

- El fluido se disuelve en la disolución formada por el sólido y un disolvente orgánico polar como el dimetilsulfóxido (DMSO) o la *N*-metil-2-pirrolidona (NMP). Se produce la expansión y sobresaturación y comienza la precipitación. El soluto se recoge en la cámara de precipitación.

- Al terminar la precipitación la cámara se lava con el antidisolvente para eliminar el disolvente líquido. La mezcla CO_2 + disolvente orgánico pasa a la cámara de separación donde se recupera el disolvente.

La expansión volumétrica del disolvente líquido es el resultado de la gran solubilidad del fluido supercrítico antidisolvente en la fase líquida. La expansión volumétrica ΔV % porcentual se define como

$$\Delta V\,\% = \frac{V(P,T) - V_0}{V_0} * 100 \qquad (1.1)$$

donde V (P, T) es el volumen de la fase líquida cargada con el antidisolvente y V_0 es el volumen de la fase líquida pura a presión atmosférica.

Muchos autores han estudiado las isotermas de expansión volumétrica de los sistemas CO_2 + disolvente [29, 43], pero también debería tenerse en cuenta el efecto del soluto en la expansión volumétrica. Este tipo de estudios son escasos. Reverchon et al. [44] han estudiado este efecto en el caso del sistema ternario CO_2 + DMSO + dextrano a 30 °C. En la Fig. 1.12 se muestran las curvas de expansión volumétrica para CO_2 + DMSO y CO_2 + DMSO + dextrano. Los porcentajes de dextrano varían entre 0.05 y 5 %. Su presencia no modifica apreciablemente la expansión volumétrica. Los valores de ΔV % para las mezclas ternarias siguen la misma isoterma del sistema CO_2 + disolvente. Aunque estos datos corresponden a una temperatura más baja que la empleada habitualmente en SAS, se pone de manifiesto que para las bajas concentraciones de soluto utilizadas en esta técnica la expansión volumétrica puede describirse usando datos binarios.

El éxito de la micronización SAS, y la morfología, tamaño y distribución de tamaños de las partículas dependen de un gran número de parámetros del proceso: temperatura, presión, concentración, elección del disolvente, modo de inyección del antidisolvente, etc. Estos parámetros influyen simultáneamente en el equilibrio de fases a alta presión, la hidrodinámica, la transferencia de masa y la formación y crecimiento de las partículas. Para comprender el proceso SAS deben tenerse en cuenta todos estos factores y las interacciones

entre ellos. Los estudios experimentales suelen explorar distintas combinaciones de los parámetros del proceso seleccionando sus valores óptimos después de un trabajo considerable. A veces se sigue una estrategia de diseño de experimentos para minimizar el número de micronizaciones. A partir de este tipo de estudios es difícil obtener conclusiones generales o reunir la información necesaria para el escalado requerido en aplicaciones comerciales. Por ello muchos autores han llevado a cabo estudios, tanto teóricos como experimentales, encaminados a establecer los fundamentos y mecanismos de la precipitación SAS. Para poder establecer estos mecanismos han de tenerse en cuenta interacciones entre el equilibrio de fases a alta presión, las variaciones de la tensión superficial, la dinámica del chorro, la transferencia de masa, y la nucleación y crecimiento de las partículas. Una revisión detallada de todas estas contribuciones está fuera del alcance de esta introducción.

Los profesores Ernesto Reverchon y María José Cocero, y sus grupos de las universidades de Salerno (Italia) y Valladolid (España), han contribuido extraordinariamente en los estudios experimentales y en el análisis de los mecanismos de precipitación SAS. Martín y Cocero [45] revisaron en 2008 las contribuciones sobre los fundamentos y mecanismos de SAS prestando atención a la mecánica de fluidos, las propiedades termodinámicas y de transporte, la transferencia de masa y la formación y crecimiento de las partículas. Como mostraron Reverchon, Brauer y sus colaboradores usando técnicas de difusión de luz y láser [46, 47], los mecanismos son el resultado de las influencias mutuas entre estos fenómenos. En dos trabajos publicados recientemente, De Marco y Reverchon [48, 49] resumieron estas contribuciones y las conclusiones más importantes.

Algunos autores intentaron explicar los mecanismos de SAS partiendo del análisis de dinámica de fluidos en la inyección de la disolución en el antidisolvente a presión. Lengsfeld et al. [50] indicaron que cuando el disolvente y el antidisolvente son totalmente miscibles la mezcla en el chorro es similar a la de un gas gracias a la desaparición de la tensión superficial dinámica asociada a la formación de una disolución supercrítica. Más tarde, Dukhin et al. [51], Sarkari et al. [52], Badens et al. [53], Gokhale et al. [54] y Obrzut et al. [55] estudiaron la atomización del chorro en gases a presión. Se observaron dos tiempos característicos: un tiempo de relajación τ y un tiempo de ruptura "break-up" del chorro t. Si $t < \tau$, existe una interfase entre el líquido y la fase fluida, y el "break-up" del chorro predomina transformando el chorro líquido en gotitas. Si $\tau < t$, cerca del orificio del nebulizador persiste un chorro corto y se produce una mezcla del chorro tipo gas. Dukhin et al. propusieron un mecanismo de

tensión interfacial dinámica (DIT) producido por gradientes de entalpía e introdujeron un nuevo modo DIT no isotermo que contribuía a la estabilidad del chorro cuando la mezcla era exotérmica. Debenedetti y Werling [56, 57] introdujeron modelos matemáticos de transferencia de masa. Baldyga et al. [58] y Martín y Cocero [59] propusieron modelos para el proceso de precipitación por encima y por debajo del punto crítico de la mezcla CO_2 + disolvente (MCP; "mixture critical point").

En concordancia con la descripción de los diferentes mecanismos de mecánica de fluidos, Reverchon et al. [60] encontraron que cuando se trabajaba a presiones por encima del MCP, los parámetros que influían en la mezcla del chorro, como el diseño del nebulizador y cámara de precipitación, o el número de Reynolds en el nebulizador, no tenían un efecto apreciable en la precipitación. Esto indica que, en estas condiciones, la mezcla entre la disolución y el CO_2 es más rápida que la precipitación, y por tanto los parámetros de mezcla no pueden influir en la misma. Sin embargo a presiones por debajo del MCP, estos parámetros tienen una gran influencia. Además en estas condiciones se observó un cambio en la morfología de la partículas, a veces las partículas se aglomeraban formando esferas huecas, lo que podría indicar que la atomización y precipitación tienen lugar por formación de gotitas. Se estableció una correlación entre las dimensiones de las partículas y la posición de las coordenadas presión y temperatura del proceso en el diagrama VLE del sistema CO_2 + disolvente. A presiones bastante superiores al MCP se obtenían nanopartículas [11, 61, 62] y un poco por encima del MCP, micropartículas [63] coexistiendo a veces las nanopartículas y las micropartículas. La uniformidad de los productos empeora cuando las condiciones de precipitación se acercan al locus crítico. En la región de vapor se forman micropartículas agregadas e irregulares y en la región líquido-vapor se forman "clusters" esféricos o aglomerados densos. Los estudios de Chang et al. [61] demuestran la relación entre la morfología de las partículas de α-chymotrypsina precipitadas a partir de sus disoluciones en DMSO y el equilibrio de fases del sistema CO_2 + DMSO. Sus resultados se resumen en la Fig. 1.13.

Se ha propuesto una interpretación de los resultados obtenidos a varias presiones [46, 48, 63] mostrando que el cambio de nanopartículas a micropartículas se debe a que compiten el "break-up" del chorro de líquido inyectado en el cámara de precipitación y la mezcla tipo gas. Cuando domina el primer proceso, se forman gotitas de líquido que producen partículas micrométricas; cuando domina el segundo, se forman nanopartículas por precipitación en la

fase fluida. La competición entre estos dos procesos puede explicarse teniendo en cuenta sus tiempos característicos: cuando el tiempo para el "break-up" del chorro es inferior al tiempo necesario para que desaparezca la tensión superficial dinámica se forman gotitas, en el caso opuesto domina la mezcla tipo gas [46, 63, 64]. Las nanopartículas se diferencian de las micropartículas en su diámetro y en su morfología esférica irregular debido a la precipitación gas-sólido en ausencia de tensión superficial. De Marco y Reverchon [47] también mostraron que estos mecanismos de precipitación pueden modularse cambiando la presión, la temperatura o la concentración del soluto, así se puede seleccionar el rango de tamaños requerido.

Los mecanismos son distintos cuando el compuesto precipita en forma cristalina [48]: en este caso hay dos posibilidades. Cuando el secado de las gotas va seguido de una cinética de cristalización rápida, los cristales tienen predominantemente forma esférica. Cuando la precipitación tiene lugar en una fase líquida expandida se obtienen cristales de diversos hábitos y dimensiones dependiendo de las interacciones con el disolvente utilizado.

Puesto que el equilibrio de fases es uno de los factores cruciales en la morfología y tamaño medio de las partículas obtenidas en el proceso SAS, se ha dedicado mucha atención en los últimos años al equilibrio de fases de las mezclas binarias formadas por el CO_2 y los disolventes orgánicos usados en SAS. En presencia de solutos como los polímeros el diagrama de fases se modifica; desafortunadamente los datos para sistemas ternarios incluyendo el soluto son escasos. Sin embargo, cuando el soluto interacciona débilmente con el CO_2, el diagrama de fases ternario coincide con el binario para las bajas concentraciones de soluto utilizadas en SAS en la región rica en CO_2, que es la región de las mezclas formadas ene este proceso. Por ejemplo, este es el caso del sistema CO_2 + DMSO + cefonicida mencionado en la sección 1.1.2. Por tanto, en muchos casos, las mezclas formadas en la cámara de precipitación pueden tratarse como sistemas binarios CO_2 + disolvente orgánico. Las propiedades volumétricas, densidades y parámetros críticos de este tipo de sistemas también han sido objeto de numerosos trabajos. Sin embargo no se ha prestado atención, con la excepción del trabajo de Dukhin [51], al calor liberado cuando el CO_2 se disuelve en el disolvente orgánico. Este calor de mezcla (entalpía de exceso) puede ser muy alto. Por tanto los efectos térmicos durante este proceso pueden influir en la separación de fases y deben tenerse en cuenta para entender mejor las micronizaciones SAS. La contribución debida a las interacciones del soluto puede despreciarse: los efectos térmicos pueden estudiarse midiendo

las entalpías de exceso de las mezclas CO_2 + disolvente orgánico formadas en la cámara de precipitación SAS.

Midiendo las entalpías de exceso del CO_2 y la *N*-metil-2-pirrolidona en las condiciones de presión y temperatura usadas en SAS, nuestro grupo ha mostrado en un estudio previo [65] que los efectos térmicos tienen un papel importante en SAS y parecen estar relacionados con la coalescencia no deseada de partículas de antibiótico obtenidas usando NMP. Las condiciones de temperatura y presión para la coalescencia coinciden con las de valores más exotérmicos de la entalpía de exceso. Se requiere un estudio sistemático de las entalpías de exceso de las mezclas CO_2 + disolvente orgánico y micronizaciones paralelas para dilucidar el efecto de la temperatura y la presión y las interacciones entre el equilibrio de fases y el calor liberado cuando se mezclan el fluido y la disolución. El calor de mezcla del CO_2 supercrítico y metanol o etanol ya se ha medido [66-68]. Sin embargo, esta magnitud no se conoce para los disolventes más utilizados en SAS como el DMSO y la acetona.

1.5. Aplicación de Precipitación por Agente Supercrítico Antidisolvente en el Desarrollo de Fármacos

La aplicación de SAS en el desarrollo de fármacos es un área de investigación muy activa [33, 35, 36]. En el caso de sustancias puras, SAS proporciona un buen control del tamaño y la morfología. Se han producido cristales, nanopartículas y micropartículas que mejoran la administración de los fármacos. Todos los estudios mencionados en la sección anterior pueden aplicarse en este caso.

La formación of micropartículas “composite” no se conoce tan bien [33, 38]. En la precipitación sobre una suspensión de partículas, las partículas actúan como núcleos para la precipitación del polímero y por aglomeración se forma una matriz polimérica de partículas encapsuladas. Este método es especialmente adecuado para materiales orgánicos insolubles como las proteínas. Para fármacos solubles en disolventes orgánicos se prefiere la coprecipitación. La precipitación de nanopartículas no conduce a coprecipitación debido al mecanismo gas-partícula que gobierna el proceso. Las micropartículas “composite” polímero-fármaco se forman por eliminación del disolvente en las gotitas de líquido. Este proceso es más complicado que el de los fármacos puros. Aparecen nuevos parámetros como la masa de polímero o la proporción polímero-fármaco.

Al contrario de la micronización de materiales puros, la coprecipitación no está bien estudiada. Como destacaron Reverchon et al. [33], aunque en muchos casos se haya usado el polímero poli-L-láctico (PLLA), no se ha llevado a cabo ninguna investigación sistemática, sobre la influencia de los parámetros SAS en las propiedades del material compuesto. Es necesario estudiar las interacciones polímero-fármaco para saber que se puede esperar si el mismo polímero se combina con un fármaco distinto.

La selección del material soporte o de recubrimiento es crucial. Debe reunir varios requisitos: biocompatibilidad, no toxicidad, conservación de las propiedades y la actividad del fármaco y afinidad con el mismo. Gracias a esta afinidad, el fármaco se incluye en el soporte en estado amorfo. El material del soporte o de recubrimiento debe ser también fácil procesable mediante SAS. La incorporación del fármaco en su estado amorfo hace que las partículas compuestas sean más pequeñas que las del material puro precipitado en las mismas condiciones. Esta es otra ventaja a añadir a las mejoras de la solubilidad, velocidad de disolución y biodisponibilidad del fármaco amorfo.

Se han usado varios polímeros en la coprecipitación SAS además de PLLA: polietilenglicol (PEG), polivinilpirrolidona (PVP), el copolímero lactida glicolida (PLGA), ácido poli-DL-láctico (PLA), eudragit. En esta tesis se ha elegido PVP porque esta lactama polimérica es uno de los principales aditivos en las formulaciones farmacéuticas. Usando PVP se mejora la velocidad de disolución y biodisponibilidad de fármacos poco solubles.

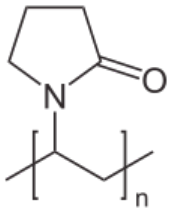

Poli[1-(2-oxo-1-pirrolidinil)etileno], nombre IUPAC del PVP.

El incremento de la velocidad de disolución se debe a la inhibición de la cristalización gracias principalmente al efecto plastificante del PVP y su adsorción superficial e impedimento estérico para la nucleación y crecimiento del cristal [69-70]. Además el PVP es un polímero sintético soluble en agua y lineal, capaz de disolverse en gran número de disolventes orgánicos. Chadha et al. [71] recopilaron las propiedades del PVP y las técnicas analíticas empleadas para caracterizar los sistemas fármaco-PVP en estado sólido o líquido. Dependiendo de las condiciones de polimerización, el PVP puede preparase en gran variedad de masas moleculares expresadas mediante los valores del parámetro *K*.

$$K\text{-valor} = [\{300\ C\log Z + (C + 1.5\ C\log Z)^2\}^{0.5} + 1.5\ C(\log Z) - C]/\{0.15\ C + 0.003\ C^2\} \quad (1.2)$$

donde Z es la viscosidad del PVP a la concentración C relativa al agua.

Las masas moleculares promedio en número ($\overline{M}_n$), promedio en masa ($\overline{M}_w$) y promedio viscoso ($\overline{M}_v$) pueden obtenerse a partir de las siguientes expresiones:

$$\overline{M}_n = 24^* K^2,\ \overline{M}_w = 15^* K^{2.3},\ \overline{M}_v = 22.22\ (K + 0.0075\ K^2)^{1.65} \quad (1.3)$$

La temperatura de transición vítrea (T_g) del PVP lineal aumenta al aumentar la masa molecular y puede calcularse según la ecuación:

$$T_g\ [^\circ C] = 175 - (9685/K^2) \quad (1.4)$$

Recientemente, el PVP se ha usado en el proceso SAS como soporte o excipiente de varios fármacos. Lim et al. [72] obtuvieron micropartículas "composite" de indometacina por coprecipitación con PVP *K*-90. La indometacina es un fármaco cristalino antinflamatorio. Uzun et al. [73] también obtuvieron micropartículas "composite" formadas por el antibiótico axetil cefuroxima y PVP *K*-30. Badens y colaboradores [74, 75] prepararon dispersiones sólidas de oxeglitazar en PVP *K*-17. Este es un fármaco nuevo usado en el tratamiento de la diabetes tipo II. Wu et al. [76] obtuvieron micropartículas "composite" formadas por piroxicam y PVP *K*-25 por PCA. También se han usado procesos afines a SAS. Corrigan y Crean [77] prepararon micropartículas "composite" de hidrocortisona-PVP mediante GAS. En la mayor parte de los casos se obtuvieron buenas morfologías y mejoras en las velocidades de disolución.

El PVP interacciona con la molécula del fármaco por fuerzas electrostáticas (ion-ion, ion-dipolo, dipolo-dipolo), fuerzas de van der Waals y enlaces de hidrógeno. Varias técnicas fisicoquímicas proporcionan información sobre las interacciones. La difracción de Rayos X (XRD), calorimetría diferencial de barrido (DSC) y espectroscopia infrarroja (IR) son las más usadas. XRD da información sobre los cambios en la cristalinidad y forma polimorfa como consecuencia de SAS. DSC puede usarse para establece las temperaturas de transición vítrea. IR se usa para detectar el enlace de hidrógeno entre el fármaco y el PVP por medio del

nitrógeno o el grupo carbonilo del anillo del pirrol. La microscopia electrónica de barrido da información sobre las morfologías del fármaco puro, el PVP y los materiales compuestos. La solubilidad y velocidad de disolución de la combinación o "composite" fármaco-PVP son también clave. Se llevan a cabo tests de disolución en un fluido intestinal simulado (pH = 7.4) y se comparan los resultados con los obtenidos para el fármaco puro.

Objetivos

Esta tesis estudia la micronización de compuestos utilizando fluidos supercríticos. Entre las diferentes técnicas posibles se eligió el método SAS por las propiedades excepcionales de los materiales micronizados utilizando dióxido de carbono supercrítico como agente antidisolvente.

La motivación de este estudio es doble y se basa en la necesidad de profundizar en el estudio de los procesos SAS para poder diseñarlos y escalarlos correctamente, y en la necesidad de desarrollar micronizaciones de formulaciones farmacéuticas.

Nuestro estudio preliminar sobre los efectos térmicos en la precipitación SAS de antibióticos usando NMP como disolvente se ha extendido obteniendo datos de calores de mezcla (entalpías de exceso) de los sistemas CO_2 + disolvente orgánico utilizados más frecuentemente en estas micronizaciones. Se ha dilucidado la interacción entre las entalpías de exceso y el equilibrio de fases en la cámara de precipitación SAS. Se han llevado a cabo micronizaciones de fármacos usando estos disolventes y CO_2 como agente antidisolvente, y se han estudiado los parámetros SAS prestando especial atención a las condiciones de presión y temperatura, el equilibrio de fases y el calor desprendido al mezclarse el fluido supercrítico y la disolución. Se han obtenido micro y nanopartículas de dos fármacos puros y micropartículas compuestas de uno de ellos.

Los objetivos específicos de esta tesis fueron:

1. Medida de los Datos de Entalpía de Exceso de los Sistemas CO_2 + Disolvente Orgánico

Las entalpías de exceso se midieron usando un calorímetro de flujo isotermo capaz de operar a alta presión disponible en nuestro laboratorio. Se utilizaron las condiciones de presión y temperatura habituales en las micronizaciones SAS. Como estos datos ya estaban disponibles para *N*-metil-2-pirrolidona, etanol y metanol, se han estudiado los disolventes dimetilsulfóxido (DMSO), acetona, *N*,*N*-dimetilformamida (DMF) y acetato de etilo (EA). Los datos de entalpías de exceso se correlacionaron usando ecuaciones de estado.

2. Estudio del Equilibrio de Fases a Alta Presión de los Sistemas CO_2 + Disolvente Orgánico. Interacción entre el Equilibrio de Fases y las Entalpías de Exceso durante los Experimentos SAS

En la bibliografía pueden encontrarse datos del equilibrio de fases isotermo (VLE) y las constantes críticas de los sistemas CO_2 + disolvente orgánico estudiadas en esta tesis. Generalmente los datos de constantes críticas son escasos. Para cada sistema se llevó a cabo una recopilación bibliográfica. En caso necesario, el locus crítico y los datos de VLE se predijeron o calcularon utilizando ecuaciones de estado. Basándose en el conjunto de datos obtenidos en los objetivos 1 y 2, se discutió el comportamiento termodinámico de las mezclas formadas en la cámara de precipitación SAS y la influencia de los efectos térmicos en el equilibrio de fases y la morfología de las partículas.

3. Construcción de un Dispositivo SAS

Se construyó en nuestro laboratorio un aparato SAS que fue validado micronizando acetato de itrio con DMSO como disolvente. Esta micronización está bien descrita en la bibliografía.

4. Micronización de Fármacos

Se llevaron a cabo experimentos de micronización para determinar las condiciones óptimas de estos procesos teniendo en cuenta los requisitos de tamaño y morfología de las partículas. Se utilizó una estrategia de diseño de experimentos para minimizar el número de los mismos. Se estudió la relación entre las condiciones de presión y temperatura, el equilibrio de fases y la entalpía de exceso. Se establecieron las condiciones óptimas de precipitación. Después de una revisión de la bibliografía se eligieron los fármacos a micronizar: el 5-fluorouracilo, ampliamente utilizado en el tratamiento de distintos tipos de cánceres, y el diflunisal, un derivado del ácido salicílico con actividad analgésica y antiinflamatoria. Ambos fármacos son poco solubles en CO_2. El 5-fluorouracilo ha sido micronizado previamente usando metanol o mezclas de metanol con otros disolventes. El diflunisal no se ha micronizado usando una técnica supercrítica. Las partículas obtenidas se estudiaron por microscopia electrónica de barrido (SEM) estableciéndose el tamaño y la distribución de tamaños. La cristalinidad y forma polimórfica de los fármacos obtenidos por SAS se determinó usando difracción de rayos X.

5. Co-precipitación de Fármacos y PVP

Se coprecipitó diflunisal usando PVP *K*-15 y *K*-30 como medio. Para elegir el disolvente puro o mezcla se tuvieron en cuenta las solubilidades del fármaco puro y del PVP y se establecieron las condiciones óptimas de precipitación. Se probaron distintas proporciones del fármaco y el polímero. Las micropartículas se estudiaron usando SEM, XRD, espectroscopia infrarroja (IR), calorimetría diferencial de barrido (DSC), y análisis termogravimétrico (TGA). Se estableció la solubilidad y la velocidad de disolución del material compuesto diflunisal-PVP y se estudiaron las interacciones entre ambos componentes. También se llevó a cabo una comparación sistemática con otros materiales compuestos fármaco-PVP obtenidos previamente por SAS.

Resumen y Conclusiones

En esta tesis se estudia la micronización de sólidos usando fluidos supercríticos partiendo de una doble motivación: la necesidad de profundizar en el estudio de los procesos SAS para poder diseñarlos y llevar a cabo su escalado y la necesidad de desarrollar las micronizaciones de fármacos. Se examina el papel de las entalpías molares de exceso en las micronizaciones SAS y se aborda la micronización de fármacos.

Capítulo 1. Introducción

La primera parte de este trabajo es una introducción acerca de los fluidos supercríticos seguida de una descripción de la producción de micropartículas usando los SCFs. A continuación se revisan los fundamentos de la precipitación SAS y su aplicación en farmacología. En las páginas precedentes de este resumen puede encontrarse una versión española completa del capítulo.

Capítulo 2. Objetivos

En este capítulo se describen los objetivos de esta tesis. En las páginas precedentes de este resumen puede encontrarse una versión española completa del mismo.

Capítulo 3. Metodología

Se describe el calorímetro de flujo isotermo de alta presión utilizado para medir las entalpías molares de exceso, H_m^E, de los sistemas CO_2 + disolvente orgánico. Se explica la metodología de los cálculos del equilibrio de fases, las entalpías de exceso y el locus crítico usando ecuaciones de estado. Se describen con detalle el aparato SAS construido en esta tesis, la estrategia para el diseño de experimentos y los métodos usados para caracterizar las partículas.

Capítulo 4. Efectos Térmicos en las Micronizaciones por Agente Antidisolvente Supercrítico

En una primera etapa se midieron las entalpías molares de exceso, H_m^E, de los sistemas CO_2 + disolvente orgánico bajo las condiciones de presión y temperatura utilizadas en las micronizaciones SAS. En una segunda etapa se estudió la interacción entre las entalpías de exceso y el equilibrio de fases en la cámara de precipitación SAS para los disolventes acetona

(ac), *N*,*N*-dimetilformamida (DMF), dimetilsulfóxido (DMSO) y acetato de etilo (EA). Esta parte de la tesis ha sido objeto de cuatro publicaciones que se incluyen en este capítulo.

Las condiciones de temperatura y presión fueron 313.15 y 323.15 K y 9.00, 12.00, 15.00 y 18.00 MPa, así como 333.15 K y 9.00 y 15.00 MPa. Para los sistemas estudiados se observaron tendencias similares en la variación de H_m^E con la fracción molar, la temperatura y la presión. La mayor parte de los procesos de mezcla fueron muy exotérmicos. H_m^E alcanzó valores mínimos de –4500 J mol^{-1}. Para casi todas las condiciones de temperatura y presión, las entalpías molares de exceso presentan este mínimo en la región rica en CO_2. En algunas condiciones, al representar H_m^E frente a la fracción molar del CO_2, se observaron secciones lineales debidas a la existencia de una región de dos fases en la que están en equilibrio una mezcla líquida y una mezcla gaseosa de composiciones dadas. Se puede demostrar que las composiciones de estas dos fases se corresponden con los valores de la coordenada *x* al comienzo y al final de la sección lineal. Los valores de las composiciones así obtenidos se compararon con los datos de VLE de la bibliografía.

La temperatura y la presión tienen un gran efecto sobre H_m^E. Para cada sistema, a una fracción molar dada, en general, las mezclas se hacen menos exotérmicas al aumentar la presión y disminuir la temperatura. El effecto de la naturaleza del disolvente orgánico depende de las condiciones de temperatura y presión. Por ejemplo, las mezclas CO_2 + EA son las más exotérmicas a las tres temperaturas y 9.00 MPa. Sin embargo, a las otras presiones estudiadas, presentan valores intermedios entre los observados para los otros sistemas.

Las entalpías molares de exceso de CO_2 + Ac, DMF o EA se correlacionaron con precisión usando las ecuaciones de estado de Peng-Robinson y Soave-Redlich-Kwong, junto con la regla de mezcla clásica con dos parámetros binarios ajustables para cada temperatura. Esta correlación no se pudo llevar a cabo para el sistema CO_2 + DMSO; el motivo puede ser el comportamiento crítico más complejo de este sistema. Además, en el caso del CO_2 + DMF, se describieron simultáneamente el equilibrio líquido-vapor y el locus crítico usando las EOS de Peng-Robinson y Soave-Redlich-Kwong, junto con la regla de mezcla clásica, y se predijeron las entalpías molares de exceso. La ecuación de Peng-Robinson proporcionó unos resultados mejores.

Las variaciones de la entalpías molares de exceso con la presión y la temperatura se analizaron teniendo en cuenta las interacciones moleculares y los datos de equilibrio de fases, densidad y paramétros críticos existentes en la bibliografía para los sistemas CO_2 + disolvente orgánico. Se llevó a cabo una recopilación bibliográfica para CO_2 + acetona, DMF, DMSO o EA. Estos sistemas han sido objeto de numerosas investigaciones debido a su implicación en las aplicaciones de los SCFs.

La entalpía molar de exceso resulta de la suma de dos contribuciones. Una de ellas es debida a los cambios en las interacciones moleculares causadas por la alteración de la estructura del disolvente orgánico líquido y la formación de complejos entre el CO_2 y las moléculas del disolvente orgánico. La segunda contribución a H_m^E se debe al cambio de estado del CO_2 desde el de un fluido similar a un gas o similar a un líquido hasta el de componente de la mezcla binaria. Designaremos a estas dos contribuciones respectivamente como contribución de interacciones moleculares y contribución de cambio de estado.

La acetona, la DMF, el DMSO y el EA son disolventes que no están asociados pero tienen todos ellos momentos dipolares grandes y presentan estructuras dominadas por las interacciones dipolo-dipolo. Por otro lado el CO_2 tiene un momento cuadrupolar relativamente grande. Estos valores de los momentos dipolares hacen que los disolventes sean líquidos muy estructurados con densidades relativamente grandes. La estructura del disolvente se altera al mezclarse con el dióxido de carbono y aparece una contribución endotérmica a H_m^E. Esta contribución se combina con otra contribución exotérmica debida a las fuertes interacciones entre el CO_2 y el disolvente orgánico resultando valores de la entalpía moderadamente exotérmicos: esta es la contribución de interacciones moleculares a H_m^E, contribución que puede esperarse que sólo cambie ligeramente al modificar la temperatura y la presión.

Para analizar la contribución de cambio de estado a H_m^E se necesita tener en cuenta el estado y las densidades de los dos componentes puros y las mezclas formadas en el calorímetro. Los disolventes orgánicos son líquidos en las condiciones de temperatura y presión de los experimentos. Sus densidades varían muy poco con la temperatura y presión. Sin embargo, el estado y la densidad del dióxido de carbono difieren mucho de unas

coordenadas (*P*, *T*) a otras. El dióxido de carbon es un fluido supercrítico que puede parecerse a un líquido cuando su densidad es grande, o a un gas cuando su densidad es pequeña.

El estado de las mezclas formadas en el calorímetro (líquido, fluido, dos-fases) puede establecerse examinando la situación de la coordenada (*P*, *T*) con respecto al locus crítico y teniendo en cuenta la composición crítica y los datos de VLE. Los sistemas CO_2 + acetona, CO_2 + DMF y CO_2 + EA son del tipo I en la clasificación de Scott y van Konynenburg; sus locus críticos completos se han calculado teniendo en cuenta los datos existentes. El comportamiento crítico del sistema CO_2 + DMSO es más complejo; puede tratarse de un tipo III o IV en esta clasificación.

El dióxido de carbono fluido se mezcla con el disolvente líquido formando una mezcla líquida o una mezcla gaseosa y otra líquida en equilibrio. Como consecuencia del cambio de estado del CO_2, esta contribución a H_m^E es exotérmica y se hace aún más exotérmica cuando se mezcla CO_2 de baja densidad. Este efecto se denomina a veces "efecto de la condensación del fluido". Cuando el dióxido de carbono entra en el calorímetro en un estado similar al de un líquido, la contribución de cambio de estado a H_m^E es pequeña y las entalpías molares de exceso pueden considerarse principalmente debidas a la contribución de interacciones moleculares a H_m^E. Cuando el dióxido de carbono entra en el calorímetro en un estado similar al de un gas, el efecto de la condensación del fluido es muy grande y la contribución de cambio de estado a H_m^E es muy exotérmica. En consecuencia, la entalpía molar de exceso alcanza valores de – 4500 J mol^{-1}.

Para una temperatura, presión y fracción molar dadas las variaciones debidas a la naturaleza del disolvente orgánico pueden atribuirse al tipo de diagrama crítico y a las diferentes interacciones moleculares en el líquido puro y las mezclas. Estas diferencias hacen variar la contribución de interacciones moleculares a H_m^E. Sin embargo, la magnitud de la contribución de cambio de estado puede esperarse que sea similar para los distintos disolventes si se fija la temperatura, presión y fracción molar y no hay equilibrio de fases.

Las mezclas formadas por CO_2 y un disolvente orgánico están implicadas en muchos procesos supercríticos además de SAS. Los datos de entalpías de exceso medidos en esta tesis

pueden usarse para modelar u optimizar estos procesos. En esta tesis el objetivo es examinar su interacción con el equilibrio de fases en el marco de los experimentos SAS.

Como ya se ha señalado el equilibrio de fases CO_2 + disolvente orgánico es uno de los factores cruciales que controlan la morfología y el tamaño medio de las partículas en el proceso SAS. La presencia del soluto puede modificar el diagrama de fases como en el caso de los polímeros. Sin embargo cuando el soluto interacciona débilmente con el dióxido de carbono, para las bajas concentraciones de soluto usadas en SAS, el diagrama de fases ternario coincide con el binario en la zona rica en CO_2, que es la zona de las mezclas formadas en SAS. Por tanto, estas mezclas pueden tratarse como sistemas binarios CO_2 + disolvente orgánico. El calor liberado al disolverse el CO_2 supercrítico en la disolución orgánica tiene un papel importante en el equilibrio de fases. El control de temperatura en la cámara de precipitación no es muy preciso y puede producirse un aumento local de temperatura. Por ello, si la precipitación comienza en condiciones de T y P de miscibilidad completa para el sistema CO_2 + disolvente orgánico, en un corto tiempo puede producirse la separación de fases.

Puesto que el CO_2 se introduce en la cámara a un flujo mucho mayor que el de la disolución y como la concentración del soluto en la misma es pequeña, la contribución a H_m^E debida a las interacciones del soluto puede despreciarse y se puede considerar que los efectos térmicos en SAS se deben a la formación de mezclas CO_2 + disolvente orgánico muy ricas en CO_2 ($x \geq 0.95$). Suponiendo un proceso adiabático y utilizando la capacidad calorífica del CO_2, pueden usarse los valores de H_m^E para estimar el incremento de temperatura en la cámara de precipitación. Estas estimaciones permiten explicar las morfologías de precipitados observadas que no eran de esperar en las condiciones de operación.

El efecto de la entalpía en el equilibrio de fase se ha mostrado para micronizaciones con DMSO como disolvente descritas en la bibliografía, que han sido llevadas a cabo en una cámara provista de ventana. Al modificarse el equilibrio de fases se modifica el mecanismo de precipitación de partículas cambia. Hay otros factores que influyen simultáneamente en la morfología de las partículas, pero el calor liberado al mezclarse el CO_2 y el disolvente polar tiene un importante papel.

Capítulo 5. Micronizaciones SAS de Fármacos

- **Validación del aparato SAS: Micronización del Acetato de Itrio**

Se eligió la micronización del YAc a partir de disoluciones de DMSO para validar el equipo SAS construido en nuestro laboratorio. Los experimentos se llevaron a cabo a temperaturas de 40 y 60 °C y presiones entre 11 y 20 MPa. La concentración del YAc se mantuvo constante en 2%. La morfología de las partículas se estudió teniendo en cuenta el equilibrio de fases del sistema CO_2 + DMSO. Las imagines SEM del YAc precipitado en condiciones de solubilidad completa del CO_2 + DMSO muestran nanopartículas esféricas discretas o ligeramente agregadas. Por el contrario al trabajar en la zona de dos fases las partículas se agregan formado un bloque. El tamaño medio de las partículas disminuye al aumentar la presión. Para establecer si las condiciones de precipitación corresponden a una o dos fases se tuvo en cuenta, además del equilibrio de fases, las entalpías de exceso de CO_2 + DMSO, puesto que el proceso de mezcla puede producir un incremento de *T* en la cámara que afecta al equilibrio de fases. Así a 60 °C y 14 MPa la mezcla del DMSO y el CO_2 es muy exotérmica y el incremento de temperatura estimado (≈ 4°C) produce separación de fases. Las condiciones de *P* y la nueva *T*, 64 °C, corresponden a la zona de dos fases donde se obtienen partículas agregadas.

Estos resultados están de acuerdo con los obtenidos por Reverchon et al. Este equipo SAS se usó para micronizar 5-fluorouracilo, diflunisal y para coprecipitar diflunisal y PVP.

- **Micronización del 5-Fluorouracilo**

El 5-Fluorouracilo (5-FU) es un fármaco de la familia de la pirimidina utilizado en el tratamiento de varios tipos de cáncer, soluble en DMSO y con una solubilidad baja en CO_2. Se eligió DMSO como disolvente. Los factores que influyen en el proceso SAS son: la concentración de la disolución (*C*), la temperatura (*T*), la presión (*P*), el flujo de la disolución (Q_L), el flujo del CO_2 (Q_{CO2}), el tiempo de secado (*t*), y el diámetro del nebulizador ($Ø_n$). En esta tesis el tiempo de secado (3 veces el tiempo necesario para llenar la cámara) y el diámetro del nebulizador (100 μm) se mantuvieron constantes. Para disminuir el número de experimentos se aplicó una metodología DOE y se utilizó el diseño 2^{5-2} fraccional factorial reduciéndose el número de experimentos a ocho. El valor de la fracción molar del CO_2 fué ≥ 0.96. Como respuesta se usaron el tamaño medio de las partículas y su morfología evaluadas a partir de las imágenes SEM.

Las imágenes SEM del 5-FU no tratado muestran partículas granuladas con un tamaño medio > 100 μm. Los experimentos SAS se llevaron a cabo a 40, 50 °C; 15, 18 MPa; y concentraciones de 1 o 2 (%). Las imágenes SEM del 5-FU precipitado indican que seis de los ocho experimentos (1, 2, 5, 6, 7 y 8) conducen a una micronización del 5-fluorouracilo. Se obtienen partículas elongadas con tamaños medios en el intervalo 216-670 nm. En los experimentos 3 y 4 no se produjo la micronización obteniéndose partículas mucho mayores.

Para una concentración dada, el tamaño medio de las partículas disminuyó al aumentar la temperatura y la presión. El orden de importancia encontrado para los factores que influyen en el tamaño medio de las partículas y su morfología fue

$$T > P > C >> Q_L > Q_{CO2}$$

Las mejores condiciones para al micronización del 5-FU fueron las del experimento 7: C = 1%, T = 50 °C, P = 180 MPa, Q_L = 1 mL/min, Q_{CO2} = 15 g/min, condiciones que condujeron al mejor tamaño medio de partícula, 216 nm.

La cristalinidad de las partículas se estudió por XRD. Para el 5-FU aparece un pico muy intenso a 28.7 grados que sugiere una orientación preferencial en esta posición. Esta orientación preferencial desaparece en el 5-FU precipitado por SAS, lo que indica una disminución de la cristalinidad.

- **Micronización del Diflunisal**

El diflunisal es un fármaco antiinflamatorio no esteroideo muy soluble en DMSO y poco soluble en CO_2. Sin embargo, experimentos preliminares llevados a cabo en condiciones similares a las de los experimentos SAS del YAc y del 5-FU mostraron que el DMSO no era un disolvente adecuado. Sin embargo, si tuvieron éxito los experimentos SAS con acetona. Estos experimentos se llevaron a cabo a 40 °C; 9, 12 y 15 MPa, y concentraciones del 2 y el 4%. Se estimó que los incrementos de temperatura dentro de la cámara de precipitación, ΔT, podían ser de hasta 5.5 grados. Como las condiciones de P y T no estaban próximas al MCP, estos incrementos de temperatura no pueden producir separación de fases.

Las imágenes SEM del diflunisal no tratado muestran barras grandes y delgadas de un material cristalino. En las del material precipitado por SAS se observan barras cristalinas delgadas y largas, unidas entre sí como si se tratase de las ramas de un árbol. La anchura de

las barras varió entre 2 y 10 μm. Las imágenes SEM indican que la cristalinidad y la morfología apenas cambian al variar las condiciones de precipitación. Resultados similares se obtuvieron al precipitar el diflunisal a partir de us disoluciones en acetona/diclorometano (DCM) (80:20, v/v %). La precipitación del diflunisal puro no parece modificarse ni con las condiciones ni con el disolvente utilizados.

Se han encontrado hasta cuatro formas polimórficas del diflunisal cristalino. Los difractogramas XRD del diflunisal no tratado y del procesado por SAS son distintos, indicando que el polimorfismo del diflunisal se ha modificado en el proceso the SAS. El fármaco precipitado exhibe la forma IV. El difractograma del diflunisal no tratado sugiere la mezcla de dos polimorfos. Esto se confirma por los termogramas DSC que muestran un pico dividido con dos puntos de fusión a 216.62 y 213.82 °C para el diflunisal no tratado y un solo pico para el diflunisal obtenido por SAS a 212.63 °C, que corresponde al punto de fusión de la forma IV.

- **Amorfización del Diflunisal por Coprecipitación con PVP**

Se consideró que la coprecipitación SAS del diflunisal con PVP era un método efectivo para incorporar el fármaco en estado amorfo. Se investigó la influencia de dos tipos del polímero en las propiedades físico-químicas del diflunisal usándose PVP *K*-10 ($\overline{M}_w$ = 10,000) y PVP *K*-30 ($\overline{M}_w$ = 40,000). La precipitación SAS de PVP utilizando etanol a las presiones de 8 y 12 MPa, temperaturas de 35 y 40 °C y concentraciones del 2% y 5% (fracción molar de $CO_2 \geq 0.96$) no tuvo éxito. Como el PVP es poco soluble en acetona, se usó una mezcla de un buen y un mal disolvente del polímero. Se eligió DCM como buen disolvente y acetona como malo, usándose la mezcla acetona/DCM (80:20, v/v %).

En primer lugar se precipitó, PVP *K*-10 con acetona/DCM (80:20, v/v %) a una temperatura de 35 °C, presión de 9 MPa, concentración del 2% y un valor de 0.97 para la fracción molar del CO_2, obteniéndose partículas esféricas con un tamaño medio de 230 nm. A continuación se coprecipitó el diflunisal con PVP *K*-10 para una proporción fármaco: polímero en masa de (50:50) a 35 y 40 °C, presiones en el intervalo de 8 a 15 MPa, concentración del 2 y 4% y dos diferentes fracciones molares del CO_2, 0.84 y 0.97. A 35 °C y presiones entre 8 y 9 MPa se obtuvieron disoluciones viscosas que se transformaron en precipitados pegajosos al aumentar la temperatura hasta 40 °C. Aumentando la presión hasta

12 MPa a 35 °C se obtuvieron globos esféricos con tamaño decreciente al aumentar la presión, pero al aumentarla hasta 15 MPa aparecía coalescencia de las partículas. Sin embargo, estaba claro que la cristalinidad del diflunisal desaparecía en el coprecipitado en comparación con el diflunisal puro obtenido por SAS a partir de la misma mezcla de disolventes.

En segundo lugar, se usó PVP *K*-30 en las mismas condiciones experimentales obteniéndose unos resultados mucho mejores. Esto puede atribuirse al efecto plastificante del. CO_2 sobre los polímeros que disminuye al aumentar la masa molecular. Al igual que en el caso del PVP *K*-10, la cristalinidad del diflunisal desapareció durante la coprecipitación con respecto al diflunisal puro obtenido por SAS a partir de la misma mezcla de disolventes. El tamaño medio del coprecipitado diflunisal + PVP *K*-30 es 5 veces más pequeño que el obtenido con PVP *K*-10. El aumento de la masa molecular trajo consigo una reducción importante del tamaño de las partículas.

Para comparar se precipitó PVP *K*-30 solo usando acetona/DCM (80:20, v/v %) a 35 °C, 14 MPa y concentración de 2 %. Las imágenes SEM muestran nanopartículas esféricas con tamaños medios de 210 nm.

Para estudiar la influencia de la proporción fármaco: polímero en los coprecipitados de diflunisal + PVP *K*-30 usando acetona/DCM (80:20, v/v %) se eligieron las proporciones en masa 75:25, 50:50 y 25:75, la temperatura de 35 °C, la presión de 14 MPa, la concentración del 2 % y un valor de 0.97 para la fracción molar del CO_2. La cristalinidad del diflunisal desapareció incluso en el coprecipitado con menos cantidad de polímero. El coprecipitado con proporción 75:25 está formado por partículas esféricas con tamaños medios inferiores a 10 μm que están muy agregadas formando bloques. El coprecipitado con proporción 25:75 está formado por partículas sueltas con tamaño medio de 460 nm y muy poca agregación en comparación con el de proporción 50:50.

Los coprecipitados diflunisal + PVP *K*-30 con proporciones en masa 75:25, 50:50 y 25:75 se caracterizaron por XRD, FTIR y DSC, estudiándose también su velocidad de disolución en comparación con la del fármaco puro. Los difractogramas XRD muestran que el diflunisal procesado por SAS es un material cristalino mientras que el PVP *K*-30 procesado por SAS es un material amorfo. La cristalinidad del diflunisal desapareció en los coprecipitados sin que

se observe variación en su amorfización cuando se aumenta el contenido del PVP *K*-30 del 25 % al 75 %. El efecto inhibidor de la cristalinidad del diflunisal causado por el polímero puede atribuirse a la interacción del fármaco con el PVP, que produce un cambio en la movilidad molecular del mismo, resultando una forma amorfa del diflunisal. El espectro FTIR muestra ensanchamientos y desplazamientos de bandas con respecto a los espectros del fármaco puro y del PVP *K*-30 que pueden atribuirse a interacciones de los grupos funcionales. El ensanchamiento de la banda correspondiente al grupo carbonilo del diflunisal (1690 cm^{-1}) en los tres coprecipitados indica la formación de un enlace de hidrógeno intermolecular entre el diflunisal y el PVP *K*-30. Todos estos resultados apuntan a un cambio importante en la simetría total de la molécula del fármaco en la matriz polimérica sólida del coprecipitado.

Para investigar mejor la interacción del diflunisal con el PVP y para comprender mejor la estructura de los coprecipitados se hicieron estudios de DSC y TGA. En los termogramas DSC de los materiales "composite" aparece una banda ancha debida a la pérdida de agua con un hombro a 75-125 °C que se desplaza a temperaturas más altas al aumentar la concentración del PVP. Esto puede deberse a la presencia de moléculas de agua en el material "composite" en una forma distinta a la del PVP y la del diflunisal puros. Los tres coprecipitados muestran dos picos de descomposición atribuidos respectivamente al polímero y al fármaco. Además hay un desplazamiento claro de la temperatura de descomposición del fármaco al aumentar la concentración del polímero a temperaturas altas que también apoya la interacción fuerte entre el diflunisal y el PVP *K*-30. Las curvas TGA de los tres coprecipitados muestran que las composiciones de los mismos están próximas a las composiciones de partida. La descomposición de los tres coprecipitados tiene lugar en dos etapas. La primera etapa comienza a una temperatura muy próxima a la temperatura de descomposición del fármaco y la segunda etapa comienza a una temperatura muy próxima a la temperatura de descomposición del polímero.

The resultados obtenidos por XRD, IR, DSC y TGA indican que la cristalinidad del diflunisal desapareció en el proceso de coprecipitation sugiriendo que el fármaco se incorpora en el seno del polímero a nivel molecular.

Se llevaron a cabo pruebas de disolución usando el método del disco rotatorio en un fluido intestinal simulado (tampón de fosfato de pH 7.4) para el fármaco puro, tratado y sin tratar, y para los tres coprecipitados obtenidos con las proporciones en masa fármaco: polímero de

75:25, 50:50 y 25:75. Los perfiles de disolución se siguieron por espectroscopia UV-VIS a 275 nm. Todas las velocidades de disolución de los coprecipitados diflunisal + PVP *K*-30 fueron superiores a las del diflunisal puro, tratado y sin tratar. A un tiempo dado, la liberación del fármaco aumentó al aumentar el contenido de PVP *K*-30; la velocidad de disolución más alta se observó para el coprecipitado con 75 % de PVP *K*-30. Para los "composite" diflunisal + PVP *K*-30 aproximadamente el 75 % del fármaco se disolvió transcurridos 20-30 min.

Las propiedades de nuestros coprecipitados son semejantes o mejores que las de otros coprecipitados fármaco-PVP obtenidos por SAS y GAS y las de la mezcla física y las dispersiones sólidas diflunisal-PVP *K*-30 descritas en la bibliografía. Deben subrayarse dos aspectos clave: la buena morfología y pequeño tamaño de los "composites" obtenidos en este estudio, y las velocidades de disolución más rápidas que demuestran el potencial del PVP como agente para la amorfización y estabilización de un fármaco poco soluble en agua como el diflunisal.